UNIVERSITY OF SOUTHAMPTON

Faculty of Engineering and the Environment

national Centre for Advanced Tribology at Southampton (nCATS)

Electrodeposition of nickel-based composite coatings for tribological applications

By

Yang He (BSc, MSc)

Supervisors: Dr. Shuncai Wang; Prof. Philippa A.S Reed

A thesis submitted to

The University of Southampton

for the degree of Doctor of Philosophy

September 2015

Abstract

The purpose of this research is to study, evaluate, and compare the different electro-deposition processes for producing nickel-based composite coatings for application in tribology, including: Ni/BMA luminescent coating, Ni-P/MoS_2 and Ni-P/WS_2 self-lubricating coatings.

In the first part, a new luminescent Ni coating containing an embedded, blue-emitting rare-earth mixed metal oxide ($BaMgAl_{11}O_{17}:Eu^{2+}$) BAM was electrodeposited successfully from an aqueous electrolyte. Two types of surfactants were utilised to investigate the effective co-deposition of these phosphors into the nickel matrix. The surfactants of non-ionic PEG (polyethylene glycol) and cationic CTAB (cetyl trimethylammonium bromide) were observed to increase the phosphor contents in the deposit from zero to 4.6% and 11.5%, respectively. A mixture of these two surfactants produced the highest particle embedded coverage (15.6%). Systematic study of the hardness, corrosion, tribological and luminescent properties of the as-deposited coating was performed before using it for wear sensing.

In the second and third parts of this research, a self-lubricating Ni-P/MoS_2 composite coating has been designed and deposited on a mild steel substrate by electrodeposition. The effect of current density, electrolyte additive and MoS_2 concentration on the structure of the coating have been investigated. The Ni-P/MoS_2 coating exhibited a dramatic reduction in friction compared to an electrodeposited Ni-P coating, the coefficient of friction against a bearing steel ball in sliding wear being as low as 0.05. The worn surfaces and the wear debris were characterised by surface analysis techniques. The composite coating showed only slight wear and oxidation compared to the severe wear and oxidation observed in the pure Ni-P coating or the uncoated mild steel substrate. It has been speculated that MoS_2 in the coating underwent shear stress-induced reorganization, fragmenting into fine crystallites and ultimately forming a smooth lubricating film.

In the final part, Ni-P/WS_2 composite coatings have been electrodeposited from an aqueous bath containing suspension of WS_2 nanoparticles (80 nm) and their tribological properties have been evaluated by a reciprocating test with bearing steel balls. Increasing the bath temperature did completely eliminate the cracks in coatings by reducing the

internal stress and prolonged the duration of the low friction coefficient. By optimizing the combinations of the WS_2 and CTAB concentrations in solution, the amount of the WS_2 particles incorporated was greatly boosted, demonstrating a highest WS_2 content of 4.8 wt%. Significantly, this Ni-P/WS_2 coating exhibited a greatly lower friction coefficient of 0.17 compared to single Ni-P (0.6).

Table of Contents

List of Tables

List of Figures

Declaration of Authorship

I, Yang He

declare that the thesis entitled

“Electrodeposition of nickel-based composite coatings for tribological applications”

and the work presented in the thesis are generated on my own as a result of original research. I confirm that:

- this work was done wholly or mainly while in candidature for a research degree at this University;
- where any part of this thesis has previously been submitted for a degree or any other qualification at this University or any other institution, this has been clearly stated;
- where I have consulted the published work of others, this is constantly attributed;
- where I have quoted from the work of others, the source is always given. With the exception of such quotations, this thesis is entirely my own work;
- I have acknowledged all main sources of help;
- where the thesis is based on work done by myself jointly with others, I have made clear exactly what was done by others and what I have contributed myself;
- parts of this work have been published as journal papers listed in Appendix: B.
-

Signed: . . . . . Date:. . . . . .

Acknowledgements

First of all, it is a genuine pleasure to express my sincere thanks and gratitude to my mentor, philosopher and guide Dr. Shuncai Wang and Prof. Philippa A.S. Reed. Their invaluable guidance, meticulous scrutiny, and scientific approach have helped me to a great extent to accomplish this work.

I would like to thank all my college in Faculty of Engineering and the Environment: Dr. Xiaohong Li, Dr. Mengyan Nie, Dr. Jurgita Zekonyte, Dr. Terry J Harvey and Dr. John Walker, who provided techniques training.

I am thoroughly grateful to Prof. Franck C. Walsh at the University of Southampton for suggestions on electrodeposition and paper corrections, Dr Hansjürgen Schuppe at the University of Southampton for assistance with the fluorescent imaging, and Dr. Yu Lung Chiu in University of Birmingham for technical support on preparation of FIB samples.

Lastly, a sincere thanks to everyone who encouraged me and shared their support: my parents and family, Wanting Sun, Isaac Robertson-Jonas, Chao Ma, Joshua Huntingford, Feifei Zhang, Liping Fang, Rong Jiang, Binyan He and Timothy Kamps.

Chapter 1 Introduction

1.1 Background and motivation

Surface coatings play an important role in prolonging the lifetime of components, improving the mechanical performance of parts and extending their application range. Coatings used for tribology can reduce wear and friction between interacting surfaces in relative motion, and make devices more efficient. There has been a growing use of these coatings in the automotive, aerospace and power generation industries [1].

It is unavoidable that the area in contact is worn or corroded faster than the remaining area, which may result in pre-failure, catastrophic damage or loss. Where it is expensive to replace the whole workpiece or costly to apply conventional inspection and downtime maintenance, there is a clear benefit in extending the coatings' life safely. This will depend on developing a health sensing system in coatings to monitor deterioration during their use.

A number of wear sensing techniques have been developed to monitor wear processes, for example: oil analysis, acoustic emission, vibration, luminescent sensors [2]. Luminescent coatings, however are a relatively new approach in these sensor techniques, with many advantages such as speed, visibility and high adaptability [3]. Luminescent coatings were first proposed in 2004 [4] to detect damage such as scratches and delamination of the coating. It utilises the fact that phosphorescent/fluorescent particles emit a constant glow under an ultraviolet (UV) light, thus such a coating can act as an interlayer that can be revealed when a top coating is worn away or corroded. Reviews of the literature, however, reveal few successful studies published in this field. Physical vapour deposition (PVD) was first used to sputter a phosphorescent / fluorescent film which emitted a constant glow under a UV light. Erbium- and samarium-doped yttria stabilized zirconia layers, for example, were deposited in thermal barrier coatings [5,6]. The disadvantage of this method is its reliance on expensive and less flexible facilities

with limited deposition rates. In addition, the produced film is in general too thin to be used as coating protection in wider engineering applications.

Aqueous deposition, as opposed to non-aqueous deposition, achieves a reasonable balance between cost and performance. Electroless deposition and electrodeposition are two classical approaches. The former has the advantage of non-line-of-sight coatings but suffers from unstable solutions as well as a slow rate process with a maximum thickness of a few microns, which again limits its applications. In contrast, electrodeposition has a much faster deposition rate and allows better control of the deposition process. It is one of most successful methods for producing composite layers by electrophoretic deposition of particles into a growing metal electrodeposit, despite the challenges including the dispersion of particles in the bath and its adhesion ability to the electrode surface. The thickness can be well controlled from a few nanometres to several hundred micrometres. A review of the literature, however, reveals few successful cases of preparation of luminescent coatings by aqueous deposition. One limited report is found on electroless deposited luminescent nickel coating [7,8]. The second case reports electrodeposited nickel and rare-earth luminescent phosphors using ionic liquids bath of dimethylsulfone and $NiCl_2$ [9]. The plating was carried out at a temperature of 130 ℃ which would prevent potential industry applications with such a high bath temperature. Furthermore, ionic liquids are expensive to scale up and can involve supply, handling and disposal problems, making their use unattractive to industry.

The first part of this thesis aims to develop a Ni coating embedded with phosphorescent particles ($BaMgAl_{11}O_{17}:Eu^{2+}$, BAM) which are used to detect the wear condition of coatings simply using an ultraviolet light. The challenge for electrodeposition in an aqueous solution is that the rare earth luminescent particles (metal oxides), of micron size, are difficult to stick on the electrode surface. Two types of surfactants - cationic (cetyltrimethylammonium bromide, CTAB) and non-ionic (polyethylene glycol, PEG) were studied to assess their enhancement of particle deposition. The particle concentrations were also investigated by steady-state and time-resolved luminescence spectroscopy to optimise the emission intensities [10].

Ni-based coatings, formed by electrochemical reduction, usually exhibit high hardness and wear resistance, with various applications in aircraft, automotive, marine, electronics and so forth [11,12,13]. It has been suggested as a promising substitute to replace hard

chrome coatings which have raised severe health and environmental problems and will soon be banned. Alternative Ni-Co and Ni-Co-P coatings have been successfully electrodeposited by our group which could provide similar or even greater benefits compared to chrome [14,15].

Nowadays, low-friction coatings have attracted much research interest due to their low energy consumption and CO_2 emission. However, the coefficient of friction for electrodeposited Ni coatings is relatively high (ca. 0.4-0.7) under dry friction. To extend the application of such electrodeposited coatings, functional particles could potentially be added into the electrodeposition bath to obtain a composite coating with enhanced properties (i.e. adhesion, wear rate reduction, load bearing capacity, low friction) [16,17]. Molybdenum disulphide (MoS_2) with characteristic lamellar structure has a super-low-friction coefficient of 0.002 in a vacuum, since the weak Van der Waals forces between adjacent lamellas allow for easy interplanar shear [18]. Several attempts have been made to achieve electrocodeposition of Ni with MoS_2 particles including Ni-MoS_2, Ni-MoS_2/Al_2O_3, Ni-W/MoS_2 and Ni-Co/MoS_2 coatings, which exhibit low friction coefficients between 0.1 and 0.4 [19,20,21,22]. But the lowest friction coefficient varies a lot in these reports and the primary factor responsible for low friction coefficient is still unclear, therefore systematic comparison of coating parameters and the resultant friction coefficient is desirable.

Electrodeposited Ni-P alloys with amorphous or nanocrystalline structures possess many advantages over Ni-metal coating including higher hardness, higher strength and better wear resistance. A Ni-P/MoS_2 composite coating is designed to outperform other metal/MoS_2 coatings, as the MoS_2 are well protected inside a Ni-P matrix with increased chemical inertness and are less susceptible to H_2O or O_2. Despite these many advances, there appear to be no reports concerning electrodepositing Ni-P/MoS_2 coating. This is because appropriate surfactant is needed to disperse the MoS_2 particles and stabilize them uniformly in the bath by increasing their wettability. In the second part of this study, Ni-P/MoS_2 coatings were codeposited with the addition of the cationic surfactant CTAB (hexadecyltrimethylammonium bromide). The coating structure and MoS_2 content was optimised by varying the current density, CTAB and particle concentrations.

In the third part of this study, systematic friction testing and wear track examination were carried out to evaluate the friction and wear properties of the as-deposited Ni-P/MoS_2

coatings and the primary factor affecting the drop in friction coefficient is also discussed. Furthermore, to clarify the lubrication function of MoS_2, a cross-section sample from the wear track was prepared by focused ion beam (FIB) and observed under TEM. A possible self-lubricating mechanism of the Ni-P/MoS_2 coatings is proposed.

Like MoS_2, tungsten disulphide (WS_2) is a widely used solid lubricant due to the easy shearing of the weak (van der Waals) interlayer bonds. WS_2 shows better lubricating performance than MoS_2 under harsh environments such as high temperature. The working temperature limitations of MoS_2 and WS_2 in air are 316 ºC and 594 ºC respectively, above which their lubricating ability is lost rapidly due to oxidation. However, the reactive dangling bonds on the prismatic edges $(10\bar{1}0)$ of WS_2 are susceptible to humidification and oxidation which usually result in degradation of lubrication. Therefore, it appears worthwhile to prepare composite Ni-P/WS_2 coatings, in which WS_2 are encapsulated in the matrix and only exposed to the air when friction occurs. In the fourth part of this work, nano-WS_2 (80 nm diameter) incorporated Ni-P coatings were electrodeposited on a mild steel substrate. Different bath temperatures, CTAB and particle concentrations were studied and estimated in an attempt to produce a composite coating with both low-friction and low-wear performance.

1.2 Outline

This thesis is divided into seven main chapters (including this introduction). These are: Chapter 1 - Introduction; Chapter 2 - Review of the literature; Chapter 3 - Experimental procedure; Chapters 4, 5, 6 & 7 - Results; Chapter 8 Overall discussion and Chapter 9 - Future work.

The literature review is contained in Chapter Two. First, it presents a general review of the literature on surface engineering and electrodeposition techniques. Subsequently, the review focuses on electrodepositing of luminescent coatings and MoS_2/WS_2 low friction coatings.

Experimental procedures are covered in Chapter Three. The general techniques employed to investigate the microstructure and mechanical properties of electrodeposited coatings are X-ray diffraction, optical microscopy, scanning electron microscope (SEM), energy dispersive spectroscopy (EDS), image analysis and Vickers hardness tests. Photoluminescence of Ni/BAM was evaluated by visible- UV/fluorescence spectrometers and Zeiss AxioSkop fluorescence microscopy. A reciprocating TE-77 tribometer was used to evaluate the friction behaviours of Ni/BAM, Ni-P/MoS_2 and Ni-P/WS_2 coatings. Alicona infinite focus microscopy, BEI in SEM, FIB and TEM were used for examination of the wear track.

The experimental results are displayed and discussed in Chapters Four to Seven. Chapter Four presents the monitoring of coating health by in-situ luminescent layers. Chapter Five presents the development of Ni-P/MoS_2 composite coatings by electrodeposition. Chapter Six illustrates the friction and wear properties of the electrodeposited Ni-P/MoS_2 coatings. Chapter Seven is concerned with the fabrication of self-lubricating Ni-P/WS_2 coatings by electrodeposition.

In Chapter Eight, overall discussion of the results has been made. Finally, overall conclusions have been drawn and proposals for future work have been made in Chapter Nine.

Chapter 2 Review of literature

2.1 Introduction to surface engineering

2.1.1 Advantages of surface engineering

Usually a machine component failure starts from the surface which cannot withstand the surrounding environment or external forces. In many cases, it may not be realistic to use expensive materials with high performance for bulk components to meet the surface service requirement. A more practical approach is to use a high-performance coating [23]. A range of coatings can improve the surface functionality of a substrate in terms of thermal, optical, magnetic, tribological and electrical properties [24]. In fact, it is now difficult to find a manufactured item which has not experienced some form of surface engineering [25].

Surface engineering is widely used in the automotive, aerospace, missile, power, electronic, machine tools, and construction industries [26]. It directly contributes to the worldwide economy. In the UK the cost of wear and corrosion are significant, up to 3% of GDP [27]. Effective use of surface engineering has great potential to produce significant economic benefits [28]. In 2005, the value of the UK coating market was approximately £21.3 billion, and those coatings further affect products with a value of over £143 billion [28].

In brief, surface engineering can increase performance, reduce costs and control surface properties independently of the substrate, offering enormous potential for [29]:

- improved functionality
- a solution to previously insurmountable engineering problems
- the possibility of creating new products
- reduction of power consumption
- conservation of scarce material resources

2.1.2 Surface engineering techniques

There are a number of general methods developed for surface engineering and coatings, as illustrated in Fig. 2.1 [30].

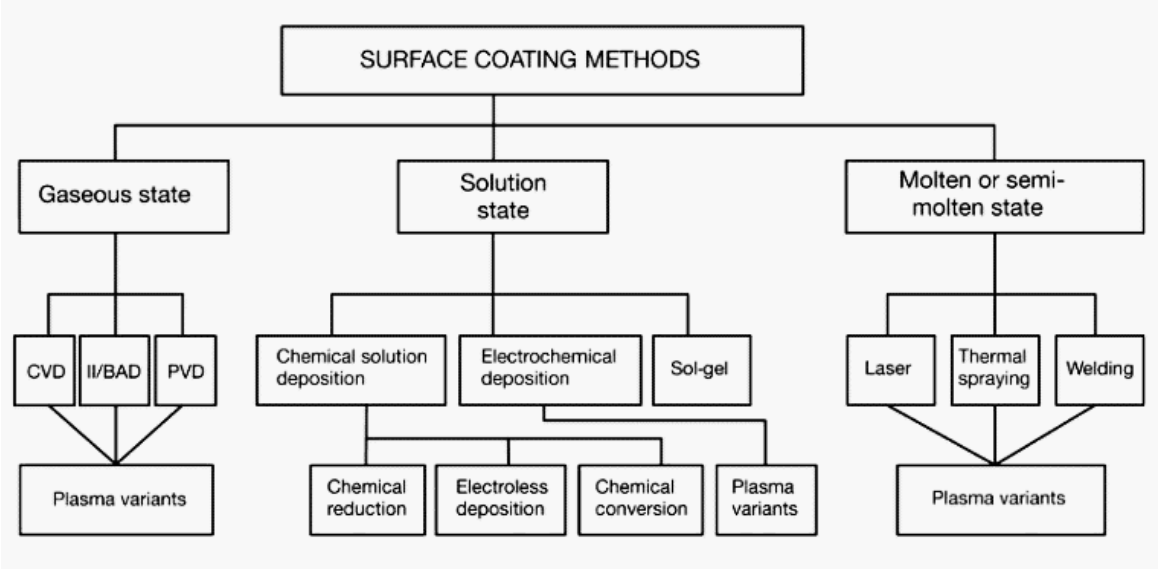

Figure 2.1 A general classification of surface engineering techniques [30].

The gaseous state method is usually used in the preparation of thin films. Thin film techniques are applied in many applications, including sports, microelectronics, magnetics, optics, micro-mechanics, bio-medical, etc. Among gaseous state techniques, PVD (physical vapour deposition) and CVD (chemical vapour deposition) are commonly used in industry. For instance, the thin films used in solar cells, flat panel displays and semiconductors, are deposited using either PVD or CVD [31].

More advanced applications of the techniques are as plasma enhanced- PVD, either magnetic sputtering or ion beam sputtering [32]. Activated by a strong electron and magnetic field or bombardment by an ion beam, high energy particles of materials in atomic form are ejected from a "target" that is a source onto a "substrate" such as a silicon wafer. The most commonly used sputtering gas is inert argon. For efficient momentum transfer, the sputtering gas should have a close atomic weight to the target, so for sputtering light elements neon is preferable, while for heavy elements krypton or xenon are useful [33,34]. Advantages of these sputtering techniques are: relatively high deposition rates and low substrate heating. However, it is hard to deposit complex "shadowed" parts as the sputtered ions fly from the target in straight lines-of-sight to the substrate.

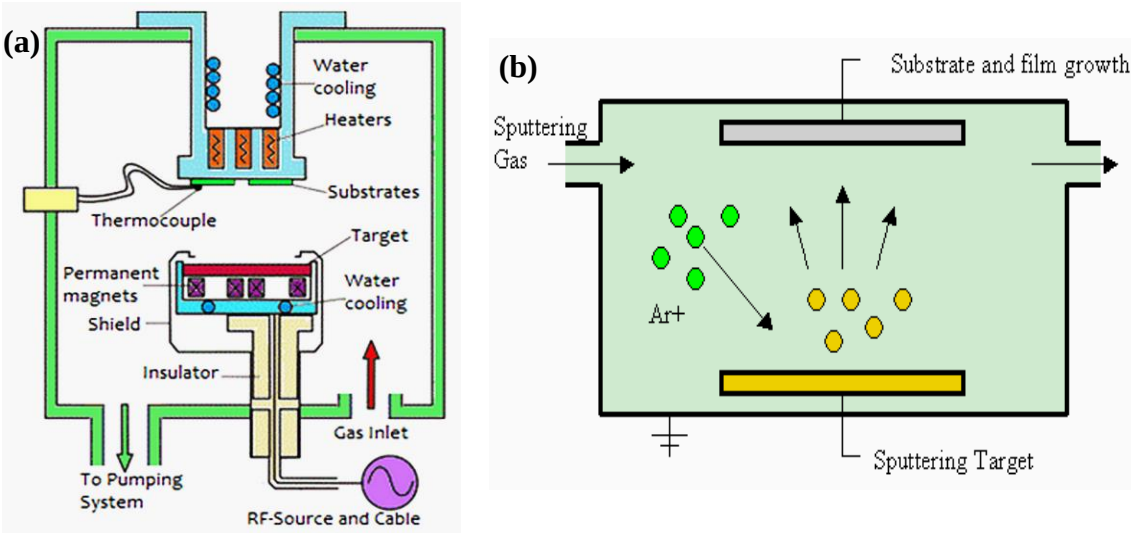

Figure 2.2 Sputtering deposition techniques - (a) magnetic sputtering, (b) Ion beam sputtering [33].

In molten or semi-molten techniques, thermal spraying is the most versatile technique available to prepare protective coatings. As listed in Fig. 2.3 oxygen and acetylene gas flowing through a flaming torch will draw in the deposition powder and mix with it. After that, the mixtures exit the torch though a nozzle and reach the target substrate. Common materials such as metals, polymers and ceramics are most commonly used as thermal sprayed coating materials [35,36,37].

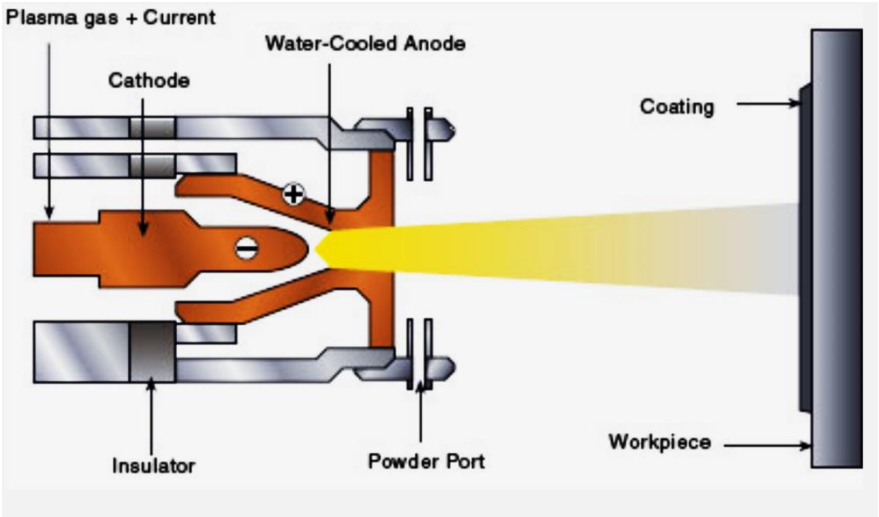

Figure 2.3 Schematic cross-section of a typical plasma spray gun [36].

The solution state technique is a surface modification process in which ions are deposited onto the substrate in an electrolyte. These processes can improve a substrate material's properties of hardness, wear resistance and corrosion resistance, thus improving the product's service life.

Electrochemical deposition involves the component being coated within an electrolyte cell which contains a chemical solution with the ionic form of the metal. The metal ions are then supplied with electrons to form a coating on the component (which acts as a cathode). The most common metals electrodeposited are nickel (Ni) and copper (Cu). The coating properties can be tailored by varying the experimental variables, for instance, temperature, current density, additives, flow condition, electrolyte composition, and so on [38]. It has many benefits over other techniques including i) suitable for preparation of pure metals, alloys and composite materials, ii) no shape limitation, iii) grain size less than 100 nm, iv) low cost, v) simple operation and vi) relatively stable.

Similar to electrodeposition, electroless deposition can deposit a metallic layer onto the surface of a part. But the process is non-galvanic, involving several simultaneous chemical reactions in an aqueous solution. The reduction reaction of the metal ion is accomplished by a reducing agent, normally sodium hypophosphite. Without the use of electrical power, the deposition rate is much slower than that by electrodeposition, therefore electroless deposition is not suitable for depositing a thick coating.

2.1.3 Composite electrodeposition

Metal matrix composite coatings can be manufactured by particle incorporation during metal deposition from a bath containing a suspension of ceramic particles [39]. The electrocodeposition process is the most widely used technique to produce a metal matrix coating due to its simplicity as schematically depicted in Fig. 2.4.

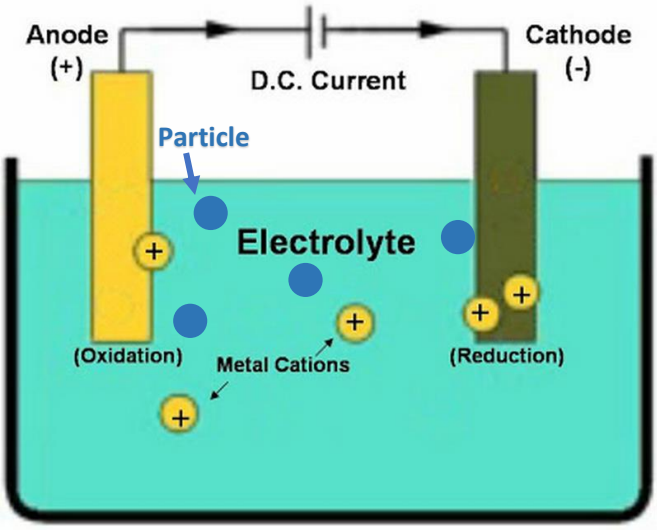

Figure 2.4 Schematic diagram of composite electroplating [40].

A growth model is important in understanding the relationship between bath composition, electrodeposition conditions and the resulting coating properties [17, 41]. Based on various approaches, a range of models have been developed to interpret the behaviour of composite electrodeposition as summarised in (Table 2.1).

Table 2.1 Summary of theoretical models for composite electrodeposition [16].

Model	Approach taken and assumptions made	Composites	Process conditions		
			Particles size /μm	Current density /mA cm^{-2}	Rotation speed / rpm
Guglielmi, 1972	Describes both adsorption and electrophoresis. The particles are covered by adsorbed metal ions. Particle characteristics and electrolyte conditions are accounted for semi-empirically. The effect of flow is not considered.	Ni-TiO_2 Ni-SiC	1-2	20-100	Not given
Celis, Roos & Buelens, 1987	Uses probability to describe the amount of particles that are likely to be incorporated at a given current density. Mass transport of particles is proportional to the mass transport of ions to the working electrode. Volume ratio of particles in the metal deposit will increase under charge transfer control and decrease under mass transport control.	Cu-Al_2O_3 Au-Al_2O_3	0. 05	0-90	400-600
Fransaer, Celis & Ross, 1992; Maurin & Lavanant, 1995	Uses trajectory to describe the codeposition of non-Brownian particles. Involves two steps: reduction of metal ions (described by Butler-Volmer expression) and codeposition of particle (described by a trajectory expression).	Cu-PS (polystyrene) Ni-SiC	11 0. 01-10	0-80 0-200	0-700 0-2000
Hwang & Hwang, 1993	An improvement of Guglielmi's model which uses three modes of current density (low, intermediate, high) to distinguish the reduction of adsorbed ion on particles. Involves three steps: forced convection of particles to surface, loose adsorption on the surface and irreversible incorporation of particles by reduction of adsorbed ions.	Co-SiC	3	1-60	400
Vereecken, Shao, & Searson, 2000	The transport of particles to the surface is controlled by convective diffusion. The influence of particle gravitational force and hydrodynamics is accounted for at various current densities. Valid only when the particle size is smaller than the diffusion layer thickness.	Ni-Al_2O_3	0. 3	5-40	500-2000
Bercot, Pena-Munoz & Pagetti, 2002	An improvement of Guglielmi's model, which incorporates a 3rd order polynomial correction to account for the effects of adsorption and flow.	Ni-PTFE (polytetrafluoroethylene)	0. 5	10-70	400-1000

In 1967 Brands and Goldthorpe reported that electrostatic force plays an important role in attracting particles from the solution to the electrode surface [42]. The first concerted model for electrodeposition was put forward by Guglielmi in 1972, involving the electrophoresis of particles, charge transfer kinetics and Langmuir adsorption [43]. In this model, particles arriving at the electrode surface are first loosely attached, and are likely to be coated by adsorbed ions and solvent molecules on the electrode surface. This loose adsorption step on the surface is easily influenced by the particle concentration in the bulk electrolyte. Then, the particles become strongly adsorbed onto the electrode due to the applied electrical field, and are incorporated into the growing metal coating. This model has been widely used to explain composite electrodeposition systems, its main shortcoming being that it doesn't consider the transportation process of ions or particles, or indeed particle properties.

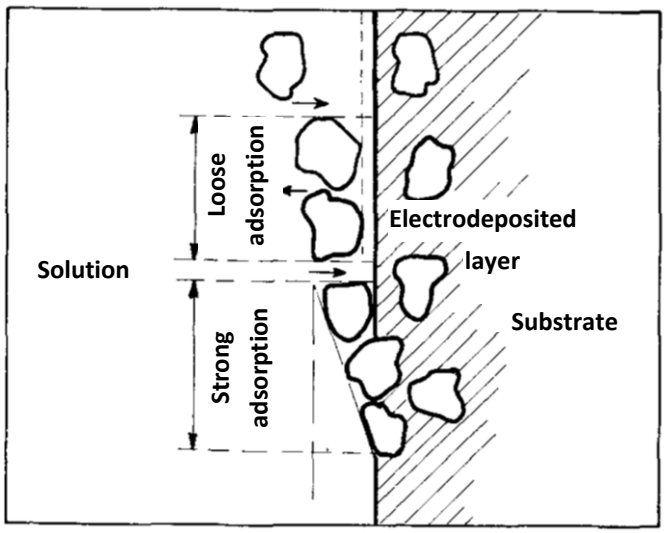

Figure 2.5 Guglielmi's electrocodeposition model [43].

By considering ion adsorption on the particles, bath agitation, convective force and electrocrystallisation, Celis, Roos and Buelens proposed an improved model in 1987 [44]. According to the Celis model, five stages occur in the electrocodeposition (ECD) process (Fig. 2.6). The suspended particles first adsorb the ions in the electrolyte to form an external ionic cloud. Afterwards the particles move to the hydrodynamic boundary layer under convection. In the third and fourth stages, the ionic particles diffuse to the electrode surface and adsorb onto the surface. In the last stage, the particles are incorporated into the metal matrix. In this step, a certain residence time is required for the reduction of ions on the particles which is subsequently followed by the particles' incorporation.

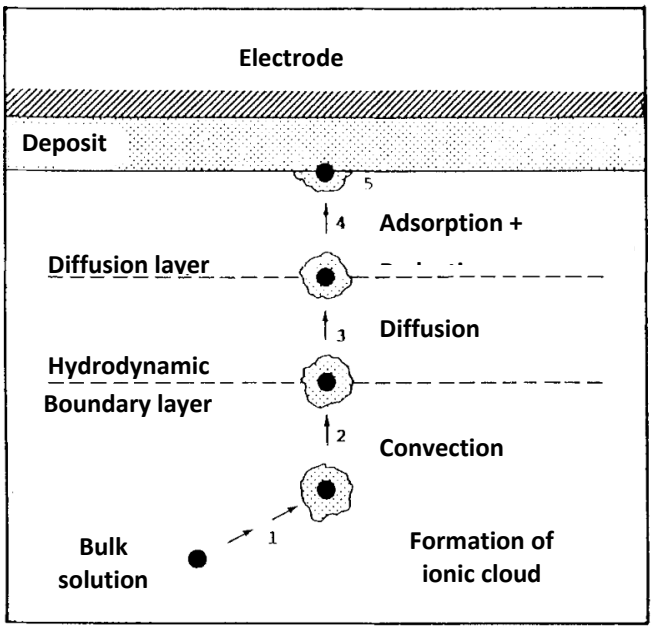

Figure 2.6 Celi's electrocodeposition model [44].

Hwang and Hwang have proposed an improved model to explain the effect of current density on the reduction of adsorbed metal ions in Co-SiC electrodeposition (Fig. 2.7). The deposition rate of the particle depends on the reduction rate of H^+ and Co^{2+} ions on the particle. Only hydrogen is reduced at low current densities. At medium current densities, the reduction rate of hydrogen reaches a limiting value and the metal ions are reduced. Both the hydrogen and metal reductions reach a limiting rate at high current densities [45].

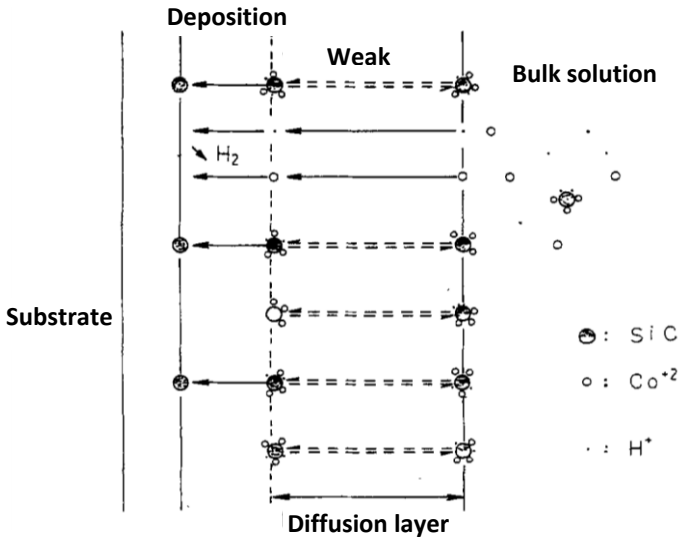

Figure 2.7 Reaction sequence of codeposition in the proposed model [45].

For larger particles (>1 μm) usually utilized in most industrial processes, the kinds of forces on the particles need to be considered. Fransaer et al. proposed a particle trajectory model to analyse the codeposition of large particles on a rotating disk electrode [46]. The

trajectory model analysed all the external forces and torques acting on the particle, such as gravitational, electrophoretic, dispersion and double layer forces. The particles in the electrolyte are first driven to the electrode surface by the dispersion and convection force. Then, there are four kinds of forces acting on the particle in the vicinity of electrode surface, as presented in Fig. 2.8. F_{adh} represents the force of adhesion, and F_{stagn} and F_{shear} are the hydrodynamic forces due to the stagnation point flow and the various shear flows. F_{stagn} and F_{adh} restrain particles on the electrode surface by producing friction force: $F_{friction} = k(F_{stagn} + F_{adh})$ where k is the static coefficient of friction. When the friction force is greater than or equal to the shear force, the particle stays on the substrate and is incorporated into the growing metal layer.

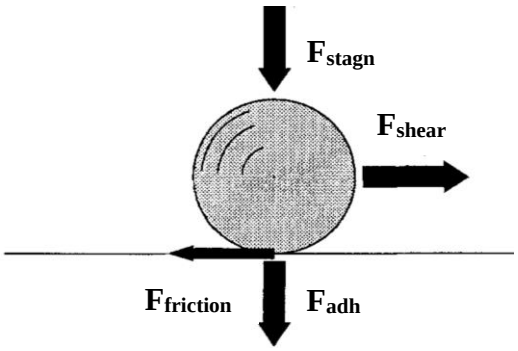

Figure 2.8 Fransaer's electrocodeposition model [46].

Vereecken, Shao and Searson analysed the gravitational forces acting and diffusion of particles of different sizes, building a model to predict the deposition rate of particles [47]. Based on Guglielmi's model, Bercot et al. considered the effects of adsorption and flow and introduced a polynomial correction [48]. All these models have helped develop a better understanding of the electrodeposition factors [49]. Although the ECD process has been studied for many years, none of the studies can fully explain the whole process. Hence, there is a need for a better fundamental understanding of the ECD process in the future as part of the successful development of composite coatings.

The particles in an electrolyte form a colloidal dispersion, which is a two-phase system. One phase is a continuous electrolyte solution, and the other is the colloidal particle. If a charged colloidal particle is put in contact with a solution with both positive and negative charged ions, the charges tend to distribute in the formation of an electrical double layer (EDL) [50]. In 1924, Stern combined the models of Helmholtz, Gouy and Chapman to describe the structure of the EDL by considering the finite dimensions of the ions [51].

According to the Stern model shown in Fig. 2.9, the EDL is divided into two layers based on electrical potential. The inner layer near the surface of the particle is called the Stern layer which exhibits rapid potential decay. And the outer layer is called the diffuse layer in which the electrical potential decays gradually. The stern layer only contains counterions (charged opposite to the surface charge) which are closely attached to the particle surface by a strong electrostatic force. The diffuse layer is made of free ions in a film of the dispersion medium, which are affected by the weaker electrostatic force on the charged particle and thermal motion.

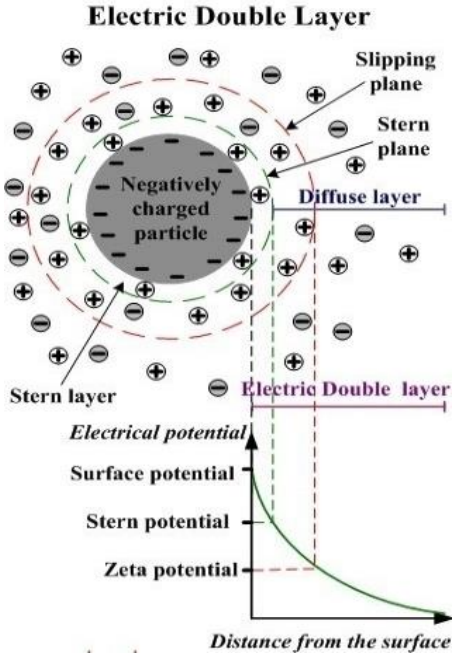

Figure 2.9 Electrical double layers of particles in electrolyte [52].

When a colloidal particle moves in the dispersion medium, a layer of the surrounding liquid remains attached to the particle (fixed layer). The boundary of this layer is called the slipping plane (shear plane). The zeta potential (ζ) is defined as the potential difference between the shear plane and the bulk solution. Since it is impossible to measure the surface potential of the particle itself, ζ is defined as an approximation of the surface potential of the particles. The magnitude of zeta potentials gives an indication of the stability of the colloidal solution. In general, particles with an absolute value of the zeta potential above 30 mV are thought of as stable [53].

The stability of a colloidal system refers to the capability of the system to remain as it is. A suspension could be thought of as stable, when the individual particles exist separately in solution and do not form aggregates over a relevant time scale. The stability is maintained by the existence of an energy barrier which prevents the proximity of particles.

Stability is usually hindered by aggregation and sedimentation phenomena. Aggregation is caused by the sum of the interaction forces between particles. If the attractive forces (such as van der Waals force) overwhelm the repulsive forces (such as electrostatic force), the particles will aggregate into agglomerates. Particle sedimentation arises from a difference of density between the dispersed and the continuous phase [54].

In order to improve the stability of colloidal systems, electrostatic stabilization, steric stabilization and gel network stabilization are the three main mechanisms for stabilization [55]. Details are as follows:

- **Electrostatic stabilization** is based on the mutual repulsion of like electrical charges. It is an effective way to counterbalance the van der Waals attraction between colloidal particles in polar liquids by providing the particles with Columbic repulsion.

- **Steric stabilization** works by covering the particles with polymers which prevents the particle from getting close enough to be in the range of attractive forces. (i.e. surfactants or other molecules at the particle surface).

- **Gel network stabilization** represents the principal way to produce colloids stable to both aggregation and sedimentation. It is commonly achieved by forming a gel network with addition of a green biopolymer, and the shear thinning effect can be observed which means the solution becomes less viscous when a stress is applied.

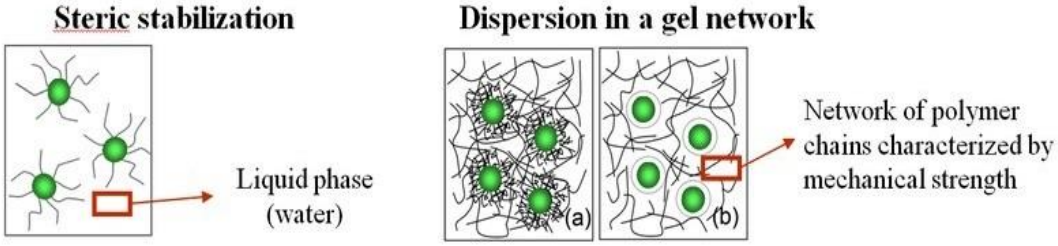

Figure 2.10 Schematic diagrams of steric stabilization and gel network stabilization of particles in electrolyte [56].

2.2 Luminescent coating for wear sensing

2.2.1 Why is wear sensing needed?

In mining, paper, chemical, oil and gas, even in the medical industries, component parts usually break down due to a number of different types of wear including adhesive wear,

abrasive wear, erosive wear, fretting wear and fatigue wear. One of the biggest advantages of an anti-wear and abrasion coating is to provide considerable improvement in the reliability of these components and extend service life. This enables equipment to be made of less expensive materials with improved surface properties.

However even with these capabilities, damage may occur beyond that which the coated component can withstand. The worn surface needs constant monitoring to prevent any catastrophic failure (once the coating is gone the substrate may experience accelerated damage). Regular maintenance is one of the solutions but may incur a heavy cost [57]. Thus an unattended machine with a wear monitoring capability is necessary in most manufacturing industries [58].

A lot of wear monitoring techniques have been developed so far. The wear sensing approaches can be classified as: oil analysis system, electric chip detector (ECD), surface roughness, vibration, acoustic emission, thermal monitor and luminescent sensing [59].

2.2.2 Wear monitoring systems

Electric Chip Detector (ECD)

ECD is based on the principle that metal particles may be an indicator of wear in the lubrication system of an aircraft engine or other system. Chip detectors could monitor these wearing systems to provide timely warning of impending failure so that maintenance can be implemented without delay [60].

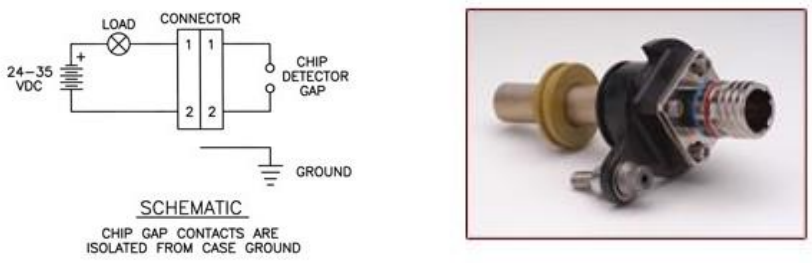

Figure 2.11 Schematic graph of electrical chip detector [61, 62].

Fig. 2.11 illustrates the structure of an ECD. The detector houses magnets connecting into an electric circuit, to capture debris particles which can bridge a gap between two electrodes. This bridging acts as a switch closure for an alarm circuit or "chip" light. If

collection numbers of these particles grow and bridge the insulated air gap between the magnets (two magnet configuration) or between the magnet and housing (one magnet configuration), the ECD will effectively close the circuit. This results in an electronic signal indicating timely maintenance. This approach has the following characteristics:

- Remote indication for on-line detection or off-site monitoring.
- Threads directly into gearbox drain port or installs in self-closing valve
- Capture efficiency enhanced by use of full-flow housing or lubricant oil/debris separator
- Flexible designs dictated by location and wear patterns in turbine engines or gearboxes

Currently, many aircraft engines have chip detectors, which are used to diagnose bearing failure. This technique, however, is used for monitoring the whole system rather than for localising the source of any debris particles detected.

Oil analysis

Machinery oil analysis is a very common diagnostic technique to monitor the wear condition of machines in many mechanical applications [63]. Not only can it monitor a machine's lubricating status but it can also detect the condition of a system by examining shape, colour and concentration of wear debris in oil. An oil monitoring system is usually composed of six techniques: atomic emission spectroscopic analysis, infrared spectroscopic analysis, ferrographic analysis, particle counter, and routine physical and chemical analysis of the oil.

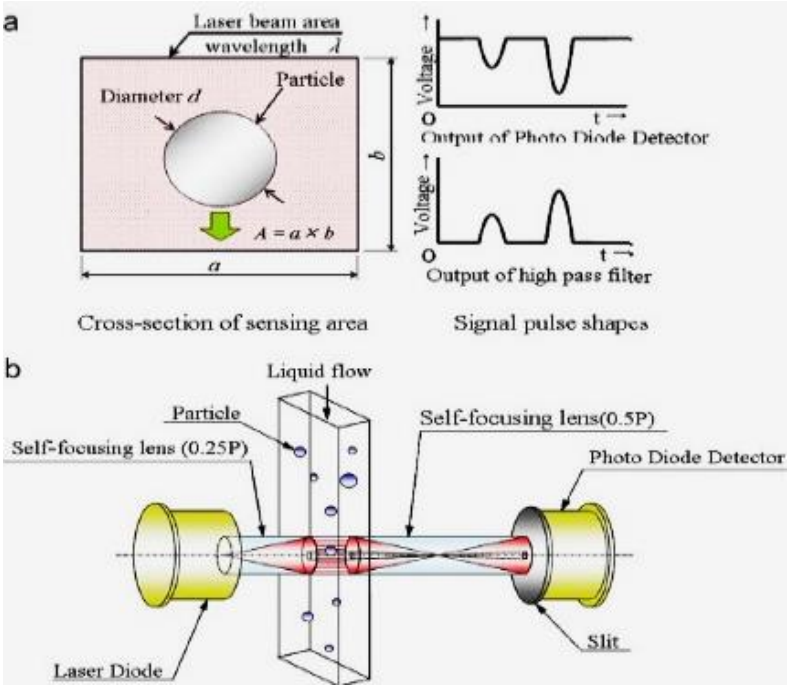

Figure 2.12 Principle and schematic view of particle counter: (a) cross-section of sensing area and signal pulse shapes and (b) schematic view [64].

The particle counter has been used in oil monitoring systems. Iwai et al. have developed an on-line particle counter with a laser beam, as shown in Fig. 2.12, to estimate the wear amount quantitatively under lubricated conditions [64]. It has been found useful for the continuous measurement of wear debris in lubricating oil in real time which is related to wear amounts and surface failure.

Oil analysis could comprehensively analyse wear for a mechanical system with the advantage of accuracy. However, such oil analysis is directly connected to large and complex testing equipment. As a result, in-situ measurement of wear debris in lubricating oil is limited.

Surface roughness

Surface roughness of a work piece is a useful parameter for wear examination. Stylus measurement of machined workpieces has been conducted in industry. However, this contact method may damage the workpiece surface and not help in the complete inspection of workpieces. Optics-based light scattering and digital image approaches are other general methods used to measure surface roughness.

Fig. 2.13 shows a system for a turning machine, including a CCD camera with the Gaussian filter (continuous filters that selectively transmit light of different wavelengths)

and backlight [65]. The measurement of the surface roughness of the turned part was realised without removing it from cutting processes, i.e. in-cycle. Tool misalignment is corrected automatically through an algorithm after inputting the images. As shown in Fig. 2.14, the surface profile of machined components can be interpreted at four different scales: form, waviness, roughness and micro-roughness [66]. The wavelength of the form is similar to the wavelength of the object. Before analysing the surface texture, the deviation between the theoretical form and measured form should be subtracted. The surface texture is divided into three parts depending on the variation rates along the horizontal direction. When the changes are slow, it can be considered as waviness. When the changes are more rapid, it is roughness which is decisive for the visual texture, friction and wear. The finest and fastest rate is called micro-roughness, composed of high frequencies. All roughness information can be evaluated to monitor the wear process.

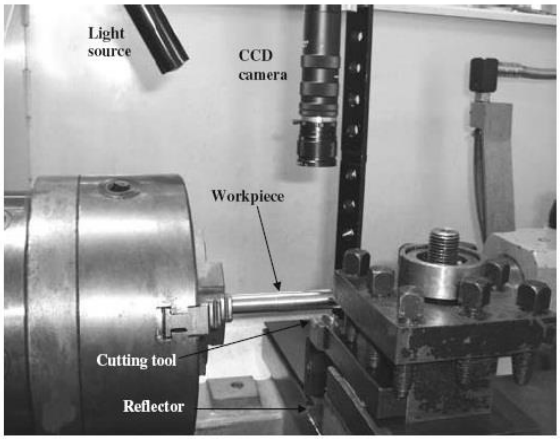

Figure 2.13 System setup on lathe machine [65].

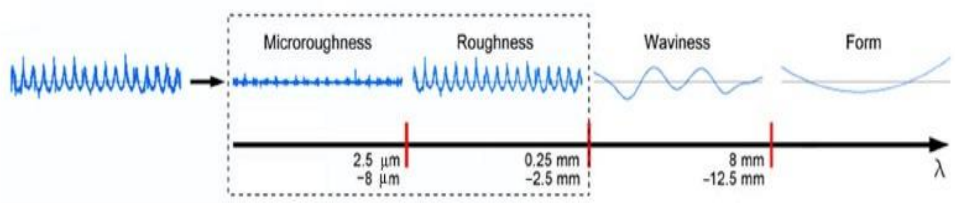

Figure 2.14 Four parts of the surface profile [66].

Vibration

Vibration analysis is mainly used for rotating machinery maintenance and fault diagnosis. Practical experience has shown that this technique provides useful and reliable information of wear failure.

Vibration occurs due to rubbing between the workpieces. Coatings often contain lamellar features, pores and cracks, so the feedback regularity of vibration signals for the coatings are obviously different from those for bulk materials. Wear damage process for coatings under rolling contact can be monitored using vibration signals [67].

Vibration information can be collected by measuring the vibration of bearing casings with seismic transducers, piezo-electric transducers or laser Doppler vibrometers. The level of vibration shows a direct relationship with the severity of wear by comparing the obtained data with historical values or established standards. Fig. 2.15 is an example of overall vibration comparison of gears in healthy and worn conditions at 1000 rpm. From this figure, different vibration levels can be observed for healthy, worn and broken gears respectively, amongst which the worn gear shows higher vibration than the healthy one. This verifies that vibration analysis can be used to assess worn and broken conditions in gears [68].

It is a complex process to interpret the vast majority of vibration signals and obtain detailed information on the workpiece. A commonly used technique is carrying out a vibration signal analysis in both time and frequency domains. The time domain is more sensitive to machine working conditions, while the frequency-based domain has a better correlation with component wear. Different frequencies correspond to certain mechanical components (for example, the various pieces that make up a rolling-element bearing) or certain malfunctions (such as blank wear or misalignment). By examining these frequencies and their harmonics, the analyst can often identify the location and type of problem. Fig. 2.16 shows the detailed vibration frequency spectra of broken and healthy gears at 1000 rpm [69]. Comparing these two pictures, it can be seen that the worn gear generated higher vibration frequencies than the healthy one.

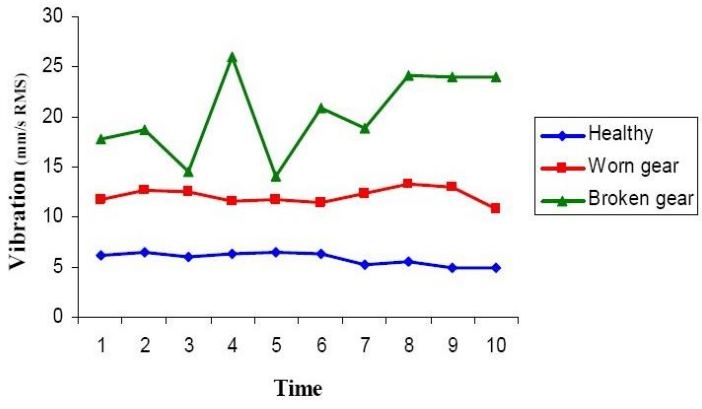

Figure 2.15 Vibration comparison of a gear in healthy and worn conditions at 1000 rpm [69].

Vibration monitoring is indeed capable of diagnosing wear problems in machines and providing warning of failure. If severe wear happens, a large amount of wear debris or deformation of component will cause an abnormal vibration frequency.

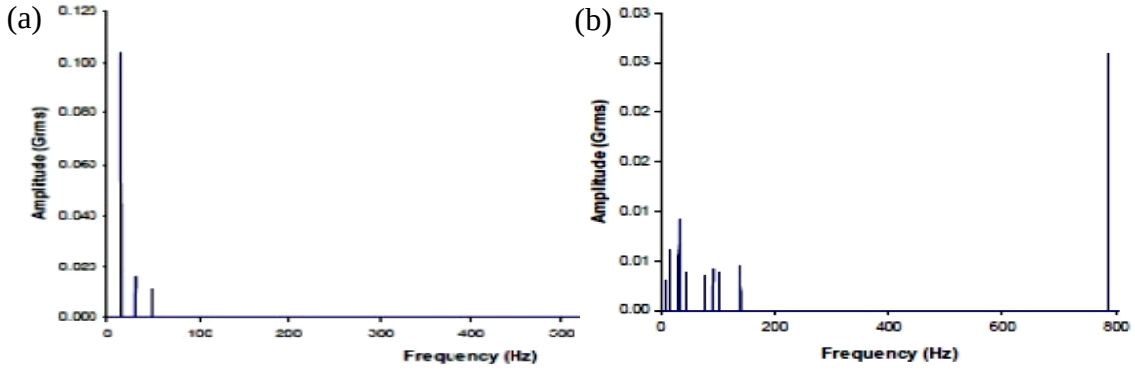

Figure 2.16 Vibration frequency spectrums of healthy gear (a) and worn gear (b) at 1000 rpm [69].

Acoustic emission

Acoustic emissions (AE) are high-frequency transient sound waves emitted when materials are undergoing deformation or fracture, accompanied by the spontaneous release of the elastic energy in materials. The energy contained in an AE signal and rate of energy dissipation are strongly dependent on operation parameters such as the rate of deformation, the applied stress, and the volume of the participating material [70]. Fig. 2.17 lists various sources of AE during turning. AE can detect most of the phenomena in machining, though it will need significant data acquisition and signal processing to clarify the source [71].

The emitted stress waves can be detected by coupling piezo-electric sensors to the surface of the structure under study, as shown in Fig. 2.18 [72]. The sensor was able to directly monitor acoustic emissions that are automatically produced within the material during the turning process. The application of acoustic emission to non-destructive monitoring of materials was often in the ultrasonic regime between 100 kHz and 1 MHz. By analysing the quantity and the properties of the acoustic emission signals, information can be obtained about the failure process of the material. This technique possesses a number of advantages: (1) it offers the possibility to perform a continuous investigation of the material, (2) processes can be monitored at the time and place of occurrence, (3) a large

structure can be monitored by a limited number of sensors, (4) the spatial location of the signal origin can be calculated by comparing the signal arrival times at a number of sensors.

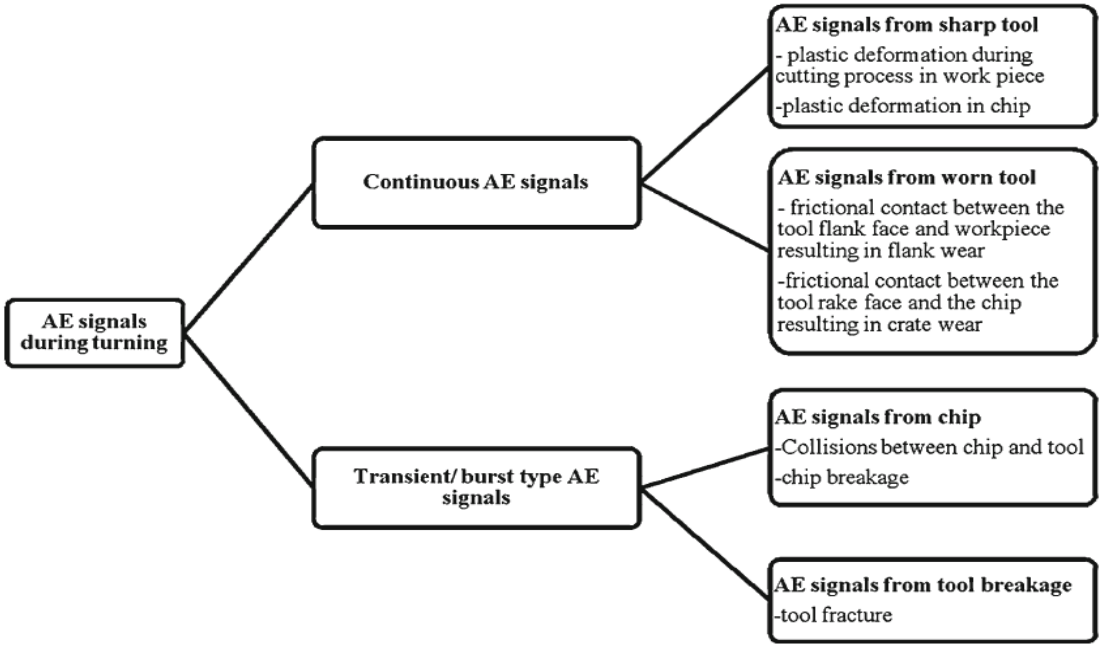

Figure 2.17 Acoustic emission during tuning process [71].

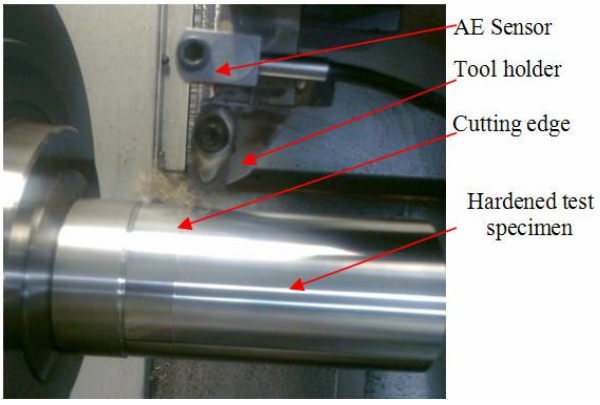

Figure 2.18 Image of AE sensing system for turning tool [72].

Many studies have attempted to create a simple monitoring system using AE sensing and the results obtained are encouraging. Fig. 2.19 shows variations in AE amplitude under a contact stress of 1.58 GPa for a running coating system [73]. As a general trend, the AE amplitude shows the following four stages: (1) Start up. The initial AE signal amplitude was high, the strong AE signal was generated due to the sharp surface but subsequently

diminished; (2) Stable stage. The AE amplitude remained at a stable value during most of the testing period; (3) Abrupt jump. An abrupt increase of AE amplitude occurred followed by discontinuous impulse-type rises; (4) Damage stage. AE amplitude sharply increased and reached a higher value due to losses of coating in the final fatigue damage stage.

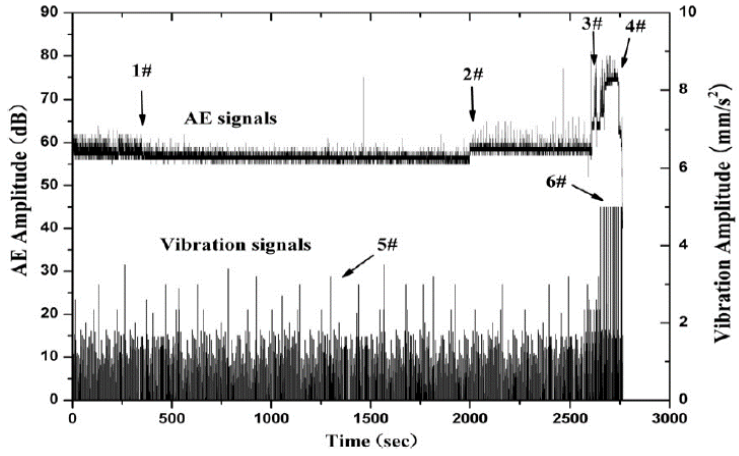

Figure 2.19 AE and vibration signals of the RCF damage process for coating under contact stress of 1.58GPa [73].

AE can detect the details of fatigue damage, such as wear, material deformation and crack growth. However, there are some limitations of acoustic emission since AE signals are heavily dependent on process parameters. It is complex to select the location for AE sensor mounting and to choose appropriate signal processing techniques. So it has been proposed that AE is only suitable as an ancillary sensing method.

Thermal monitor

Wear processes normally give rise to temperature increases. It has been found that there is a critical interface temperature for each alloy at which the wear rate suddenly increases and a transition from mild to severe wear takes place leading to sudden failure [74].

As shown in Fig. 2.20, sliding interface temperature shows a close relation between wear and the friction response of these alloys (3kgf load, against hardened ground steel En-31 disc). Interface temperature increases as the sliding distance increases. The friction of

coefficient during the sliding of all aluminium alloys (irrespective of silicon content) first decreases slowly with the rise in interface temperature and then abruptly increases beyond a certain critical temperature [75].

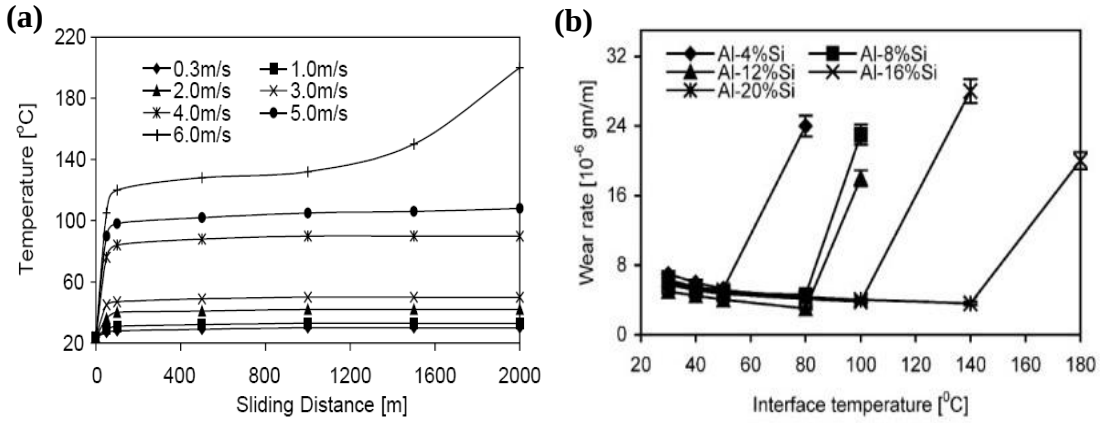

Figure 2.20 (a) Interface temperature vs sliding distance for cast Al-20% Si alloys at different sliding speeds, (b) Wear rate vs. interface temperature for different cast Al-Si alloys [75].

For temperature measurement, thermal radiation or conduction is basically used. Infrared temperature sensing devices have been used by detecting thermal radiation. The technique is widely explored because it enables measuring temperature from a distance, which is of paramount importance when detecting inaccessible objects. For instance, Al-Habaibeh and Parkin [76] used low cost infrared cameras to inspect temperatures in the cutting tool tip as well as at the chip-tool interface, shown in Fig. 2.21. The normal and faulty conditions of manufacturing processes can be quickly distinguished from the image difference. However, due to the large thermal gradient in junctions, the infrared technique leads to errors in the measurement. Davies et al. defined a standard uncertainty of the temperature measurements is ±52 ℃ at 800 ℃ with an infrared imaging microscope [77].

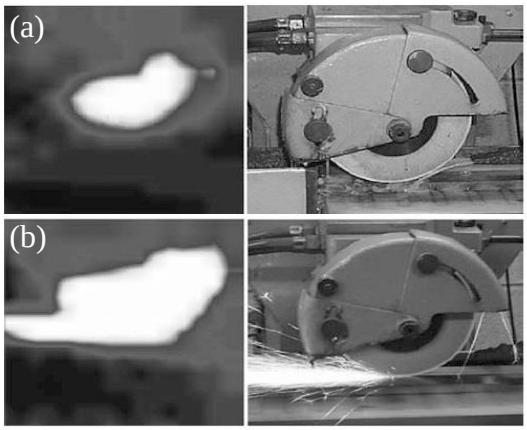

Figure 2.21 Infra-red image of (a) faulty and (b) normal grinding process [76].

Another prevailing temperature measurement method is based on thermal conduction, which could improve the accuracy of temperature sensing at a point. Rao et al. used a thermocouple to measure the nodal temperature and developed an online wear sensing method. The method could be easily adapted for a variety of workpieces without extensive experimentation and provides an accurate estimation of wear [78]. Nevertheless, the disadvantages should also be noted. The embedded or dynamic thermocouples are usually generated by photolithography and laser structuring methods, which cannot be applied to every cutting material or coating.

2.2.3 Luminescence coating as a damage sensing approach

Due to its intensive light emission under UV illumination, luminescent coatings have been developed to monitor coating damage. It has been characterized as a visualization technology for "invisible" damage [79]. It could potentially sense small damage directly that other techniques are less able to verify.

A smart wear sensing coating has been developed. The layered structure is shown schematically in Fig. 2.22 with doped yttria stabilized zirconia (YSZ) layers as sensor materials [6]. The main layers of coating were single-phase lubricant (molybdenum disulphide), which was prepared by magnetron sputtering. Yellow luminescent coating (YSZ: Er) and blue luminescent (YSZ: Sm) coating were imbedded at specific depths by pulsed laser deposition from rotating YSZ targets with the desired doping concentrations of rare-earth metal. During the wear test, a Raman probe was used to detect the signal of luminescent materials.

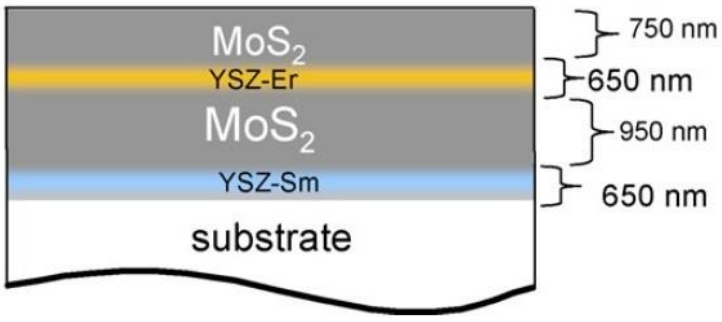

Figure 2.22 Schematic diagram of multi-layered coating with imbedded, luminescing wear sensors layers [6].

Fig. 2.23 shows the results of luminescent spectroscopy at different numbers of wear cycles. Initially, there was only a Raman scattering signal from MoS_2. After 10k cycles, there existed new peaks corresponding to the yellow luminescent coating, indicating the wear depth reached 1400 nm. After 150 k cycles of wear tests, the peaks at 1100 cm^{-1}, 1280 cm^{-1} appeared which corresponded to the spectra of blue luminescent coating, showing all anti-wear coatings were worn off.

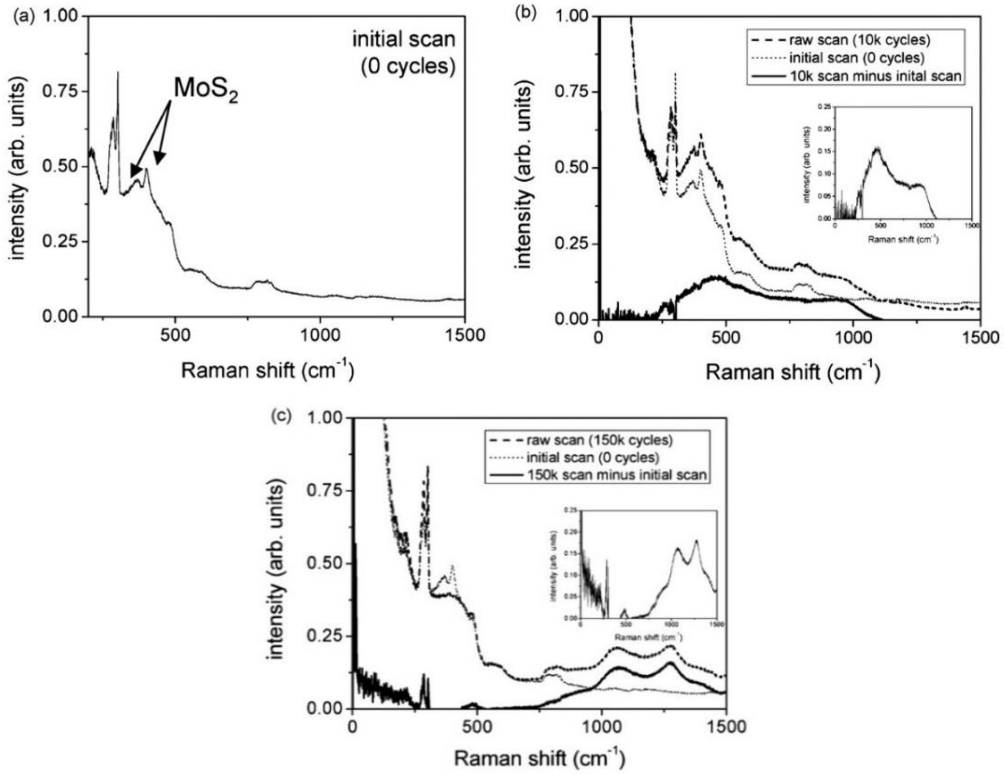

Figure 2.23 Luminescent spectroscopy at different wear cycles: (a) 0, (b) 10k and (c) 150 k [6]

Since luminescence light from the wear surface travels to the detector within a few nanoseconds, this provides a practically instantaneous response from the sliding surface, allowing the wear track to be considered a virtually stationary surface within the time frame of signal acquisition. The sensor concept, therefore, can be equally applicable for use at relatively high sliding and/or rotating velocities, such as those expected in aircraft turbine engine components [80].

Xu and his team members created a new technique to diagnose the damage in structures and their severity simultaneously by utilizing elastic-luminescence [81]. For this luminescence, the intensity is proportional to real-time strain energy in the elastic region. They coated the surface of structures with luminescent paint, which could emit light on the device for mechanical stimulation. When the structures are subjected to force or

vibration, the stress fields and levels become plainly visible because of the elastic-luminescence phenomenon. At the same time, the location of cracks that do not appear on the surfaces of structures were also visible in real time due to a pattern of luminescence intensity distribution on surfaces generated by stress.

Fig. 2.24 shows the simultaneous measurement of a defect and stress distribution by luminescent coating. Paint containing elastic-luminescent materials ($SrAl_2O_4$:Eu) was applied to a metal plate. The “invisible” fatigue crack could be seen on the coated metal plate with a load of 20 N. Under a large load of 12 kN, stress concentration at the crack tip is evident. It appears the technology could be used as a simple, fast and reliable method to detect potential surface defects in machines.

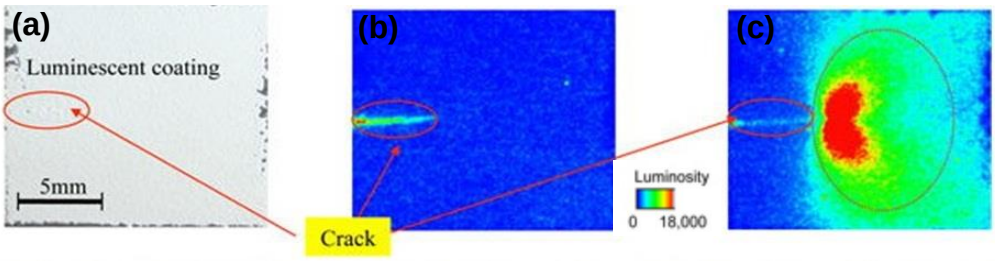

Figure 2.24 (a) Photo of a metal plate with elastic-luminescent coating; (b) Luminescent image under the application of a small load (20N); (c) Luminescent image under the application of a large load (12kN) [82].

2.2.4 Electrodeposition of luminescent coating

2.2.4.1 Introduction of luminescent materials

Luminescence is a form of cold light emitted by the substance with energy beyond thermal equilibrium. Many kinds of excitation can cause luminescence phenomenon, which could be accordingly defined as photo-, electro-, sono- and tribo- luminescence [83]. Depending on the time length of luminescence, it has also been classified into two types: fluorescence and phosphorescence with the decay time of luminescence of less than 10 ms and more than 0.1 s respectively [84].

The luminescence of inorganic solids can be divided into two mechanisms: luminescence of isolated centres and luminescence of semiconductors. The isolated luminescence occurs due to the energy transition between different levels of single ions or complex ions. In this case, the transition rate obeys the relevant quantum-mechanical selection rules which are reflected in the intensity as well as the decay time of the transition. Excitation

and emission can be localized to one centre, such as (WO_4) in $CaWO_4$ (Fig. 2.25 (a)). They can also be separated from each other (Fig. 2.25 (b)): excitation on the sensitizer (e.g. Ce^{3+} in $LaPO_4$: Ce^{3+}, Tb^{3+}) is followed by emission on an activator (e.g. Tb^{3+} in $LaPO_4$: Ce^{3+}, Tb^{3+}). The other case of semiconductor luminescence (Fig. 2.25 (c)) normally relies on impurity states within the band gap (e.g. donor-acceptor pair luminescence in ZnS: Ag^+, Cl^-) [85].

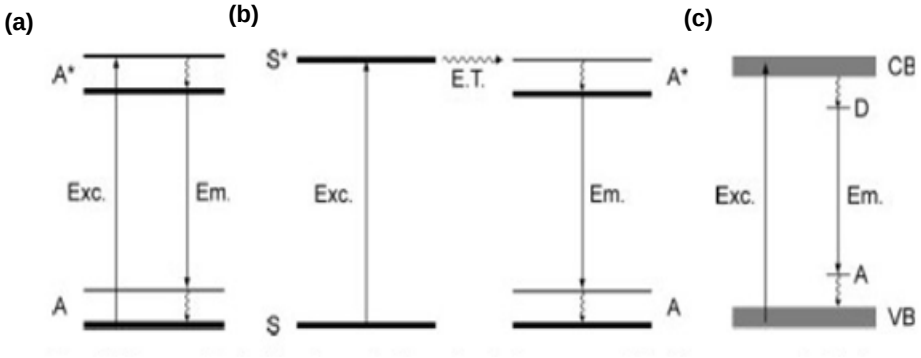

Figure 2.25 Schemes illustrating the underlying physical processes of luminescence (a, b) on the isolated centers and (c) in semiconductor [85].

Inorganic luminescent materials have been found as early as the tenth century in China and Japan as well as at the end of the Middle Ages in Europe. The first luminescent materials were naturally doped willemite, scheelite, or calcite crystals. All these luminescent materials were mined from the earth. In 1671, Kirchnes intensified the luminescence of Baryte by heating it with carbon black, $BaSO_4 + 4C = BaS + 4CO$. From then on, large amounts of luminescent materials have been produced artificially. The detailed development of luminescent materials is given in Table 2.2.

Table 2.2 Early mile stones in the discovery of luminescent materials and devices [85].

Year	Kind of discovery	Excitation source	Type of luminescent material	Emission color
~1600	Stone of Bologna	sunlight	$BaSO_4$ (BaS)	yellow
1858	Geißler's tube	gas-discharge (Hg)		UV
1859	Becquerel	gas-discharge (Hg)	ZnS	yellow-white
1895	X-rays (by Röntgen)		none (photographic plate)	
1896	X-ray intensifier (by Pupin)	X-ray	$CaWO_4$	blue
1896	Fluorescent lamp (by Edison)	gas-discharge (Hg)	$CaWO_4$	blue
1897	Braun's tube	cathode-ray	$CaWO_4$	blue
1916	Neon discharge lamp (by Claude)	gas-discharge (Ne)	none	red
1925	Black-and-white television	cathode-ray	$ZnS:Ag^+$; $(Zn,Cd)S:Ag^+$	blue; yellow
1937	Neon discharge lamp (by Claude)	gas-discharge (Ne)	$CaWO_4$; $Zn_2SiO_4:Mn^{2+}$	blue; green
1938	Fluorescent lamp	gas-discharge (Hg)	$MgWO_4$; $(Zn,Be)_2SiO_4:Mn^{2+}$	blue-green; green-red
1941	Radar screen	cathode-ray	$(Zn,Cd)S:Cu^+,Al^{3+}$	green
1946	Insect lamps	gas-discharge (Hg)	$CaWO_4$	blue
1960	Color television	cathode-ray	$ZnS:Ag^+$; $(Zn,Cd)S:Cu^+,Al^{3+}$; $(Zn,Cd)S:Ag^+$	blue; green; red
1960	Laser (by Maiman)	gas-discharge (Hg)	$Al_2O_3:Cr^{3+}$	red
1972	Computed tomography (by Houndsfield)	X-ray	$NaI:Tl^+$	green
1972	Rare-earth phosphors	gas-discharge (Hg)	$Sr_3(PO_4)_5Cl:Eu^{3+}$; $LaPO_4:Ce^{3+},Tb^{3+}$; $Y_2O_3:Eu^{3+}$	blue; green; red

In 1971, rare earth element-based luminescent materials were found by Koedam and Opstelten, which marked a significant improvement in luminescence levels in modern times. Colour rendering index (CRI) is defined as a light source's ability to show the real colour of an object compared to a reference source such as daylight. Both the CRI and the energy efficacy of fluorescent lamps based on rare earth emitters are considerably higher than in the case of lamps based on conventional halophosphates [86]. In such lamps, a CRI over 80 can be obtained at an efficacy of 100 lmW^{-1}.

In most cases, the rare ions (Tb^{3+}, Gd^{3+}, Eu^{3+}) show narrow emission, the spectrum in Fig. 2.26 contains sharp lines, leading to a high efficiency and high lumen equivalent. Furthermore, these optical transitions are generally very slow (from microseconds to milliseconds) [87].

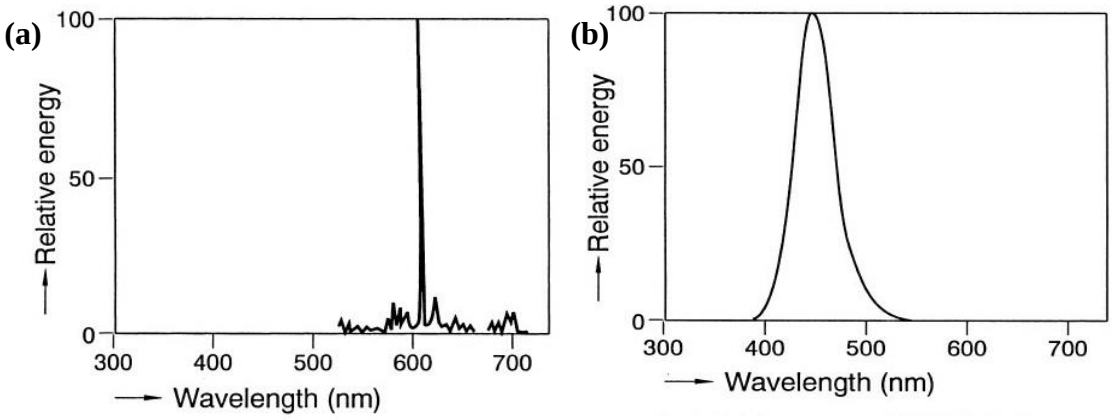

Figure 2.26 Emission spectrum of (a) Y_2O_3: Eu and (b) $BaMgAl_{10}O_{17}$:Eu [87].

However, there are also a number of rare earth ions such as Ce^{3+} and Eu^{2+}, showing emission spectra of broad bands, as shown in Fig. 2.26 (b). For example, the emission takes place on Eu^{2+} in $BaMgAl_{10}O_{17}$, where the optical emission originates from the 5d-4f energy transition. As d electrons participated in the chemical bonding, the d-f emission spectrum consists of broad bands. Additionally, the d-f optical transitions are commonly very fast (a few microseconds or less). To develop luminescent coatings, appropriate coating technologies will need to be established.

2.2.4.2 Deposition of luminescent coatings

Light-emitting composite coatings can be achieved by adding luminescent particles to the electrolyte. Luminescent nickel coatings were first prepared by Feldstein via an electroless deposition process [88]. Coatings with calcium tungstate BAM phosphors showed a blue emission upon UV irradiation (254 nm), while coatings with calcium halophosphate BAM phosphors emitted a whitish light [89]. By electroless plating from an aqueous plating bath, Das et al. developed red-emitting nickel coatings containing $YVO_4:Eu^{3+}$ BAM phosphors with a maximum loading of 14.5% (v/v) [90]. Advantages of using rare-earth BAM for a luminescent coating are the high colour purity because of the line emission by the trivalent rare-earth (lanthanide) ions and the possibility of tuning the emission colour by choosing an appropriate rare-earth ion.

Compared to electroless deposition of composite coatings, an electrocodeposition technique is much faster and allows better control of the deposition process. However, rare-earth BAM phosphors are hydrophilic and a hydration layer will form on their surface, which prevents the phosphors contacting the electrode, so it is difficult to incorporate these into metal coatings from an aqueous electroplating bath [91]. In addition, small particles can aggregate in an aqueous solution.

Ganapathi et al. reported luminescent nickel coatings containing red-, yellow-, green- or blue-emitting rare-earth BAM phosphors could be prepared by co-deposition from a new non-aqueous electrolyte [9]. The electrolyte was composed of acetamide, dimethylsulfone, and anhydrous metal chlorides. By varying deposition parameters, optimized coatings with a uniform particle distribution were obtained.

The emission properties of the composite coating were investigated by steady-state and time-resolved luminescence spectroscopy. Fig. 2.28 shows that the luminescence spectra of composite nickel coatings were similar to those of the pure BAM powder. Both the blue-emitting phosphor, $BaMg_2Al_{16}O_{27}:Eu^{2+}$ ($BAM:Eu^{2+}$), and corresponding Ni composite coating exhibit broad-band luminescence under excitation at 330 nm, due to allowed 5d/4f transitions in the range 370-570 nm centered at 455 nm [9].

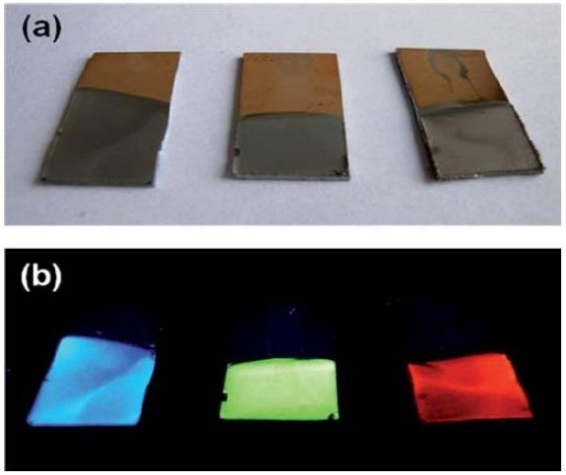

Figure 2.27 Nickel coatings with blue ($BaMg_2Al1_6O_{27}:Eu^{2+}$), green ($Gd_2O_2S: Tb^{3+}$) and red emitting ($Y_2O_3: Eu^{3+}$) rare-earth phosphors: (a) under daylight and (b) under UV illumincation [9].

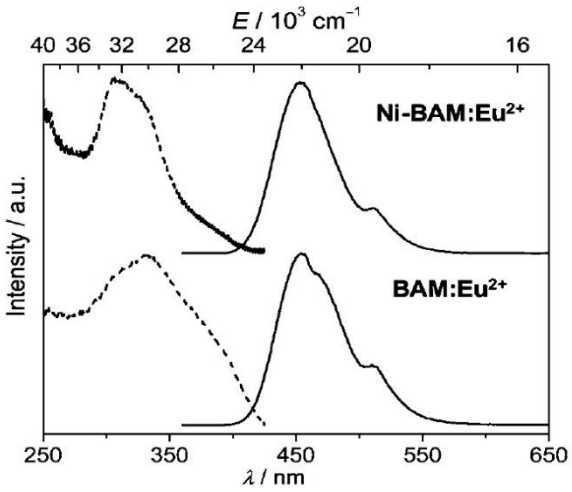

Figure 2.28 Excitation (dashed line: 450 nm) and emission (330 nm) spectra of $BaMg_2Al_{16}O_{27}:Eu^{2+}$ powder and composite nickel coating with embedded $BaMg_2Al_{16}O_{27}:Eu^{2+}$ phosphors [9].

2.2.5 Summary

Many attempts have been made in the past and some progress has been achieved in wear monitoring. Some of these are machine monitoring techniques, which detect different signals from coating and materials, and discern the severity of wear of the coating. Some concentrate on wear product monitoring techniques, which utilize measuring apparatus to detect the wear products like wear debris, thickened oil etc. However, few systems have been successfully applied in industry. The primary challenges for these applications can be summarized in four ways:

(1) Most techniques have been developed based mainly on mathematical models, which require numerous empirical data or system specific calibration, such as Acoustic emission;

(2) Some assembled sensors cannot localise the damage source accurately, such as Electric Chip Detector (ECD), Temperature, Spindle power/current;

(3) Sensor measurement is often not close to real-time due to a lack of high-speed signal processing and adaptive control(e.g. Oil analysis system);

(4) A signal processing algorithm is required to extract the most useful information from the signals' response (e. g. Vibration, Surface roughness).

To overcome these challenges, some researchers have tried to integrate several technologies, which may enhance the accuracy of the results. For example, Tangjitsitcharoen et al. carried out sound signal measurement along with force, vibration, and AE signal measurement in order to improve a sensor fusion approach [92]. But this may represent an expensive approach and also increase the complexity of a wear sensing system.

Luminescence is an important development as a sensor of wear and has the following advantages:

(1) It can be embedded easily and economically along with the lay-up of the coated or composite materials in a nonintrusive way;

(2) When friction damage occurs in the luminescent composite, it will lead to light emission. Since the luminescence light emission is fracture-initiated, no signal should be generated until damage occurs;

(3) An array of luminescence sensors may also allow real-time damage location monitoring by determining the wavelength of the emitted light from different depths.

In summary, luminescent coatings are a promising technique but require further research for reliability and robustness. Many methods have been attempted to achieve luminescent coating, including paint, pulsed laser deposition system, electroless plating and

electroplating. All these studies aim to prepare luminescent coatings with high luminescent efficiency, high hardness and high corrosion resistance. Composite electroplating attracts great interest due to its easy controllability and good mechanical properties. However, the dispersion property of particles in the electrolyte is crucial for the quality of the coating.

The focus of this project is building up a wear damage sensor with a luminescent coating. To obtain a composite coating with highly distributed phosphors, electroplating parameters, additives and codeposition mechanism will be investigated. The electrodeposited luminescent coating could be designed as pretreatment step of the substrate, and then an anti-wear coating can be added. The concern is whether such a luminescent interlayer will emit light under UV only when the anti-wear coating suffers severe wear. Also, the intensity of the sensor output could be indicative of the extent of wear damage.

2.3 Low friction coating for replacing Cr coating

2.3.1 Electrodeposited Ni-P coating for the replacement of hard Cr

2.3.1.1 Why is Cr prohibited?

Chromium (Cr) coatings are widely used for decorative and engineering industries [93,94]. Decorative Cr has a thickness lower than 500 nm, protecting the component against tarnish, scratch and corrosion. Hard Cr usually has a thickness more than 1 μm and hardness more than 700 HV, with excellent wear and corrosion resistance. It has been widely used in aerospace, automotive and general engineering industries for over 80 years to improve the wear resistant and life time of surfaces. According to statistics, the worldwide market value was $ 3.2 billion for hard Cr and $ 16 billion for decorative chrome in 2003.

However, the current method for producing Cr plating involves hexavalent chromium which is extremely toxic and carcinogenic. Workers exposed to Cr (VI) may suffer liver and kidney damage or failure, burns, and anaemia. And toxic pollution from this plating process also causes serious dangers to the environment and human health. Furthermore, the current efficiency of the Cr plating process is around 18% as more than 80% of the electricity is consumed by the evolution of hydrogen, resulting in a huge waste of energy.

In view of these facts, the use of hexavalent Cr has been gradually limited within many countries. In the European Union, restriction of the use of Cr (VI) plating has been effective in new electrical and electronic equipment from July 2006 and effective in car manufacture from July 2007. In the United States, the new standard of 5 mg/L for Cr (VI) has been implemented rather than the old standard of 52 mg/L if the Cr plating is dispensable. In China, the "restriction of the use of Cr (VI) in electrical and electronic equipment" directive became effective on March 2007. In consequence, finding substitutable materials, alternative technologies and new designs to replace hard Cr coating has attracted increasing scientific and industrial attention [95,96,97].

The ideal substitute must not only be wear and corrosion resistant but also must be cost-competitive, environmentally friendly and not suffer from hydrogen embrittlement. Table 2.3 shows the comparison of technology options to produce replacement materials for hard Cr coating. Among many potential alternatives, electrodeposition of Ni series coatings is a promising substitute for Cr as they use the same basic equipment as Cr plating and possess lower production cost. Large quantities of electrodeposited materials have been investigated, including Ni-W, Ni-P, Co-W, ternary or quaternary alloys and functionally graded deposits (FGDs).

Hexavalent chromium is carcinogenic and could cause serious damage to health through inhalation. Comparably, the carcinogenic potency of various nickel compounds widely depends on the basis of solubility and the route of exposure [98]. The Environmental Protection Agency (EPA) classified the hexavalent chromium as Group A (Carcinogenic to humans) and nickel carbonyl as Group B (Likely to be carcinogenic to humans), whereas soluble salts of nickel including nickel sulphate and nickel chloride have not been evaluated as a class of compounds for potential human carcinogenicity. According to another criterion- REGULATION (EC) No 1272/2008, nickel sulphate is classified as Category 2 (suspected human carcinogens) or even lower grade Category 3. Some studies have reported that nickel sulphate via inhalation is not carcinogenic in either rats or mice. Thus, the drive to successfully electrodeposit Ni-based coatings with performance comparable to Cr coatings is urgent and necessary.

Table 2.3 Category of possible non-chromium replacement [99].

Possible Non- Chromium replacement	Limitations
Dry surface treatments * HVOF thermal spraying * Physical vapor deposition * Chemical vapour deposition	• Line-of-sight application
Electroless deposition *Nickel-tungsten * Nickel-boron *Nickel-diamond composite * Nickel-phosphorous	• Chemicals are unstable
Electrodeposition * Nickel-cobalt * Nickel-tungsten * Ni-phosphorous * Tin-cobalt	• The conductivity of substrate

2.3.1.2 Properties of electrodeposited Ni-P coating

Electrodeposition as a traditional industrial activity has been used for over 150 years. The Watts nickel plating solution is the most commercialised system for many Ni alloys' deposition, as the Watts bath usually contains mainly $NiSO_4$ $6H_2O$ as listed in table 2.4, with the advantages of low maintenance cost and very low health risk.

Employing a Watts bath, many alloy deposits including Ni-W, Ni-Co, Ni-P and ternary or quaternary alloys have been obtained, which were considered as having the potential to replace conventional hard chromium deposits [100,101,102]. Among these deposits, Ni-P alloys with varied compositions and microstructures have been extensively studied due to their high hardness, excellent wear / corrosion resistance and their relatively stable electrolytes [103,104]. The hardness of both the electroplated and electroless plated Ni-P is generally harder than the pure Ni, and can become close to or even higher than that of conventional hard Cr after heat treatment over 400 ℃. Heat-treated Ni-P alloy favours the

formation of Ni_3P which is a hard intermetallic compound with high thermodynamic stability, producing the effect of precipitation hardening.

Table 2.4 Composition of Watts nickel plating solution.

Chemical Name	Formula	Bright	Semi-bright
Nickel sulfate	$NiSO_4$ $6H_2O$	124-249 g/L	187-250 g/L
Nickel chloride	$NiCl_2$ $6H_2O$	50-125 g/L	25-38 g/L
Boric acid	H_3BO_3	31-44 g/L	31-44 g/L

The following section will review some characteristic properties of Ni-P deposits such as structure, hardness and wear resistance. Recent developments (including our group's work) related to Ni-P coatings will also be discussed.

Structure

The microstructure of as-deposited Ni-P coatings changes significantly as the P concentration in the deposits increases, as revealed by the XRD data in Fig. 2.29 [105,106]. For the pure Ni deposit without P, a sharp XRD peak resulting from the (200) plane of Ni implies that this deposit is crystalline with preferred orientations. For the Ni-P coating with 4 wt% P, the (200) peak almost disappears while the intensity of the (111) peak markedly increases. P was thought to accelerate the growth rate of (111) facets rather than (200) facets. As the P content further increases to 8 wt%, the peak intensity drops significantly, indicating a loss in the degree of crystallinity. The diffraction peak almost disappears for the Ni-P coating with a P content of 14 wt%, suggesting the existence of a nanocrystalline or amorphous structure. Due to the atomic size difference between Ni and P, alloying with P would cause a distortion of the base Ni lattice. As the concentration of P content increases to a certain value, serious lattice distortion will evolve into the effective breaking of the Ni crystal lattice, resulting in an amorphous phase.

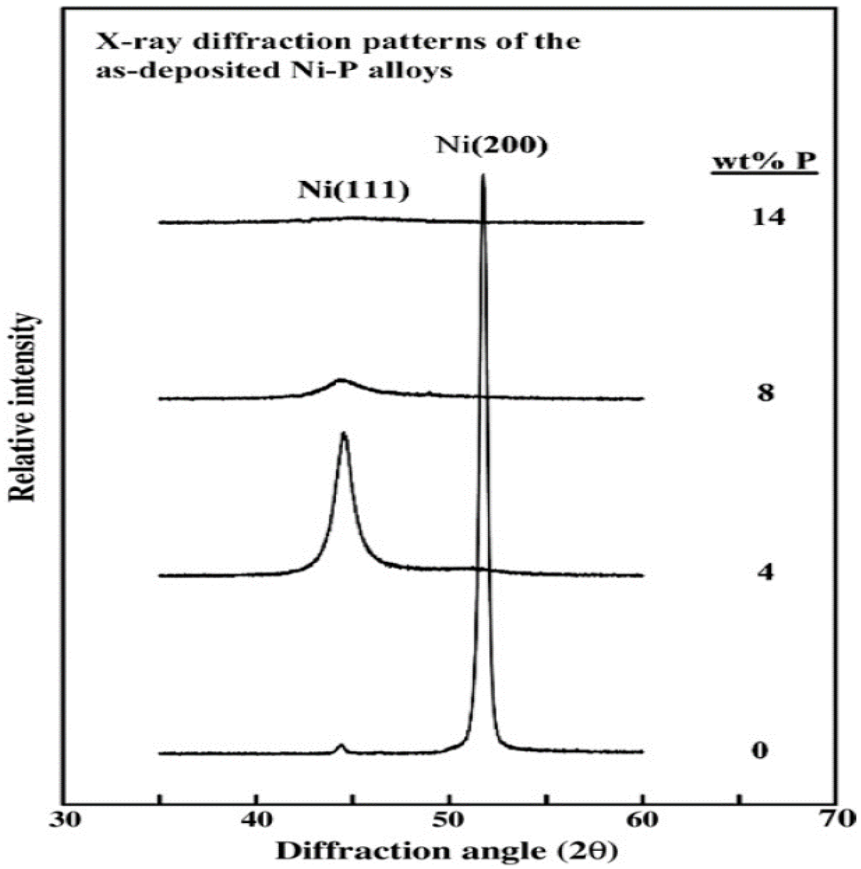

Figure 2.29 X-ray diffraction patterns of as-deposited Ni-P alloys with various P contents [106].

The change in Ni-P crystallinity with various P contents has also been verified by TEM, as shown in Fig. 2.30. The micrograph in Fig. 2.30(a) shows the (111) plane of the lattice for Ni without P has plane distances of 0.204 nm. The micrograph in Fig. 2.30(b) shows that Ni-4wt% P clearly contains both crystalline and amorphous phases. The size of the dispersed crystalline phase ranges from 1 to 10 nm, which has a much lower P content of 0.9 wt% than the surrounding amorphous phase of 3.9 wt% P (detected by EDS in the TEM). As the P content increases to 8 wt% in the coating, shown in Fig. 2.30 (c), the number and size of the nanocrystalline phases decrease dramatically. The nanocrystalline phase also has a lower P content compared to the surrounding amorphous phase. It has been proposed that the existence of P in the deposit decreases the grain size, which brings about the nanocrystalline phase dispersed in an amorphous matrix [106]. Furthermore, after alloying with atoms, the Ni (111) lattice constant expands from 0.204 nm for pure Ni to 0.221 nm for Ni-4P coating and 0.230 nm for Ni-8P coating.

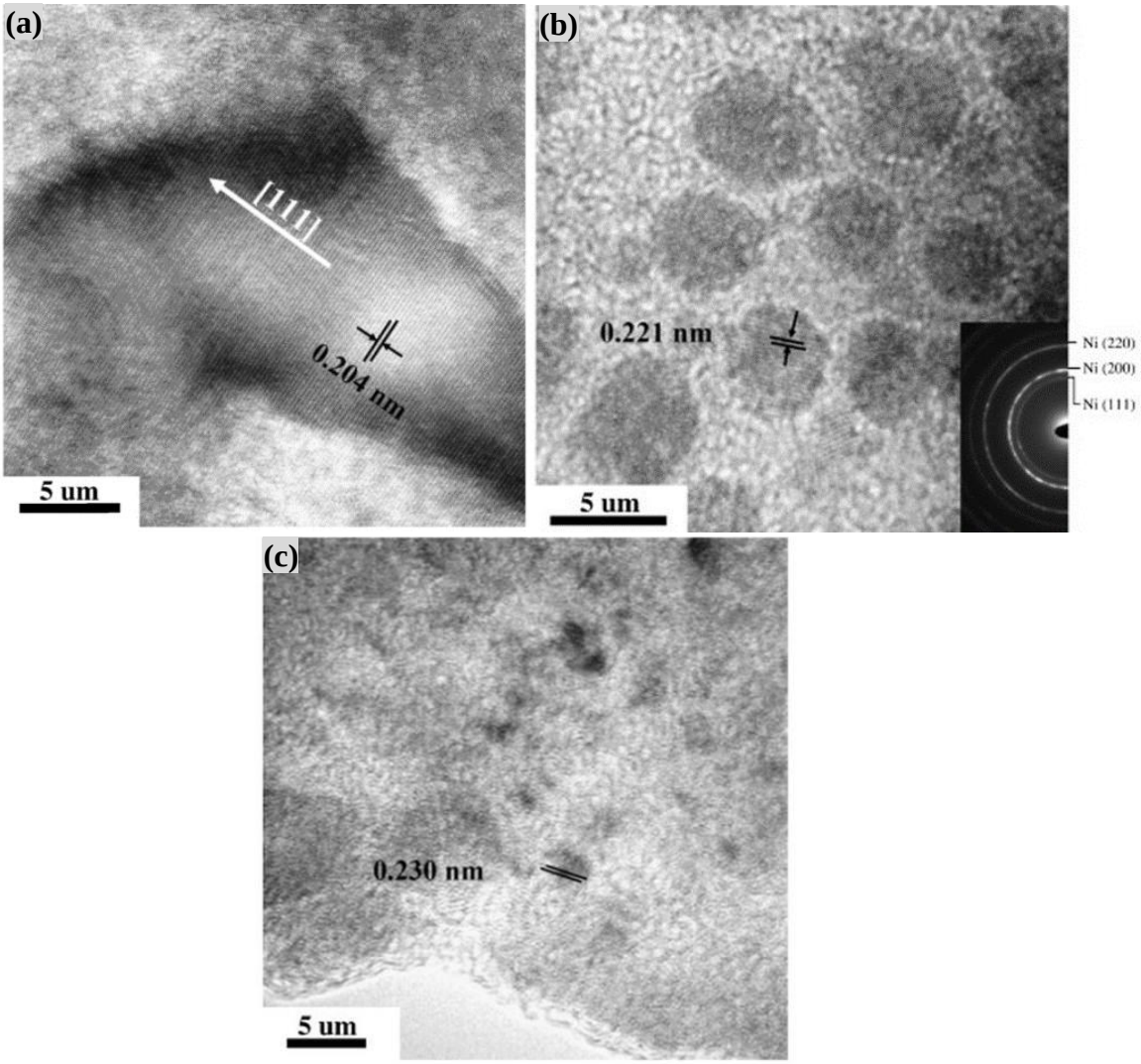

Figure 2.30 HTEM micrographs of (a) pure Ni coating, (b) as-deposited Ni-P alloy with 4 wt% P and (c) as-deposited Ni-P alloy with 8 wt% P [106].

Hardness

The hardness of Ni-P deposits is related to their crystal properties, which are significantly influenced by the P content. For Ni-P coatings with different P contents produced in a citric acid modified Watts bath with the addition of phosphorous acid (H_3PO_3), the micro-hardness of the as-deposited and heat-treated coatings are summarized in Fig. 2.31. Without P, the pure nickel shows a hardness of 220 HV. The codeposition of P in the Ni matrix could significantly increase the hardness of the coating and the as-deposited Ni-P alloy has a peak hardness of 620 HV at a content of 4 wt% P. Then the hardness decreases monotonically as the P content increases further.

Usually, the maximum hardness of Ni-P deposits occurs at an intermediate P content, but the exact content varies from case to case. It is noteworthy that the Ni-P deposited either

in a similar Watts bath containing phosphorous acid without citric acid, or in a sodium hypophosphite bath usually display a maximum hardness at the higher range of 7-9 wt% P. Evidently, the addition of citric acid leads to a coating with maximum hardness at a lower P content of 4 wt%. This has been attributed to the chelating effect of citric acid with Ni^{2+} ion to form stable five- or six-membered rings, which leads to the increase of overpotential for Ni^{2+} reduction [107,108]. As a result, the grain size refinement effect is more prominent than in those coatings electroplated from a citric acid-free bath. In other words, the grain size of the Ni-P deposit decreases to a greater extent at the same P content with the addition of citric acid into the bath.

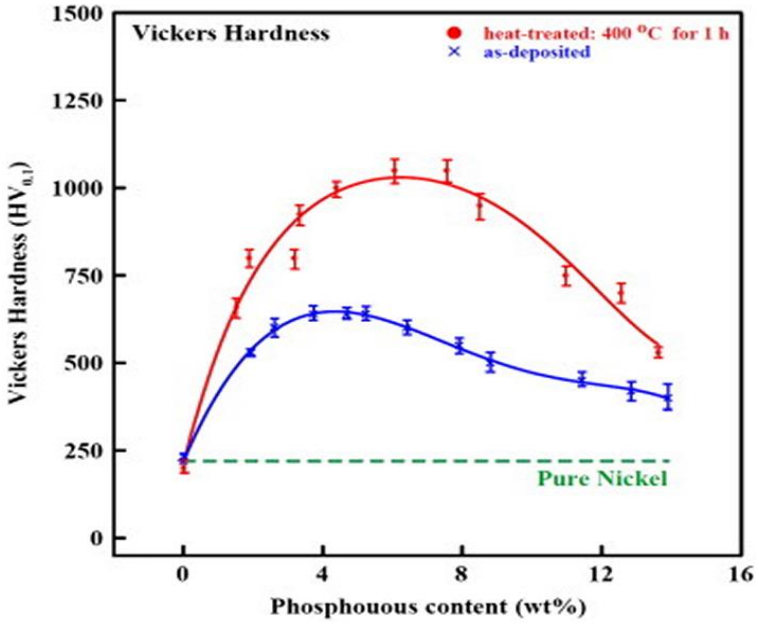

Figure 2.31 Micro-hardness of pure Ni, as-deposited Ni-P and the heat-treated Ni-P electrodeposits containing different amounts of P [106].

After heat-treatment, the hardness of Ni-P alloys increases substantially, and have been suggested as the most wear resistant nickel alloys [109]. As shown in Table 2.5, the Ni-P coating shows a Vickers hardness of 865 and 1082 HV respectively after heat treatment at 300 °C and 400 °C for 1 h, higher than that of hard Cr. The significant hardness increase is associated with a structural change in the coating. Various studies [110,111] have shown that heat-treated Ni-P alloys favour the formation of Ni_3P which is a hard intermetallic compound with high thermodynamic stability, producing the effect of precipitation hardening. If the annealing temperature exceeds 500 ℃, the hardness of the Ni-P alloy coating decreases drastically. This softening phenomenon for the Ni-P alloy at high temperature is due to the conglomeration of the Ni_3P particles, reducing the number of hardening sites. On the other hand, P was also removed from the alloy, resulting in a separate phase of soft nickel within the matrix and further reducing the bulk hardness.

Table 2.5 Effect of heat treatment on the hardness of Ni-P alloys [109].

Material	Microhardness (HV)
AISI 304 stainless steel	380 ±20
As deposited Ni-P alloys	618 ±20
300 ℃ heat treated Ni-P alloys	865 ±20
400 ℃ heat treated Ni-P alloys	1082 ±30
500 ℃ heat treated Ni-P alloys	901 ±20

Wear resistance

Due to the high hardness and good ductility, Ni-P deposits are expected to have good wear resistance [112]. Fig. 2.32 summarizes the relationship between Taber abrasive wear index and hardness for pure polycrystalline and nanocrystalline Ni, as-plated Ni-P and heat-treated Ni-P coatings [113].

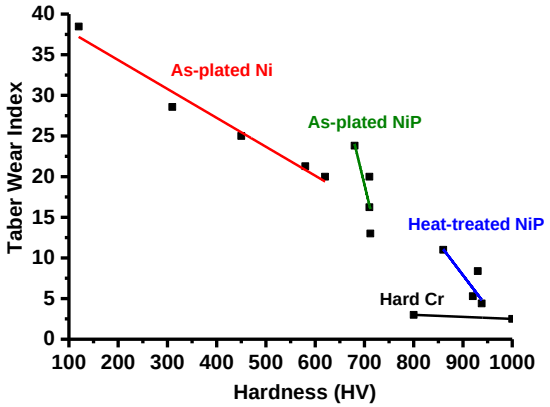

Figure 2.32 Relationship between Taber abrasive wear index and hardness for pure polycrystalline and nanocrystalline Ni, as-plated Ni-P and heat-treated Ni-P coatings [113].

The Taber Wear Index (TWI) is calculated by measuring the loss in weight (in milligrams) per thousand cycles of abrasion. The lower the wear index, the better the wear resistance. The TWI for Ni with different crystalline sizes vary from 40 to 18 and for Ni-P (9 wt% P) it is around 16, while as-heated Ni-P have a TWI range of 3-10 and chrome plate has a TWI value around 3. By comparison, some conclusions can be drawn. Firstly, the Taber abrasive wear resistance is linearly proportional to the hardness of coatings in each group. Secondly, the abrasive wear resistance has been considerably increased as the hardness is improved through many mechanisms including: (a) grain size decrease for pure nanocrystalline Ni, (b) alloying with P for as-plated nanocrystalline Ni-P and (c) heat

treatment for heat-treated nanocrystalline Ni-P. Thirdly, the wear resistance of Ni-P coatings are comparable to hard chromium in some respects, and hence could be developed to substitute for hard chromium.

A novel Ni-P gradient alloy with a graded change of P content in the growth direction of the deposit was designed and electrodeposited to further improve the wear resistance of Ni-P coatings [114]. The schematic graph and results are shown in Fig. 2.33. It can be seen that heat-treated Ni-P gradient deposits have both improved friction and wear properties in comparison to conventional hard Cr deposits when sliding against a silicon nitride ball under unlubricated conditions. The friction coefficients of graded Ni-P alloys vary in the range of 0.44-0.47 if subjected to different heat treatments, which are lower than the friction coefficient of heat-treated hard Cr deposits in the range of 0.53 to 0.58. It also illustrates that the layered Ni-P deposit shows the lowest wear rate, 1/3-1/2 of that of monolayer Ni-P deposits, and 15% lower than that of a conventional hard Cr deposit. So it appears that Ni-P deposits with graded changes in composition and microstructure throughout the thickness could be a good substitute to replace hard Cr deposits.

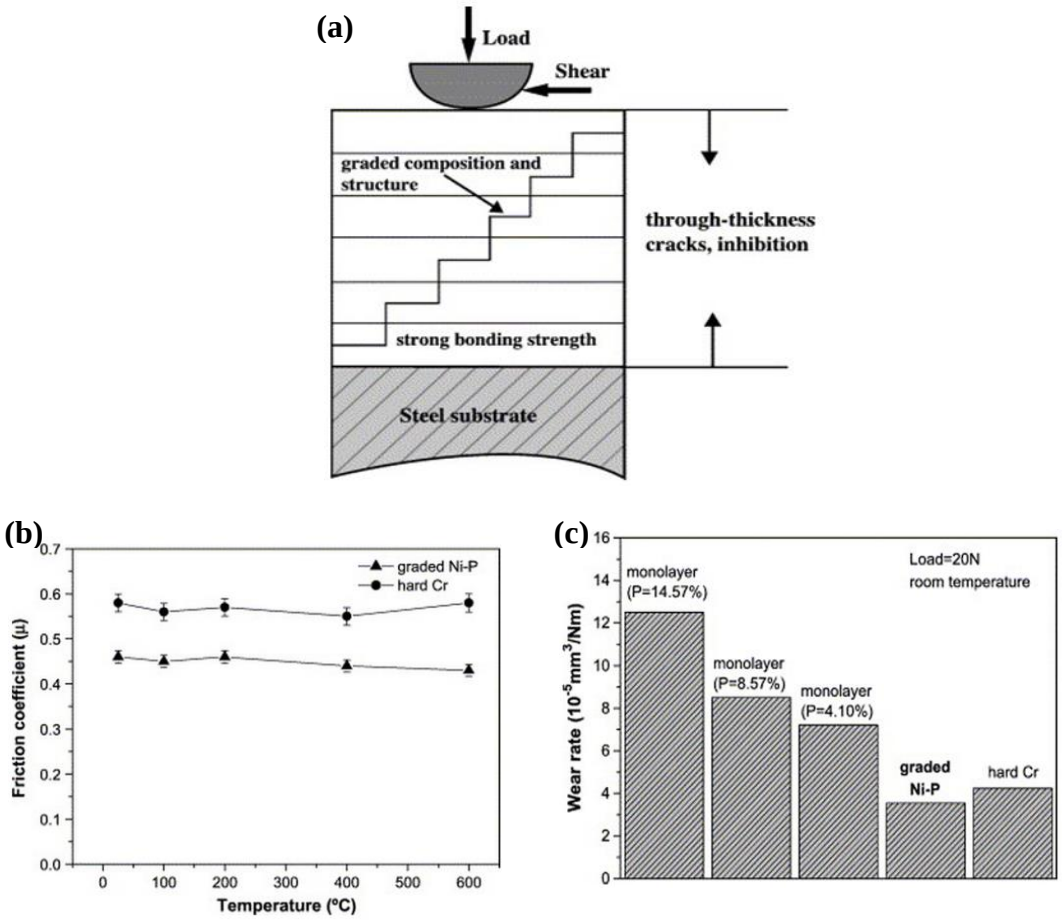

Figure 2.33 (a) Schematic diagram of Ni-P gradient deposits; (b) Effect of temperature on the friction of heat-treated Ni-P gradient; (c) Wear rate comparison of graded Ni-P, Hard Cr and different monolayer Ni-P [114].

2.3.1.3 Recent developments and our group's work

The as-heated Ni-P coating seems to have promising prospects for replacing hard Cr. However, the brittleness and the reduced integrity of alloy deposits after heat treatment has restricted their complete replacement of hard chromium, especially for anti-wear applications in a progressive environment, such as under conditions of high speed and heavy load. Under these conditions, significant through-thickness cracking has been observed for Ni-P deposits with high thickness [115,116,117].

Many attempts have been made to tackle the disadvantages of Ni-P coatings and further improve their performance. The properties of Ni-P coatings can be modified by either alloying with other metals such as molybdenum or tungsten, or codepositing with functional particles. Significant improvements have been achieved on Ni-P based ternary alloys, and the following section is a summary of some related works including our group's contribution.

A composition modulated coating consisting of alternate layers of ternary Ni-P-W alloys with different phosphorus and tungsten contents, has been produced by electrodeposition from a single bath using pulsed current [118]. The Ni-10%P-10%W layers were deposited during the low current density step of 20 mA cm^{-2}, whereas the Ni-5%P-45%W layer was deposited during the high current density step of 200 mA cm^{-2}. The cross section of the multi-layered coating was examined in the TEM, as shown in Fig. 2.34. Generally, the layers are regularly spaced and also uniform in thickness. The layer thickness is about 4 nm for this coating. The dark layers are the W-rich layers while the W-poor layers are light-coloured layers. The interfaces are relatively sharp, and both layers are amorphous or nanocrystalline with grain size smaller than the minimum layer thickness (3 nm).

By changing the alternate time length of pulse current, the layer periodicities (bilayer thickness) could be 6, 20, 60, 200, 600 and 2000 nm with a total coating thickness of 25 μm. Unlubricated sliding wear behaviour was evaluated for the different modulated coatings. The friction coefficients for the different coatings did not show any big difference, with an average of about 0.9. Fig. 2.34(b) lists the wear volume loss of multi-layered coatings with different layer periodicities versus loads. It can be observed that the wear volume values are relatively low at the first point, indicating the significant antiwear

protection of a multilayered coating under low load conditions. The wear volume values stay very low for all coatings up to a critical load of 500 g. As the applied load increase further, the wear volume increases more rapidly and the wear rates vary for the coatings with different layer periodicities (2000 nm to 60 nm). Those coatings with small layer periodicity are more resistant to wear than the coatings with large layer thickness. Such increased wear resistance of the small layer periodicity coatings (up to 60 nm) is attributed to an increased number of interfaces in the structure compared to the larger layer periodicity coatings, which could make wear cracks deflected and absorb more energy during their propagation.

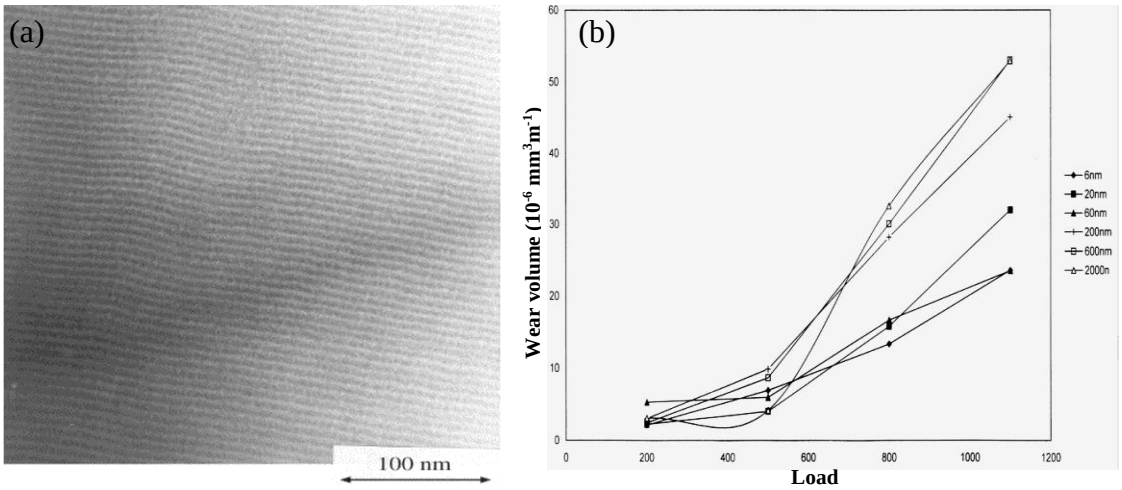

Figure 2.34 (a)TEM images of the cross-section of a multilayered Ni-P-W coating; (b)Wear volume of the multilayered coatings on the pins, normalized per meter of sliding distance versus normal load [118].

Our group's work on the electrodeposition of Co-Ni and Ni-Co-P alloys for replacing hard Cr has been carried out for several years. Nanocrystalline Co-Ni-P coatings with different contents of Co were electrodeposited on mild steel substrate from electrolytes consisting 40 g/L $NiSO_4 \cdot 6H_2O$, $CoSO_4 \cdot 7H_2O$, 20 g/L NaH_2PO_2 and additives. Fig. 2.35 shows the surface morphologies of the Co-Ni-P coating after heat treatment at different temperatures for 1 h. The as-deposited samples exhibit a smooth surface with a low surface roughness (Ra=1.6 nm). During the annealing process from 200 ℃ to 500 ℃, some pits along the boundaries of clusters have been observed at first, which are gradually covered by oxide clusters generated at a higher temperature. The EDS result indicates that the composition of the as-deposited sample is 62 at.%Co -15 at.%Ni -23 at.%P. The oxidation of the coating surface starts from 300 ℃, which corresponds to the surface morphology evolution shown in Fig. 2.35(c).While the content of oxygen increases with

the increasing annealing temperature, the content of nickel and phosphorous in the surface drops to 0 when the temperature reaches to 500 ℃. The top layer of the coating annealed at 500 ℃ is $Co_{0.6}O$, which is a mixture of CoO and Co_2O_3.

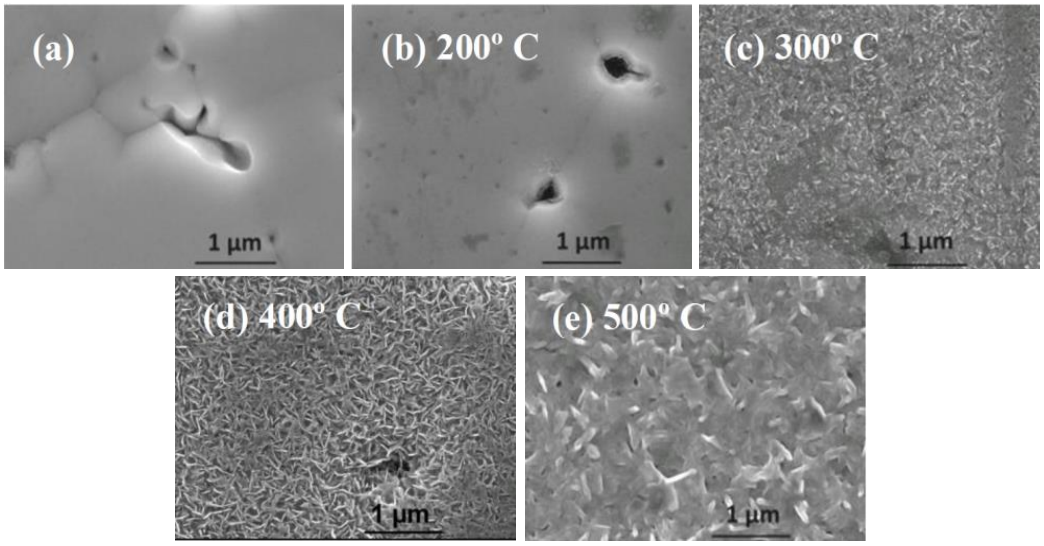

Figure 2.35 SEM micrographs of (a) as-deposited coating and (b)-(e) heat-treated coatings at different temperatures: 200°C, 300°C, 400°C, 500°C for 1h[15].

Fig. 2.36 shows the wear rates of heat-treated Co-Ni-P coatings compared with hard chromium. The wear rates of Co-Ni-P coatings are one order of magnitude lower than that of hard chromium [15]. The Ni-Co-P coating annealed at 400 ℃ has a wear rate of $4*10^{-6}$ mm^3 $N^{-1}m^{-1}$, much lower than that of the as-deposited Co-Ni-P. It is due to the maximum hardness of 980 HV for the coating heated at 400 ℃ for 1 h. The superior wear resistance could enable it to replace hard chromium in a wide range of applications, such as marine engineering, automotive components and pipelines for chemicals or waste water.

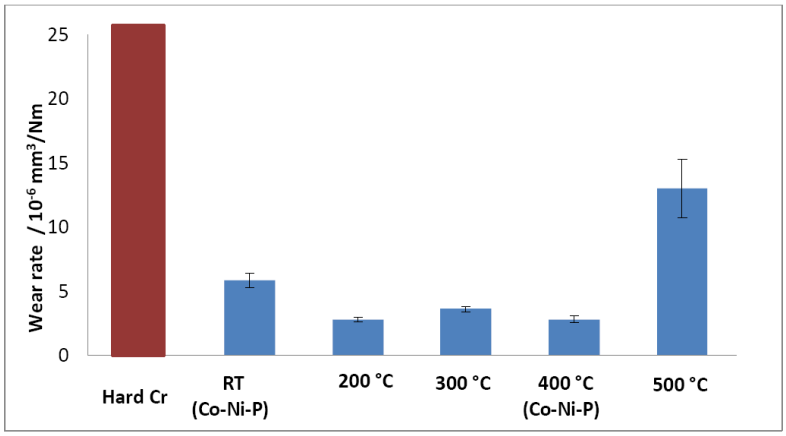

Figure 2.36 Comparison of wear rates between hard chromium coating and Co-Ni-P coating annealed at different under dry sliding wear conditions [15].

2.3.2 Solid lubricant

Solid lubricants are materials in the solid phase which are used for reducing friction and wear between two sliding surfaces. During the friction process, solid lubricants could fill in surface valleys and smooth asperity peaks as they have strong adhesion to the substrate, forming effective boundary lubrication films. Unlike the oil or grease fluid lubricant films which only produce hydrodynamic lubrication at high speed without high contact pressure, the lubrication performance of solid lubricants is unaffected by a load, temperature or speed. Due to these characteristics, solid lubricants are widely applied for extreme conditions such as high temperature, high vacuum or high load, where liquid lubrication is neither feasible nor recommended.

Based on crystal structure and chemical process, solid lubricants can be classified into different categories as shown in table 2.6 [119]

Table 2.6 Categories of lubricants in terms of materials [119].

Classification	Typical examples (Friction coefficient)
Soft metal	Ag (0.2-0.35) Pb (0.15) Au (0.2-0.3) In (0.15-0.25) Sn (0.2)
Carbon based solids	Diamond (0.02-0.1) DLC (0.003-0.5) Hollow C nanotubes (0.2) Fullerenes (0.15)
Lamellar solids	MoS_2 (0.002-0.25) WS_2 (0.01-0.2) Graphite (0.07-0.5) H_3BO_3(0.02-0.2)
Single oxides	B_2O_3 (0.15-0.6) Re_2O_7 (0.2) MoO_3 (0.2)
Mixed oxides	CuO-Re_2O_7 (0.3-0.1) CuO-MoO3 (0.35-0.2) Cs_2O-SiO_2 (0.1) PbO-B_2O_3 (0.2-0.1)

The main applications of solid lubricants and coatings are in the space industry and/or extreme environments, their advantages and disadvantages have been addressed by the National Aeronautics and Space Administration (NASA) [120].

Table 2.7 Advantages and disadvantages of coatings with solid lubricants [120].

Advantages	Disadvantages
• Are highly stable in high-temperature, cryogenic temperature, vacuum, and high-pressure environments • Have high heat dissipation with high thermally conductive lubricants, such as diamond films • Have high resistance to deterioration in high-radiation environments • Have high resistance to abrasion in high-dust environments • Have high resistance to deterioration in reactive environments • Are more effective than fluid lubricants at intermittent loading, high loads, and high speeds • Enable equipment to be lighter and simpler because lubrication distribution systems and seals are not required • Offer a distinct advantage in locations where access for servicing is difficult • Can provide translucent or transparent coatings, such as diamond and diamond like carbon films, where desirable	• Have higher coefficients of friction and wear than for hydrodynamic lubrication • Have poor heat dissipation with low thermally conductive lubricants, such as polymer-based films • Have poor self-healing properties so that a broken solid film tends to shorten the useful life of the lubricant (However, a solid film, such as a carbon nanotube film, may be readily reapplied to extend the useful life.) • May have undesirable colour, such as with graphite and carbon nanotubes.

The friction coefficient of solid lubricants exhibit a wide range, since it can be influenced by either the specific form of solid lubricants such as a thin film, powder, composite and amorphous states, or the test environment and configuration. Among all these different solid lubricants, lamellar solid lubricants such as dichalcogenides (MoS_2, WS_2) or graphite attract a lot of attention in academia and industry since these can provide very low friction coefficients, usually in the range of 0.002-0.25. Such excellent performance is directly related to their crystal structures. For example, in the MoS_2 molecule, there is powerful covalent bonding between atomic species, while there is only a very weak Van der Waals attraction between lattice layers. So, in the direction of motion the lamellae can easily shear over each other.

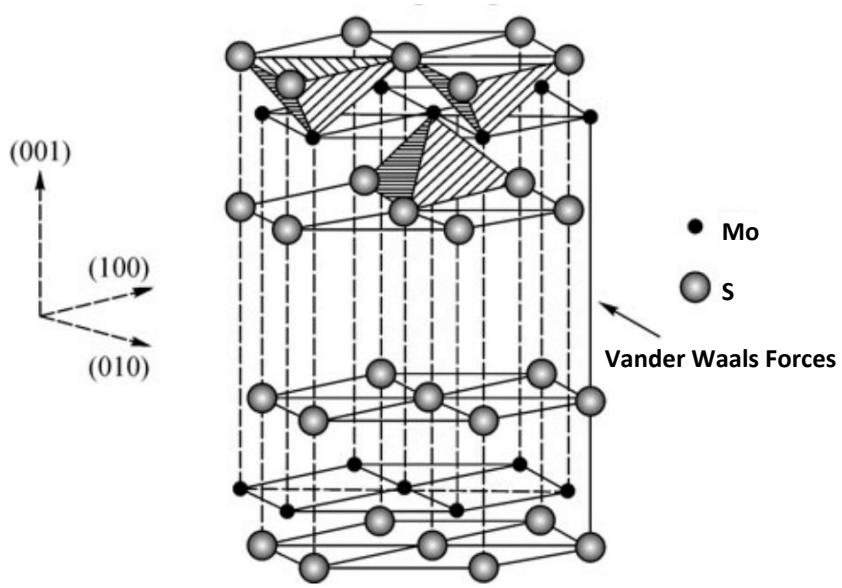

Figure 2.37 The crystal structure of MoS_2 [121].

MoS_2 occurs naturally in the form of thin solid veins within granite, which is mined and highly refined to produce purity suitable for lubricants. Unlike graphite, MoS_2 performs well in high-vacuum conditions because there is no vapour present between the MoS_2 lattice plates. A considerable amount of literature has been published on the most commonly used lamellar compound solid lubricant - MoS_2 [122]. The use of molybdenum disulphide as a lubricant by the US National Advisory Committee for Aeronautics (NACA) in 1946 is considered as the initiating study of MoS_2, laying the foundation for its expanded applications in aerospace and road vehicles in the following years.

Vacuum sputtering of MoS_2 film is a remarkable application technique for depositing this material. It was first devised in 1967 by Spalvins, which was then investigated later and

has now been widely utilized as a standard industrial process [123]. However, the early MoS_2 thin film deposited by a direct current (DC) sputtering apparatus was just a near-stoichiometric crystal with a porous, columnar structure [124]. Owing to this structure, the D.C. sputtered MoS_2 films usually exhibit higher friction coefficients and shorter wear lives compared to the more newly developed films produced by ion beam assisted deposition and close-field unbalanced magnetron sputtering methods. The latter techniques can deposit a MoS_2 film of perfect stoichiometry, purity and basal plane orientation parallel to the substrate. It has been reported by Martin and co-workers [125] that the MoS_2 films produced by these methods can achieve friction coefficients as low as 0.002 in ultrahigh vacuum. So far, molybdenum disulphide has been successfully produced on surfaces by various techniques, including burnishing, vacuum sputtering, and air spraying and more recently by other advanced surface engineering processes like ion beam and laser assisted deposition.

Even with its super lubricating performance, MoS_2 film is mainly used in limited conditions e.g. at room temperature in an inert atmosphere or ultrahigh vacuum. In these conditions, the MoS_2 exhibits some of the lowest friction coefficients. In contrast, its tribological performance degrades remarkably in the presence of humidity because it is prone to water adsorption - known as the hygroscopic effect. Additionally, it also oxidizes readily in oxygen-containing atmospheres at elevated temperature, which causes irreversible damage to the film and has a seriously detrimental effect on its lubricating ability [126,127]. The service temperature of MoS_2 is determined by: (i) Microstructure characteristics such as crystal structure, crystallite size and surface roughness etc. (ii) The service conditions such as atmosphere, humidity and air flow rate etc. (iii) Expected frictional properties and durability requirements. Normally, MoS_2 just oxidizes slowly in atmospheres up to 315 ℃ (600 ℉). It has been reported that for MoS_2 powders which are loosely-compacted with mean particle size of 1 μm, the maximum service temperature was 400°C (752°F) at a modest air flow rate, with 50% of MoS_2 oxidized to MoO_3 [128]. Kohli and Prakash studied the variation of the frictional characteristics of burnished MoS_2 coatings as the temperature increased from 25 ℃ to 350 ℃. The results are shown in Fig. 2.38 [129]. It is clear from the plot that the friction coefficient keeps on dropping with the increase of temperature till 80 ℃, after which it stays nearly constant till 120 ℃ and then starts rising slowly.

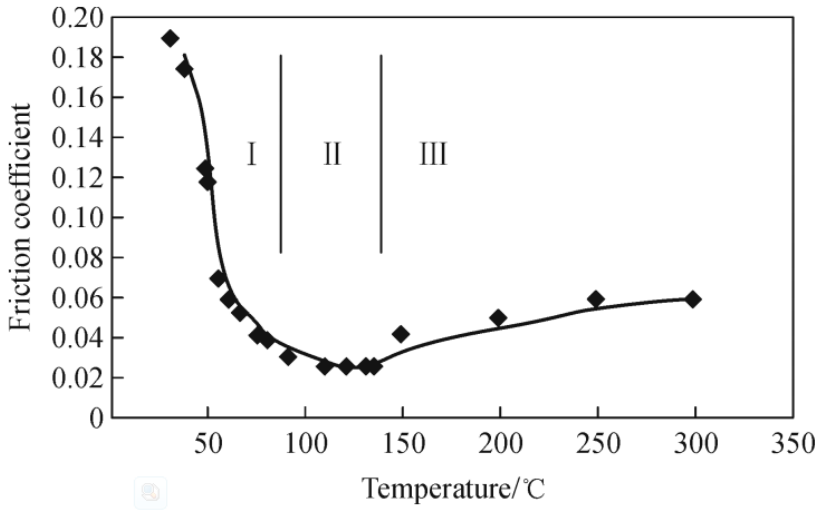

Figure 2.38 Temperature dependence of friction coefficient of MoS_2 burnished coatings [129].

To overcome these limitations, preparation of composite coating was thought to be a feasible way. In composites, the MoS_2 particles are isolated from water vapour and oxygen, and suppress the formation of porous, columnar microstructures [130]. The schematic graph of a proposed composite coating is shown in Fig. 2.39 [126].

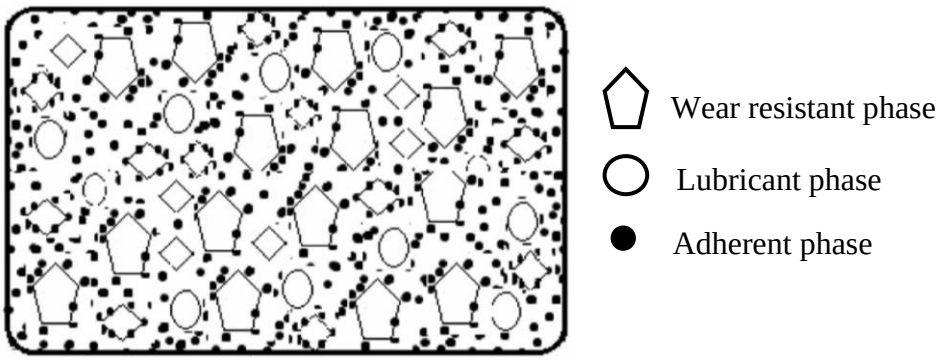

Figure 2.39 Schematic of a hybridized composite coating containing both wear resistant and lubricant phase [126].

Various metals (e.g. Au, Ni, Ti, Pb, C, etc.) and compounds (TiN, PbO, SbO_3, etc.) have been codeposited into MoS_2 films to form composites [131,132]. In 1984, Spalvins reported that MoS_2 films containing 5 at.-% cosputtered Au showed less friction than pure MoS_2 film in dry air, which was related with its densified structure after co-sputtering [133]. Hilton et al. did sputter composites of MoSx with Ni and multilayers of Au-Pd with MoSx, which both showed the basal-plane oriented structure as well as good wear characteristics [134]. The improved tribological performance obtained has been attributed

to the sacrificial oxidation of the Ni metal during the wear process, resulting in more pure MoS_2 crystallites.

Teer and co-workers produced MoS_2- films with Ti of different percentages by closed-field magnetron sputtering and tested their performance on cutting and forming tools [135]. At the end of the deposition process, the titanium sputter target was switched off to deposit final layers consisting of pure MoS_2. From the TEM image in Fig. 2.40, it is clear that it is crystallized MoS_2 with (0 0 2) planes on the top but the co-deposition layer inside doesn't illustrate any crystalline structure. Furthermore, it is impossible to detect any elemental titanium within the coating either as layers or individual particles using SEM/EDS, demonstrating a uniform distribution of Ti across the entire coating. The MoST (Ti-MoS_2) composite has a hardness of between 1000 and 2000 HV depending on the Ti content. The high hardness indicates that the titanium is present in solution within the MoS_2 lattice and produces strain. The Ti content was also found to be effective in improving the performance of the coating, achieving a low friction coefficient of 0.005 using ball-on-disc tests at a load of 10N under dry nitrogen gas. It was suggested that titanium presented an 'oxygen gettering' effect during both deposition and the wear process, protecting the MoS_2 film against oxidation. MoS_2 films alloyed with Cr, W, Mo and Zr were also produced, which resulted in harder coatings in all cases but didn't provide better tribological performance than the Ti alloyed MoS_2 film [136].

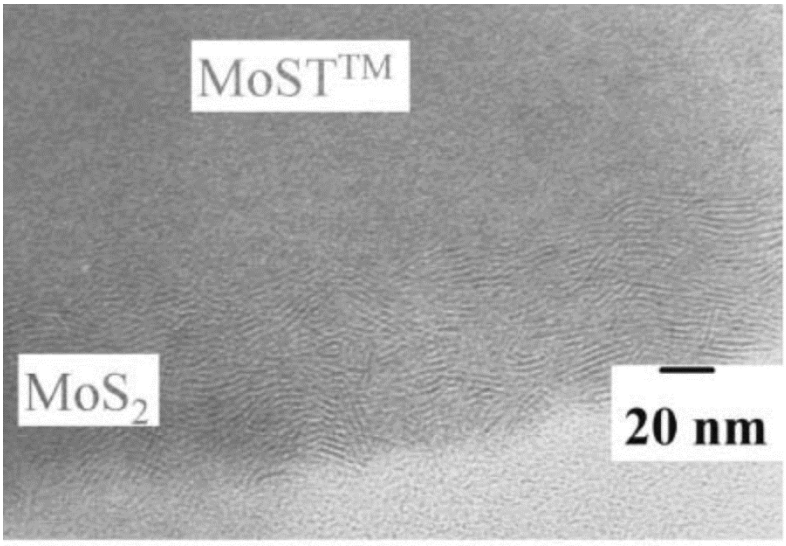

Figure 2.40 TEM micrograph of MoST (Ti-MoS_2) [137].

Simmonds et al. investigated the effect of dopant choice and concentration on the resulting tribological and mechanical behaviour of cosputtered films of MoS_2 [138]. Au, Ti, Cr and WSe_2 were selected to be cosputtered with MoS_2 film, among which the best result was shown by composites with WSe_2, followed by Au, Ti and Cr.

Electrodeposition is one of the most common ways to prepare a composite coating, consisting of a metal or alloy matrix containing a dispersion of second phase particles [16,139]. Based on the Ni alloy electrodeposition bath, different kinds of particles can be added, including hard oxide or carbide particles, such as Al_2O_3, SiC, TiO_2, WC, SiO_2, or solid lubricants, such as PTFE, graphite or MoS_2, or even liquid-containing microcapsules to improve wear resistance and/or to reduce friction [140,141,142]. The related work of the electro codeposition of metal with WS_2 or MoS_2 will be reviewed in the following section.

2.3.3 Electrodeposited low friction Ni/MoS_2 coatings

Due to ongoing global energy shortages and the environmental problems caused by fuel emission, there is a push for industry to use low friction components to reduce overall fuel consumption. Layered (2H) transition metal sulfides like MoS_2, are widely used solid lubricants with very low friction coefficient in vacuum, but they are easily oxidized in humid and oxygen-rich environments since the dangling bonds of their rim atoms are very active. In addition, these solid lubricants are soft and easily worn. So, before using them in many circumstances, the first step is to modify the properties of MoS_2 coatings by adding metal or sometimes compound (dopants) to form composite or composite multilayer coatings. A lot of studies have proved that the combination of metals and solid lubricants can improve the tribological properties of coatings by changing their structure.

With the increasing availability and decreasing cost of MoS_2 particles, there is a growing interest in the electrolytic codeposition of particles to combine the mechanical advantage of electrodeposited hard Ni-series coatings and low friction characteristic of solid lubricants. It is estimated that such a deposited composite coating could exhibit intrinsic low friction and high mechanical strength. Since the major challenges facing the electro-codeposition of Ni alloys and lubricant particles (such as including codepositing a sufficient number of particles and avoiding the agglomeration of particles suspended in bath) have been tackled gradually, such electrodeposited coatings seem to have a very

promising future to protect various substrates adequately, with a possible application in replacing Cr coatings.

Electrodeposited low friction Ni/alloy coatings with MoS_2 incorporation thus attract a lot of interest in the coatings industry and their development will be discussed in more detail in the following paragraphs.

Wang [19] studied the role of surfactant on MoS_2 incorporation into a Ni matrix during electrodeposition. It was found that positive ions of surfactant (Benzyl Ammonium Salts, BAS) tend to be effectively absorbed on the surface of MoS_2 particle causing electrostatic attraction to the cathode. The microstructure of the MoS_2 codeposition layer is shown in Fig. 2.41(a) and pores (as arrowed) are observed. The more BAS was added the less porosity was observed in the deposited coating. This has been explained in the following way. When BAS is adsorbed on the particle surface, the conductivity of MoS_2 will decrease. Then, more Ni atoms are deposited homogeneously over a wider area rather than deposited on preferred conductive positions, resulting in a smoother layer with lower porosity similar to the codeposition of non-conductive particles. The strong adhesion between the deposited layer and the substrate when employing BAS may result from the lower porosity of the deposited layer.

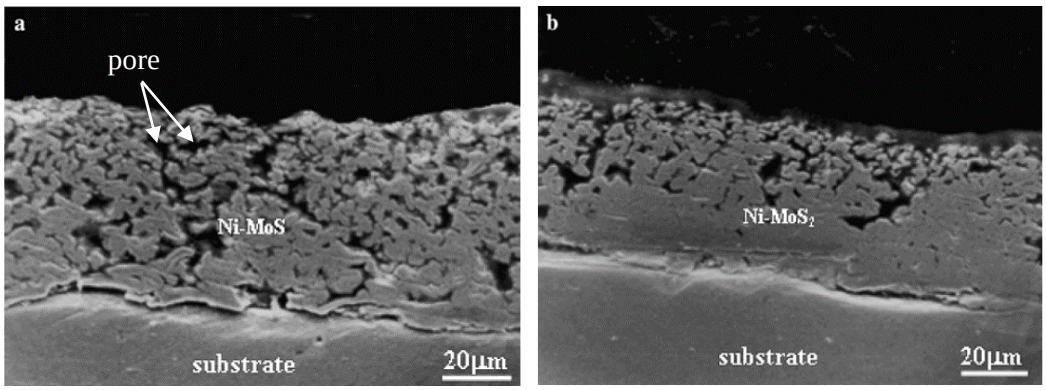

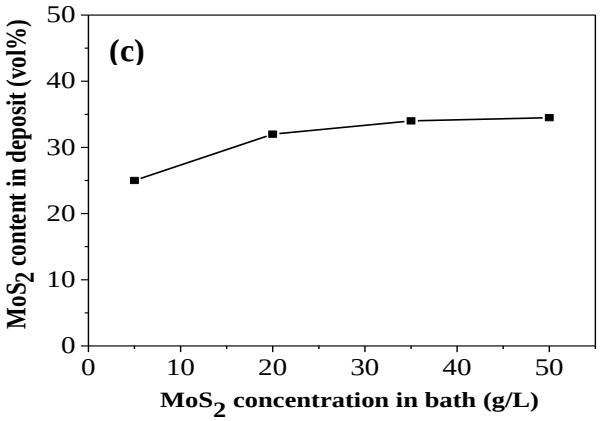

Figure 2.41 (a) Cross-section microstructure of MoS_2 with less surfactant addition (BAS 0.05); (b) Cross-section microstructure of MoS_2 with more surfactant addition (BAS 0.10); (c) Effect of MoS_2 loading on the extent of codeposition of MoS_2 (pH=5, T=45 °C, rpm=500, BAS 0.1 g) [19].

Cardinal, et al. [21] developed Ni-W-MoS_2 composite coatings by a pulse plating technique. As shown in Fig. 2.42, the Ni-W coating shows a uniform structure, with a thickness of ~ 40 μm, whereas coatings with MoS_2 incorporation show a more sponge-like structure, with larger average thickness (80 μm~ 180 μm). The Ni-W/MoS_2 composite coatings deposited in a bath with 0.5 g/L MoS_2, have a somewhat compact structure with small pores and good substrate adhesion. But incorporating more MoS_2 particles into the coating will result in poor substrate adhesion and more pores in the coating structure.

The incorporation of MoS_2 (bath concentration 0.5 g/L) into the nanostructured Ni-W coating can lower the coating friction coefficient by 50% to 0.13. However, the coatings deposited at higher MoS_2 bath concentrations (1 g/L and above) present non-constant friction coefficients with maximum values exceeding 0.4. This may relate to their sponge-like structure and very rough and inhomogeneous surfaces. The important finding of this work is that the co-deposition of MoS_2 particles into Ni-W alloys could significantly enhance the frictional properties of the coating, especially for a coating containing fewer pores.

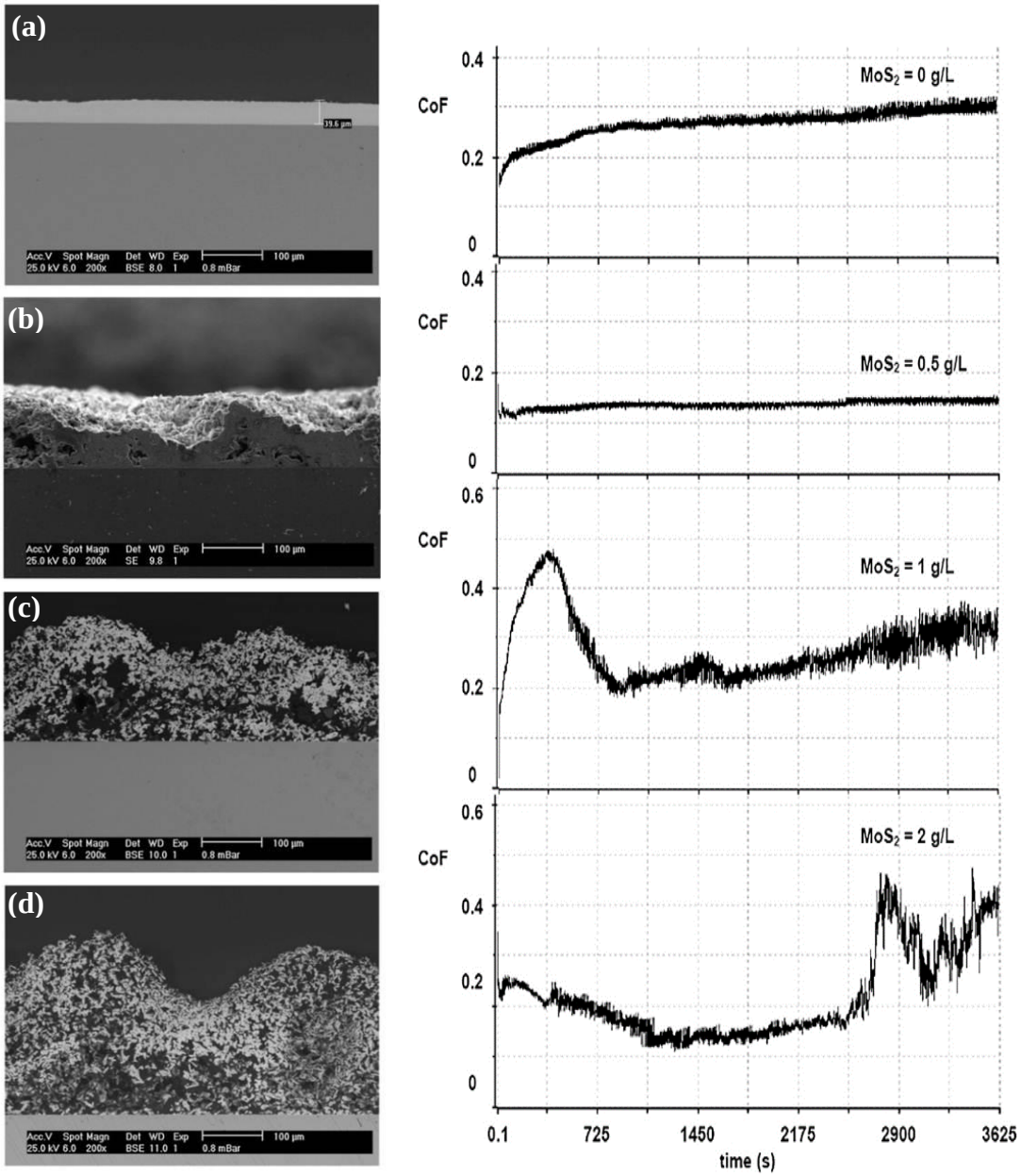

Figure 2.42 SEM images and friction coefficients of Ni-W electrodeposits as a function of increasing MoS_2 bath concentration: (a) 0 g/L, (b) 0.5 g/L (c) 1 g/L and (d) 2 g/L [21].

Shi et al. [22] reported the preparation and performance investigation of nano-sized MoS_2 reinforced Ni-Co composite coatings obtained by electrodepositing. The plating bath contains 200 g/L $NiSO_4$, 40 g/L $NiCl_2$, 20 g/L $CoSO_4$, 30 g/L H_3BO_3,1 g/L MoS_2 nanoparticles (20 nm), and a suitable amount of sodium lauryl sulphate.

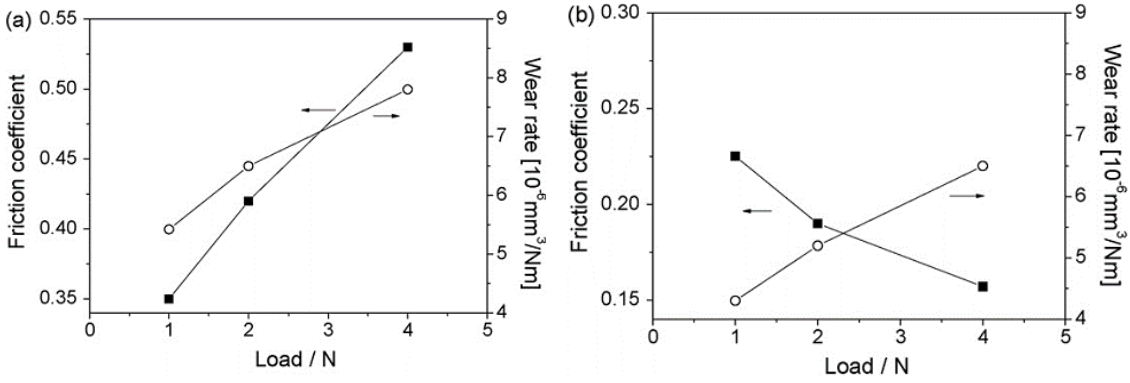

Figure 2.43 Friction coefficient and wear rate of (a) Ni-Co and (b) Ni-Co/MoS_2 composite coating against SAE52100 steel ball at different loads [22].

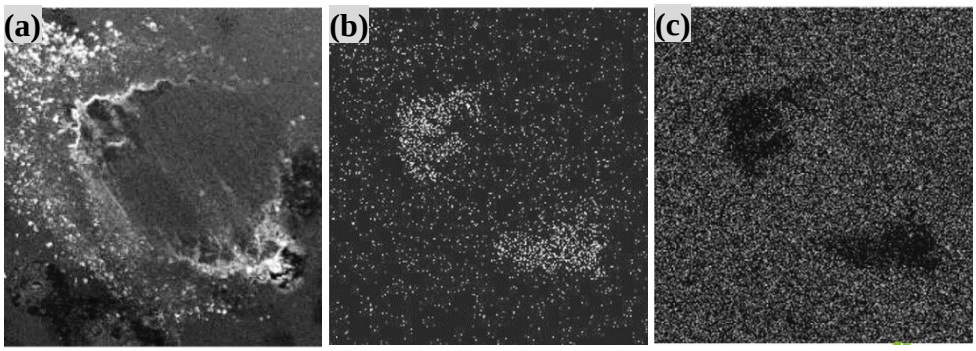

Figure 2.44 SEM morphologies of (a) wear scar of the steel ball (150 ×), (b) S distribution and (c) Fe distribution thereon (against Ni-Co/MoS_2 composite coating at a load of 2.0 N) [22].

At the load of 4 N, the Ni-Co coating shows a friction coefficient of 0.53 and a wear rate of 7.8 × 10^{-6} mm^3 N^{-1} m^{-1} while the Ni-Co/MoS_2 1 g/L coating shows a lower friction coefficient of 0.16 and wear rate of 6.5 × 10^{-6} mm^3 N^{-1} m^{-1}. The averaged friction coefficient of the Ni-Co/MoS_2 composite coating decreases from 0.23 to 0.16 with a load increasing from 1.0 N to 4.0 N, which was attributed to the formation of a lubricating transfer layer on the counterpart surface during sliding. This observation is consistent with the typical variation of the friction coefficient as a function of load for other MoS_2 coatings [143].

2.3.4 Electrodeposited low friction Ni/WS_2 coatings

With the same lamellar structure, WS_2 exhibits better low-friction properties than MoS_2 at high-temperature as MoS_2 can rapidly oxidize to MoO_3 at atmospheres above 316 ℃ while WS_2 has a good thermal stability up to 594 ℃. The friction coefficient of WS_2 could

be as low as 0.1 in argon at 815 ℃. However, the prismatic edges $(10\bar{1}0)$ of WS_2 are still susceptible to humidification or oxidation which usually leads to degradation of the low friction property.

To take advantage of its low friction properties, Ni/WS_2 composite coatings have been developed. There are mainly two kinds of WS_2 used for a preparation of Ni/WS_2 composites: IF (inorganic fullerene-like) and 2H (layered platelets). Compared to WS_2 platelets, the fullerene variant shows more interesting tribological performance due to the layered hollow and quasi-spherical structure where the edge effect is no longer in effect and the particles are more inert to chemicals. But IF-WS_2 particles are manufactured at high temperatures which are costly. In addition, the IF-WS_2 particles are easily deformed under high load × velocity and hence lose the beneficial shell structure.

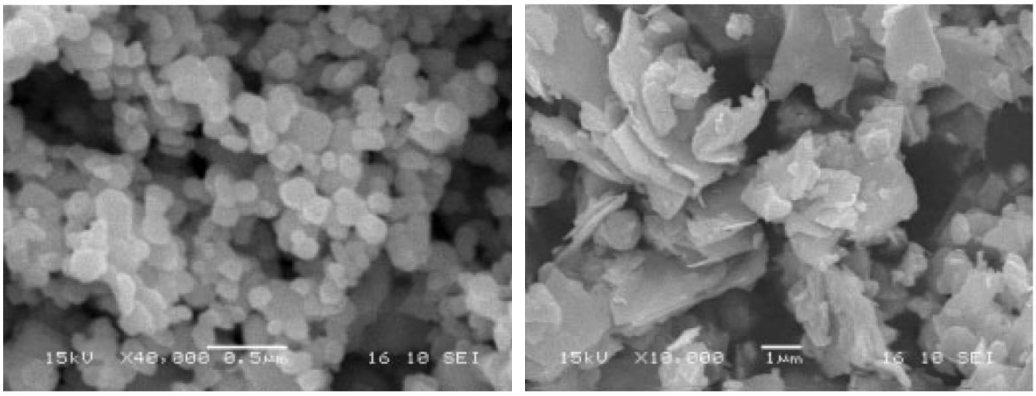

IF-WS_2 2H-WS_2

Figure 2.45 SEM images of IF-WS_2 and 2H structure (platelets form) WS_2 powders [144].

Redlich et al. have applied the electrodeposited Ni/IF-WS_2 coating to archwires in orthodontics [145]. Compared to the Ni coating, the electrodeposited Ni/IF-WS_2 coating showed a rough surface. The friction test showed a 60% reduction of the friction force between coated rectangular archwires and self-ligating brackets in comparison with uncoated archwires, shown in Fig. 2.46(d). IF-WS_2 nanoparticles could not only serve as an excellent lubricant but also protect the metal surface against oxidation.

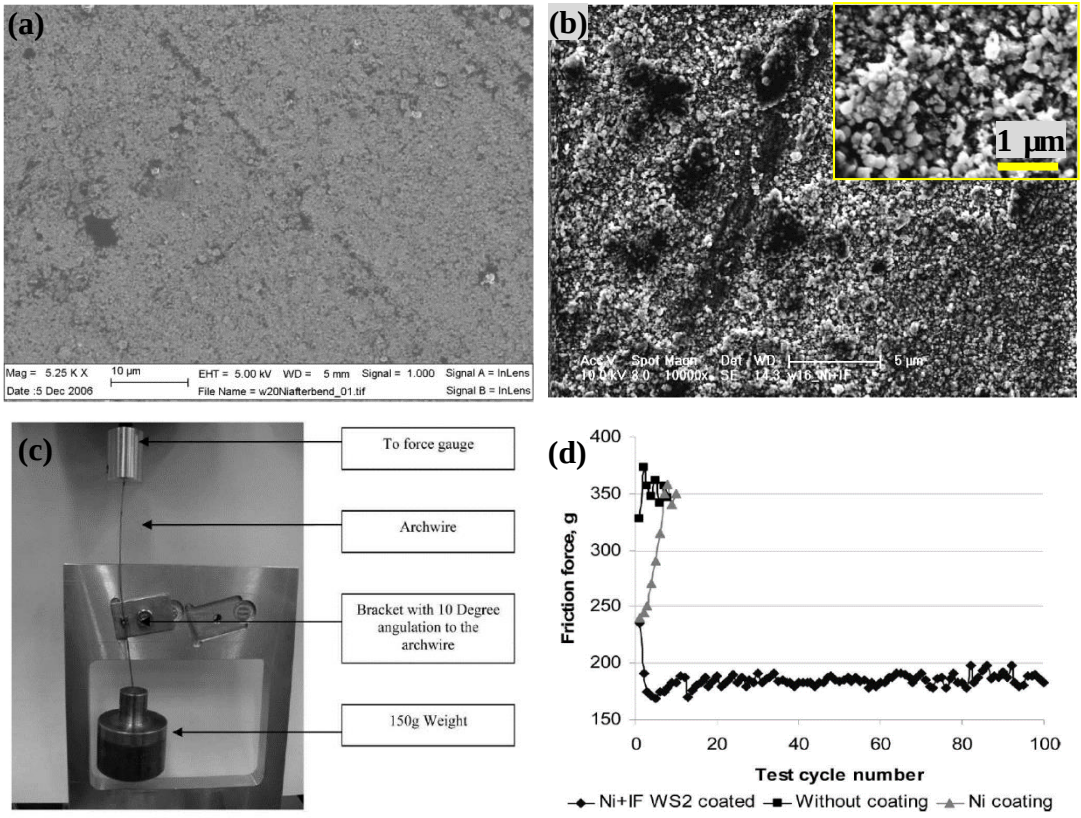

Figure 2.46 SEM images of (a) Ni deposit and (b) Ni+IF-WS_2 deposits, (c) friction force measuring instrument, (d) Time evolution of the friction force between the bracket and the archwire for the orthodontic wires with various coatings [145].

A newly electrodeposited Ni-P with a high content of fullerene-like WS_2 was tested by Andr é et al., in comparison with three successful commercial coatings; MoST, Graphit-iC and BalinitC [146]. Graphit-iC and BalinitC are carbon based (DLC) coatings and the tested MoST coating is a MoS_2/titanium composite. It was found that the new coating of electrodeposited Ni-P incorporating IF-WS_2 nanoparticles showed a high potential as a low-friction coating (Fig. 2.47). The coefficient of friction fell below 0.05 in friction test against the bearing steel ball, comparable to that of the commercially produced MoST coating. The examination of the cross-section of the wear tracks showed the formation of tribofilm on both mating surfaces. TEM observation displayed the fragmented WS_2 particles in the uppermost part of tribofilm and the basal planes in the lamellar WS_2 structure were parallel to the surface (Fig. 2.48). The easy shearing property of these basal planes could largely reduce the friction force.

Table 2.8 Description of the tested coatings: Ni-P/WS_2, MoST, Graphit-iC and BalinitC [146].

Coatings	Method of deposition	Description	Nominal thickness	Roughness Ra
Ni–P + IF-WS_2	Electrodeposited	~70% IF-WS_2 in a Ni–P matrix	~4–10 µm	475 nm
MoST	Sputtered	MoS_2 + Ti	~1.3 µm	7–12 nm
Balinit C	Sputtered	Carbon based (a-C:H:W)	~1 µm	7–12 nm
Graphit-iC	Sputtered	Carbon based, graphitic microcrystalline structure	~2.5 µm	7–12 nm

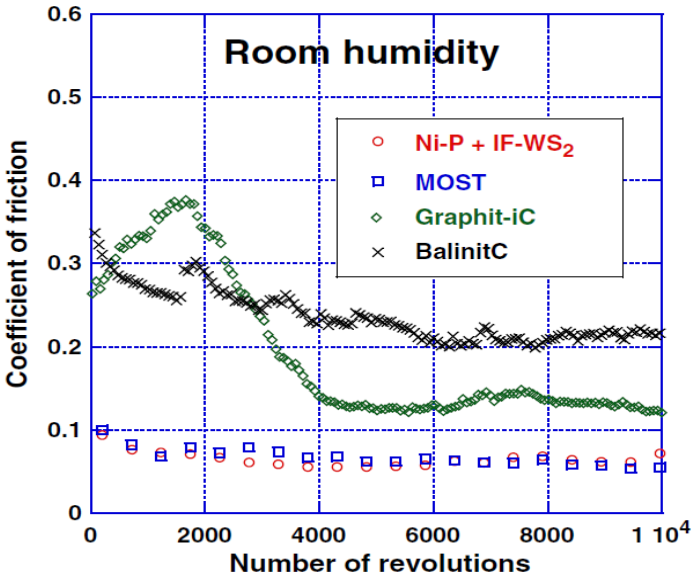

Figure 2.47 Coefficient of friction versus number of revolutions in ball-on-disc tests in humid air for four types of coatings [146].

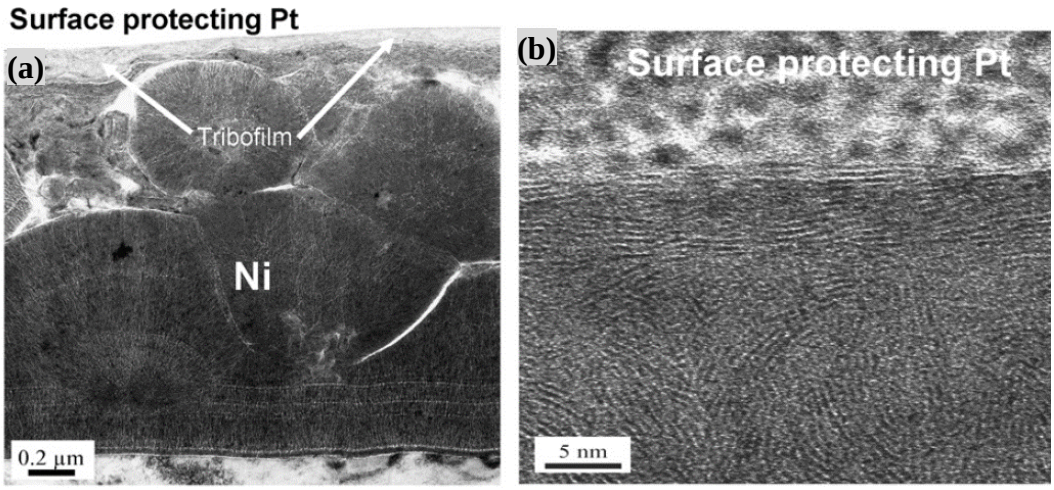

Figure 2.48 (a) Image of the cross section through the Ni-P + IF-WS_2 coating after friction test; (b) HRTEM image of the outer most part of the tribofilm on the Ni-P + IF-WS_2 coating [146].

Similar to the electrodeposition of Ni/WS_2 coatings, Fe-Ni-C/WS_2 self-lubricating nanocomposite with a few percent of fullerene-like WS_2 nanoparticles (<150 nm) was prepared by Rapoport et al. using powder metallurgy processes [147]. The experiment demonstrated very significant improvements in both lifetime and performance of the Fe-Ni-C sample with IF-WS_2 nanoparticles incorporated. As shown in Fig. 2.49, the composites show a low coefficient of friction even under high load of 840 N. Comparably, IF-impregnated sample showed a lower rate of 16.9×10^{-11} mm^3/ mmN than the reference metal sample with a wear rate of 76.4×10^{-11} mm^3/mmN.

The possible lubrication mechanism was proposed as follows: momentary confinement of the nanoparticles in larger cavities prevents the run-away of the nanoparticles from the contact area and protects them against damage and oxidation. In the friction process, the IF WS_2 particles are confined in a nanoscopic cavity (Fig. 2.50(a)), therefore they roll under the effect of the shear forces in the friction system and reduce the friction. In addition, IF nanoparticles in nanoscopic cavities serve as spacers to prevent direct contact between the asperities of the mating surfaces. These factors together provide low friction and high wear resistance.

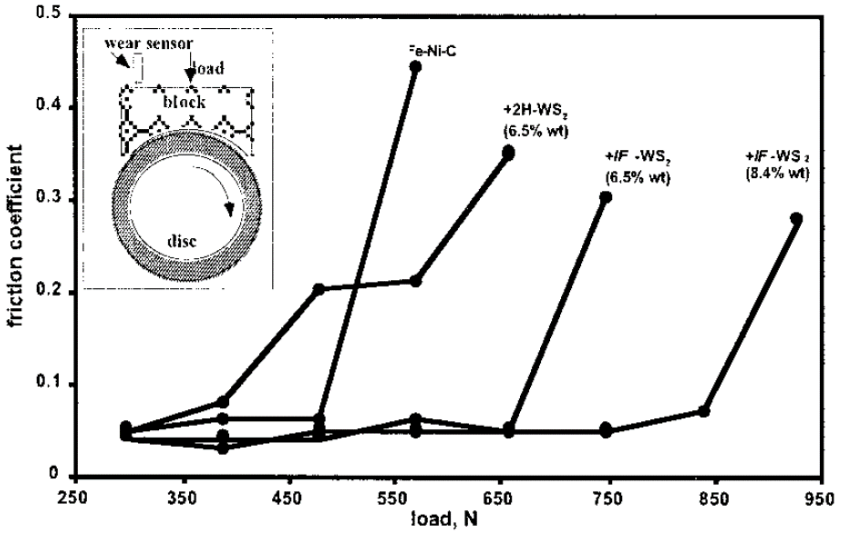

Figure 2.49 Friction coefficient vs load (in N) of porous Fe-Ni-C and Fe-Ni-C/WS_2 blocks against hardened steel disk. In these experiments, after a run-in period, the loads were increased from 30 kg with an increment of 90 N and remained for 1 h under each load. Velocity is 1 m/s [147].

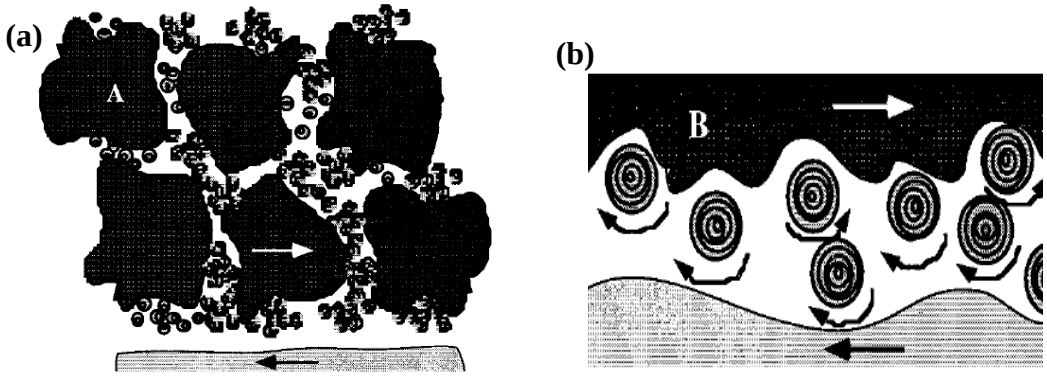

Figure 2.50 (a) The release of impregnated IF-WS_2 nanoparticles from the pores to the mating metal surfaces; (b) the interlocking of the IF-WS_2 nanoparticles at the metal surface by nanometric cavities [147].

Chen et al. have successfully prepared Ni-P/WS_2 coating by an electroless plating technique [144]. As listed in table 2.9, a great decrement in the fiction coefficient and wear rate was found for these coatings with a smallest friction coefficient of 0.03. The SEM images in Fig. 2.51 show that the wear surface of the Ni-P/IF-WS_2 coatings is smooth without obviously worn scars, while more severe wear can be found on other coating surfaces. The advantages of the WS_2 spherical nanoparticles were as follows: (i) rolling function; (ii) working as spacers to prevent direct surface contact in air.

Table 2.9 The results of tribological measurement for electroless deposited coatings [144].

Coating	Mass loss of block/mg	Friction coefficient
Ni-P	15.6	0.090
Ni-P-(2H-WS_2)	5.2	0.062
Ni-P-graphite	4.3	0.067
Ni-P-(IF-WS_2)	3.0	0.030

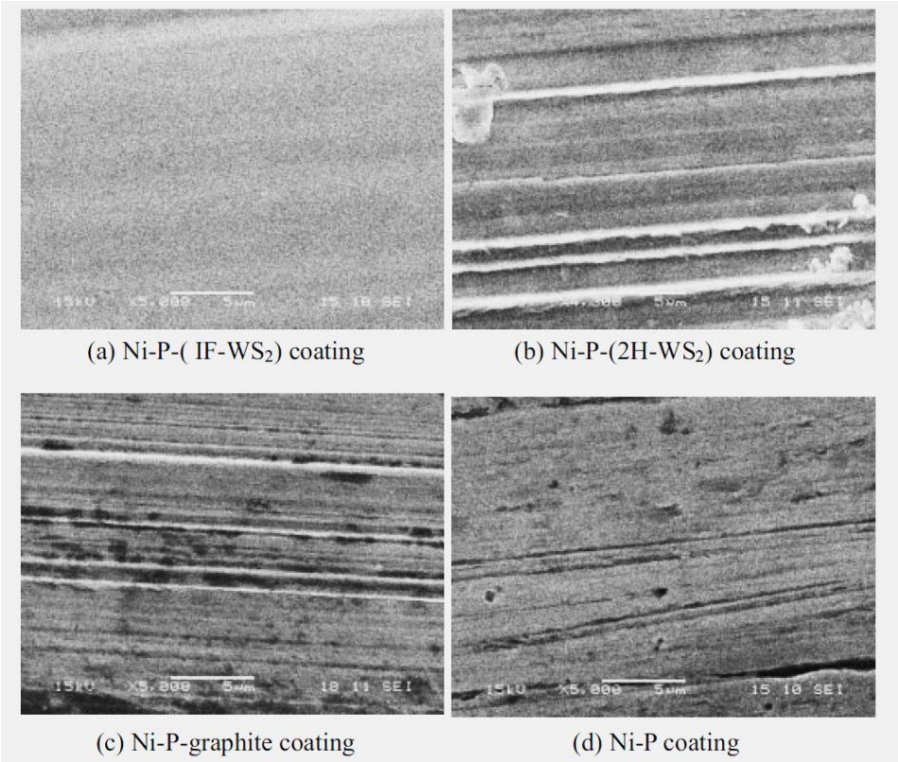

Figure 2.51 SEM images of worn surface of the electroless deposited coatings [144].

Ranganatha et al. have obtained Ni-W-P and Ni-W-P/nanoWS_2 by an electroless plating method [148]. The incorporation of WS_2 particles into a Ni-W-P alloy coating reduced the coefficient of friction from 0.16 to 0.11. In addition, the corrosion resistance of the latter has been improved: the corrosion rates of the coatings for Ni-W-P and Ni-W-P/WS_2 were 8.219 $\times 10^{-7,}$ and 7.986 $\times 10^{-7}$ g/h respectively in 3.5 wt% NaCl solutions.

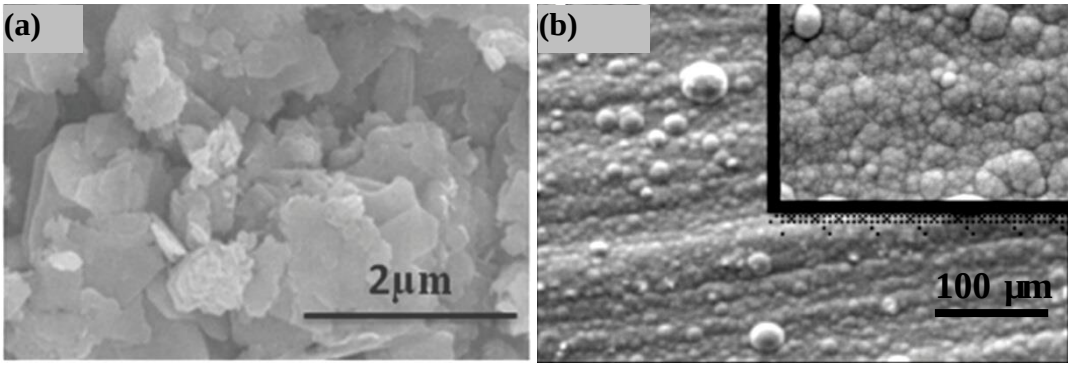

Figure 2.52 SEM images of (a) WS_2 particles and (b) the deposited Ni-W-P/WS_2 coating [148].

2.3.5 Summary

Electrodeposited Ni/alloy coatings are widely used in the chemical, mechanical and electronic industries due to their wear and corrosion resistance properties. They have been

considered as an alternative for hard Cr which has been gradually prohibited in Europe and the USA. Our group (amongst others in the research community) has already carried out a lot of research on electrodepositing Ni-Co and Ni-Co-P coatings to replace hard Cr, with comparable high strength, high hardness and good wear resistance being produced.

The main issue associated with the Ni/alloy coatings is their high coefficient of friction, which results in energy waste and material degradation. Thus electrodeposited Ni-based coatings containing lubricating particles attract more and more interest, as they usually show reduced friction and improved machine efficiency.

The MoS_2/WS_2 solid lubricants demonstrate very low friction (0.002-0.25) because of their lamellar structure, which are ideal in preparing a self-lubricating composite coating. So far, there are many reports in the literature about using electrodeposition to produce composite coatings such as Ni/MoS_2, Ni-Co/MoS_2, Ni-W/MoS_2, and etc., which show considerably reduced friction in atmosphere conditions compared to metal coatings. Composite Ni-P coatings with embedded MoS_2/WS_2 particles as the reservoir of lubrication have a promising future but very limited attempts have been made so far by electrodeposition. In this work, an attempt has therefore been made to develop low-friction Ni-P/MoS_2 or Ni-P/WS_2 composite coating by an electrodeposition technique.

The two strands of the thesis work therefore focus on optimisation of electrodeposition processes to incorporate: (i) luminescent particles (for wear detection) and (ii) MoS_2/WS_2 particles (to improve coating wear performance). An understanding of how and why electrodeposition parameters control successful incorporation of such secondary particles (and what is the optimum particle configuration) opens up the opportunity to produce highly tailored coatings for a range of wear service conditions.

Chapter 3 Experimental methodology

3.1 Electrodeposition

Luminescent Ni and low friction Ni-P/MoS_2, Ni-P/WS_2 coatings were electrodeposited on a mild steel substrate using direct-current electrodeposition. The composition of the substrate is listed in Table 3.1.

Table 3.1 Composition of AISI 1020 substrate [149].

Element	C	Si	Mn	P	S	Cr	Fe
wt%	0.20	0.19	0.45	0.04	0.05	0.16	98.91

An electroplating pre-treatment is required, for the following reasons:

A. Oils/lubricants: If oils are not totally removed from the surface, the products will suffer severe plating problems including adhesion failure, blisters, skip plating, etc. These oils may also poison the plating solution, resulting in a series of significant problems.

B. Rust: Rust easily forms on the surface of the substrate material in a wet climate. Plating over a rusted surface will cause the following problems: adhesion failures, blisters, strains, pitting, poor corrosion resistance, etc.

C. Scales/oxides: Oxides appear on the substrate exposed in air. Oxide layers can inhibit the electroplating process and affect the quality of the coating.

In order to get a fresh substrate surface for successful electroplating, the pre-treatment procedures adopted were as follows: Polishing with 320, 800 and 1200 grit grinding papers (Struers, waterproof SiC papers) → water rinse → rinse with 3 vol% detergent solution (Teepol multi-purpose detergent) to remove oil / grease → water rinse →10 vol% HCl acid soak for 10 s to remove rust and oxide layer → rinse in distilled water → electroplating.

Fig. 3.1 shows the experimental setup for electrodeposition of a composite coating. A TTi QL355T power station was used as the power source. The bath temperature (as listed in subsequent chapters) was maintained by a Grant LTD6G water bath. The solution was continuously stirred by a PTFE-coated magnetic stirrer bar (6 mm diameter × 30 mm length) at 100 rpm. The anode for electrodeposition was a pure Ni sheet (purity 99.5%) with a thickness of 1 mm supplied by Goodman Alloys Ltd (Yorkshire, England). The cathode substrate was 3 mm thick AISI 1020 mild steel with a hardness of 120 HV. Both the anode and cathode were cut by a guillotine into sizes of 80 mm × 10 mm. During the deposition process, the cathode was held parallel to the anode with an inter-electrode gap of 25 mm. The detailed electrolytic composition, applied current density, plating time and pH are specified in the next two chapters.

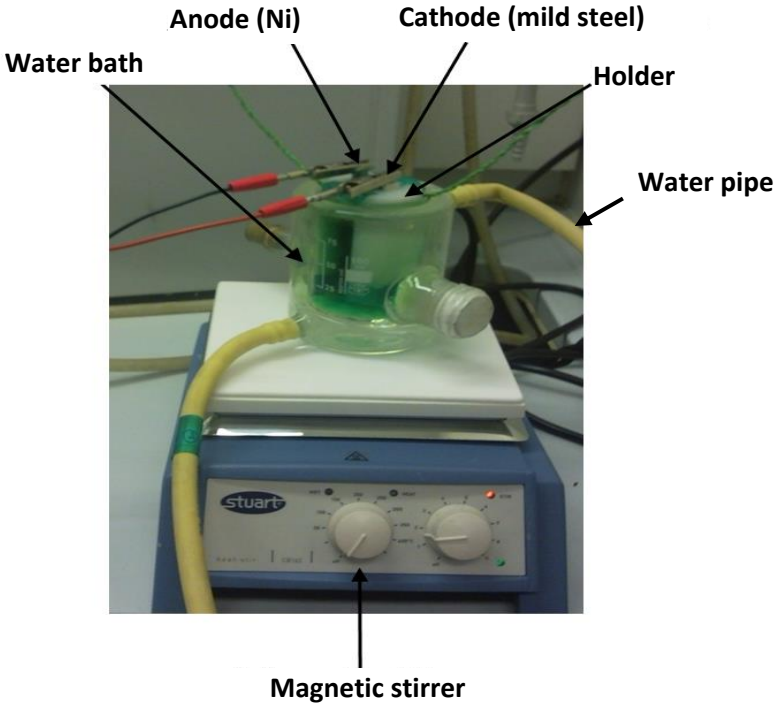

Figure 3.1 Experimental setup for electrodeposition of composite coating.

3.2 Characterisation techniques

3.2.1 Materials characterization

3.2.1.1 Scanning electron microscopy (SEM)

Samples were ultrasonically cleaned in acetone. Observations of the surface morphology of as-deposited coatings, worn and corroded surfaces were conducted in a JEOL JSM 6500 SEM. The applied voltage was 15 kV while the working distance was 10 mm.

The surface morphology was observed by collecting the imaging signals from secondary electrons (SE) and backscattered electrons (BSE) generated by a finely focused electron beam. The quantity of electrons backscattered is proportional to the mean atomic number (Z) of the sample material. Thus in BSE mode, the fluorescent particles ($BaMgAl_{11}O_{17}:Eu^{2+}$) or solid lubricant particles (MoS_2) which have lower mean atomic number appear as black spots while the Ni matrix coating appears white.

With the energy dispersive X-ray spectroscopy (EDS) system, quantitative elemental (heavier than boron) information can be obtained from characteristic X-rays emitted as a result of bombardment. EDS spectra were acquired for 60 s at 15 kV and electron current of 0.3 nA. The elemental (O, Ni, P, Mo, S) mapping of the wear track was performed at the same current density for 30 minutes.

In the EDS spectrum, the Y axis represents the counts of X-rays received by the detector and the X axis represents the energy level. The energy level of these X-rays is associated with the elements and shell levels (K, L, M, etc.), at which an electron vacancy can be created in the specific shell. K line intensity is normally the strongest in the line series and listed at the head of the spectrum, therefore widely used for identifying the element being characterised. For elements with a high atomic number, the K lines generated may be not sufficiently distinctive for element identification and lower-energy X-rays will also be used, e.g. the L or M lines.

3.2.1.2 Image analysis

The particle size and the area percentage of the particles in the composites were estimated using an open source software - ImageJ 1.49. This is written by the National Institute of Health, USA, and is freely available in the public domain. The obtained SEM images were first converted to TIFF format in grey-level mode for processing and analysis. Then a binary image was created by setting a “threshold” range between 0 and 255 grey level (Fig. 3.2(b)). Pixels in this range are converted to black and the rest become white. In the third step, the particle sizes were analysed by noting the range of particle areas measured and the results were exported into a table (Fig. 3.2(c)). Finally, the particle area percentage value was obtained by dividing the sum of all particle areas by the total coating area observed.

Particle size (d) refers to the diameter of particle, which can be calculated using the following equation:

$$d = 2\sqrt{F/\pi} \qquad (3.1)$$

where π is the ratio of a circle's circumference to its diameter (3.14159) and F is the measured area of the particle. In this calculation, the particles are therefore assumed to be circular. This approach will not distinguish between particles that are close together and the varying shape of the particles is not considered [150].

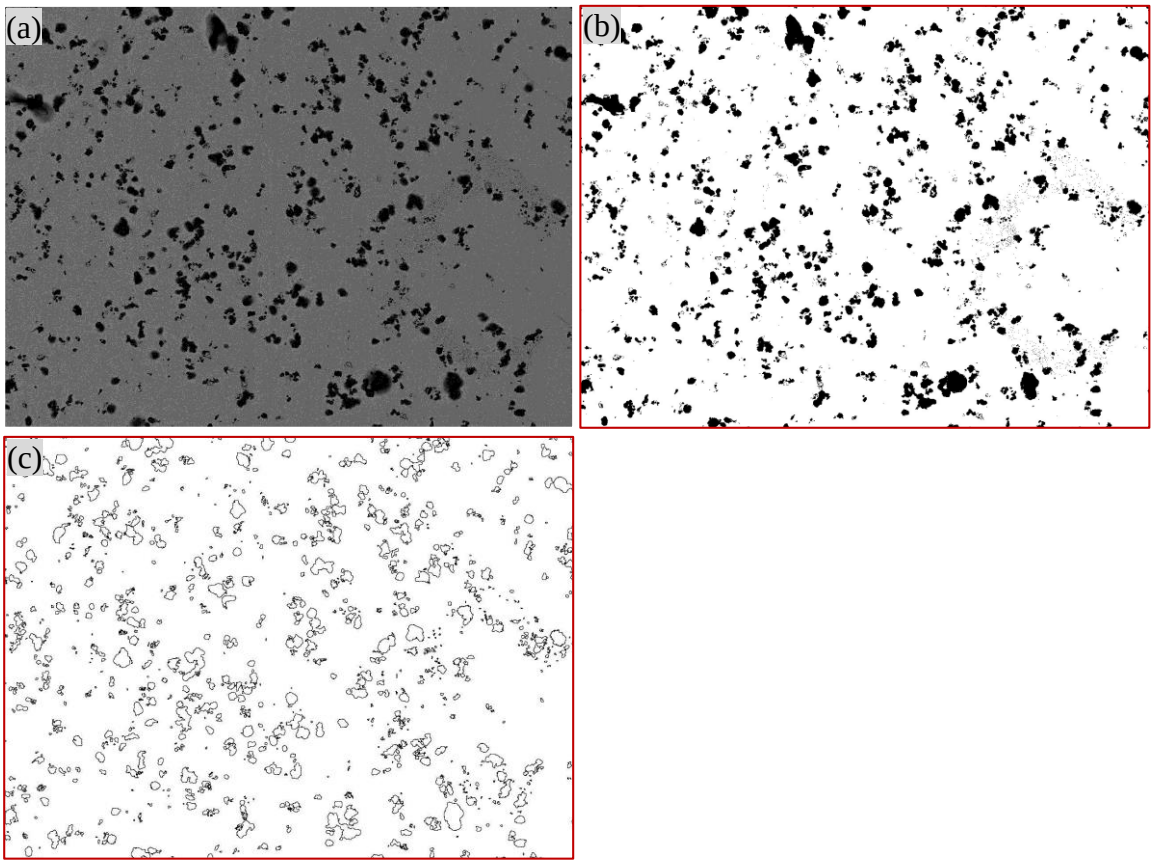

Figure 3.2 (a) BEI image and (b) binary image produced by thresholding of the electrodeposited Ni/BAM coating; (c) outlines of particles in coating (used to calculate area fraction and particle diameter).

3.2.1.3 3D surface model

To better understand the surface roughness, 3D reconstruction of surface topography and analysis was done from tilted SEM images (+5 °, 0 °, -5 °) using a stand-alone stereographic software package MeX in the SEM. In the first step, the corresponding points in the two images are automatically matched. Then, based on parameters including working distance, tilt angle and pixel size, the surface topography is reconstructed through appropriate

trigonometric calculations. The resulting digital 3D surface model can be used for various analyses.

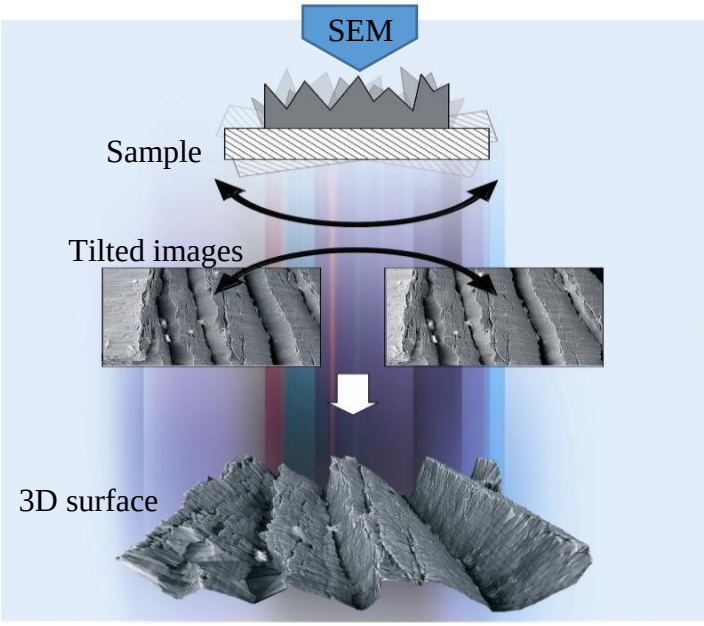

Figure 3.3 Underlying principles of 3D surface construction based on tilted SEM images [151].

3.2.1.4 Transmission electron microscopy (TEM)

Particle samples were ultrasonically dispersed in alcohol. A drop of suspension was transferred to an amorphous carbon film supported on a copper grid and dried in air.

TEM specimens of deposited coatings were prepared by electro polishing. The procedures are as follows:

(1) Removing nickel plating from substrate with a knife,

(2) Punching the nickel coating to standard 3 mm diameter disc,

(3) Twin jet polishing to obtain a thickness less than 100 nm: Twin jet polishing was carried out in an electrolyte of 10% perchloric acid, 15% acetic acid and 75% methanol at -40 ℃ with a 30 V direct current [152].

A JEOL JEM 3010 operating at 300 kV with the highest resolution of 0.21 nm has been

utilized to observe the thin area of the specimen foil. TEM could be used to determine the grain size as well as its distribution and to discriminate phases and crystallography.

3.2.1.5 FIB

Focussed Ion Beam (FIB) is very useful for preparation of TEM cross-sections. A CFEI Quanta 3D FEG FIB-SEM was used to prepare TEM samples. A trench depth of 15 μm was produced on either side of the area of interest and the sample was thinned to approximately 100 nm. A glass needle and a micromanipulator were used to hold the membrane and the final specimen was transferred onto a TEM grid with carbon film.

3.2.1.6 X-ray diffraction (XRD)

XRD is a powerful technique widely used for studying the microstructure, phase identification, and compound analysis of materials. The as-deposited sample was cut into 1×1 cm, packed horizontally into an XRD sample container by Blu-Tack. The structure and compound analysis of these were examined using a Bruker GADDS diffractometer with a Cu Ka radiation, scanned at 0.02°/s in the 2 theta range from 10° to 90°.

The average crystallite size (d) can be estimated by applying the Scherrer equation [153]:

$$d = \frac{0.9\lambda}{B\cos\Theta} \qquad (3.2)$$

where λ is the wavelength of the X-rays (0.154 nm for Cu Ka radiation) and Θ is the Bragg diffraction angle. B is the full width at half maximum height of the peak.

The calculated crystallite size estimated from this method is normally smaller than the observed grain size obtained by TEM. In addition to differing sample size effects for the two techniques, there are many other factors affecting the width of diffraction peak, including crystal lattice imperfections, stacking faults, microstresses, strains, coherency strains and sub-boundaries [154]. When materials have undergone severe plastic deformation, dipolar dislocation walls (without differences in orientation) also break down coherency of X-ray scattering and affect the estimated crystallite size [155].

3.2.2 Mechanical and corrosion property tests

3.2.2.1 Microhardness measurement

Microhardness tests of coatings were made by a Matsuzawa MHT-1 Vickers microhardness indenter and a load (F) was applied to make an indention so small that an optical microscope is able to measure its size. The indenter is a diamond pyramid with a square base and an angle of 136° between opposite faces. The specimens were measured with an applied load of 100 g for a dwell time of 15 s. Once the test is complete the diagonal lengths of the indentation are measured and the mean *d*, in mm, is calculated [156]. The Vickers hardness *HV* is given by the following equation:

$$HV = \frac{2F\,sin\frac{136^\circ}{2}}{d^2} \tag{3.3}$$

where *F* is in kgf and *d* (mean value of *A* and *B*) is in millimetres.

An average of 5 measurements was conducted on each sample to obtain an average value of Vickers hardness. The depth of indentation is approximately 2.1-2.7 μm (diagonal length is 15-19 μm), much lower than the luminescent coating depth range from 20 to 30 μm. A cross-section hardness study was also used to investigate to what extent the indent (and its surrounding deformation) is contained within the coating.

The error or uncertainty in measurement was estimated in terms of the standard deviation and shown as an error bar in subsequent graphs. The standard deviation was calculated using this formula:

$$\sigma = \sqrt{\frac{1}{N}\sum_{i=1}^{N}(x_i - \mu)^2} \tag{3.4}$$

Where σ represents standard deviation, μ is the mean of all values, x_i is the individual measurement value and *N* is the total number of measured values.

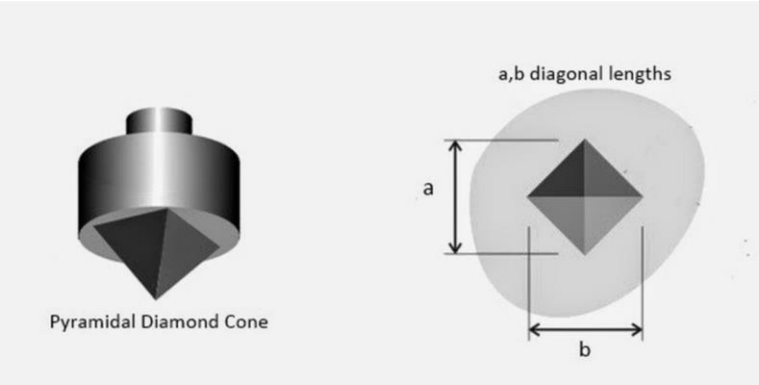

Figure 3.4 Schematic of Vickers microhardness indenter [157].

3.2.2.2 Pin-on-flat wear test

The friction and wear behaviour of the coated specimens was tested using a reciprocating pin-on-flat TE-77 tribometer (Fig. 3.5) at room temperature. The counterpart body was an AISI-52100 bearing steel ball (diameter 6 mm) with a hardness of 700 HV. The tests were carried out under the following conditions (avoiding complete coating failure): a load of 14 N (resulting in 1.58 GPa Hertzian contact pressure), a sliding frequency of 1 Hz and a sliding stroke of 2.69 mm. The friction force is recorded automatically by a piezo electric transducer.

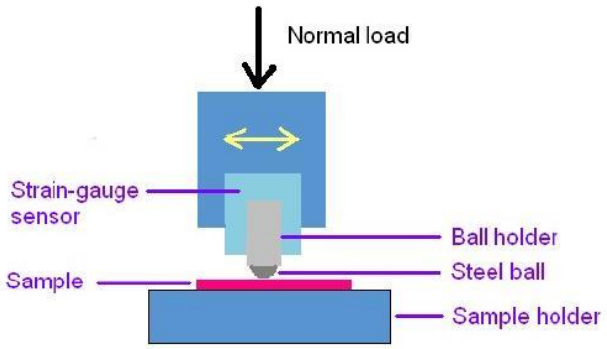

Figure 3.5 Schematic diagram of the wear test on pin-on-disk TE-77 tribometer [158].

Table 3.2 Chemical composition of AISI 52100 bearing steel.

Composition	C%	Si%	Mn%	Cr%	Mo%	Ni%	S%
AISI 52100	0.95-1.10	0.15-0.35	0.50	1.30-1.60	0.08	0.25	0.25

3.2.2.3 Alicona infinite focus microscopy

The infinite focus microscope made by Alicona is a fully digital light microscope and includes newly-developed 3D measurement and image analysis capabilities. This system allows the capturing and calculation of focussed images effectively compared to conventional optical microscopy, images with almost 1000-times enlarged depth-of-focus can be captured, visualized and analysed.

The wear track profile after sliding tests, which typically has large depth over 10 μm, can be scanned by the Alicona microscope. Subsequently, the wear rate can be calculated using the following equation：

$$K = \frac{V}{SF} \tag{3.5}$$

Where V is the wear volume in mm^3, S is the total sliding distance in metres and F is the normal load in Newtons.

3.2.2.4 Potentiodynamic polarization test

The potentiodynamic polarization technique was used to measure the corrosion property of the coatings by continuously scanning the potential while monitoring the current response [159]. A polarization curve can determine the corrosion rate by calculating the corrosion current. The electrochemical measurement was carried out in a three electrode cell. The sample with the electrodeposited coating was used as the working electrode, with a platinum counter electrode and a saturated calomel electrode as a reference electrode. The corrosion potential (E_{corr}) and the corrosion current density (J_{corr}) were obtained with the Tafel extrapolation method from potentiodynamic anodic polarization curves. Polarization experiments were performed in 3.5 % NaCl solution at room temperature with an AUTOLAB PGSTAT30 potentiostat/galvanostat system, scanning from -1000 mV to +1000 mV *vs.* the calomel electrode at 50 mV/s scanning speed.

Linear polarization resistance refers to a linear approximation of the polarization behaviour at potentials near the corrosion potential, where the slope of plotted potential

versus current will yield a polarization resistance (R_p). The analysis was performed at a scanning rate of 0.1 V/s within 10 mV of the corrosion potential where the current is 0. With R_p experimentally measured, the corrosion current density (J_{corr}) is calculated following the Stern-Geary relationship [160]:

$$J_{corr} = \frac{B}{AR_p} \qquad (3.6)$$

Where B is a constant (in mV), A is the polarised area (in cm^2), and R_p is the polarization resistance (in ohms).

3.2.2.5 Luminescence characterization

Photoluminescence excitation and emission spectra were acquired at λ_{em} = 450 nm and λ_{ex} = 330 nm by Cary visible- UV/fluorescence spectrometers ($slit_{ex}$ = 5 nm, $slit_{em}$ = 5 nm). Fluorescence microscopy is also used to characterise luminescence phenomena of organic or inorganic substances using an optical microscope. A Leica DM LB2 30W Fluorescence Microscope (upright fluorescence microscope) was applied to observe the luminescence of coating, using a 260 nm filter.

Chapter 4 The monitoring of coating health by in-situ luminescent layers

4.1 Introduction

Luminescent Ni coatings consist of nickel deposits and luminescent particles in which the latter will emit a constant glow when exposed to UV light. Such coatings can serve as a stand-alone “indicator layer” to check the structural state of health.

So far, there is no work on electrodeposited metal coatings containing BAM phosphors using an aqueous bath. The phosphor particles are highly hydrophilic with a hydration layer typically formed on the surface of these particles. The repulsive hydration force between particles and the electrode will prevent the former from being deposited in the substrate. Cationic surfactants have been reported to effectively enhance the deposition, which not only improves the stability of particles’ suspension but also charges non-conductive particles positively via electrostatic adsorption.

The research in this chapter aims to develop a Ni coating with embedded phosphors ($BaMgAl_{11}O_{17}:Eu^{2+}$) which are used to monitor the wear condition of coatings simply using an ultraviolet light for detection. The effect of surfactants of CTAB and PEG, together with particle concentration levels on the electrodeposition process and the corresponding tribological and corrosion properties of the coatings are also investigated.

4.2 Experimental details

The basic solution for nickel plating can be seen in Table 4.1. The as-received phosphors ($BaMgAl_{11}O_{17}:Eu^{2+}$) are 2-5 μm in diameter. Four concentrations of 2, 5, 8 and 10 g/L BAM phosphors in electrolyte composition were investigated. To minimize the effect from impurities, all chemicals used were analytical grade.

The plating bath was kept at a pH value of 4.5, which has been reported to induce the

lowest internal stress during Ni electroplating [161]. The pH was adjusted by H_2SO_4 or NaOH. The bath was mixed under ultrasonic agitation. The electro-deposition was performed with stirring at 45°C and a current density of 4 A dm^{-2} for 45 min.

Table 4.1 Electrolyte composition for the electrodeposition of luminescent coating.

Chemical	Composition	Content (g/L)
Basic solution	$NiSO_4.6H_2O$	250
	$NiCl_2.4H_2O$	45
	H_3BO_3	40
Phosphors	$BaMgAl_{11}O_{17}:Eu^{2+}$	2, 5, 8, 10
Additives	Cetyltrimethylammonium bromide (CTAB)	0.1
	Polyethylene glycol (PEG) WM6000	2

4.3 Results

4.3.1 Design of luminescent coating for wear monitoring

In the present study, two types of luminescent coatings were designed. One is to incorporate luminescent particles into the functional top layer (Fig. 4.1(a)) and another is into the underlayer, as shown in Fig. 4.1(b). These luminescent particles appear normal under visible light, but emit colours under an ultraviolet (UV) light. For the coating in Fig. 4.1(a), the disappearance of the luminescence under UV light is a sign of coating damage and thus recoating may be required. In comparison, the observation of coloured light in Fig. 4.1(b) indicates that the functional coating has worn / corroded away. With a portable UV light/torch, the emitting coating can be inspected periodically even when the component part is still in service.

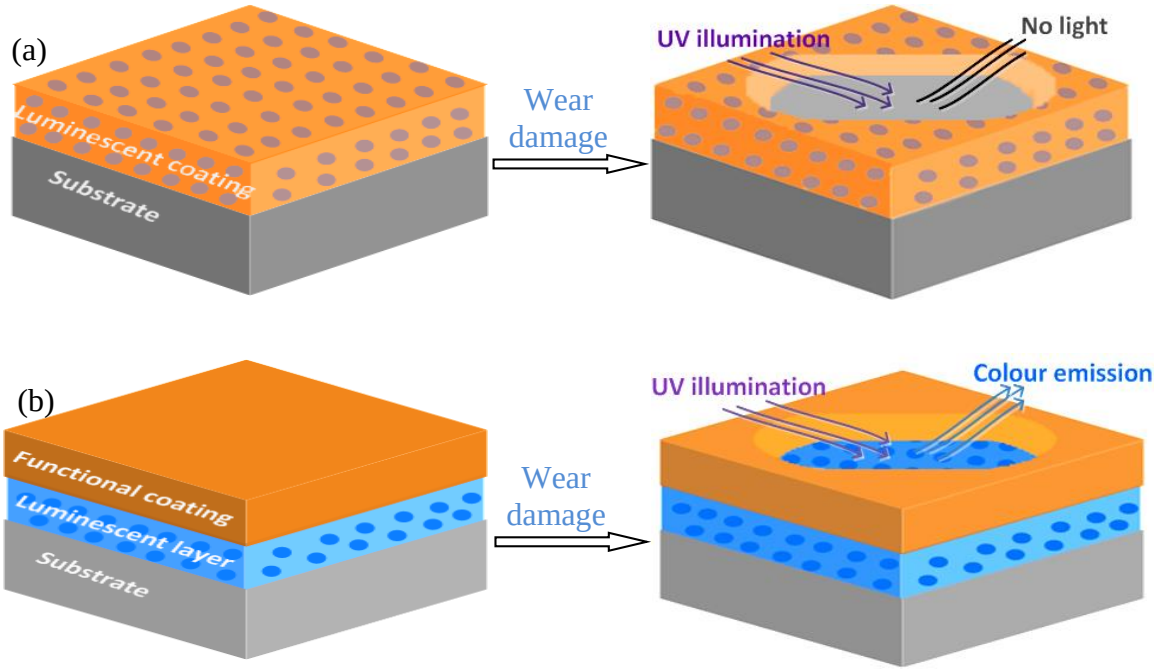

Figure 4.1 Illustrations showing luminescent particles codeposited as top layer in (a) or interlayer in (b), and the coating appearance in the damaged area after wear.

4.3.2 Morphology of Ni/BAM coating

The as-received BAM phosphors were imaged by secondary electrons in the SEM as displayed in Fig. 4.2(a,b). The majority of the as-received BAM phosphors are angular, with a diameter of 2-5 μm. Particle size distribution was estimated on the SEM image using Image J software and the result is displayed in Fig. 4.2(c).

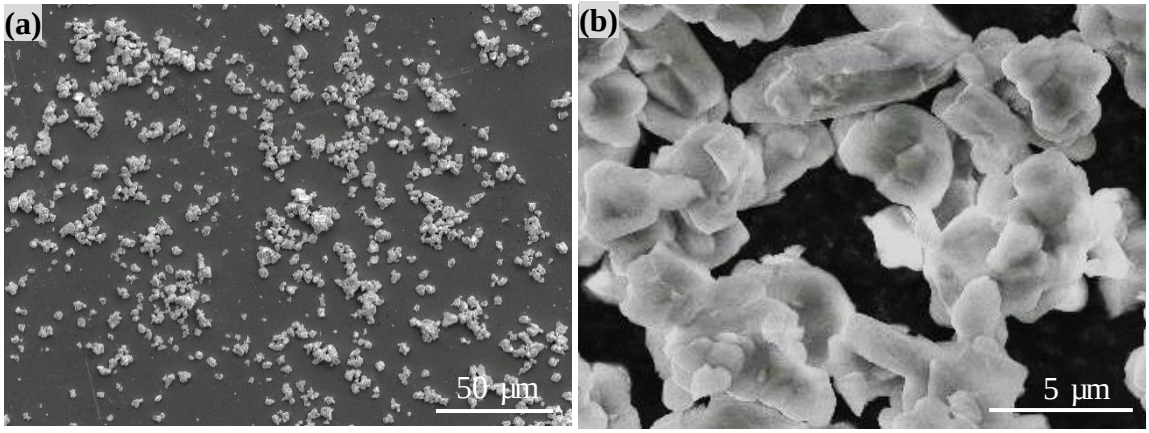

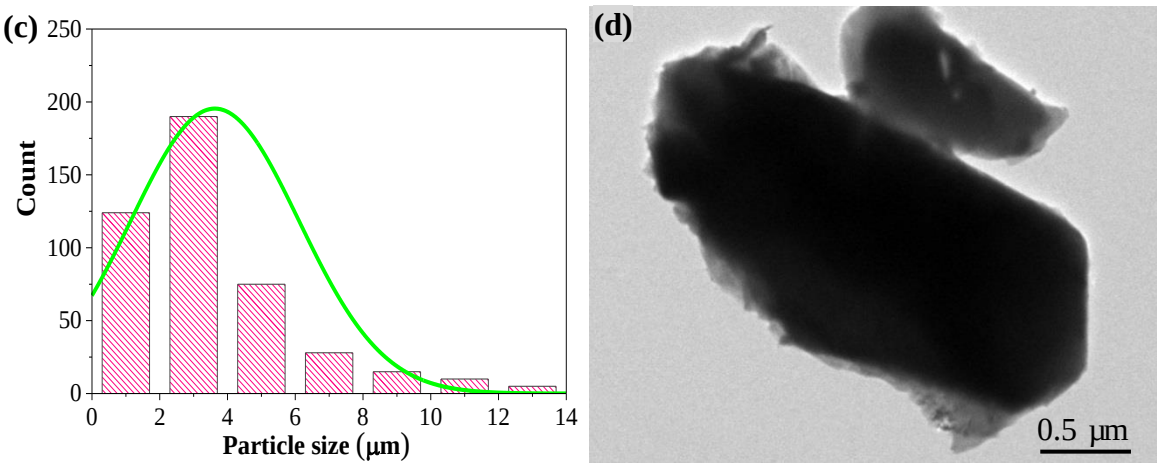

Figure 4.4.2 (a-b) SEI images of as-received BAM phosphors; (c) measurement of particle size distribution of phosphor; (d) TEM image of BAM phosphor.

After the electrodeposition process, the BAM phosphors distributed uniformly in the Ni matrix (Fig. 4.3(a, b)). The cross-section of this coating in Fig. 4.3(d) demonstrates that the phosphors were well embedded inside of Ni coating. Additionally, no void was found in the interface, indicating a good adhesion between the composite coating and the substrate. The voids near the top surface were formed by pull-off of particles during mechanical polishing.

Comparison of the electrodeposited BAM phosphors in the coating and the as-received BAM phosphor particles has been made by EDS (Fig. 4.3(c), Table 4.2). The similarity in compositions in terms of O, Mg, Al, Ni, Ba, Eu suggested that there was no reaction between Ni and BAM. The BAM phosphors after electrodeposition could retain the luminescence of the as-received particles. EDS was limited to the top surface of the exposed BAM phosphors to assess any changes in the phosphor after deposition, the Ni peak due to the matrix was very weak.

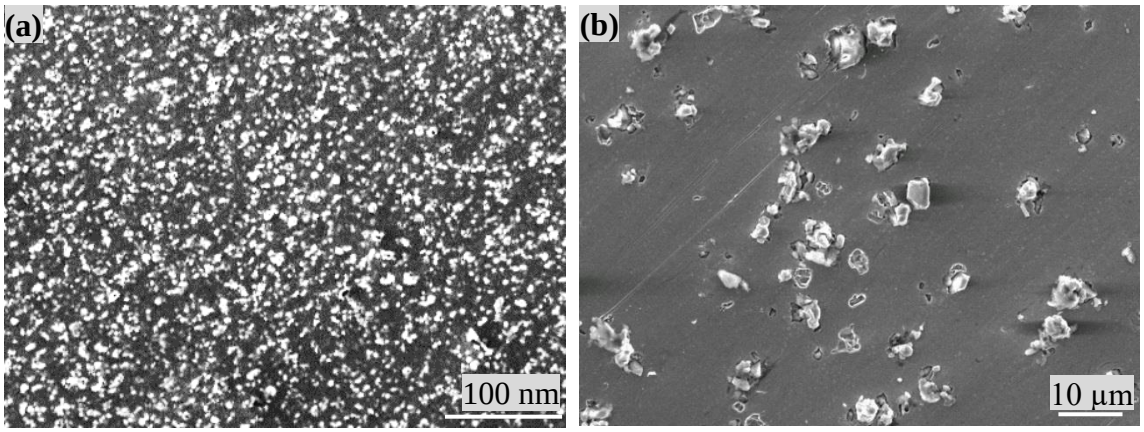

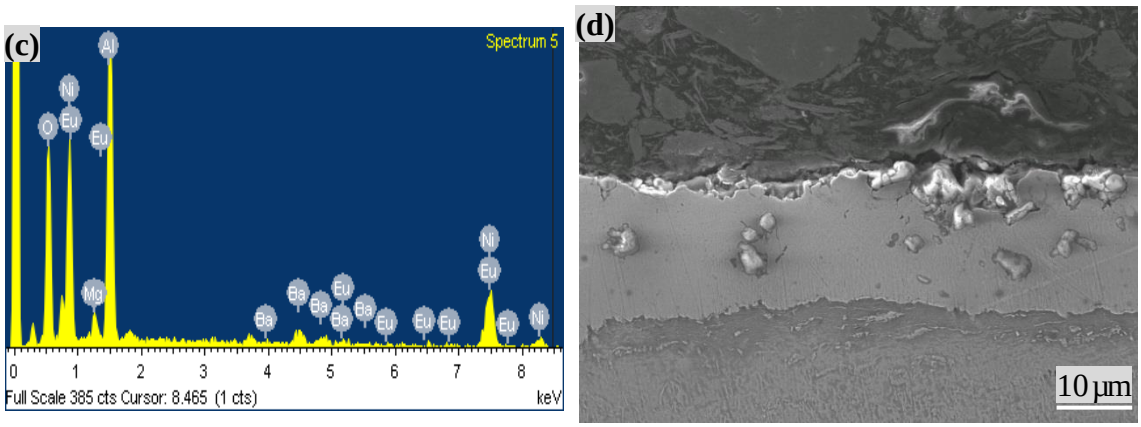

Figure 4.3 (a, b) Morphologies and (c) EDS spectrum of the electrodeposited luminescent coating from a bath solution with 5 g/L phosphors; (d) SEI image of the cross-section of luminescent coating.

Table 4.2 EDS quantitative analysis of the as-received and the electrodeposited BAM phosphors.

Element (Atom %)	O K	Mg K	Al K	Ba L	Eu L
As-received BAM	61.7 ±0.8	3.2 ±0.6	32.2 ±1.5	2.5 ±1.7	0.4 ±0.7
BAM in coating	61.2 ±1.1	3.4 ±0.3	33.0 ±0.9	2.1 ±1.0	0.3 ±0.2

4.3.3 XRD analysis

Fig. 4.4 displays the XRD patterns of the BAM phosphors and the luminescent Ni/BAM composite (deposited at 5 g/L BAM). The coating exhibits strong preferred (111) and (200) textures which are parallel to the surface. As noted in early reports [162], the predominant (111) plane in Ni alloy deposit is associated with preferred growth along the [111] direction to minimize surface energy. The remaining small peaks at 32°, 33°, 36°, 42°, 58°, 59° and 67° are in good accordance with the XRD peaks of the as-received BAM phosphors.

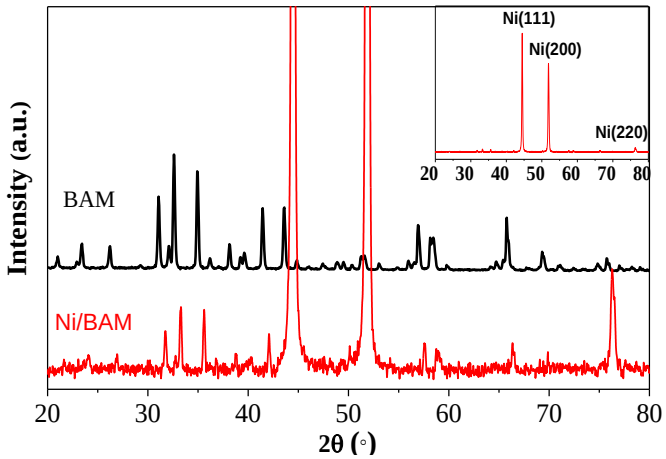

Figure 4.4 X-ray diffraction patterns of luminescent Ni/BAM composite coating and BAM phosphors, the inset is XRD of Ni/BAM in full scale.

The phosphors in the solution after electrodeposition were collected for XRD examination. They display a similar XRD spectrum to the as-received phosphors and there is no noticeable shift in all the peaks of BAM, which further demonstrate the structural stability of the BAM phosphors in solution.

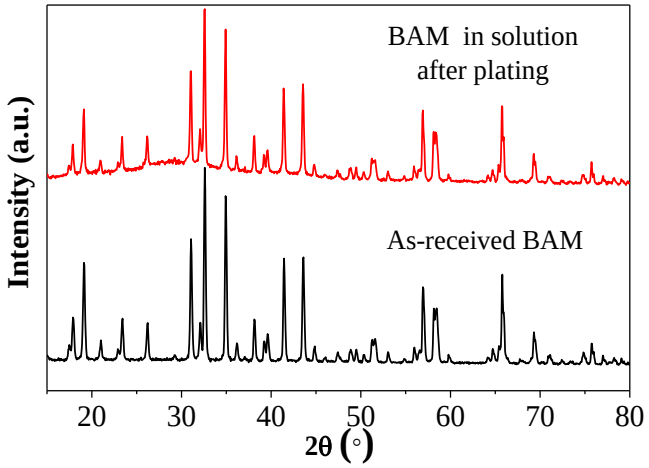

Figure 4.5 XRD patterns of BAM phosphors of the as-received and after electrodeposition.

4.3.4 CTAB surfactant

The amount of BAM codeposited in the coating depends on the content of CTAB as shown in Fig. 4.6. Without CTAB in the solution, the as-deposited coating barely shows the existence of BAM phosphors. BAM gradually increased in the coating with increasing concentration of CTAB in solution. The highest density of BAM phosphors can be found in the coatings from the electrolyte with 0.05 g/L- 0.1 g/L CTAB additions.

The area coverage of BAM phosphors in the coating is summarized in Fig. 4.6(f). The amount of CTAB in the bath significantly affected the coverage of BAM, with a maximum BAM coverage of 12 % at a CTAB concentration of 0.1 g/L. The surfactant CTAB will have charged cations on the particle surface and thus the BAM phosphors would be electrostatically attracted to the cathode. If the concentration is higher than a certain amount (around 0.08 g/L in this study), the residual CTAB molecules in solution would be adsorbed on the electrode surface, leading to an increase of overpotential and the electrochemical reduction of hydrogen on the electrode. This will inhibit the adsorption and incorporation of particles.

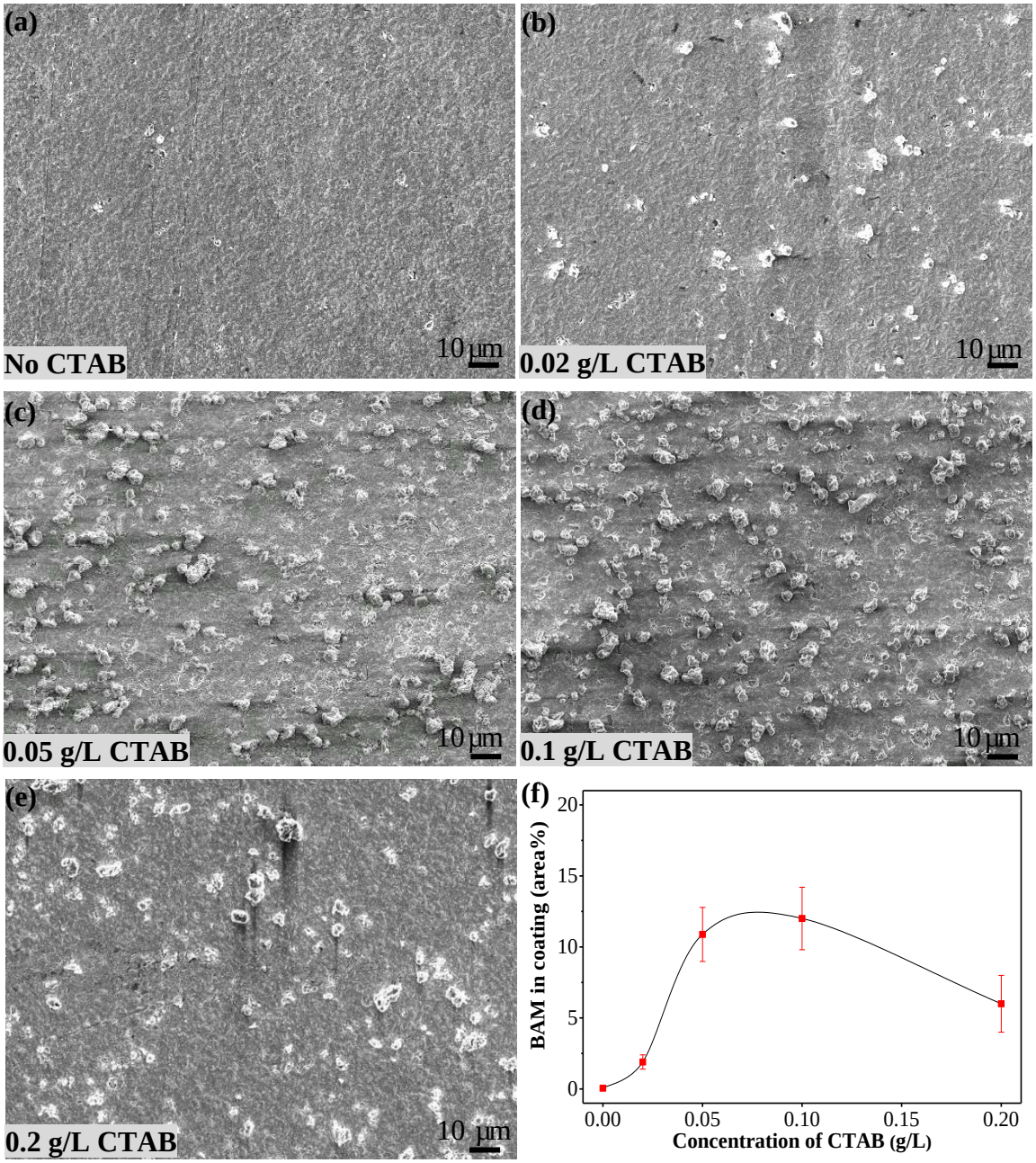

Figure 4.6 Morphology of Ni-BAM coatings deposited from bath with different CTAB concentrations: 0, 0.01, 0.02, 0.05, 0.1, 0.2 g/L (C_{BAM} = 5 g/L, J = 2.5 A dm^{-2}, t = 45 min), (f) Area coverage of BAM in coating plot versus plating time.

The X-ray patterns of the coatings deposited in solution with various CTAB concentrations are shown in Fig. 4.7. All the coatings have textures of Ni (111) and (200) planes, with little intensity at the (220) reflection. With the increase of the concentration of CTAB, the intensity of the (111) texture enhances while the intensity of the (200) reflection reduces.

It is widely accepted that, at the initial stage, electrodeposited coatings generally retain the structure of the base metal (so called epitaxy). The influence of the substrate becomes

weak with increased deposition time, and then the orientation of electrodeposit structures is determined more by bath composition and plating conditions. Since the deposition time for Ni/BAM preparation is 45 minutes and other plating conditions are fixed, the preferential orientation of crystals in Ni-P/MoS_2 is considered to be caused by the bath composition.

In this situation, the change of the preferred crystal orientation can be attributed not only to the engulfing of particles in the Ni matrix, but also to the inhibition effect of the adsorbed CTAB on the electrode surface which can slow down propagation steps, occupy growth sites, and/or modify the activity of emerging structural defects. H^+ adsorption takes place preferably on the surface of the particles, hindering the reactivity of other chemical reductions from Ni ions. In addition, residual CTAB molecules in the bath are more easily adsorbed on the (200) planes than on the (111) planes due to the higher adsorption energy, limiting the growth of crystals in the [100] direction. When the concentration of CTAB is low (0.05 g/L), this effect is not evident as most CTAB is adsorbed on the surface of the BAM phosphors. As the CTAB concentration increases over 0.1 g/L, more free CTAB molecules start to adsorb on the surface of deposits and the crystals along [100] direction are largely forbidden. Thus, the close-packed (111) plane dominates in the deposits with a high concentration of CTAB.

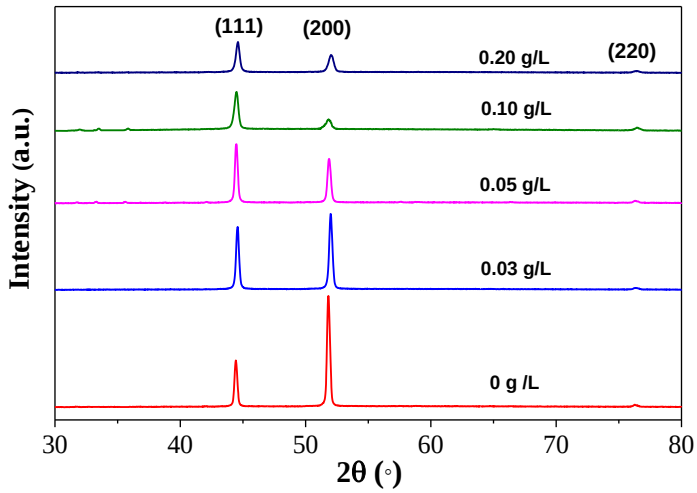

Figure 4.7 XRD patterns of the Ni-BAM coatings deposited from bath with various CTAB concentrations: 0, 0.01, 0.02, 0.05, 0.1, 0.2 g/L (J = 2.5 A dm^{-2}, t = 45 min, no saccharin).

4.3.5 Saccharin additive

Without saccharin added into the electrolyte, the grain sizes of the coatings are in a range of a few hundred nanometers to a few microns (Fig. 4.8). When the content of saccharin in solution is fixed at 2 g/L, as shown in Fig. 4.8(c), the surface became smooth. The SEM image at high magnification in Fig. 4.8(d) shows very fine crystallites measuring in tens of nanometres.

The obvious change in morphology proves the crucial effect of the saccharin content on the growth of the Ni deposits. The additions of saccharin into the Ni, Ni-Fe, and Ni-Co electrodeposition systems have been found to inhibit the growth of pyramidal crystals, reduce surface roughness and increase surface brightness [163,164,165,166].

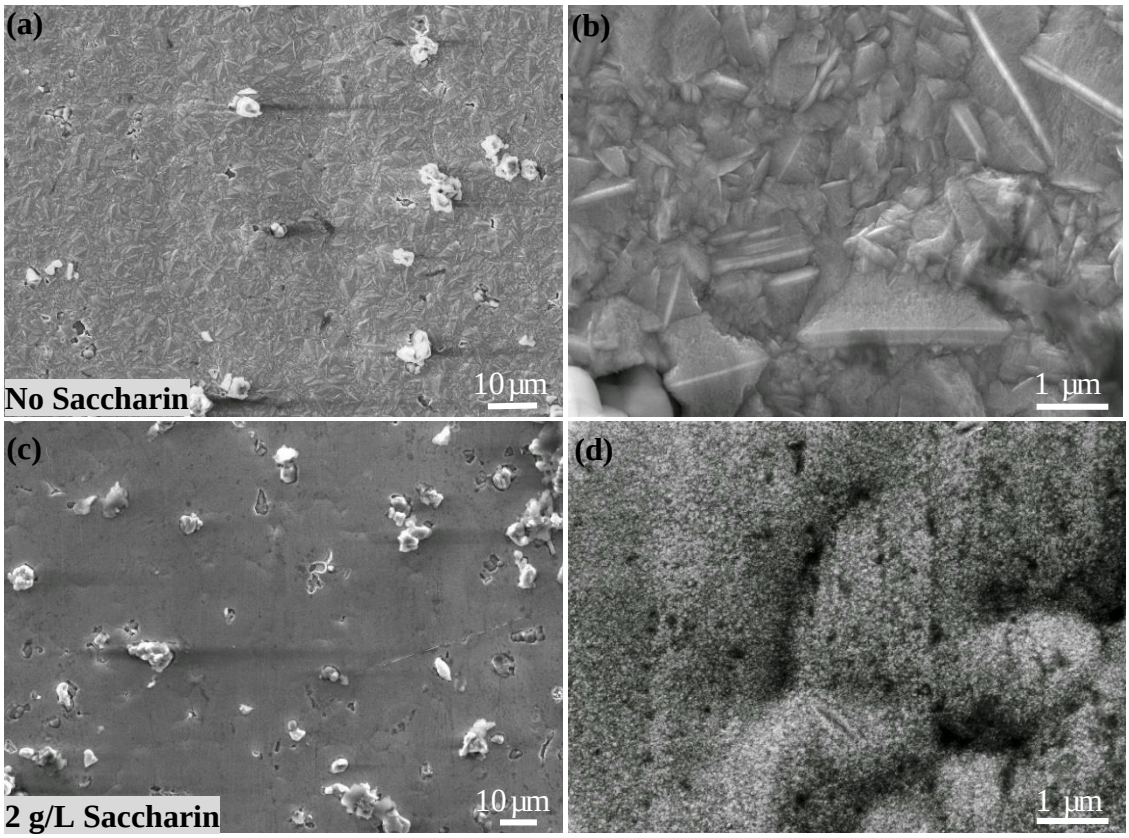

Figure 4.8 SEI image of Ni-BAM coating deposited from a solution (a, b) without saccharin or (c, d) containing 2 g/L saccharin (C_{BAM} = 2 g/L, J = 2.5 A dm^{-2}, t = 45 min, CTAB= 0.1 g/L).

X-ray diffraction was utilized to study the structure change of the Ni deposits with saccharin. Fig. 4.9(a) displays the XRD patterns of the Ni/BAM composites deposited from solutions without saccharine and with 0.2, 1 and 2 g/L saccharine. These patterns revealed the face-centered cubic (fcc) structure of the electrodeposited Ni. The peaks at

44 °, 51 ° and 76 ° belong to the (111), (200) and (220) plane of an fcc structured Ni. All the Ni composites have a dominating (111) plane parallel to the surface. The peak width of the Ni/BAM composite becomes much broader as the concentration of saccharine in the bath is fixed at 1 or 2 g/L, which indicates the decrease in the crystallite size of the Ni/BAM composite coating. From Eq. 3.1, the mean crystallite sizes were calculated as 23.9 nm, 19.5 nm, 11.7 nm and 9.2 nm respectively for the Ni/BAM composites deposited from varied solutions without saccharine and with 0.2, 1 and 2 g/L saccharine.

Saccharin can be absorbed on the surface of the deposit by filling its non-sharing lone pair of electrons into the 3d orbits of nickel atoms to form coordinate bonds [167]. This process handicaps the discharge of metal ions from solution and greatly increases the overpotential of electroplating as the current density is a constant value. As the growth of the electrodeposited layer consists of both nucleation and crystal growth, there is a competition between these processes [168]. The high overpotential promotes new nuclei and limits the growth of crystals.

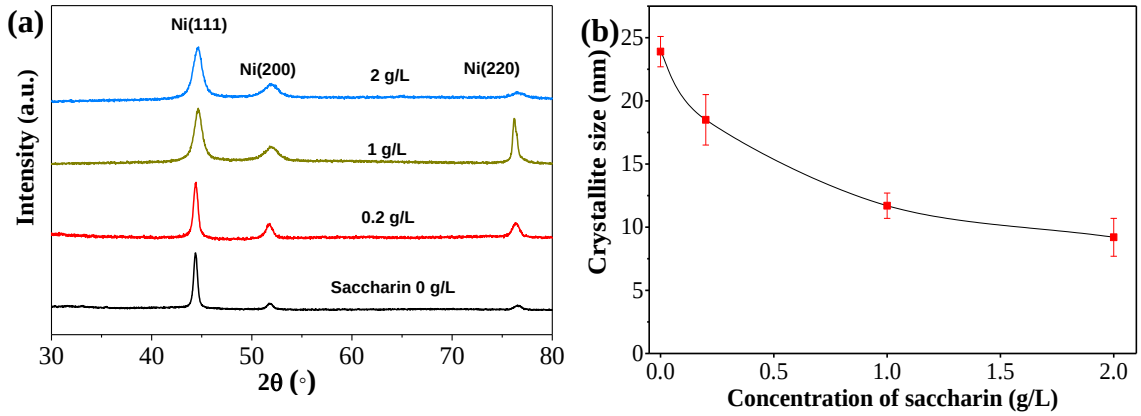

Figure 4.9 (a) X-ray diffractions of Ni/BAM coatings deposited under different saccharin concentration; (b) Relationship between the crystallite size of coating and the concentration of saccharin in bath.

4.3.6 Deposition time

BSE images of fluorescent Ni coatings with different plating times are shown in Fig. 4.10(a-d). The distribution of phosphors was calculated by field estimation using grey scale images. The area coverage of phosphor particles in the deposited coatings against different plating times is presented in Fig. 4.10(e). The area coverage of the phosphors increases dramatically to 10.0% at 30 min, and then drops down a little. This increase of BAM phosphors in the coating can be attributed to the increased depth of coating, which

can accommodate bigger phosphors.

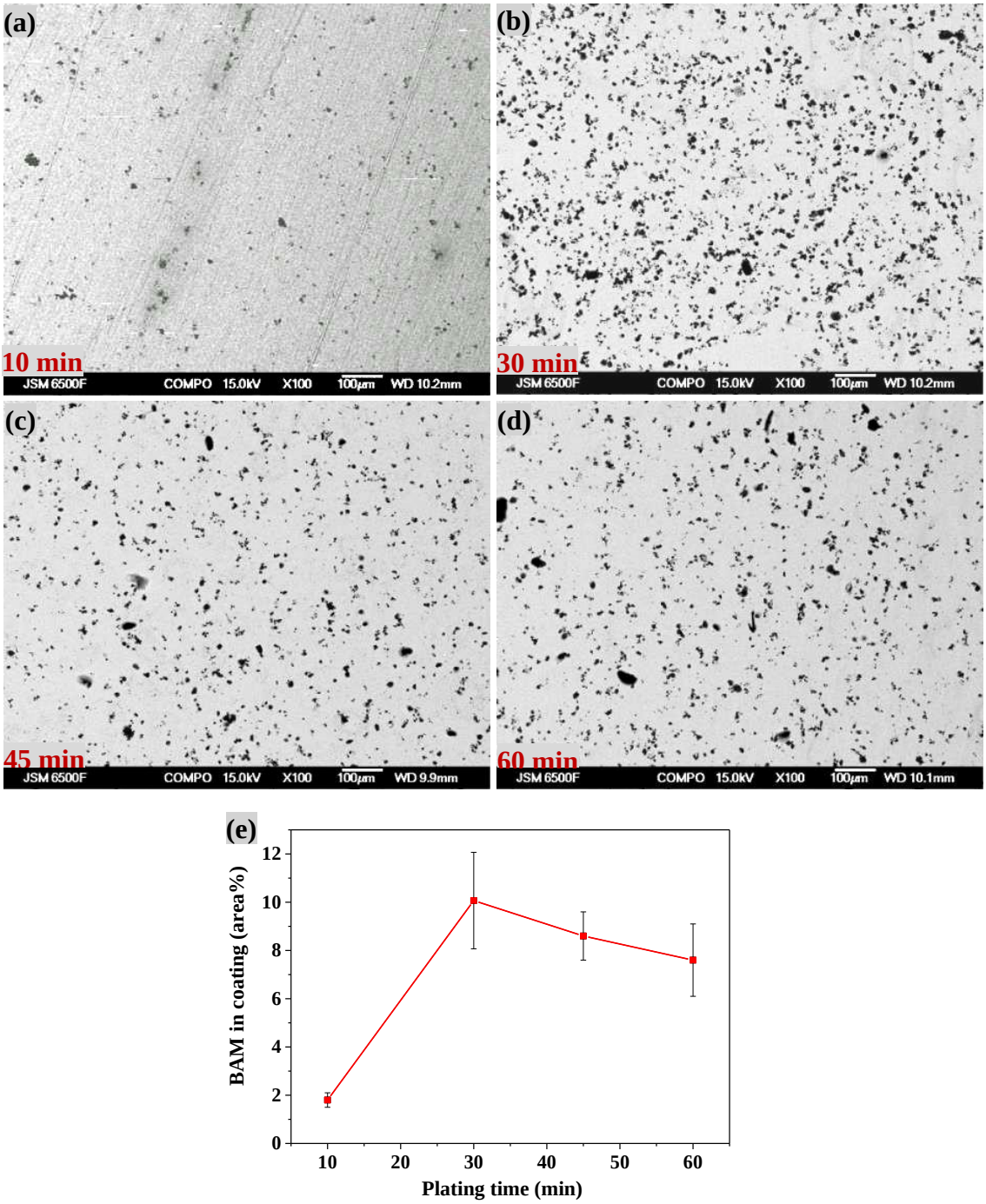

Figure 4.10 BSE images of luminescent Ni coating after different plating time: (a) 10min, (b) 30 min, (c) 45 min, (d) 60 min (C_{BAM} = 10 g/L, J = 4 A dm^{-2}); (e) Area coverage plot versus plating time.

4.3.7 Phosphor concentration

Further research has been carried out to investigate the effect of BAM phosphor concentrations. As illustrated in Figs. 4.11(a-d), the coverage percentage of BAM phosphors in the composite coating initially increases as the particle concentration in the

electrolyte increases. It reaches the maximum value of 15.9% at 5 g/L (Fig. 4.11e). Afterwards, the area coverage decreases slowly and drops to 10.9% at 10 g/L. This phenomenon could be explained as follows: At the lower levels of BAM concentration, the majority of the BAM phosphors are co-deposited with Ni. Over a certain concentration (5-8 g/L), the BAM phosphors easily aggregate and sedimentation occurs. The large aggregates are hard to keep at the electrode surface to incorporate into a growing Ni film. These two factors combined will lead to relatively lower particle contents in the composite coating over a certain level of BAM particle content.

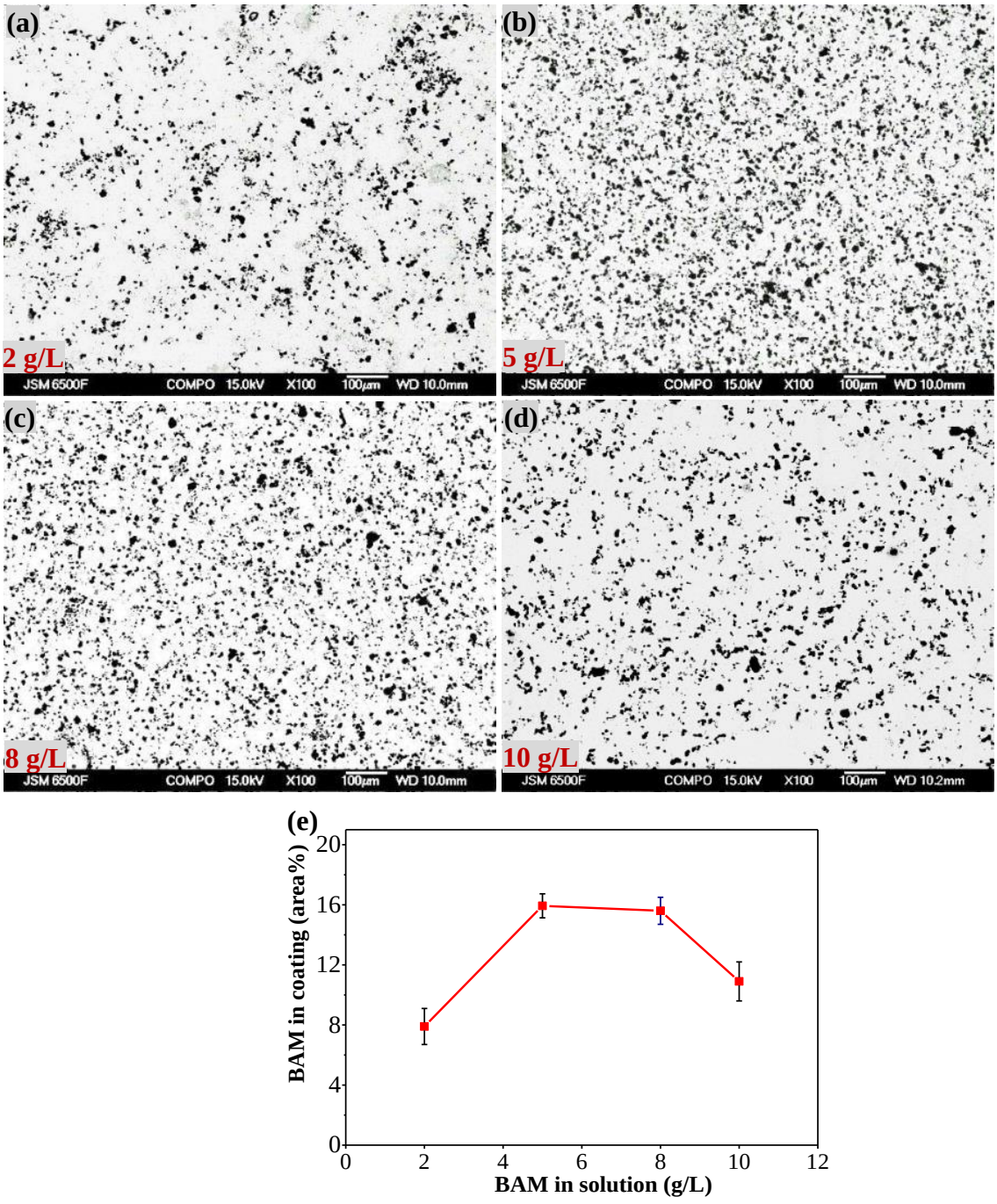

Figure 4.11 (a-d) BSE images and (e) coverage measurement of luminescent Ni coatings deposited in the solutions with different phosphor concentrations as seen in individual pictures (t = 45 min, J = 4 A dm^{-2}).

Photoluminescence emission and excitation spectra of BAM:Eu^{2+} BAM powder and Ni-BAM:Eu^{2+} coating were acquired at λ_{em}= 450 nm and λ_{ex}= 330 nm as illustrated in Fig. 4.12(a). The excitation spectrum of BAM consists of a broad band centered at 324 nm and two shoulders at 270 and 380 nm, which are attributed to the electron transitions from the ground state $^8S_{7/2}$ of Eu^{2+} with $4f^7$ configuration to ($4f^6$) 5*d* of Eu^{2+} [169]. Under excitation at 330 nm, the BAM exhibits broad-band emission in the range 375-560 nm with a maximum at 453 nm. This is due to the transition of the Eu^{2+} ion from lowest 5*d* excited state to the 4f ground state. The composite nickel coating possesses similar luminescence spectra to the BMA:Eu^{2+} powder, demonstrating the BAM particle structure was unchanged after electrodeposition.

Fig. 4.12(b) shows the corresponding photoluminescence spectra of composite coatings excited at 330 nm. The emission wavelength of Ni/BAM samples was always *ca.* 452 nm and the shape of spectra did not shift at a higher loading of BAM phosphors in the electrolyte. The luminescence intensity of the coating deposited at 5 g/L BAM was 10 times higher than that of the coating deposited at a bath particle loading of 2 g/L. Fig. 12(c) shows that the luminescence intensity of the coating increased at a higher coverage of BAM in the coating. The fitting curve obeys an exponential relationship between luminescent intensity and BAM content in the coating: $y = 53 + 0.37 \times \exp(0.48 \times x)$. The intensities increased quite slowly at a particle coverage below 12%, but increased rapidly when the particle coverage reached 14-16% towards the end of the deposition. The slope of the tangents at the 7.9% and 15.5% BAM in the coatings were 8 and 310 respectively, with a difference of *ca.* 39x.

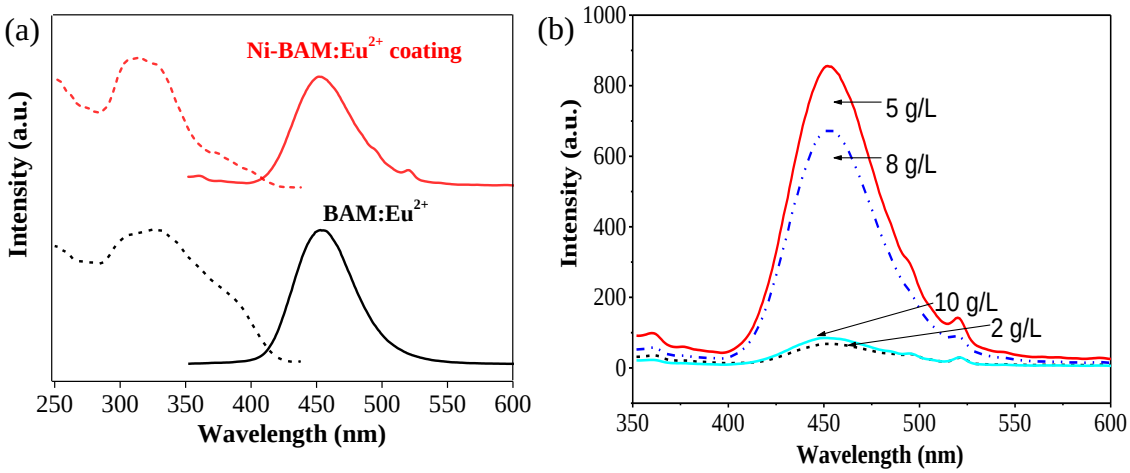

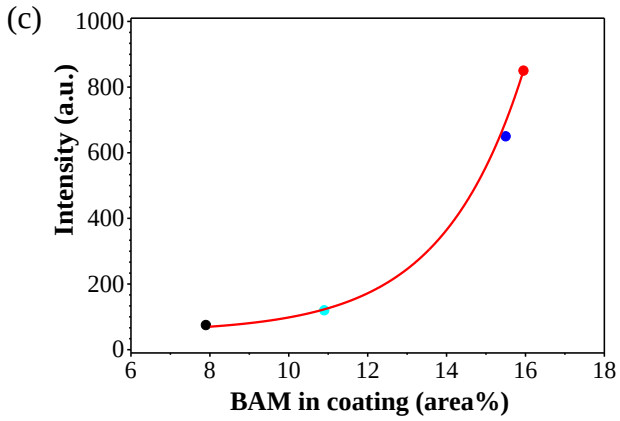

Figure 4.12 (a) Spectrum comparison between BAM phosphor and Ni-BAM coating; (b) photoluminescence emission spectra of Ni-BAM coatings deposited in the solutions with different particle concentrations: 2 g/L, 5 g/L, 8 g/L, 10 g/L (t = 45 min, J = 4 A dm^{-2}); (c) intensity of UV emission vs the coverage of BAM in coating.

4.3.8 Comparison of the effect of surfactants on composite coatings

Electrodeposited coatings were prepared in the basic electrolyte with and without surfactants. In the absence of surfactants, the coating showed a smooth surface (Fig. 4.13(a)). EDS confirmed it to be pure nickel where BAM phosphors were barely observed. In the PEG electrolyte bath, an averaged 4.6% area coverage of BAM phosphors were co-deposited but not uniformly distributed, as shown in Fig. 4.13(b). In the electrolyte bath with CTAB, the BAM powders were well embedded in the Ni coatings (Fig. 4.13(c)) and its coverage reached 11.5%. In the electrolyte bath with the addition of both PEG+CTAB surfactants, the deposit consisted of denser phosphors, as shown in Fig. 4.13(d). The area coverage of phosphors averaged 15.6% which is almost the sum of those from solutions with a single surfactant as shown in Fig. 4.13(e). Fig. 4.13(f) shows the photoluminescence spectra of composite coatings excited by 330 nm UV light. The emission wavelength of Ni/BAM samples was *ca.* 452 nm, which corresponds to the transition of Eu^{2+} ion from its lowest 5*d* excited state to the 4*f* ground state. The luminescence intensity of the coating deposited with PEG+CTAB addition was 4 times higher than the coating from a bath containing PEG.

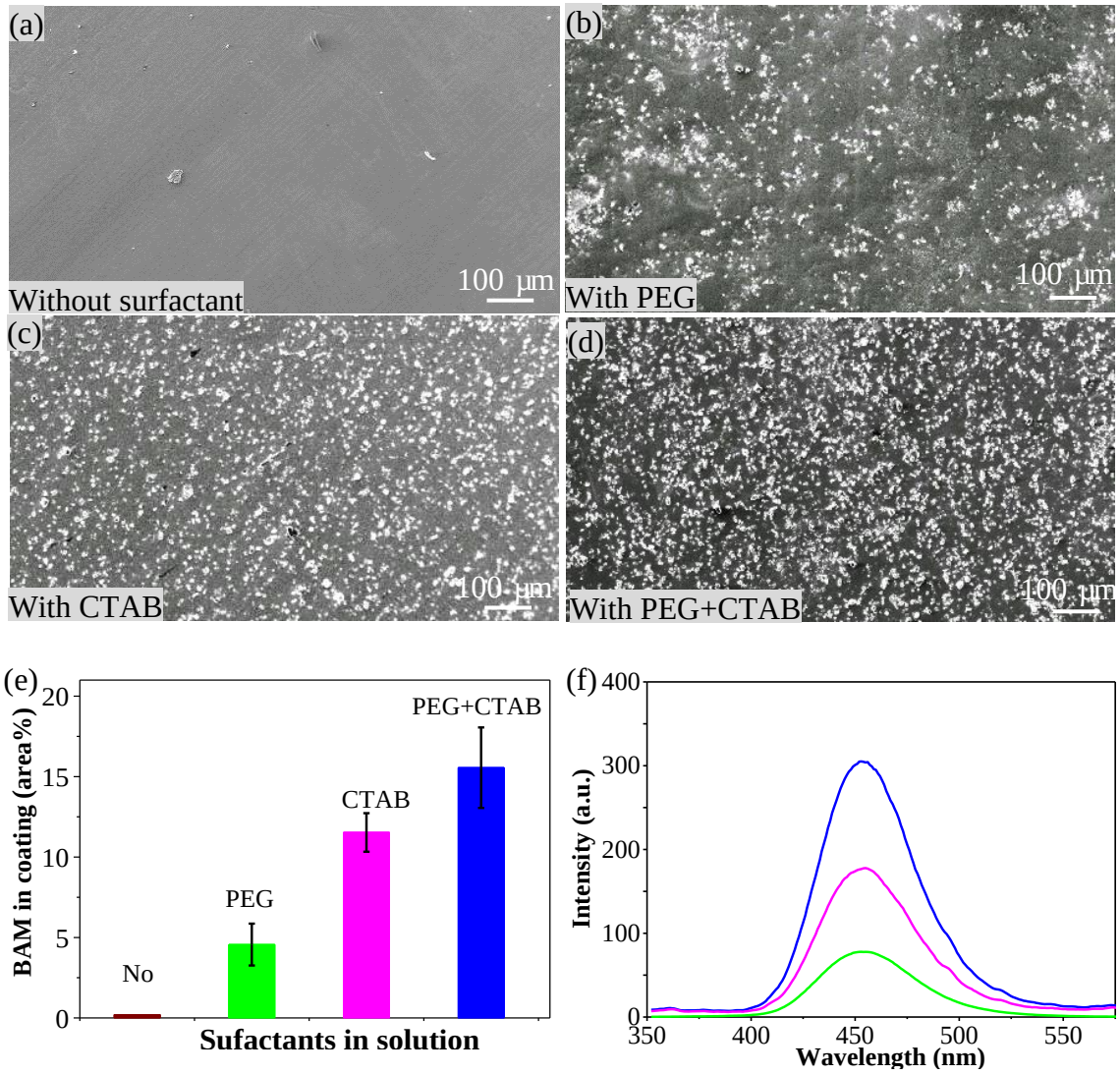

Figure 4.13 (a-d) SEI images showing embedded BAM in Ni coatings deposited without and with surfactants PEG, CTAB and combined PEG - CTAB, respectively; (e) area coverage of BAM phosphors in these coatings; (f) photoluminescence emission spectra of the Ni/BAM coatings deposited with different surfactants.

Fluorescent microscopy was used to detect the luminescence density of the Ni-BAM coatings. All fluorescent images were probed with DAPI filter (excitation, 350 nm; emission, 450 nm). Fig. 4.14(a) shows the BAM phosphors emitting blue in the coating surface recorded in UV light. In a systematic study, coatings were prepared from electrolyte with PEG addition (Fig. 4.14(b)) or CTAB and PEG addition (Fig. 4.14(c)). With the PEG addition, few BAM phosphors were observed scattered within the coating. Most of the coatings were not able to emit light. With the addition of CTAB and PEG, large numbers of BAM phosphors are distributed homogeneously as light emitting sources in the layer. This result confirms that the CTAB is effective in changing the dispersion of phosphors and enhancing the electrostatic adsorption of phosphors on the cathode by increasing their positive charge.

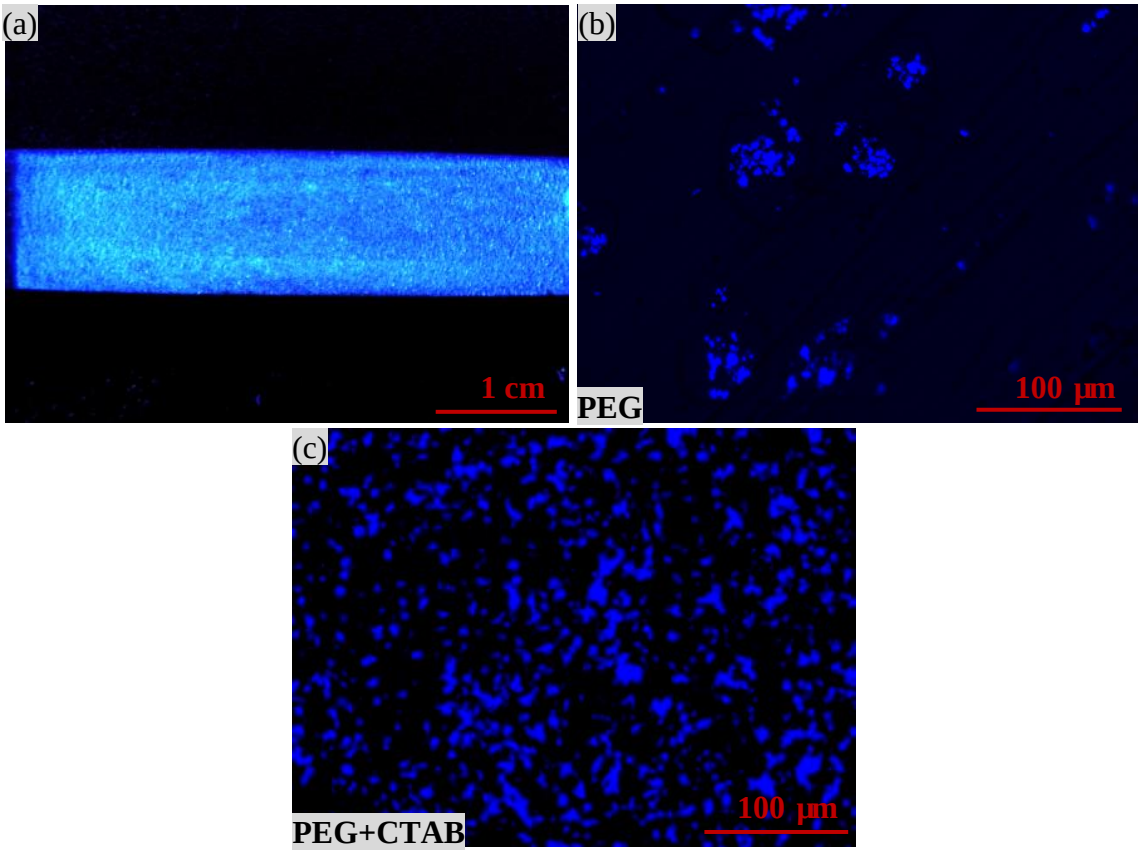

Figure 4.14 (a) Digital image of luminescent coating under 365 nm UV illumination; (b-c) fluorescence images of Ni-BAM: Eu^{2+} coatings deposited with different surfactants.

Linear sweep voltammetry (LSV) was used to characterize the electrochemical performance of the electrodes. The test was conducted in three-electrode cell at a linear potential scan rate of 10 mV s^{-1} over a potential range of 0 to 1.2 V. Fig. 4.15 shows the cathodic LSV curves recorded for Ni and Ni-BAM (5 g/L) with and without additives to the basic solution. It indicates that all the depositions start at a potential of approximately -0.83 V versus SCE. As the potential becomes more negative than -1.0 V, the current density rapidly becomes more negative. The addition of BAM phosphors appears to slow down the rate of current density increase, which can perhaps be attributed to the steric hindrance of the non-conducting BAM phosphors [170]. At the current of 4 A dm^{-2} used for the electrodeposition, the potential for the Ni-BAM deposition is -1.2 V. With the PEG addition, the potential extends to be more negative at -1.3 V. This is believed to be due to the adsorption of the PEG onto the electrode surface, which then took up some available sites and made charge transfer unavailable at these sites. More negative overpotential means lower current efficiencies, as a large current will produce intensive hydrogen which accordingly affects the coating quality. With the addition of PEG + CTAB, the

potential moves towards a more positive value at -1.1 V. It is therefore seen that with the addition of the double additives, the codeposition of Ni and BAM will be more effective.

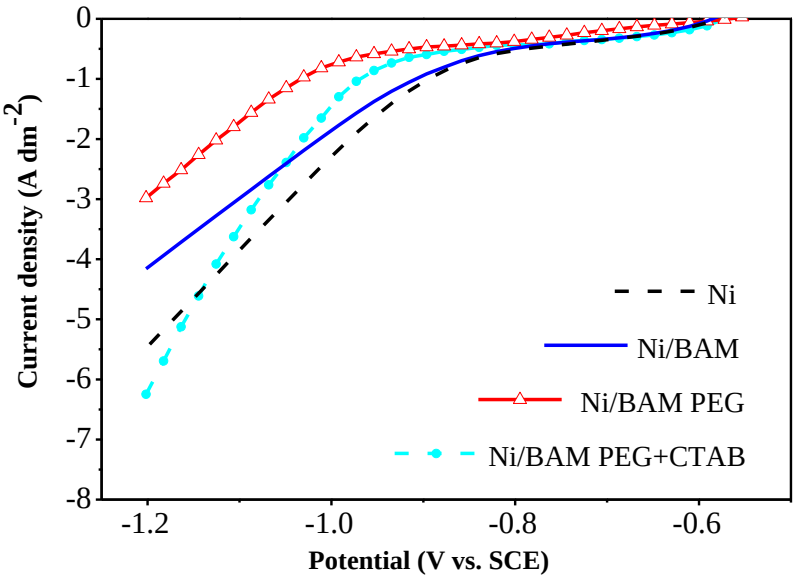

Figure 4.15 LSV profiles of Ni and Ni-BAM electrodeposition (C_{BAM} = 5 g/L) with and without additives in the basic solution. (C_{PEG} = 2 g/L, C_{CTAB} = 0.1 g/L).

4.3.9 Microhardness and tribological properties

The respective coefficients of friction for Ni and Ni/BAM coatings are recorded in Fig. 4.16(a). The friction coefficient of the pure Ni coating was lowest at an average of 0.55. The luminescent Ni coatings had an initial friction coefficient of 0.7 during the first 100 s, which was caused by the initially rough surface of the luminescent coating. After this "running in" process, the coatings with lower BAM coverages (4.6%) show the friction coefficient dropped down to a steady value of approx. 0.6; the friction coefficient for the composite coatings with higher BAM coverage (11.5%, 15.6%) remained at ca. 0.7. The friction coefficient increased at a higher content of BAM phosphors. Although the friction coefficient for the BAM phosphors is not available, it can be expected that it should be much higher than Ni.

Fig. 4.16(b) shows the hardness and wear rate (sliding under ambient air) of the composite coatings as a function of BAM phosphors in the coatings. The hardness of the Ni deposit was measured in the range of 450 ± 15 HV. For the Ni luminescent composite coatings, the hardness values are in the range of 495 to 599 HV. As seen in the HV data in Fig. 4.16(b), they are almost proportional to the embedded particle contents in the coatings,

i.e. the BAM phosphors reinforce the Ni deposit. The strengthening effect could be explained in terms of an Orowan hardening mechanism [171], whereby dislocations bow around BAM phosphors which act as dislocation pinning sites resulting in an increase in the flow stress. The coating with 15.6% BAM shows the highest value of 599±29 HV, which corresponds to the maximum amount of phosphors observed in the coatings. In contrast, their wear rates are a negative gradient linear relationship with the BAM contents in the coatings. The pure Ni coating has a wear rate at 4.8×10^{-4} mm^3 N^{-1} m^{-1}, whereas the wear rates of the luminescent Ni coatings are lower, ranging from 2.4×10^{-4} to 3.9×10^{-4} mm^3 N^{-1} m^{-1}. It is evident that the codeposited phosphors improve the wear resistance of the Ni coating when sliding against the steel ball counterpart. The result is not unexpected as it is in general a rule that the higher the hardness the lower the wear rate.

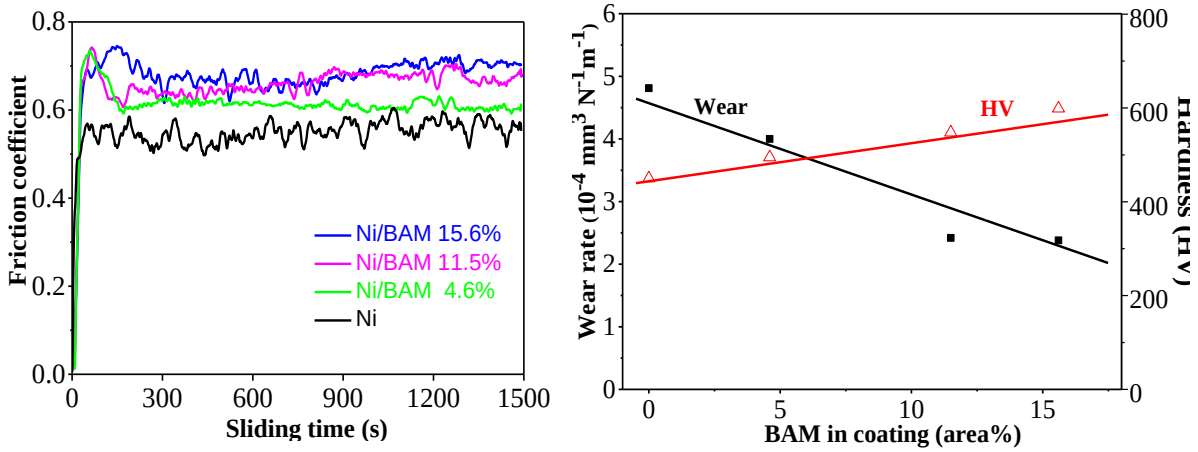

Figure 4.16 Relationships of coefficient of friction against sliding time for the Ni and Ni/BAM coatings; (b) wear rate and hardness of Ni/BAM coatings vs the BAM content in coating (t = 45 min, J = 4 A dm^{-2}).

Fig. 4.17(a-d) show the wear tracks of the Ni coatings consisting of 0%, 4.6%, and 15.6% BAM phosphors, respectively. Non-continuous patches in dark contrast were observed within all three wear tracks. Noticeably, the 11.5% BAM coating contains lots of uniformly distributed small patches, which were formed on the top of the BAM phosphors. A comparison of their composition in Fig. 4.17(e) shows that there is the highest content of iron and oxygen in the Ni/BAM 11.5% coating, suggesting the steel ball was oxidising and transferring material to the counterpart.

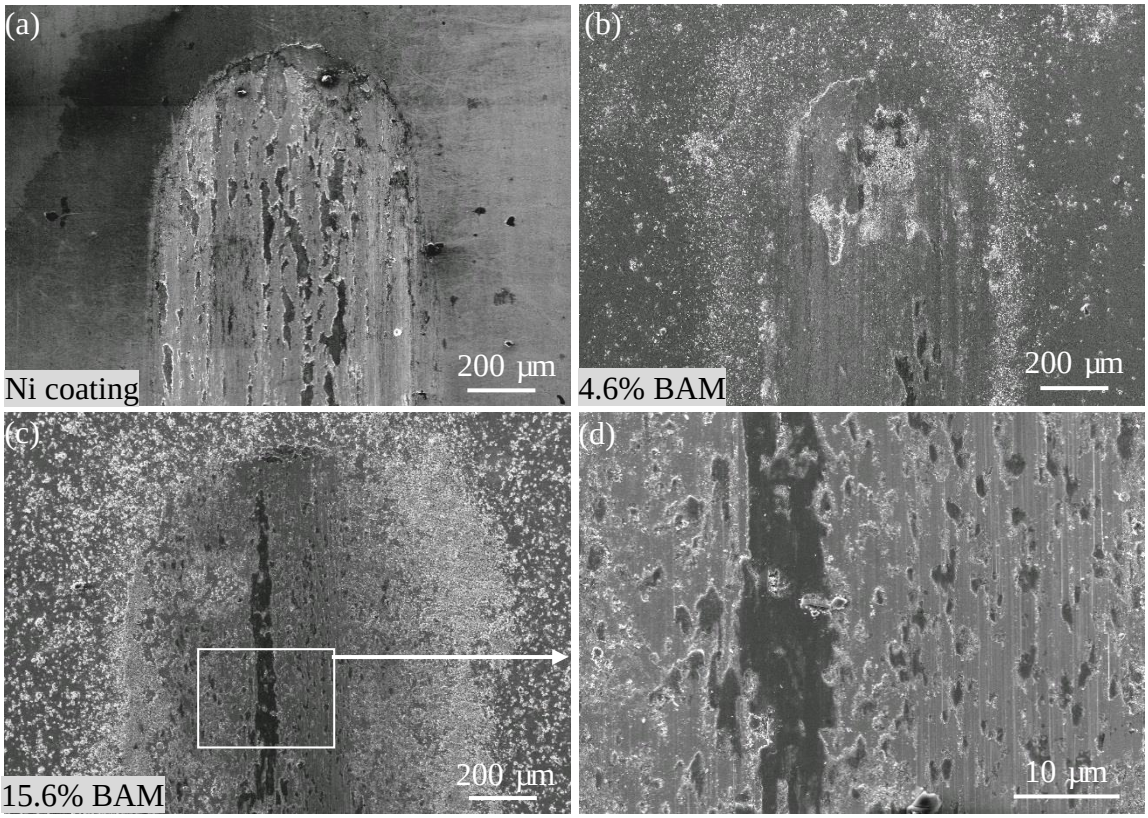

(e)

Element (wt%)	Ni	4.6 % BAM	15.6 %BAM
O K	8.9	10.5	14.8
Ni K	87.6	87.0	63.2
Fe K	3.5	2.5	22.0
Al K	-	-	0.5

Figure 4.17 SEI images of wear tracks on different coatings (a) Ni, (b)Ni/BAM 4.6%, (c,d) Ni/BAM 15.6%; (e) EDS comparison of the whole wear track in Ni, 4.6% and 15.6% Ni-BAM coating.

Fig. 4.18(a-c) show the morphologies of the wear tracks on counterpart balls after the friction test. The counterpart ball displays a smaller wear track after sliding against Ni/BAM composite coatings than sliding against the Ni coating. This may be related to the increased hardness in the composite coating, which can reduce the wear of coating. Fig. 4.18(d) shows the composition of the wear tracks on counterpart balls. Higher nickel and oxygen levels were found on the counterpart ball after sliding against the coating with higher BAM content.

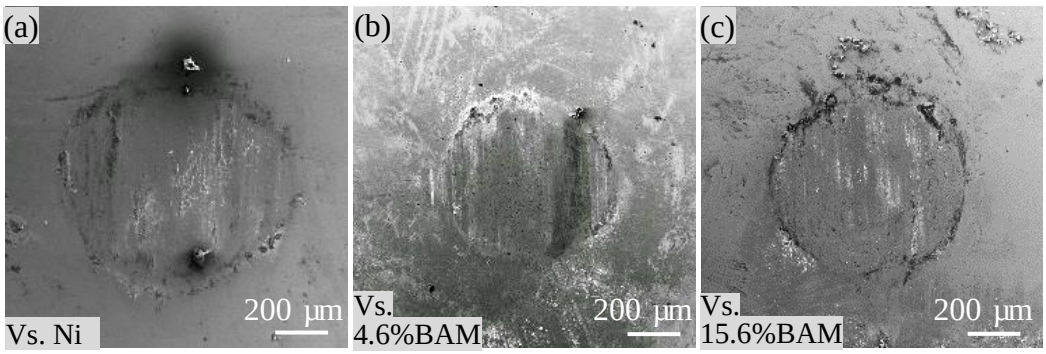

Element (wt%)	Vs. Ni	Vs. 4.6% BAM	Vs. 15.6%BAM
O K	5.4	6.6	6.8
Cr K	1.6	1.3	1.1
Fe K	85.3	83.5	77.4
Ni K	7.7	8.6	14.7

Figure 4.18 Morphologies of the counterpart balls after 1500 s friction test against (a) Ni, (b) Ni/BAM 4.6% and (c) Ni/BAM 15.6% coatings; (d) EDS comparison of the wear track in these counterpart balls.

4.3.10 Corrosion resistance of the Ni/BAM coating

The polarization curves of the steel substrate, Ni coating and Ni-BAM (5 g/L) coating are illustrated in Fig. 4.19. The electrochemical parameters such as corrosion potential (E_{corr}) and corrosion current (J_{corr}) were collected using the Tafel extrapolation method [172] and listed in Table 4.3. The steel substrate shows the most negative corrosion potential (E_{corr}) of -701 mV, with a high corrosion current density (J_{corr}) of 3.89×10^{-5} A cm^{-2}. The potentiodynamic curve shapes of the Ni-BAM and pure Ni coating are similar with active oxidation reaction at the anode and oxygen reduction at the cathode. Due to the positive shift of the polarization curves, there should be no defects present in the tested coating samples [173]. The Ni-BAM composite coating displays a more positive E_{corr} of -460 mV and lower J_{corr} of 5.79×10^{-6} A cm^{-2} than the Ni coatings of -485 mV, -4.93×10^{-5} A cm^{-2}.

The corrosion rate is in direct proportion to the corrosion current density. The relation between them follows this relationship:

$$v = 3.73 \times 10^{-4} \times J_{\text{corr}} \times (M/n) \qquad (4.1)$$

where v = corrosion rate (g $cm^{-2}s^{-1}$), J = corrosion current density (A cm^{-2}), M = molar mass (g mol^{-1}), n = number of electrons involved in the electrochemical reaction. The corrosion current density of the Ni/BAM coating is much smaller than the Ni coating, consequently, the corrosion rate is slower and the corrosion resistance is stronger.

The improved corrosion resistance of the Ni-BAM coating was correlated with the presence of the inert BAM phosphors. The phosphors could improve the corrosion resistance in the two following ways [174,175]. Firstly, the phosphors fill some areas of the Ni matrix, forming inert barriers and blocking the initiation and progression of corrosion. Secondly, the dispersed BAM phosphors and the nickel matrix could form many "corrosion microcells". Nickel metal acts as the anode, while the phosphors act as the cathode in "corrosion micro-cells", as the standard potential of the BAM phosphors is more positive than that of nickel. Such corrosion micro-cells will aggravate the anode polarization. With a uniform distribution of BAM phosphors in the coating, homogeneous corrosion rather than localized corrosion dominates. Thus, the Ni-BAM coating appears to provide adequate protection to the substrate [176].

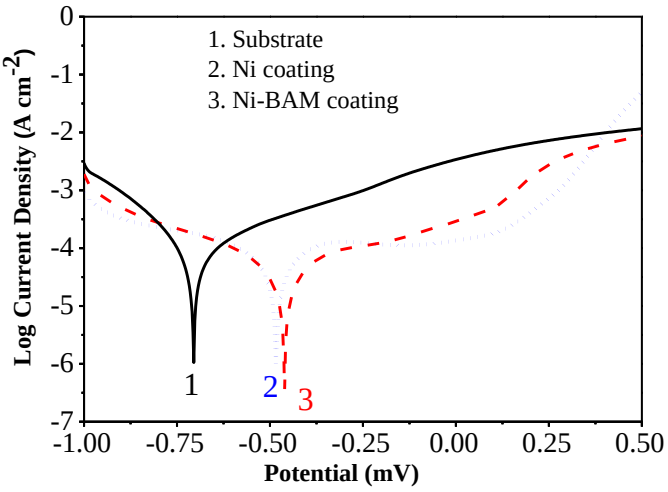

Figure 4.19 Polarization curves of substrate, Ni coating and the luminescent Ni coating (curve 1: steel substrate, curve 2: pure Ni coating, curve 3: Ni-BAM coating).

Table 4.3 Corrosion potential (E_{corr}) and corrosion current (J_{corr}) for Substrate, Ni coating, Ni-BAM:Eu^{2+} coating in NaCl solution.

	Substrate	Ni coating	Ni-BAM:Eu^{2+}
E_{corr} (mV)	-701	-485	-460
J_{corr} (A cm^{-2})	3.89×10^{-5}	4.93×10^{-5}	5.79×10^{-6}

4.4 Discussion

4.4.1 Working mechanism of CTAB and PEG on the electrodeposition of Ni/BAM

As indicated in Fig. 4.13, the surfactants are crucial to deposit satisfactory ceramic-metal composite coatings: with the addition of PEG, CTAB and PEG+CTAB, the area coverages of the embedded BAM phosphors have increased from nil without surfactant to 4.6%, 11.5% and 15.6%, respectively.

As an inert particle in a bath grows into the deposit this involves convection, diffusion and then adsorption and reduction at the electrode surface, before particles can be embedded in the metal [41, 177, 178]. When the adhesion force is strong enough to resist the shear force caused by gravity, particles begin to incorporate into the growing metal layer. For micron size (>1 μm) particles with a high density (> 3.2 g cm^{-3}) as in this study, the gravity force is larger than the sum of other forces. Therefore, the majority of the particles can't stick on the electrode surface and no effective incorporation of particles can occur (Fig. 4.20a). Without surfactant, the particles tend to settle out at the bottom of the electrolyte.

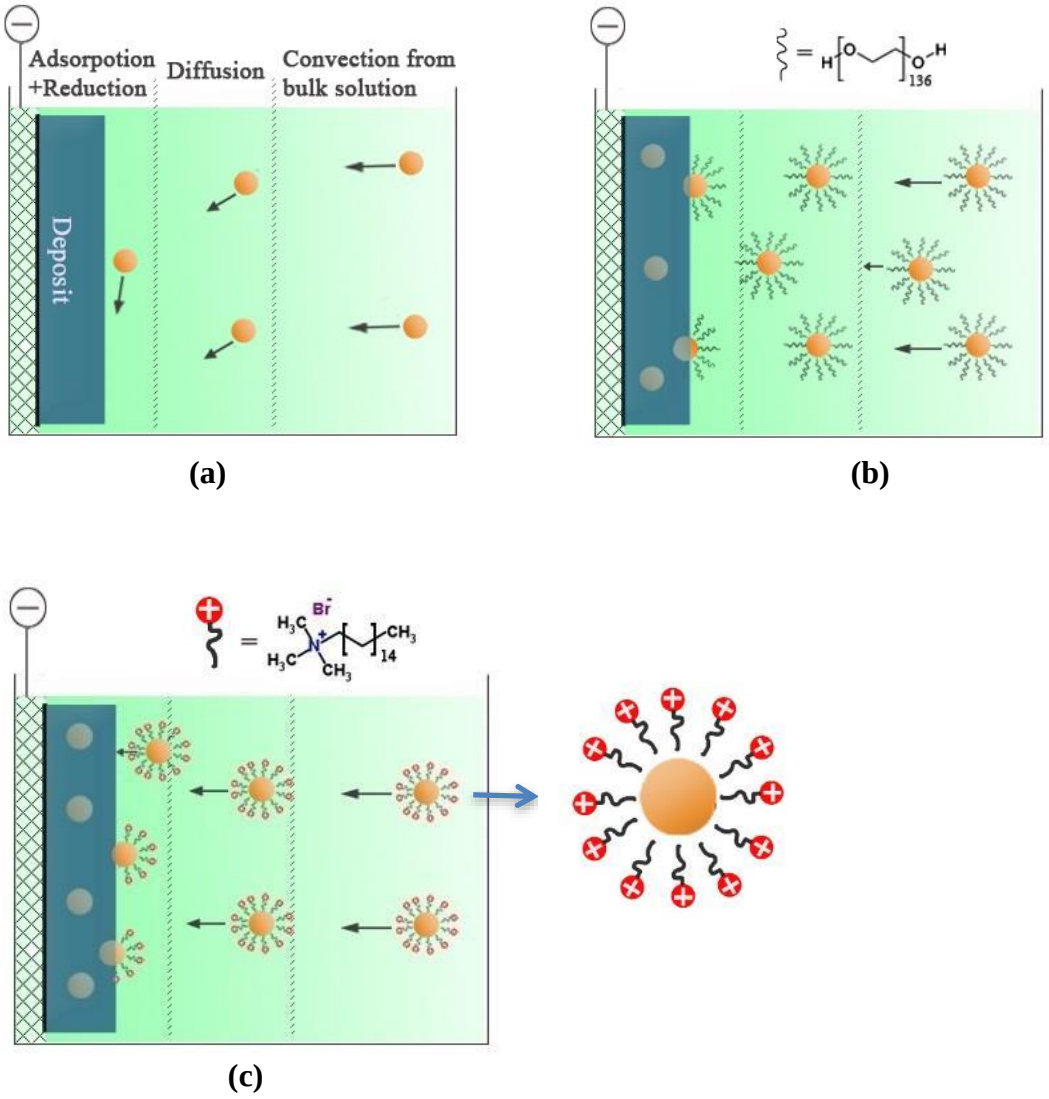

Figure 4.20 Schematic illustration of the codeposition process of particles in electrolyte with a) no surfactant, b) PEG or c) CTAB.

PEG (M_n=6000) is a non-ionic surfactant with a long chain structure H-(O-CH_2-CH_2)$_{136}$-OH. With such a structure PEG is hydrophilic in water (H-OH). In the electrolyte solution, The OH^- of PEG will migrate into the BAM particles and H^+ toward water (Fig. 4.20b). The adsorbed PEG layer can provide steric separation and its hydrophobicity can inhibit the particles from merging into larger aggregates, so less sedimentation was expected. With the applied potential, the hydrogen-bond of PEG will be attracted strongly by existing electrons in the cathode. The electronic force will hold the particles on the electrode surface longer and enhances the incorporation of particles into the metal matrix.

The CTAB molecule, $(C_{16}H_{33})N(CH_3)_3Br$, is a long chain cationic surfactant. It consists of a hydrophobic tail and a non-charged hydrophilic head (as shown in Fig. 4.20c): the

former part preferentially adsorbs on particles, whereas the latter part avoids particles [179,180]. This electrostatic repulsion helps to produce a stable dispersion in the electrolyte. As a cationic surfactant, CTAB can not only improve the stability of particle suspension but also charge the non-conductive particles positively via electrostatic adsorption [181]. Therefore, the cationic particles will be attracted strongly to the cathode surface under the applied potential. This helps explain why the particle area coverage with CTAB was 6.9% higher than that with PEG.

With the addition of both PEG and CTAB, the area coverage of BAM particles was 15.6% which is almost the sum of the separate surfactant effects. It indicates that both effects of CTAB and PEG work on the particle surface, so the embedded ceramic particles could be maximised by (1) the suspension enhanced by PEG and (2) the increase of the adhesion force between the cationic particles and the cathode by CTAB.

The non-ionic surfactant PEG and the cationic surfactant CTAB have different effects on the electrodeposition reaction, as indicated in the LSV curves of Fig. 4.15. The adsorption of the PEG onto the electrode surface took up some available sites and made charge transfer unavailable at these sites [170] which caused the resistance to increase as well as the overpotential. A highly negative overpotential usually results in intensive hydrogen evolution which may block the deposition of particles and Ni ions. The situation is quite different for CTAB, as it is a redox-active cationic surfactant. If the applied deposition potential becomes more negative than its reduction potential, the CTAB molecule (with or without BAM connected) on the electrode will be reduced and CTAB in the solution will diffuse toward the cathode surface, which compensates the curve shift in Fig. 4.15. As a consequence, it is more effective on the deposition of particles and a higher percentage of BAM can be achieved during the composite electrodeposition process.

With the addition of two surfactants, the LSV of Ni/BAM electrodeposition is similar to that from a bath containing CTAB in Fig. 4.15. This may indicate that the individual particle is covered by a mixture of CTAB and PEG. It also explains why the particle area coverage is almost the sum of those by individual CTAB and PEG additions. The anionic/non-ionic surfactant combination has been reported to improve the embedment of particles in other composite plating systems such as Ni/PTFE (polytetrafluoroethylene polymer composite), Ni-P/PTFE or Ni-TiO_2-SiO_2 [182,183,184].

4.4.2 Effect of saccharin on grain refinement

As illustrated in Fig. 4.9, the crystallite size of the coating was easily controlled within a certain range by varying the saccharin concentration. In electrodeposition, three important factors are considered to reduce the crystallite size: (1) high overpotential or high current density, (2) high concentration of adsorbed ions, and (3) slow flow of adsorbed ions. These factors may work separately or simultaneously to promote the formation of nucleation or dislocation and therefore reduce crystallite size [185].

Saccharin ($C_7H_5NO_3S$), a typical hardening additive, is an aromatic compound containing unsaturated sulfanilamide base. The formula structure is as follows:

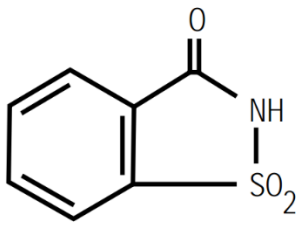

In saccharin molecules, the lone-pair electrons on the oxygen atom could easily fill the 3*d* orbitals of the nickel atoms, forming a stable coordination with it. Hence, during electrodeposition, there is a strong interaction between the surface atoms of Ni deposits and the saccharin additives. Due to the large size of the coordination compound, the surface migration of the metal ions on the electrode are largely suppressed, which provokes disorder incorporation of adsorbed atoms (*ad*-atoms) into the lattice or inhibits the surface diffusion of *ad*-atoms to growing centres [186]. In the meantime, a significant increase of electrode overpotential occurs, which will cause a rapid formation of a large number of new crystal nucleus. The result of the combined effect of the two processes is that the crystallite size of deposits has been dramatically reduced.

The deposits produced with the addition of saccharin in solution usually exhibit higher tensile strength, higher hardness, and relatively lower ductility.

4.4.3 Applications

Two types of luminescent coatings in Fig. 4.1 have been successfully prepared. Fig. 4.21 exhibits the cross section view and the corresponding worn surface under UV. For the top layer with the embedded phosphors as illustrated in Fig. 4.21(a), the worn through area on the coating did not show any light emission while the surrounding area showed clear blue-light emission (Fig. 4.21(b)). For the phosphors embedded in the interlayer (Fig. 4.21(c)), the illumination in the worn through surface is the opposite (Fig. 4.21(d)). These layers can be extended further to produce multiple colour layers including red green and blue for functional coatings.

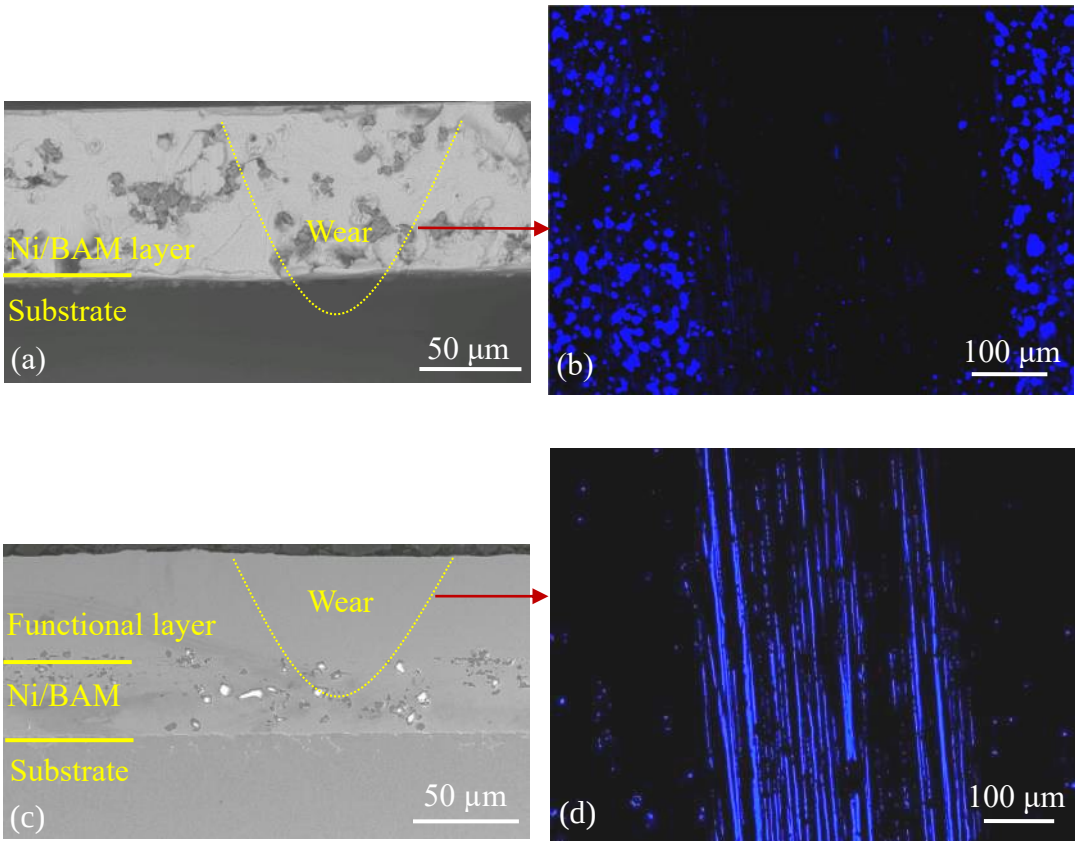

Figure 4.21 (a, b) cross-sectional SEI image of Ni/BAM coating and the luminescent image of the coating wear under UV illumination; (c,d) cross-sectional SEI image of the two-layer coating system and the plan-view luminescent image of coating wear under UV illumination.

Luminescent material embedded in a Ni coating or attached into a composite structure could act as a real-time damage sensor. When the damage/fracture occurs in the host composite, it will result in a light emission under UV illumination. It is worthwhile to identify the specific characteristics of the Ni luminescent coating and its ability to become

a successful optical damage sensor. The main characteristics are characterised and listed as follows:

(1) The luminescent Ni coating exhibits blue colour under UV, with sufficient intensity to be easily observed with naked eye. Fig. 4.21 shows that the light signal from the point of fracture to the detector is strong enough to be detected.

(2) The luminescent coating may work independently or in a multilayer structure. The huge advantage of a fully embedded structural health-monitoring system is that one could discern the structural state of health with only a minor weight increase.

(3) For the double layer system, the sensor layer could sense the nature and magnitude of structural damage as the damage occurs in real time and send out information on the level of damage.

4.5 Summary

Composite luminescent coatings - $BaMgAl_{11}O_{17}:Eu^{2+}$ doped Ni coatings have been successfully prepared in an aqueous nickel plating electrolyte, key findings are highlighted as follows:

1. The non-ionic PEG and cationic CTAB surfactants have incorporated BAM phosphors into the nickel coatings using an aqueous nickel plating electrolyte, with area coverages of 4.6% and 11.5%, respectively. The PEG suspends the phosphors in the bath by adsorbing on its surface and increasing steric hindrance. The cationic surfactant CTAB shows a higher impact on the incorporation of particles as it can change the net charge on particles and increases the migration force to the cathode. A combination of CTAB+PEG improved further on the area coverage of BAM phosphors to be 15.6%.

2. The crystallite size of coating was well controlled from 23 nm to 9 nm by varying the concentration of saccharin, which was thought to increase electrode overpotential, speed up the nucleation of Ni crystallites and retard their growth.

3. Ni/BAM coating shows successfully a distinct blue colour under UV illumination, which can be applied as either top layer or underlayer for the monitoring of wear progress.

4. The as-deposited coatings possess a highest hardness of 599 HV and a lowest wear rate of 2.4×10^{-4} mm^3 $N^{-1}m^{-1}$ which is half that of pure Ni coatings. The luminescent coating also displays better anti-corrosion properties than pure Ni coating. These factors prove the possibility of using such coatings in wear sensing applications.

Chapter 5 Development of Ni-P/MoS_2 composite coatings by electrodeposition

5.1 Introduction

MoS_2/metal coatings usually exhibit exceptional low friction and high wear resistance properties. However, they are difficult to electrodeposit onto steel due to uncertainty around how to optimise composite electrodeposition, especially for the codeposition of semiconductive particles like MoS_2. Such particles will influence the distribution of the electric field on the electrode, which may cause pores and high internal stress in the coating. In this chapter, an attempt has been made to electrodeposit Ni-P/MoS_2 coatings on mild steel by optimizing current density, the concentration of additives (CTAB), and particle concentration. Additionally, coating structure, surface roughness and MoS_2 content were characterized and evaluated.

5.2 Experimental details

The coatings were deposited on a mild steel substrate which was polished using 120 and 800 grit silicon carbide paper, washed with detergents to remove oil residue, dried with paper towels and afterwards activated in 10% hydrochloric acid for 10 seconds to remove any oxide films and to obtain an active fresh surface. Finally, the substrate was rinsed with distilled water before the electrodeposition process was started. These steps ensured a good adhesion between the coating and substrate.

The electrolyte solution with the composition is listed in Table 5.1. Nickel sulphate hexahydrate and sodium hypophosphite were included to supply nickel ions and phosphorous ions respectively for the coating deposition on the cathode. Boric acid was used as a pH buffer, and CTAB as the surfactant was used to aid particle deposition. Molybdenum disulphide as solid lubricant was used with particles 0.5-2 μm in diameter.

All ingredients are added one by one to be dissolved by magnetic stirring and ultrasonic mixing. The solution in the beaker was heated by a water bath with a controlled temperature of 60 ˚C and stirred at approximately 120 rpm.

Table 5.1 Electrolyte composition for the electro-deposition of Ni-P/MoS_2 coating.

Chemical compound	Concentration (g/L)	Sourced from
$NiSO_4 \cdot 6H_2O$	220	Sigma-Aldrich
H_3BO_3	30	Sigma-Aldrich
NaH_2PO_2	10	Sigma-Aldrich
$NiCl_2 \cdot 6H_2O$	45	Sigma-Aldrich
$HOC(COOH)(CH_2COOH)_2$	12	Sigma-Aldrich
CTAB	0.1 / 0.2 / 0.3 / 0.5	Sigma-Aldrich
MoS_2	1 / 3 / 7 / 10 / 20	ST-Nano Science&Technology

5.3 Results

5.3.1 Morphology and microstructure

The as-received MoS_2 particles were examined using both SEM and TEM. The SEM image in Fig 5.1(a) shows that the as-received MoS_2 lubricants are randomly shaped flake-like particles, with a diameter from 1 to 4 μm. Fringes can be seen in the HRTEM image, exhibiting a spacing of 0.63 nm which is in accordance with the interlayer distance of the (002) plane of MoS_2. The Fourier transform of this image indicates the particle is polycrystalline.

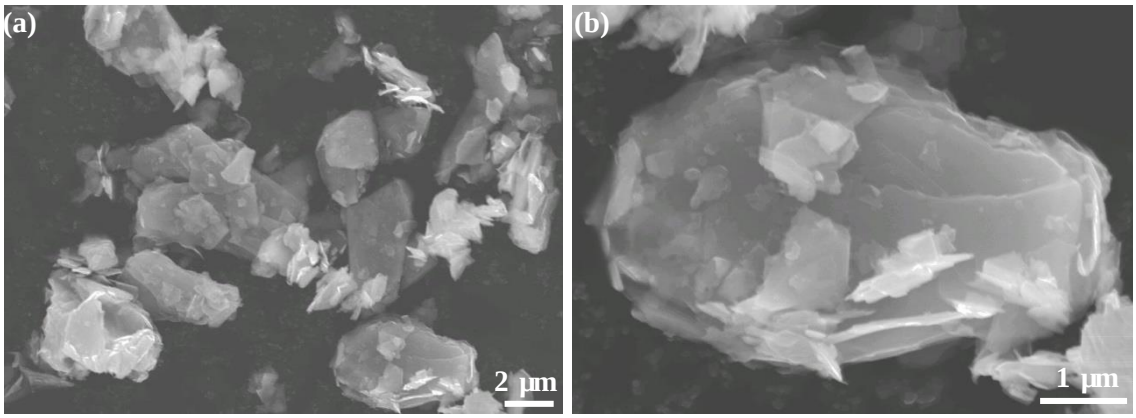

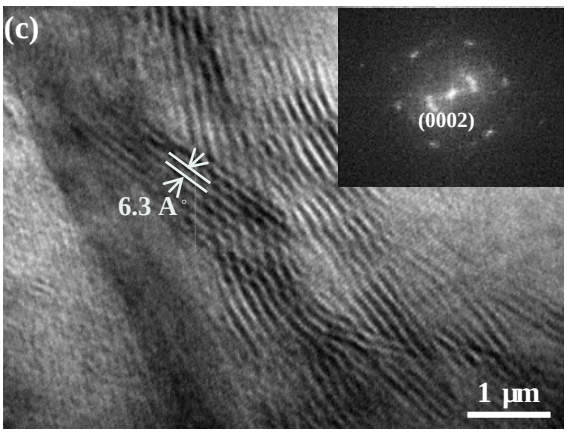

Figure 5.1 (a, b) SEI images and (c) TEM image of as-received MoS_2 particle; the inset image is the Fourier transform of the TEM image.

The Ni-P/MoS_2 coating was electrodeposited for 45 minutes from a solution with 1 g/L MoS_2. Under SEM, Ni-P coating displays a relatively smooth surface. In contrast, the Ni-P/MoS_2 composite coating shows a rough surface decorated with nodules. The high-magnification image shows numerous small MoS_2 particles on the surface. The thickness of the coating is around 25 microns (Fig. 5.2(d)).

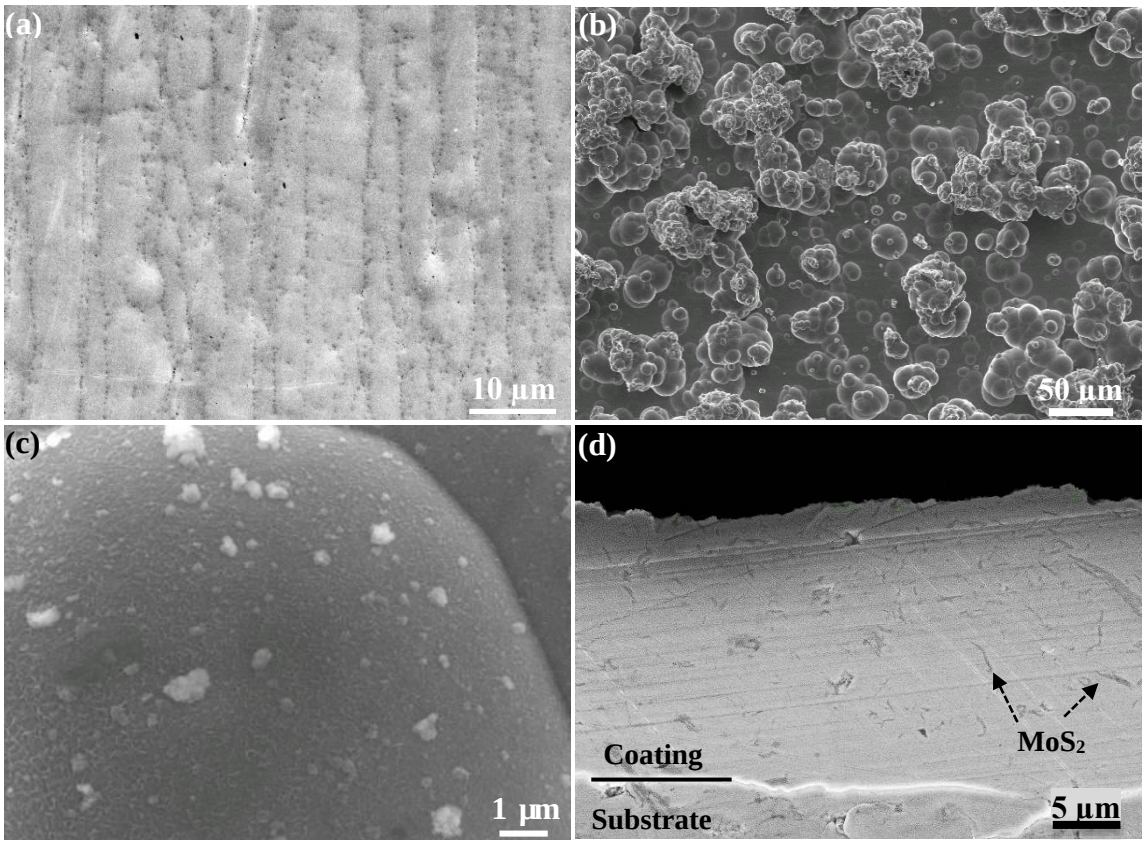

Figure 5.2 (a) SEI image of Ni-P coating; (b) (c) plain view and (d) cross-sectional view SEI images of the Ni-P/MoS_2 coating deposited from electrolyte with 1 g/L MoS_2.

The XRD patterns of the prepared Ni-P/MoS_2 coating display a broad peak of Ni (111) at 45°, as can be seen in Fig. 5.3. By analyzing this peak with the Scherrer Equation, the crystallite size is found be 1.8 nm. This deposit appears to have an amorphous or nanocrystalline structure as amorphous materials still have some short-range order. The remaining peaks at 14°, 32°, 33°, 36°, 39°, 50°, 58° and 60° are in accordance with the standard peaks of the MoS_2 (JCPDS Card number 00-024-0513), and the average crystallite size is calculated to be 70 nm by applying the Scherrer equation to the (002) peak.

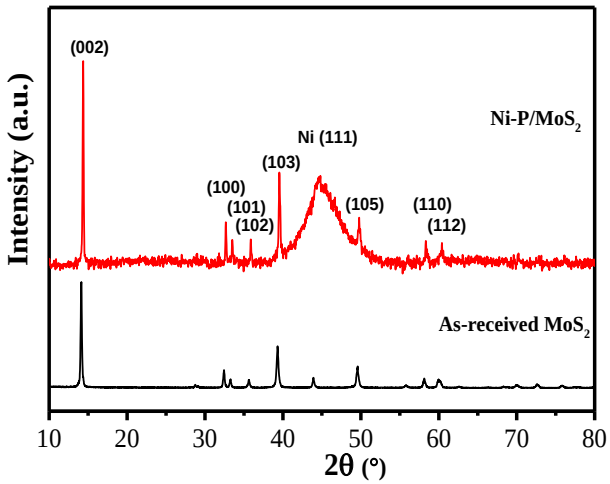

Figure 5.3 X-ray diffraction patterns of as-received MoS_2 particles and Ni-P/MoS_2 composite coating (J = 2.5 A dm^{-2}, C_{MoS2}= 10 g/L).

5.3.2 MoS_2 on the growth of coating

As shown in Fig. 5.2, the pure Ni-P coating has a relatively flat surface while the surface of the Ni-P/MoS_2 composite coating is very coarse. Thus, it is worthwhile to study the effect of MoS_2 on the growth of the coating by examining the composition of the nodule protrusion and base area using EDS.

In Fig. 5.4, spectrum 1 was taken from the dome of the nodule cluster and spectrum 2 was taken from the surrounding flat area. The quantities of Ni, P, Mo and S in these areas were compared. It is clear from the results that there is significantly more molybdenum and sulphur present within the dome than the surrounding area (nearly zero), implying that the MoS_2 particles sparked the growth of the nodule from the relatively flat Ni-P

coating base. This is because Ni atoms are more easily deposited on the top of the adsorbed MoS_2 particles.

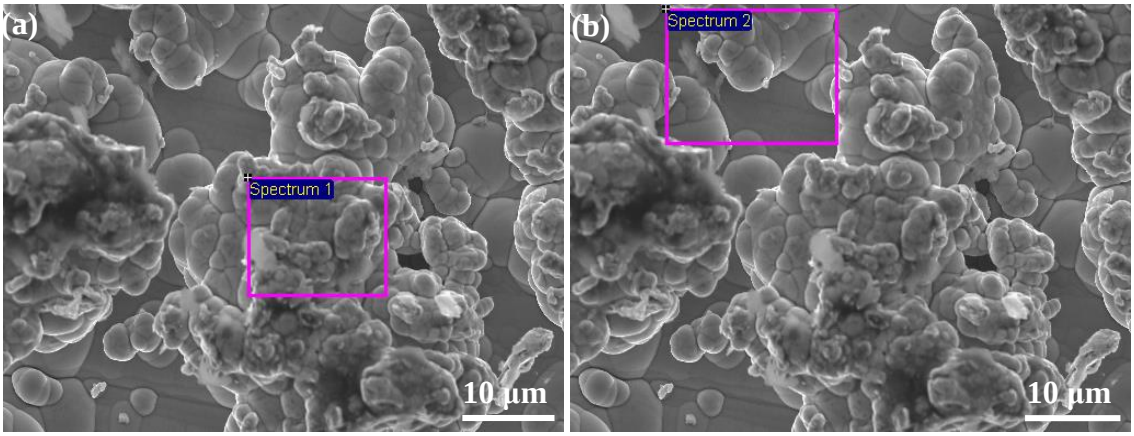

(c)

Spectrum 1		Spectrum 2	
Element	Weight	Element	Weight %
Ni	87.6 ±1.1	Ni	95.1 ±1.2
P	8.8 ±0.7	P	4.5 ±0.6
Mo	2.5 ±0.6	Mo	0
S	1.1 ±0.4	S	0.4 ±0.3

Figure 5.4 (a-b) Plane view SEI images of Ni-P/MoS_2 1 g/L coating; (c) EDS analysis of the nodule and base area in the sample.

5.3.3 Current density

Applied current density greatly affects the structures of composite coatings, including the size, shape and distribution of the deposit. This effect is more significant for a composite electrodeposition bath containing conductive particles like metal particles or semiconductive particles like MoS_2 than composite coatings with inert particles like SiC, as the former two could greatly change the electric field distribution on the electrode surface under high current density [187].

Fig. 5.5 shows that the coating surface contains a network of cracks when the applied current density is 5 A dm^{-2}, becoming wider as the current density increases to 7 A dm^{-2}. This is attributed to the generated internal stress during Ni-P/MoS_2 electrodeposition, exceeding the fracture strength of the deposit. Paseka et al. reported that the internal stress

of Ni-P became higher with increasing current density as the further absorption of hydrogen occurred [188]. In our experiments, the maximum current density for producing a coating without cracks is 2.5 A dm^{-2}. This result is in line with previous reports that the current density of 3 A dm^{-2} produces the minimum internal stress in the Ni-P/SiC deposits and higher current density results in cracks above 4 A dm^{-2} [189].

The P content was obtained by doing EDS examination across the whole area shown in Fig. 5.5. It can be seen from Fig. 5.6 that the phosphorus content in the deposit decreases as the current density increases. P cannot be deposited alone but only by codeposition with iron-group metals, so the reduction speed of phosphorus ions is much slower than that of nickel ions especially at high current density. It has been stated that during Ni-P electrodeposition pure phosphorous can be generated through the following indirect mechanism: (1) $H_2PO_2^- + 2H^+ + e^- \rightarrow P + 2H_2O$; (2) $Ni^{2+} + 2e^- \rightarrow Ni$; (3) $2H^+ + 2e^- \rightarrow H_2$ [190].

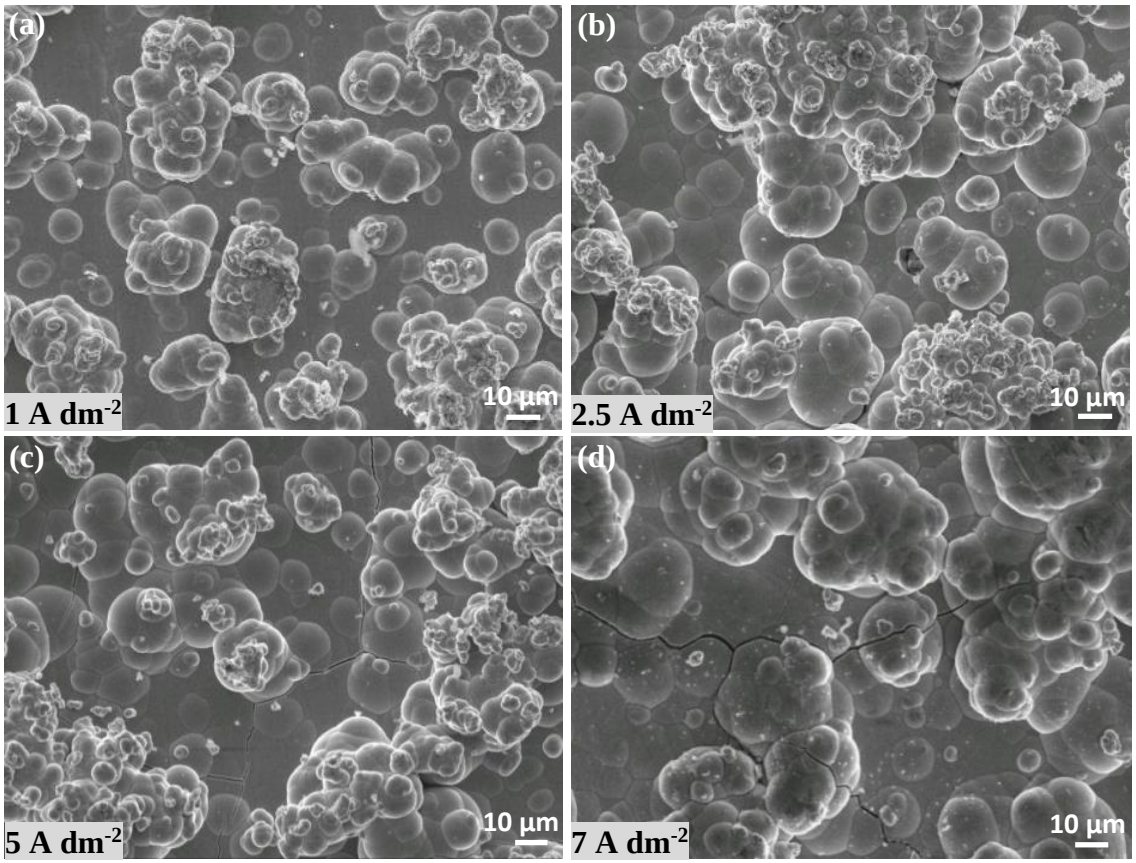

Fig. 5.5 (a-d) SEI images of Ni-P/MoS_2 coatings obtained in the same solution under different current densities as indicated in individual picture (C_{MoS2} = 10 g/L, t = 45 min, C_{CTAB} = 0.1 g/L).

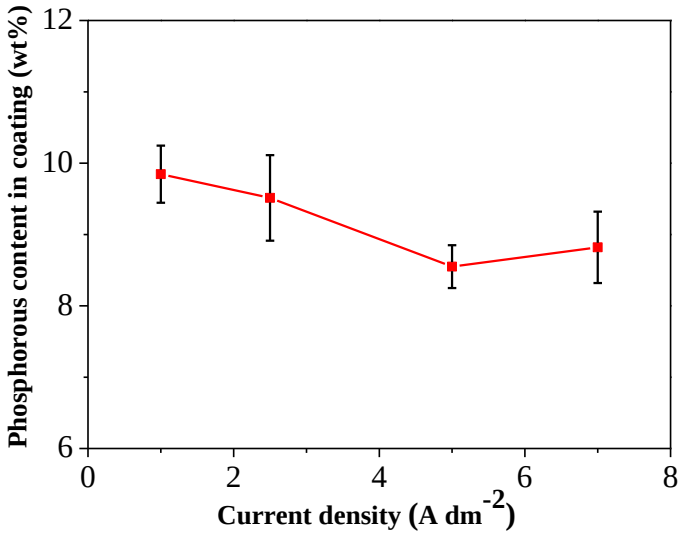

Figure 5.6 Weight percentage of phosphorus in the coating examined by EDS vs. applied current density for electrodeposition.

5.3.4 CTAB concentration

Fig. 5.7 shows SEM images for the composite coatings deposited in the baths with different CTAB concentrations (0.1, 0.2, 0.3 and 0.5 g/L). The composite coatings deposited at 0.1 or 0.2 g/L exhibit relatively flat surfaces with few pores. More holes could be observed by SEM in coatings deposited at 0.3 g/L. At 0.5 g/L CTAB concentration, the coating has large pores as well as nodules. This coating is partially delaminated from the substrate owing to its highly porous structure.

Fig. 5.8(a) shows the content of MoS_2 particles incorporated into the coatings as a function of the concentration of CTAB in the bath. The incorporated MoS_2 content initially increases with the CTAB concentration and reaches a maximum of 11.8 wt% at a concentration of 0.3 g/L. However, a further increase of surfactants resulted in a sharp decrease of particle content in the composite coating. This phenomenon can be explained as follows: at first, all the surfactant will cover the MoS_2 particles. At a certain point, the plating bath becomes saturated with the surfactant so that all MoS_2 particles are fully surrounded by surfactant molecules. Once the surfactant concentration exceeds this level, the CTAB will start to adhere on the cathode and hence hinder the codeposition process of Ni^{2+} and MoS_2, i.e. slowdown the coating rate. In addition, as the MoS_2 particles are much larger than that of Ni^{2+}, the diffusion of MoS_2 particles from solution towards the cathode will be more suppressed than that of Ni^{2+} which leads to very few MoS_2 particles being embedded in the electrodeposited Ni-P matrix.

The phosphorous content remains unchanged as the concentration of surfactant in bath increases from 0.1 g/L to 0.3 g/L, as illustrated in Fig. 5.8(b). However, when the surfactant reaches 0.5g/L, the P content in the coating drops considerably. This is also related to the hindrance effect of CTAB on the deposition process after the saturate concentration is reached, producing large amounts of hydrogen and changing the pH value near the electrode surface. As the complex reaction of $H_2PO_2^-$ to P occurs just in a limited pH range around 4, the content of electrodeposited P decreases a lot.

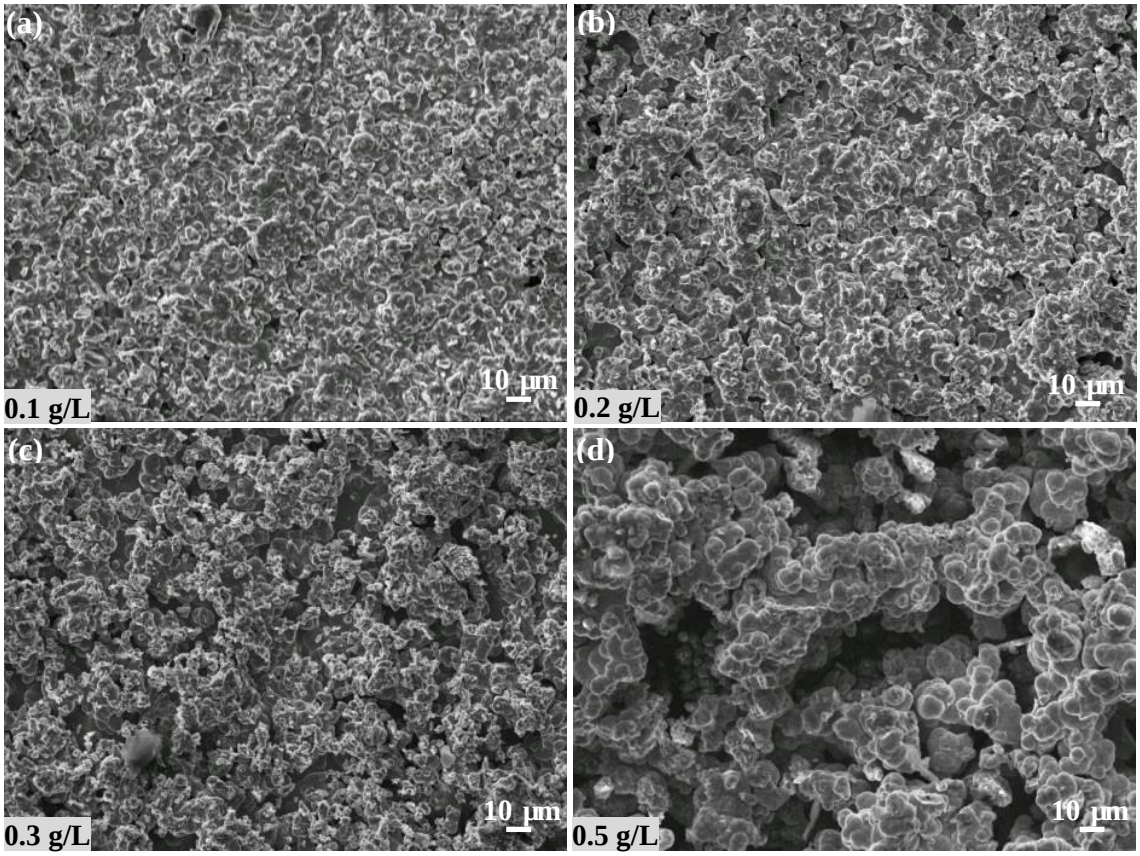

Figure 5.7 (a-d) SEI images of Ni-P/MoS_2 coatings deposited from solutions with different CTAB concentrations (as indicated in individual picture) (C_{MoS2} = 10 g/L, t = 45 min, J = 2.5 A dm^{-2}).

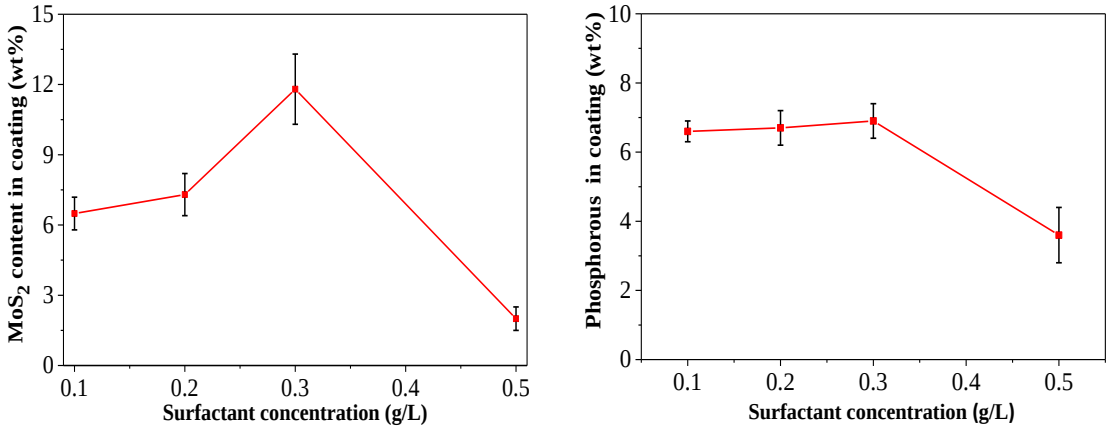

Figure 5.8 Weight percentage of (a) MoS_2 and (b) phosphorus in the coating vs. the CTAB concentration in bath.

5.3.5 Particle concentration

It is widely thought that very rough coatings cannot withstand high load pressures and hence will wear out fast during friction service conditions. A systematic study of coating parameters has therefore been carried out to reduce the surface roughness, including adjustment of current density, CTAB and particle concentration.

The concentration of the MoS_2 in the electroplating bath was found to have the most significant impact on the coating roughness and the content of incorporated particles in the coating. The coating morphologies of coatings deposited at different particle concentrations are shown in Fig. 5.9 (a, c, e, g, i). The composite coatings deposited with up to 3 g/L of MoS_2 exhibit rough surfaces with some high nodules. Further increase of the MoS_2 concentration in the electrolyte leads to refinement in the microstructure.

The 3D surface reconstructions with a pixel size of 0.2 μm are shown in Fig. 5.9 (b, d, f, h, and j). The red/pink colours represent the large peaks and troughs, which can be seen clearly on the particle concentrations of both 1 to 3 g/L. Further increase of particle concentration shows a small colour contrast, suggesting a nearly flat surface. However, electrolyte viscidity and serious coacervation of the particles are increased when the particle concentration reaches 20 g/L in the electrolyte, which is unfavorable to achieve further refinement in the structure.

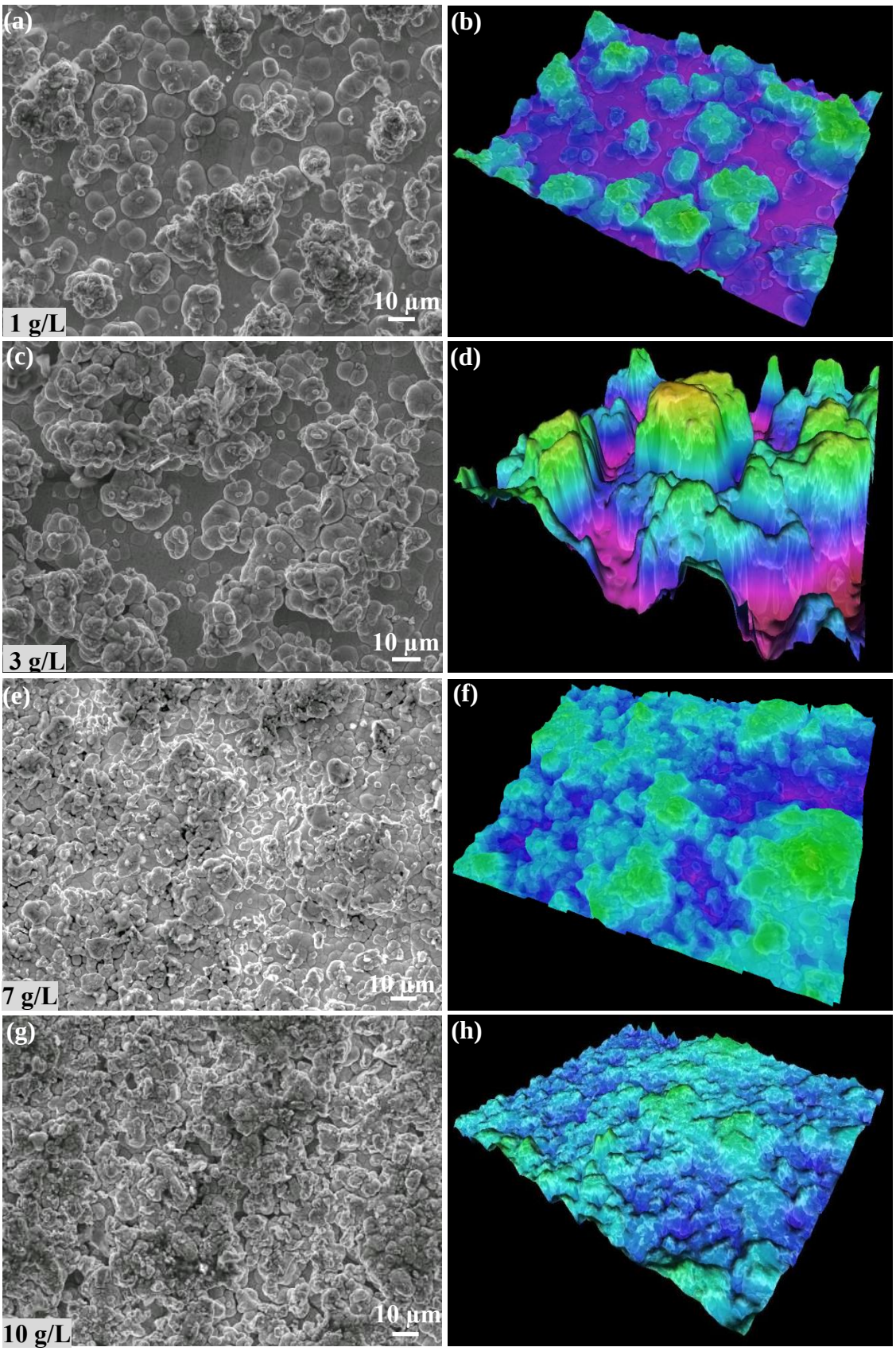
(a)
10 µm
1 g/L
(b)
(c)
10 µm
3 g/L
(d)
(e)
10 µm
7 g/L
(f)
(g)
10 µm
10 g/L
(h)

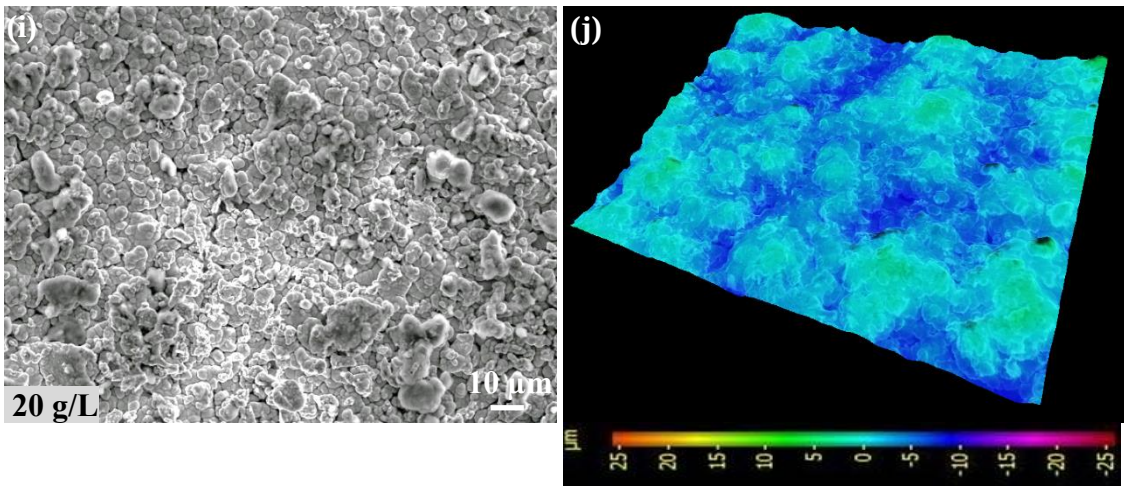

Figure 5.9 (a, c, e, g, i) SEI images and (b, d, f, h, j) 3D surface reconstructions of the Ni-P/MoS_2 composite coatings obtained in the solution with different MoS_2 concentrations as indicated separately in figures (C_{CTAB} = 0.1 g/L, t = 45 min, J = 2.5 A dm^{-2}).

Surface area roughness (S_a) of composite coatings was also measured using MeX software and listed in Fig. 5.10. The roughness value increases as the concentration of MoS_2 increases from 1 to 3 g/L in the plating baths, because the sites of the particle clusters will be increased on the cathode and disturb the uniform current distribution on the solution/cathode interface. Ni-P is preferably deposited on the top of these particles, creating more and more nodules, hence the larger *Sa* value. Once the concentration is high enough, as it is at 7 g/L, the nodules induced by a large number of particles will collide with each other at the early stage of deposition to form a new flat platform rather than growing up. Thus, the roughness is reduced.

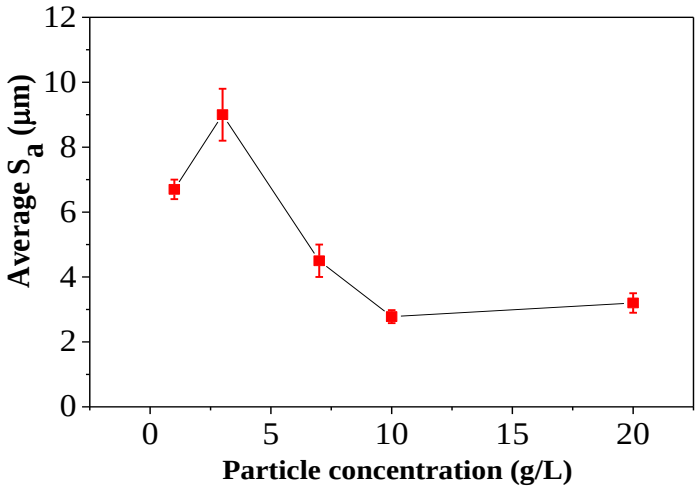

Figure 5.10 Relationship between surface area roughness (S_a) and MoS_2 concentration in solution at a current density of 2.5 A dm^{-2} (C_{CTAB} = 0.1 g/L, t = 45 min).

The embedded MoS_2 particles appear as a greyer colour in a BSE image. Observations of the cross-sectional BSE images of Ni-P/MoS_2 composite coatings (Fig. 5.11) confirm that

the content of the MoS_2 particles in the composite coatings increased substantially as the particle loading in the plating solution increases from 1 to 10 g/L but was almost unchanged with a further increase of the particle concentration to 20 g/L. Moreover, the agglomeration of MoS_2 particles is clearly seen in the Ni-P/MoS_2 20 g/L composite coating. The elongated particles are attributed to the deformation of MoS_2 during the polishing process.

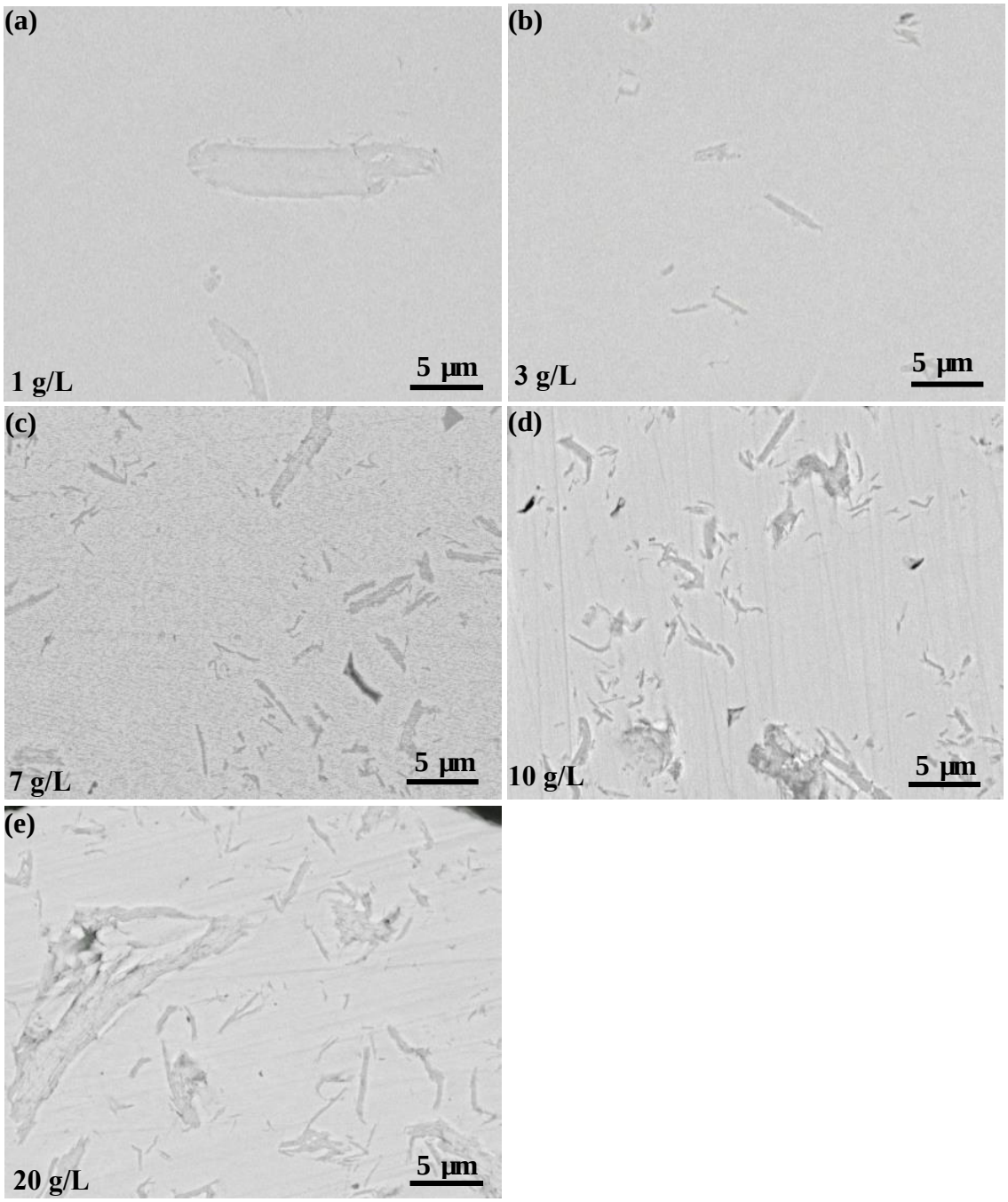

Figure 5.11 (a-e) Cross-sectional BSE images of Ni-P/MoS_2 coatings obtained in the solutions with different MoS_2 concentrations as indicated in individual picture (C_{CTAB} = 0.1 g/L, t = 45 min).

Fig. 5.12(a) shows the content of incorporated particles in the deposits versus the concentration of particles in the bath. Upon increasing the amount of particles dispersed in the bath to 10 g/L, the fraction of incorporated particles greatly increases from 1.2 wt% to 7.9 wt%. These results could be explained by Guglielmi's two-step adsorption model where a higher particle concentration in the plating bath increases the adsorption of particles, thus resulting in a higher incorporation percentage [191]. However, no obvious change can be found for the particle content in deposits when the particle concentration in the bath goes up to 20 g/L, as aggregation phenomena may be present in the bath at over saturation concentration. It has been suggested that the maximum concentration of suspended particles in the electroplating solution is limited by the content of surfactant [192]. Fig. 5.12(b) shows a gradual decrease in the content of phosphorous in the coatings as the particle concentration in the bath increases, which is partly associated with the increasing weight percentage of incorporated particles in the coating. On the other hand, the increasing presence of MoS_2 particles will restrict phosphorus production due to enhanced adsorption of H^+ on the surface of particles [193].

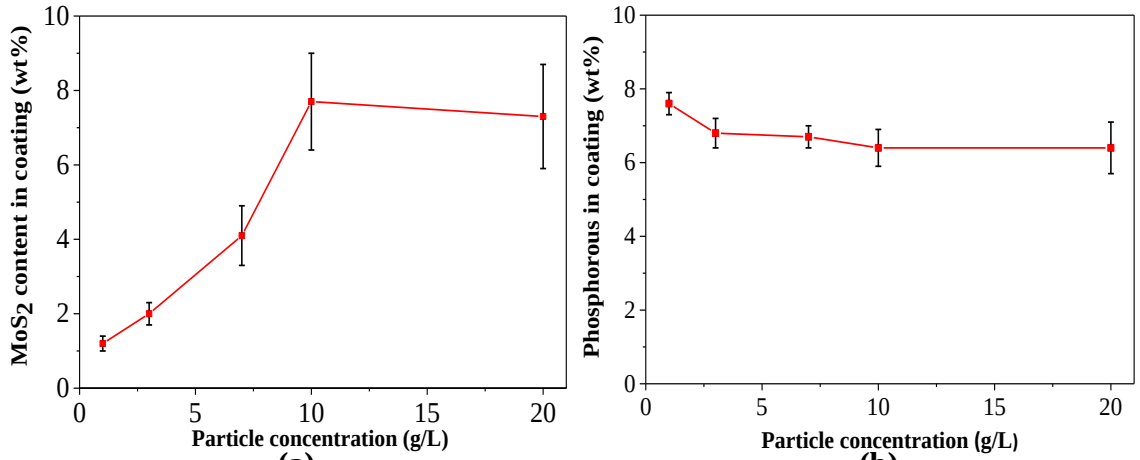

Figure 5.12 Weight percentage of MoS_2 (a) and phosphorus (b) in the coating vs. the particle concentration in bath.

The XRD patterns of the Ni-P/MoS_2 coatings are illustrated in Fig. 5.13. A broad peak around 45 ° appears for all coatings, which is attributed to (111) of the Ni phase. A small Ni (220) peak at 76 ° existed in the Ni-P coating but disappeared for the Ni-P/MoS_2 coatings. The predominant (111) plane in all deposits was associated with low surface energy during electrodeposition [194].

The crystallite size of the Ni-P phase was estimated by applying the Scherrer equation to the diffraction line of Ni (111) and the broad maximum of amorphous-like phase. The

calculated crystallite size is 2.7 nm for Ni-P coating. Comparably, the crystallite size decreases to 1.8 nm for the coatings with MoS_2 addition regardless of MoS_2 concentration. The refinement is ascribed to the adsorption of nanoparticles on the cathode which act as nucleation sites for Ni deposition and increase the nucleation rate of Ni [195,196]. On the other hand, the particles increase the charge-transfer resistance of electroplating processes and therefore cause higher cathodic potential which is preferred in crystalline refinement. The peaks located at 14 °, 33 °, 36 °, 39 ° and 50 ° are consistent with the standard peaks of the hexagonal MoS_2 (JCPDS Card number 00-024-0513). Clearly, higher contents of MoS_2 particles were indicated where the stronger XRD peaks appeared.

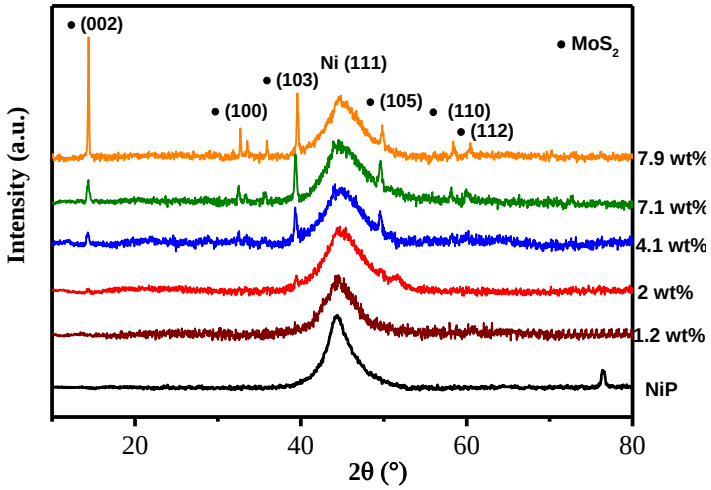

Figure 5.13 X-ray diffraction patterns of Ni-P and different Ni-P/MoS_2 coatings obtained in the solution with different MoS_2 concentrations.

5.3.6 Microhardness test

The Vickers hardness test was conducted using a diamond tip micro-indenter and the hardness value was calculated from indentation using the relevant formula specified in the experimental methodology. However, due to the rough surface of the samples, it was hard to get defined indentation marks. Thus indentation was carried out on the cross-section of the coatings to acquire the hardness data accurately. As shown in Fig. 5.14, all Ni-P/MoS_2 coatings possess improved hardness in a range of 605 to 627 HV compared to the Ni-P coating at 530 ± 60 HV. The hardness increase of the composite coating is attributed to the decreased crystallize sizes from 2.7 nm to 1.8 nm (Fig. 5.10) as the increase in grain boundary area could reduce dislocation mobility [171,197]. However, there is no obvious change of hardness among the different Ni-P/MoS_2 composite coatings.

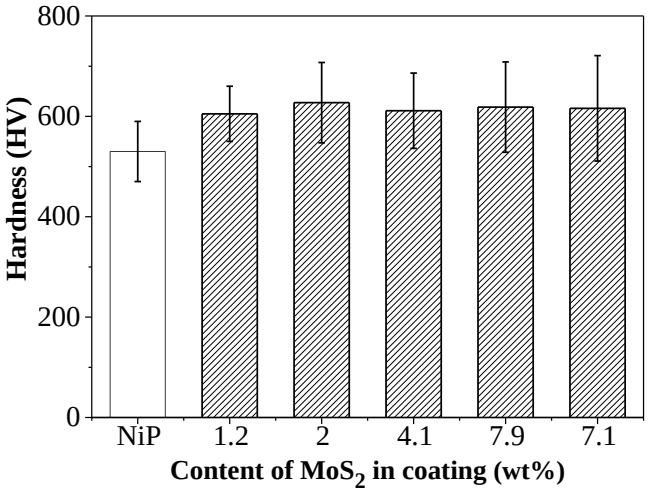

Figure 5.14 Relationship between Vickers hardness and MoS_2 particle content in coating.

5.3.7 Heat treatment

The evolution of the X-ray diffractograms with the annealing temperature for Ni-P/MoS_2 sample is illustrated in Fig. 5.15. After heat treatment at 300 ℃ the sample presents similar X-ray diffraction patterns to the as-deposited case although with higher intensity and narrower peak width. This indicates the crystal growth of the Ni crystallites. Ni_3P phases appeared during the one hour of annealing at 400 ℃ [198]. The further heat treatment at 500 ℃ resulted in narrower XRD peaks for Ni-P and Ni_3P, indicating the increase of crystallite size. No obvious change can be found in the Ni_3P phase when the sample was annealed at 600 ℃, however, the oxide NiO with peaks at 38 °, 43 ° and 62.5 ° appeared in the XRD diffractogram. The results are in close agreement with those obtained for electrodeposited Ni-P and sputtered Ni-Cr-P-coated samples [196,199,200,201].

The crystallite size was calculated from the XRD peak at 44.5 ° using the Scherrer equation. Fig. 5.16 shows that the crystallite size of the Ni phase increases significantly after heat treatment. The initial coating has a very small crystallite size of 2.0 nm, which was increased to 12 nm, 29 nm, and 59 nm respectively after heat treatment at 300 ℃, 400 ℃ and 500 ℃. The average crystallite size didn't increase further after heat treatment at 600 ℃.

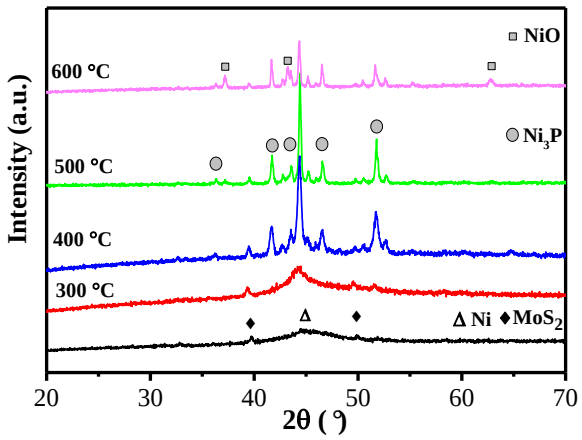

Figure 5.15 X-ray diffraction patterns of Ni-P/MoS_2 coating after 1 h heat treatment in air at different temperatures: 300 ºC, 400 ºC, 500 ºC, 600 ºC.

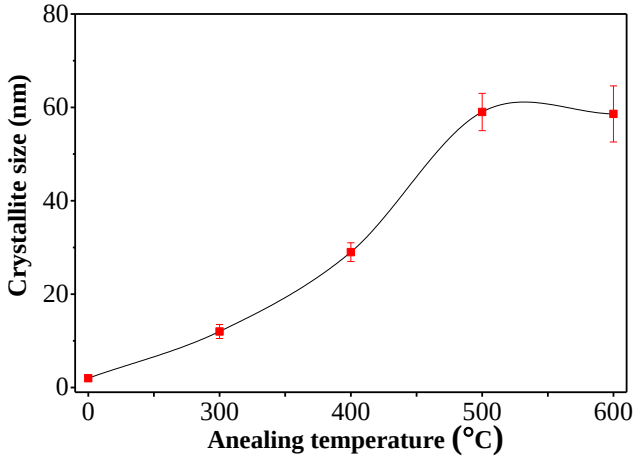

Figure 5.16 Change of the crystallite size of coating after 1 h heat treatment at different temperatures: 300 ºC, 400 ºC, 500 ºC, 600 ºC.

The annealing temperature also has a prominent effect on the hardness of the Ni-P/MoS_2 composite coatings. As can be observed in Fig. 5.17, heat treatment at 200 ℃ doesn't cause noticeable variation in hardness. There is a rapid increase of hardness from annealing at 300 ℃ due to the precipitation of Ni_3P based on the XRD results. Heat treatment at 400 ℃ leads to the maximum Vickers microhardness at 1150 ±120 HV. This improvement is attributed to the formation of the Ni_3P crystals, which are widely distributed and induce precipitation hardening [202]. The precipitation hardening has also been reported in the literature such as Ni-P/WC_2, Ni-P/SiC_2 [203,204,205]. The hardness starts to decrease when heat-treated at 500 ℃ as Ni_3P crystals grow. After annealing the coating at 600 ℃, the surface oxidation phenomena, verified by EDS and XRD analysis, led to a small drop of Vickers microhardness due to the formation of Ni oxide.

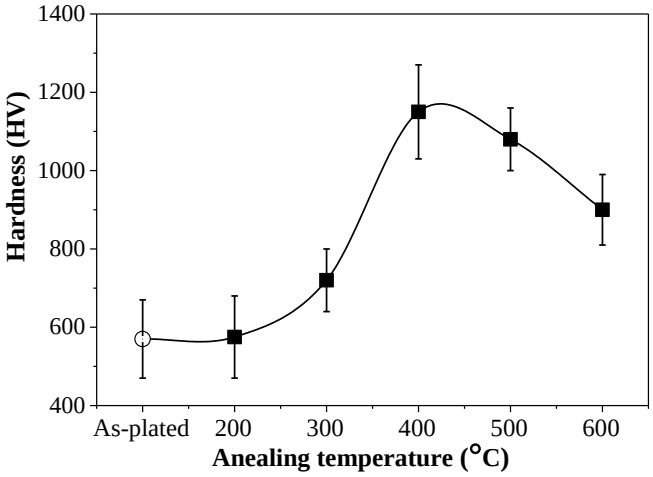

Figure 5.17 Change of the microhardness of the Ni-P/MoS_2 coatings as a function of annealing temperature.

5.4 Discussion

5.4.1 Effect of particles on the growth of the coating

In Section 5.3.2, it has been argued that the MoS_2 particles enhance the growth of nodules from the metal matrix, resulting in a rough surface. It is important to elucidate further the electrodeposition mechanism of the Ni-P/MoS_2 composite coatings.

It is well known that, during metal or alloy electrodeposition, the distribution of current over the smooth surface of electrodes is uniform, thereby all the metal ions moving in the electrolytic solution are subject to the same effect of the Coulomb force E^*q_t (E represents the electric field, q_t represents the charge of ions) [206, 207]. The deposition rate remains constant at the different sites on the substrate, therefore a homogenous coating is expected to be produced. However, the situation was different for composite electrodeposition of Ni-P/MoS_2. The change is directly related to the non-uniform distribution of current on the electrode surface with adsorbed particles. When conductive or semi-conductive particles were added into the electrolytic solution, the electrolytic current concentrated in the vicinity of particles on the cathode (bigger E) as illustrated in Fig. 5.18. In consequence, the ions in solution move at higher velocity υ towards these tip points due to the bigger Coulomb force E^*q_t, speeding up the crystal growth at these locations and creating many deposit protrusions on the surface. This mechanism fits the Ni-P/MoS_2 electrodeposition system quite well. As a result, a rough surface was obtained for the Ni-P/MoS_2 coating while the Ni-P displayed a flat surface.

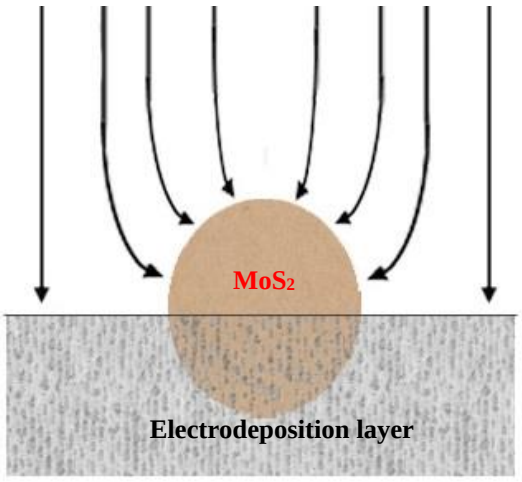

Figure 5.18 Schematic showing current distribution on the electrode in composite electrodeposition.

5.4.2 MoS_2 content in the Ni-P/MoS_2 composites

MoS_2 in the Ni-P/MoS_2 composites plays a critical role in improving the properties of the composite coating. Therefore, it is worthwhile to investigate the factors influencing the incorporation percentages (wt%) of MoS_2 particles in Ni-P, including the CTAB additive and MoS_2 particle concentration. CTAB is advantageous to the codeposition of MoS_2. Wang [19] has proposed that positive ions in CTAB tend to be absorbed on the MoS_2 particle surface causing electrostatic attraction to the cathode. Similar results are found in the Ni-P/MoS_2 electrodeposition system. Without CTAB, MoS_2 particles are scarcely embedded into the Ni-P coating. The content of MoS_2 in the coating increases as the amount of CTAB in solution increases.

The MoS_2 content in the coating is also related with the MoS_2 concentration in the bath. According to the Gugliemi's two step adsorption model [191], the codeposition particle will go through two consecutive adsorption stages: In the first step, particles reaching the electrode surface are loosely attached, and are covered by adsorbed ions and solvent molecules on the electrode surface. During the second step, the particles become strongly adsorbed onto the electrode due to the applied electrical field, and are incorporated into the growing metal coating. This first loose adsorption step is easily influenced by the particle concentration in the bulk electrolyte. The EDS results in Fig 5.12 clearly illustrate that the content of MoS_2 particles in the coating increases substantially as the particle concentration in the bath increases from 1 to 10 g/L in good agreement with this model. A similar result was also observed by Wu et al. for Co-Ni/Al_2O_3 [208]. No obvious change was found for the MoS_2 content in the coating with further increases in the MoS_2 solution

concentration to 20 g/L, which could be attributed to the particles' saturation adsorbed on the cathode surface.

5.5 Summary

- Ni-P/MoS_2 composite coating has been successfully produced by direct current electrodeposition from an aqueous bath. Due to the semi-conductor nature of the MoS_2 particles, the as-deposited coating shows a markedly rough surface with many nodule protrusions. XRD results reveal that the composite coating has an amorphous or nanocrystalline structure.

- The current density used in the electrodeposition process should be lower than 5 A dm^{-2}, otherwise cracks will form in the coating because of the high internal stress caused by a high current.

- During the electrodeposition, the number of particles incorporated into coatings mainly depend on the concentrations of surfactant and particle loading in the bath. The addition of CTAB is effective to incorporate particles into the coating, however, a higher CTAB concentration over 0.2 g/L resulted in a porous structure. As the MoS_2 concentration in bath increases, the particle content in the electrodeposited coating first increased rapidly and then remained constant (ca. 7.5wt% MoS_2) for the bath of MoS_2 concentration exceeding 10 g/L.

- The Ni-P/MoS_2 composite coatings show higher hardness than the substrate and the Ni-P coating, ranging from 605 HV to 627 HV. The variation of the MoS_2 content in composite coatings doesn't exhibit an obvious direct effect on the hardness of Ni-P/MoS_2. Heat treatment results in a significant improvement in hardness. The hardness reached as high as 1150 HV after calcination at 400 ℃ for 1 hour, which was attributed to the precipitation hardening from Ni_3P.

Chapter 6 Friction and wear properties of the electrodeposited Ni-P/MoS_2 coatings

6.1 Introduction

MoS_2 solid lubricant has been successfully electrodeposited with Ni-P in the previous chapter. Examination of its friction behaviour, wear resistance and oxidation is crucial in assessing its deployment in potential applications. It is also important for a better understanding of the low friction behaviour of MoS_2-containing coatings which could be used as self-lubricating coatings. The cross section of the wear track was sectioned by a focused ion beam (FIB) and observed under TEM to study the MoS_2 deformation modes during wear.

6.2 Experimental details

A reciprocating TE-77 tribometer (Phoenix, UK) was used to evaluate the friction behaviour in air with a relative humidity of 50% at 25 ℃. The counterpart body was an AISI-52100 bearing steel ball (diameter 6 mm) with a hardness of 700 HV. The tests were done under the following condition: a load of 14 N (initial Hertzian contact pressure of 1.58 GPa), a sliding frequency of 1 Hz and a sliding stroke of 2.69 mm. The frictional force was recorded automatically by a piezoelectric transducer.

6.3 Results

6.3.1 Friction coefficient

Wear testing was carried out on the Ni-P/MoS_2 coatings deposited at different MoS_2 concentrations (Section 5.3.5). Fig. 6.1 shows the friction coefficients against time for the substrate (AISI 52100), Ni-P, and Ni-P/MoS_2 composite coatings. The friction coefficient of the mild steel substrate increases gradually and afterwards stays around 0.6 during the remaining test time. The pure Ni-P coating produced has a friction coefficient slightly

lower than the substrate, fluctuating but relatively stable at 0.45 for the majority of the test duration.

In contrast, the friction coefficients of all composite coatings are distinctly lower. For the Ni-P/MoS_2 1.2 wt% coating, the coefficient of friction started low at 0.1 but increased sharply to 0.5 and fluctuated with time. The friction coefficient of the 2.0 wt% MoS_2 coating started at 0.1 and slowly increased to 0.3. With the increase of MoS_2 (4.1 wt% and 7.1 wt%) in the coatings, the coefficients of friction started from 0.05 and increased gradually with the testing time. The 7.9 wt% MoS_2 composite coating exhibits a steady low friction coefficient of 0.05 with time. In order to test the durability of this coating, a 1-hour reciprocating test was carried out, which demonstrated a low constant friction coefficient without any sign of being broken down.

These results confirm that the addition of solid lubricant to the electrolyte effectively reduces the friction of the resultant Ni-P coating. The more MoS_2 incorporated in the coating the lower the friction coefficient that can be obtained. It appears that the Ni-P/MoS_2 7.9 wt% coating, deposited from the concentration of 10 g/L MoS_2 in the solution, has sufficient solid lubricant to form a complete tribofilm and accordingly achieved the lowest friction rate.

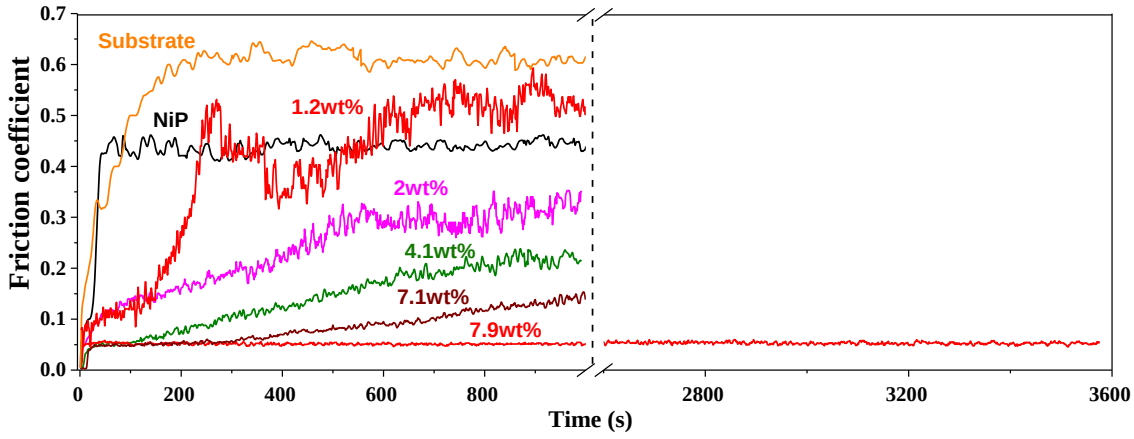

Figure 6.1 Relationship between friction coefficient and time for different sliding against bearing steel ball (C_{CTAB} = 0.1 g/L, J = 2.5 A dm^{-2}, t = 45 min).

6.3.2 Wear track analysis

After 1000 s wear test, the morphology of wear tracks on the substrate was checked under SEM and displayed in Fig. 6.2. Deep grooves and delamination were observed in the wear

track of the steel substrate. The substrate (mild steel) was soft so ploughing occurred, causing deep grooves. Repeated displacement of material caused small voids near the surface through fatigue; eventually these voids grow and converge to form large wear debris. Due to the relatively high coefficient of friction the interface temperature would rise, soften the surface of the substrate and increase the adhesive strength of the contact points. This ultimately resulted in severe adhesive wear.

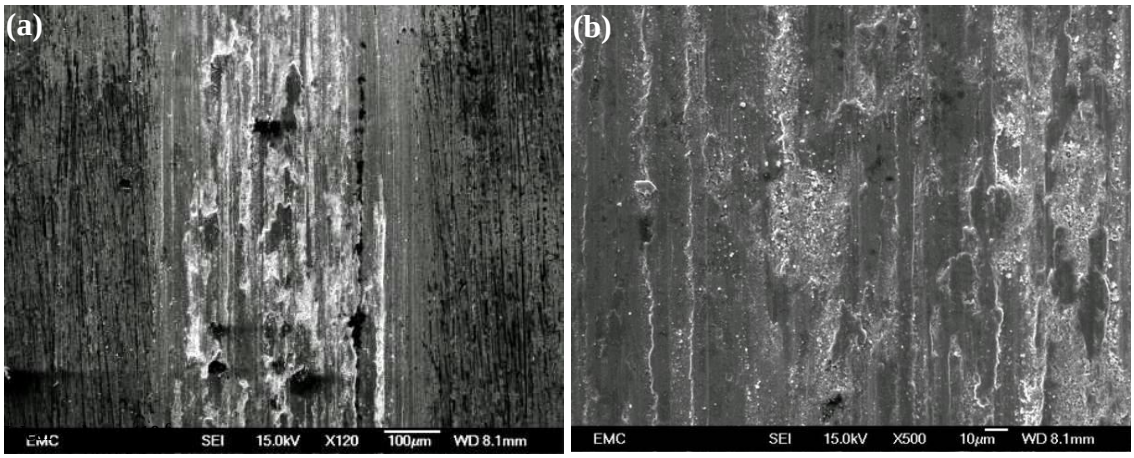

Figure 6.2 Morphology of the wear track on mild steel substrate at different magnifications.

In comparison, only fine grooves and scars with shallow depth were found on the wear track of Ni-P, parallel to the sliding direction (Fig. 6.3). Adhesive wear is defined as the transfer of material from one surface to the other which may later be removed as wear debris [209]. Several factors such as hardness, degree of solubility of the interacting surfaces and the rate of formation of surface oxide film could influence the rate of adhesive wear [210]. As the Ni-P and the chrome steel ball have lower mutual solubility than the pairing of mild steel substrate and chrome steel ball, the adhesive wear on the Ni-P coating is much slighter than that observed on the substrate. In addition, the improved hardness of the Ni-P coating compared to the substrate also plays a role in the mild wear and improved wear resistance behaviour. The wear track exhibits an oxygen content of 11.3 wt%, suggesting the occurrence of oxidation.

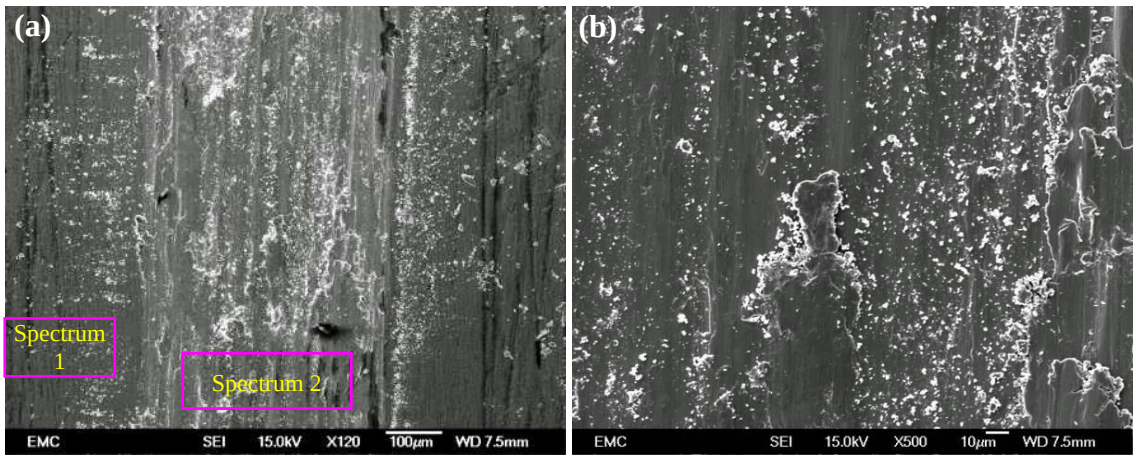

(c)

Element (Weight%)	Spectrum 1	Spectrum 2
O K	1.7 ±0.4	11.3±0.6
P K	9.4 ±1.0	8.6 ±0.9
Fe K	0	2.3 ±1.0
Ni K	88.9 ±1.6	77.8 ±2.1

Figure 6.3 (a,b) Morphology of the wear track on Ni-P coating after 1000s test at different magnifications, (c) EDS comparison of coating and wear track.

The wear track on the Ni-P/MoS_2 1.2 wt% coating was examined after 100 s friction test, as shown in Fig. 6.4(a). This is called the "run-in" stage (polishing) of the friction process for the composite coating. On the outer edges of the track, the worn surface is very smooth. The high contact stress combined with shear stress from the movement of the pin would cause the nodules in the coating to be crushed and cut. The debris particles, generated from nodules with richer MoS_2, traveled reciprocally in the contact zone where they effectively formed a lubricating transfer film contributing to the low coefficient of friction. At the center of the wear track, the surface appears slightly rougher where there is a higher level of deformation under the contact stress of the pin due to its spherical shape.

As shown in Fig. 6.4(b), delamination grooves appear in the coating after the 1000s test. The breakup corresponds to the sharp rise of the friction coefficient seen in Fig. 6.1. Due to the existence of nodules, the shear and contact stress is higher than the smooth Ni-P coating. Cracks thus formed in the surface, propagated and eventually converged to form a large hole in the coating. The further wear mechanisms observed here were associated

with the mild steel (substrate) on the bearing steel (pin) contact. Thus, it caused a high coefficient of friction.

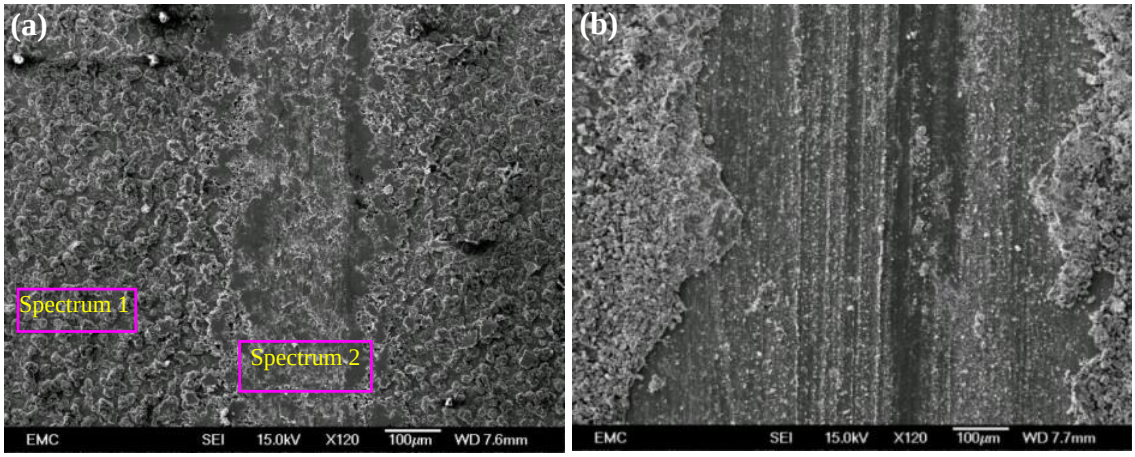

(c)

Element (Weight%)	Spectrum 1	Spectrum 2
O K	2.8 ±0.2	4.2 ±0.5
P K	8.4 ±1.0	9.8 ±0.7
S K	0.3 ±0.3	1.2 ±0.4
Ni K	87.8 ±0.8	82.4 ±1.1
Mo L	0.9 ±0.7	2.4 ±0.7

Figure 6.4 Wear tracks of 1.2 wt% MoS_2 sample tested after (a) 100 s and (b) 1000 s, (c) EDS comparison of coating and wear track.

As shown in Fig. 6.5, the wear track of 2.0 wt% MoS_2 sample had fewer scratches across its width. With the increasing amount of lubricant, more dark patches were observed and were identified as a MoS_2 rich tribofilm. After the 1000s friction test, a complete polishing tribofilm was formed. The compositions of the wear track were investigated using EDS. It shows high levels of oxygen, indicating oxidation occurred on the coating during the test. The MoS_2 concentration accumulated on the wear track with a higher percentage than the remaining area. The dominating oxides, which may include MoO and NiO, should be the factor explaining the relative higher coefficient of friction (0.3).

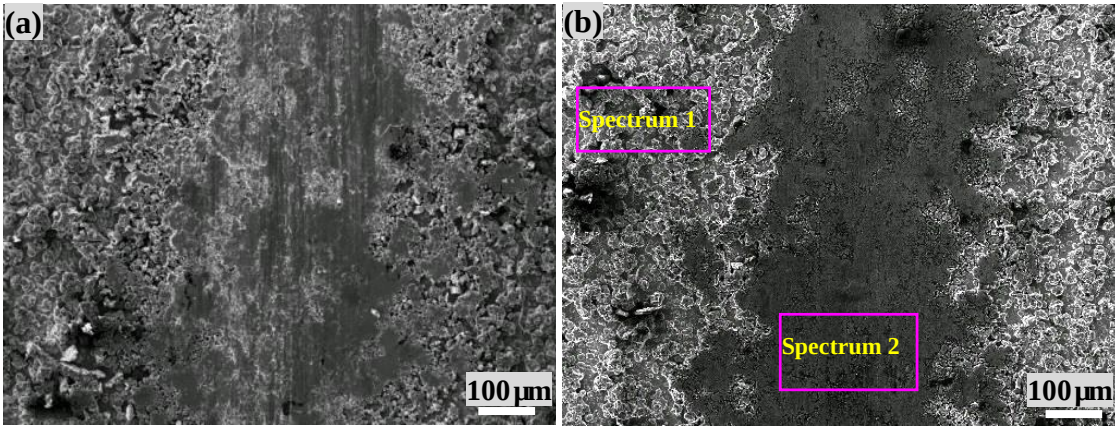

(c)

Element (Weight%)	Spectrum1	Spectrum 3
O K	3.4 ±0.3	10.9 ±0.5
P K	6.7 ±0.7	7.6 ±0.6
S K	0.6 ±0.5	1.8 ±0.8
Ni K	87.8 ±1.5	75.1 ±2.2
Mo L	1.4 ±0.6	2.6 ±0.3

Figure 6.5 Wear tracks of 2 wt% MoS_2 sample tested after (a) 100 s and (b) 1000 s, (c) EDS comparison of coating and wear track.

The high concentration of MoS_2 particles in the Ni-P/MoS_2 4.1 wt% coating led to a relatively flat surface as shown in Fig. 6.6. The shallow tribofilm layer maintained very well during the 1000 s test. By comparing the EDS spectra of coating and wear track, it was noticed that the MoS_2 suffered less oxidation in the tribofilm and hence provided low coefficients of friction.

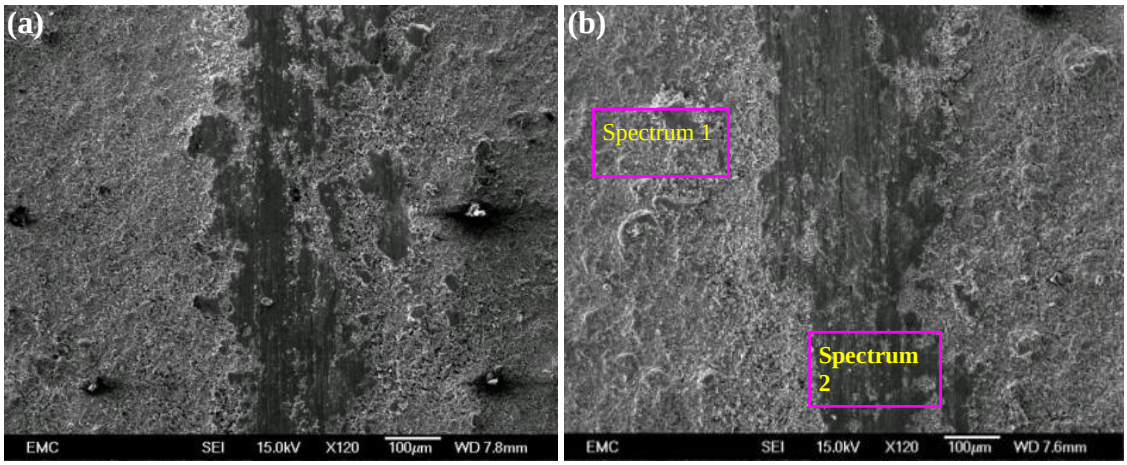

(c)

Element (Weight%)	Spectrum 1	Spectrum 2
O K	2.2 ±0.7	4.3 ±0.8
P K	6.2 ±0.6	7.0 ±0.2
S K	1.3 ±0.3	3.1 ±0.6
Ni K	87.5 ±1.8	81.1 ±0.5
Mo L	2.8 ±0.9	4.5 ±0.2

Figure 6.6 Wear tracks of 4.1 wt% MoS_2 sample tested after (a) 100 s and (b) 1000 s, (c) EDS comparison of coating and wear track.

The 7.1 wt% MoS_2 coating only shows slight wear. After 100 s the wear track in Fig. 6.7(a) shows that the pin specimen were in contact only with the top areas on the surface. The wear track grew and connected after 1000 s with more material worn away.

As expected the 7.9 wt% sample shows the least wear damage. After 100 s the wear track in Fig. 6.8(a) is very narrow and the gaps between the smooth areas indicate that the pin specimen is in contact only with the top areas of the surface, suggesting the excellent support ability of this coating to load. After 1000 s the wear track grows very little in width but clearly has worn away more material. The EDS test illustrates that no oxygen increase could be found on the wear track after 1000 s test, indicating there was no heating up of the coating during the wear test to cause the metals Mo/Ni oxidation. Accordingly MoS_2 can be protected from oxidation.

Overall, the above results demonstrate that the embedded MoS_2 particles in the matrix could reduce friction coefficient and improve wear resistance by forming a MoS_2

lubricating layer on the sliding interface. Good load-bearing ability was found on the 7.1 wt% and 7.9 wt% MoS_2 samples. Oxides could be formed as the tribofilm in the low MoS_2 containing coatings due to heating up by wear. Other MoS_2 based coatings like Ti-MoS_2 or Mo-MoS_2 have also been reported to provide high load-bearing capacity [136,211].

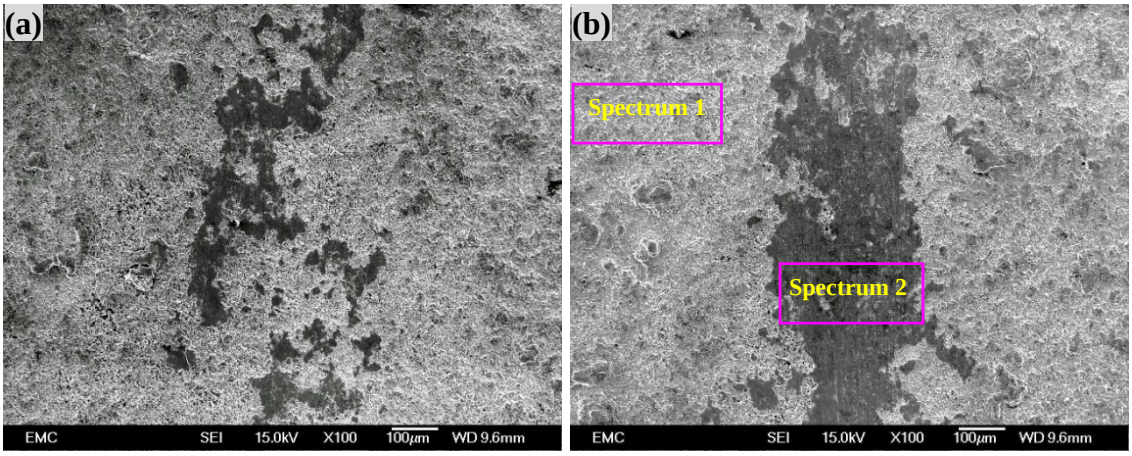

(c)

Element (Weight%)	Spectrum 1	Spectrum 2
O K	2.6 ±0.5	4.1 ±0.6
P K	6.5 ±0.4	7.0 ±0.5
S K	2.8 ±0.3	3.6 ±0.2
Ni K	83.8 ±1.7	79.8 ±1.1
Mo L	4.3 ±0.5	5.5 ±0.3

Figure 6.7 Wear tracks of 7.1 wt% MoS_2 sample tested after (a) 100 s and (b) 1000 s.

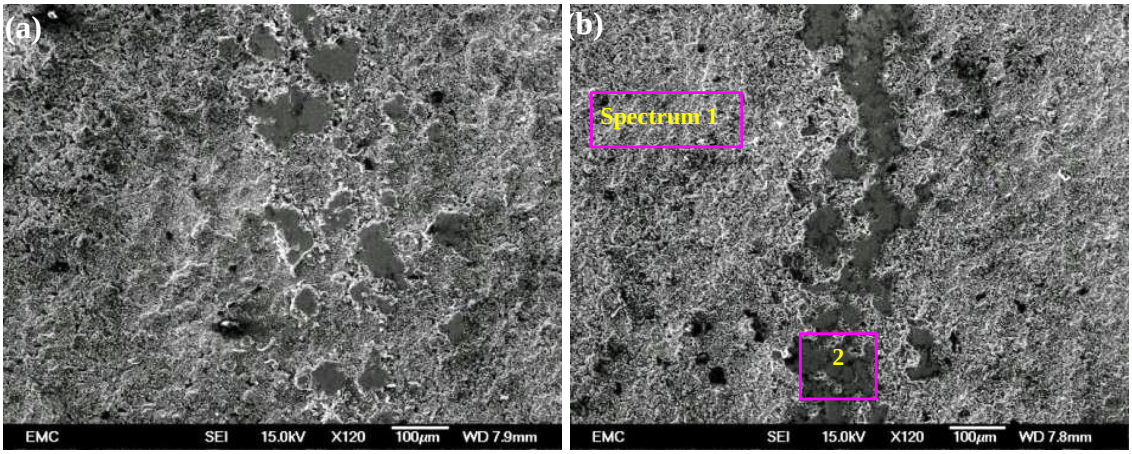

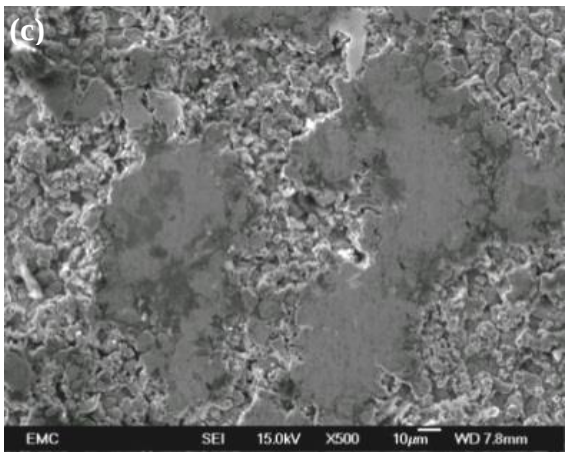

(d)

Element (Weight%)	Spectrum 1	Spectrum 2
O K	3.2 ±0.5	3.8 ±0.4
P K	6.1 ±0.8	5.4 ±0.7
S K	3.1 ±0.6	4.1 ±0.3
Ni K	82.8 ±1.5	79.1 ±1.6
Mo L	4.8 ±0.6	7.6 ±0.4

Figure 6.8 Wear tracks of 7.9 wt% MoS_2 sample tested after (a) 100 s and (b) 1000 s; (c) morphology of wear track at high magnification, (d) EDS comparison of coating and wear track.

Wear track width was also measured for composite coatings, which could indicate the wear resistance of the composite coatings. After 100 s the wear track width is very small for all composite coatings and the gaps between the smooth areas indicate that the pin specimen is in contact only with the tops of the tallest domes. It is easy to see that the wear track becomes wider after a longer test. Among them, the Ni-P/MoS_2 7.9 wt% coating shows the smallest change as test time increases from 100 s to 1000 s, meaning the wear rate is very low.

Not surprisingly, as the particle content increases the width of the wear track generally decreases. It is especially evident after the 1000s sliding test, as the Ni-P/MoS_2 7.9 wt% coating only shows one-third of the wear track width on the Ni-P/MoS_2 1.2 wt% coating. This is due to the more uniform and smoother surface morphology seen on the higher concentration samples. As previously discussed these samples have low roughness so the contact pressure exerted on the surface will be considerably less than on the lower concentration samples.

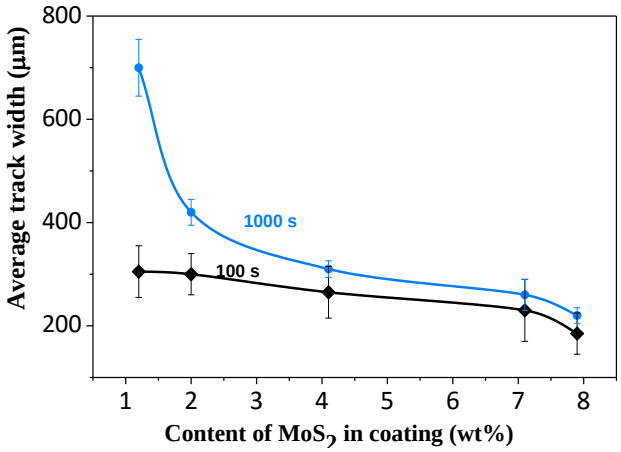

Figure 6.9 Relationship between average wear track width and MoS_2 particle content in samples tested for 100 s and 1000 s.

6.3.3 Reconditioning of MoS_2 particles in coating

A FIB-SEM system was used to examine the cross-section of the wear track and the change of MoS_2 in the coating after the friction test. The cross-section liftup of the 7.9 wt% sample is shown in Fig. 6.10.

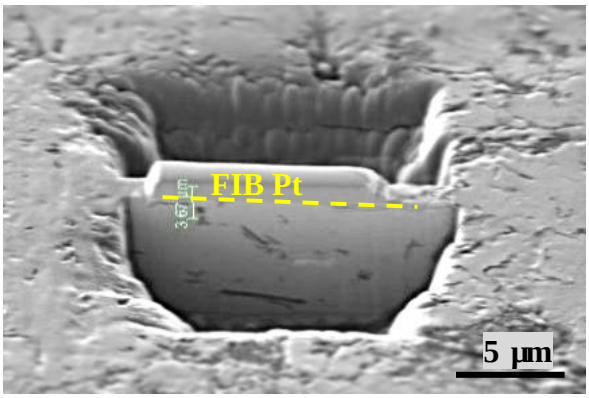

Figure 6.10 FIB image of the cross-section of wear track in 7.9 wt% sample after milling two trenches.

Afterwards, TEM was applied to explore the detail of the shear-induced MoS_2 evolution. The central image in Fig. 6.11 shows the BSE cross-section at low magnification. The top is the coating surface, and the greyer areas are MoS_2 particles. It is clearly shown that the shape of the MoS_2 particles changes from the as-received angular to elongated needles. It is interesting seeing that closer to the sliding surface, the MoS_2 particles are aligned more closely parallel to the surface. The high-resolution TEM images show the (002) plane is constantly parallel to the elongated direction of the MoS_2 particles. It can be concluded

that the MoS_2 particles will be broken into a number of pieces. These fractured MoS_2 will find it energetically more favourable to rotate than the whole particles. It also seems that the load induced the MoS_2 to form needles whose planes were parallel to the c axis.

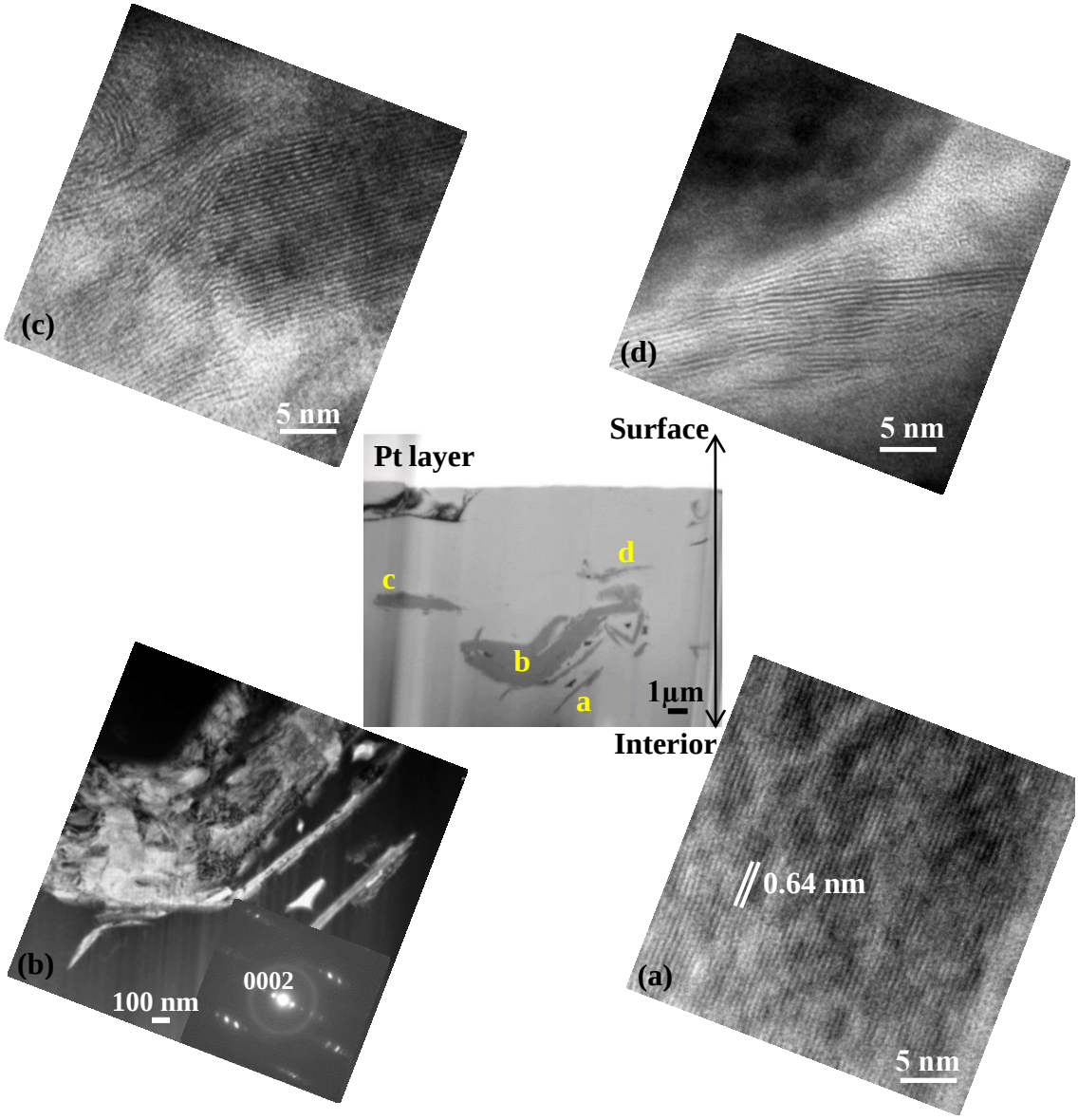

Figure 6.11 (Center) BSE image of the FIB cross-sectional sample from the wear track of Ni-P/MoS_2 7.9 wt% coating, (a-d) HRTEM images of MoS_2 particles with different distribution depths in coating.

6.3.4 Oxidation and wear resistance

BSE techniques were employed to examine the composition difference between the wear track and coating in Fig. 6.12a. The dark contrast in the wear shows Fe oxides. Less

oxidation of NiP/FeO on the Ni-P coating is shown in Fig. 6.12b. In Ni-P/MoS_2 composite coatings, with the increase of MoS_2 the wear track appear brighter. This indicates that less oxidation occurred with the increase of MoS_2 in the coatings. Heating up by friction was the reason for oxidation in the lower MoS_2 composite coatings.

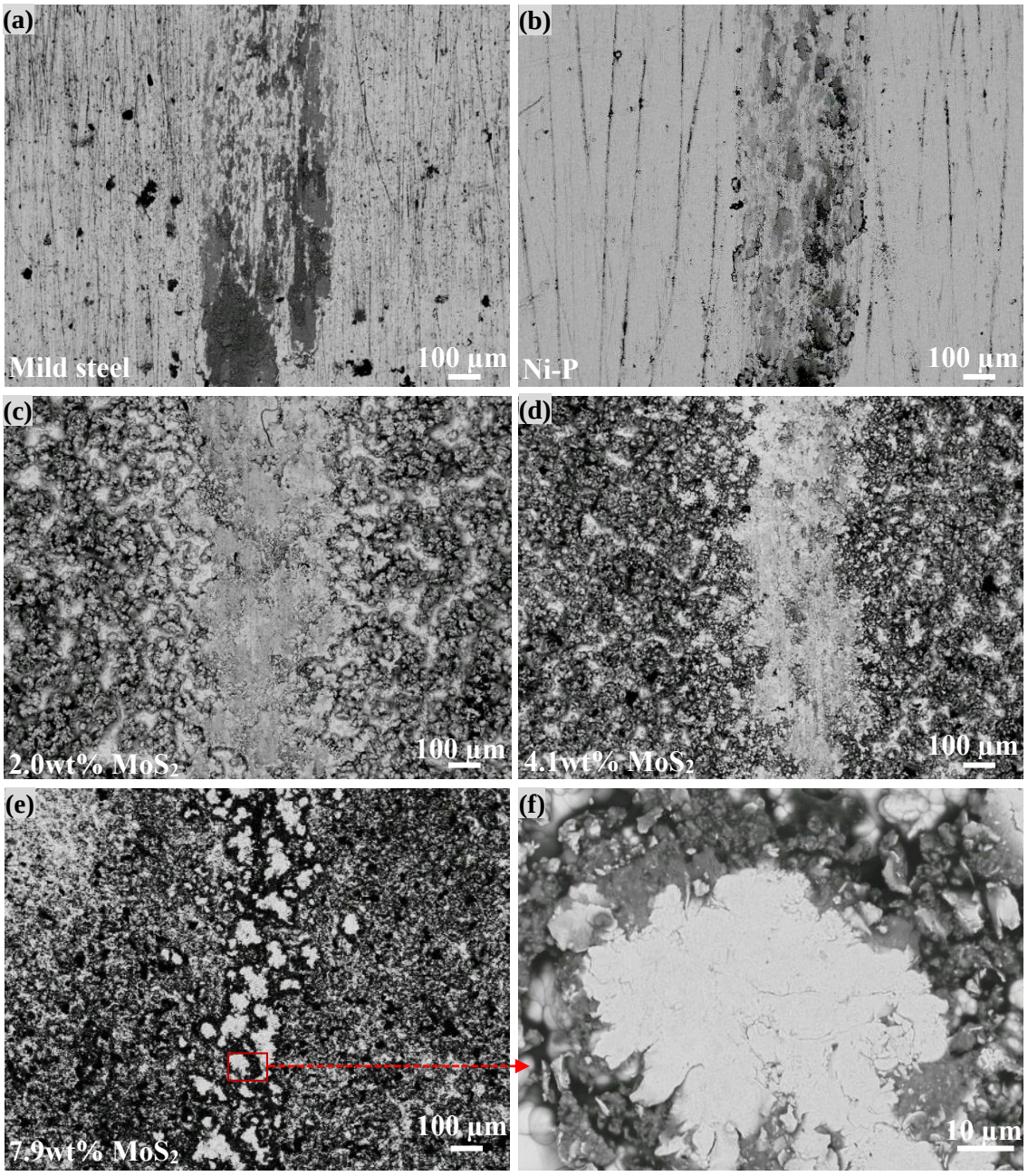

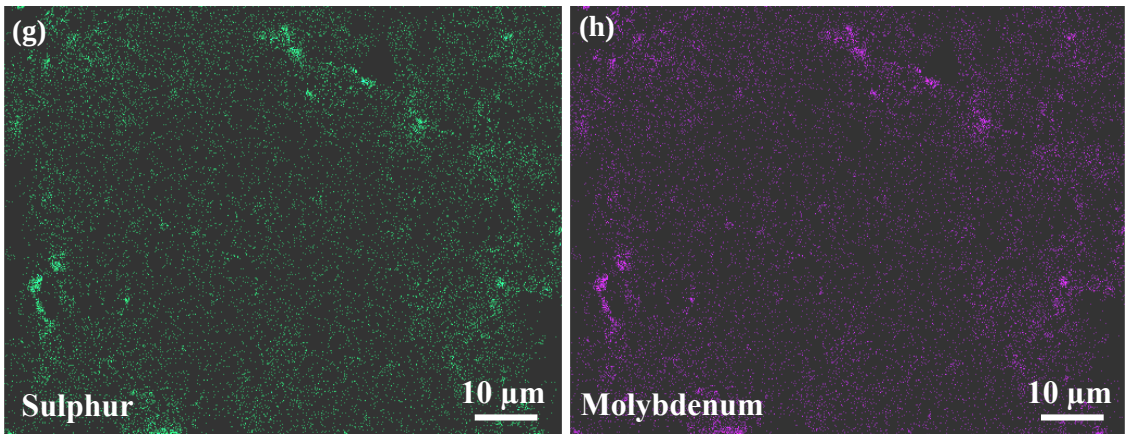

Figure 6.12 (a-f) BSE images of the wear track for different coatings after friction test and (g,h) elemental mapping of the wear track of (e).

Oxygen element mapping is displayed in Fig. 6.13. For the mild steel substrate, the oxygen concentration in the wear track is obviously higher than the remaining area, indicating severe oxidation during wear in air. The Ni-P showed improvement in oxidation resistance, displaying a similar slight increase but with less intensity on the wear area. In contrast, the oxidation was barely observed for the coating with 7.9 wt% MoS_2.

The quantities of oxygen in the wear tracks after wear have been plotted in Fig. 6.14. All the Ni-P/MoS_2 coatings exhibit lower oxygen than a pure Ni-P coating does. As the content of MoS_2 in the coating increases, the oxygen decreases in the wear track. The 7.9 wt% MoS_2 coating exhibits negligible oxygen. The decreased oxidation is attributed to the formation of a MoS_2-mixed lubricating tribolayer on the interface, isolating the coating from the air and reducing the frictional heat in the meantime.

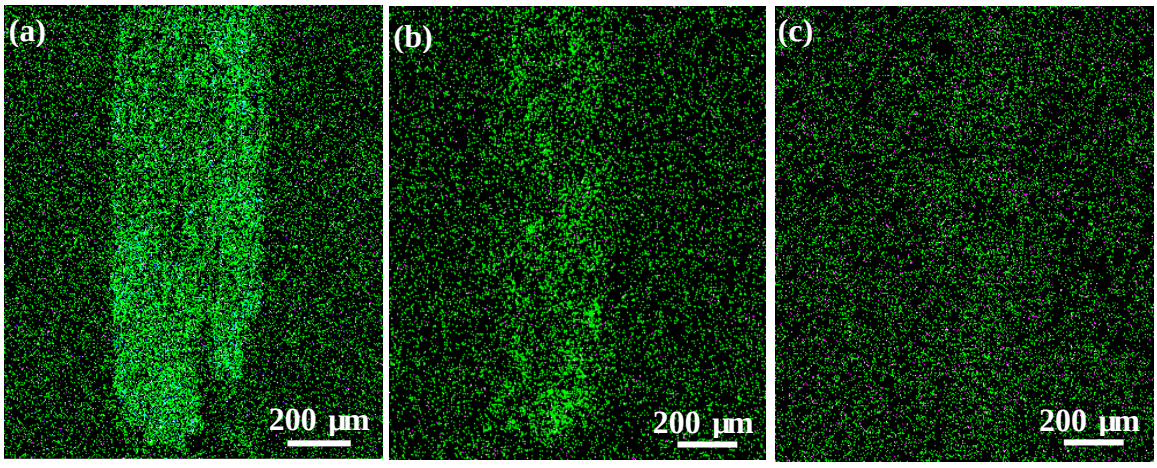

Figure 6.13 Oxygen mapping analysis of the wear track for the substrate, Ni-P coating, and Ni-P/MoS_2 7.9 wt% composite coating after 1000 s friction test.

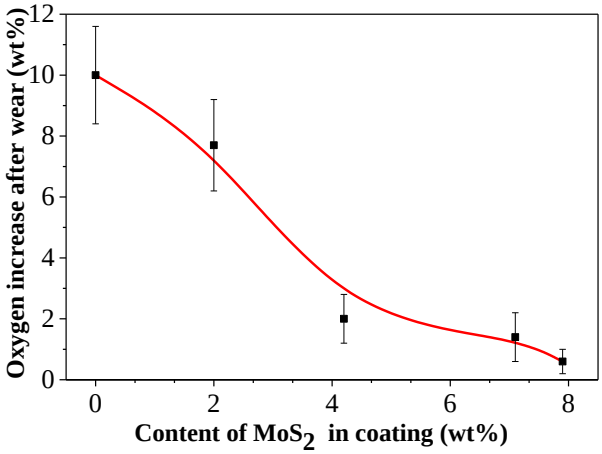

Figure 6.14 Relation between the content of MoS_2 in coating and the increase of oxygen in wear track for different Ni-P/MoS_2 coatings.

6.3.5 Wear on counterpart ball

The worn surfaces of counterpart balls (bearing steel) after sliding against the substrate and different coatings for 1000 s at 14.0 N are illustrated in Fig. 6.15. A lot of wear debris exist on the counterpart ball after sliding against the mild steel substrate. The higher hardness of the counterpart ball (700 HV), compared to the substrate (260 HV), resulted in less damage on the ball. The debris were scuffed from the substrate and thus no defined scar appeared. Comparably, the wear scar on the counterpart ball after sliding against Ni-P coating had much less debris in Fig. 6.15(b). A large amount of wear debris is fabricated on the surface of the counterpart ball against Ni-P/MoS_2 1.2 wt% coating, as the nodules in the coating are likely to fragment into fine debris during the friction test. Much fewer and smaller debris were generated on the counterpart ball against the Ni-P/MoS_2 2.0 wt% coating. In contrast, after sliding against the Ni-P/MoS_2 4.1 wt%, Ni-P/MoS_2 7.9 wt% and Ni-P/MoS_2 7.1 wt% coatings, the counterpart balls display continuously lubricated tracks without noticeable debris. Therefore, the increase of MoS_2 content in the coating could not only improve the wear resistance of the coating but effectively protect the counterpart ball from wear.

The compositions of the counterpart balls after friction test were examined and illustrated in Table 6.1. The counterpart balls possessed higher O contents when tested against 1.2 wt% or 2.0 wt% MoS_2 coatings than that found when tested against single Ni-P. The rough structure of these coatings generated more oxides due to frictional heat. As the

contents of MoS_2 in the coatings increase, the oxidation had lessened quickly on the counterpart balls. When the content of MoS_2 was raised to 7.9 wt% in the coating, the steel ball consisted of mostly Fe and few O. The excellent oxidation resistance is due to the embedded MoS_2 in the coating producing a transferred lubricating tribofilm on the counterpart ball and thus preventing direct contact with air during the friction process.

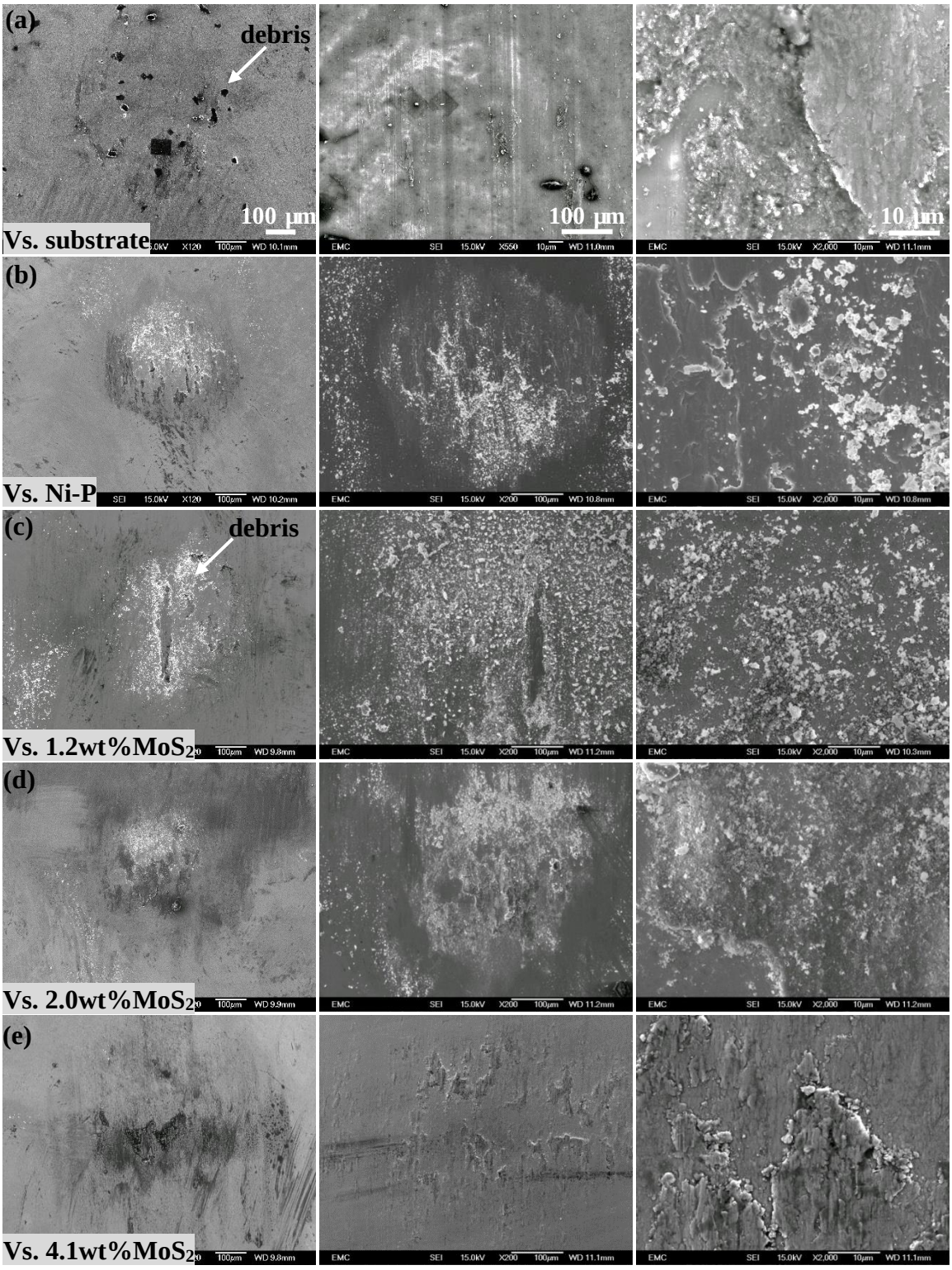

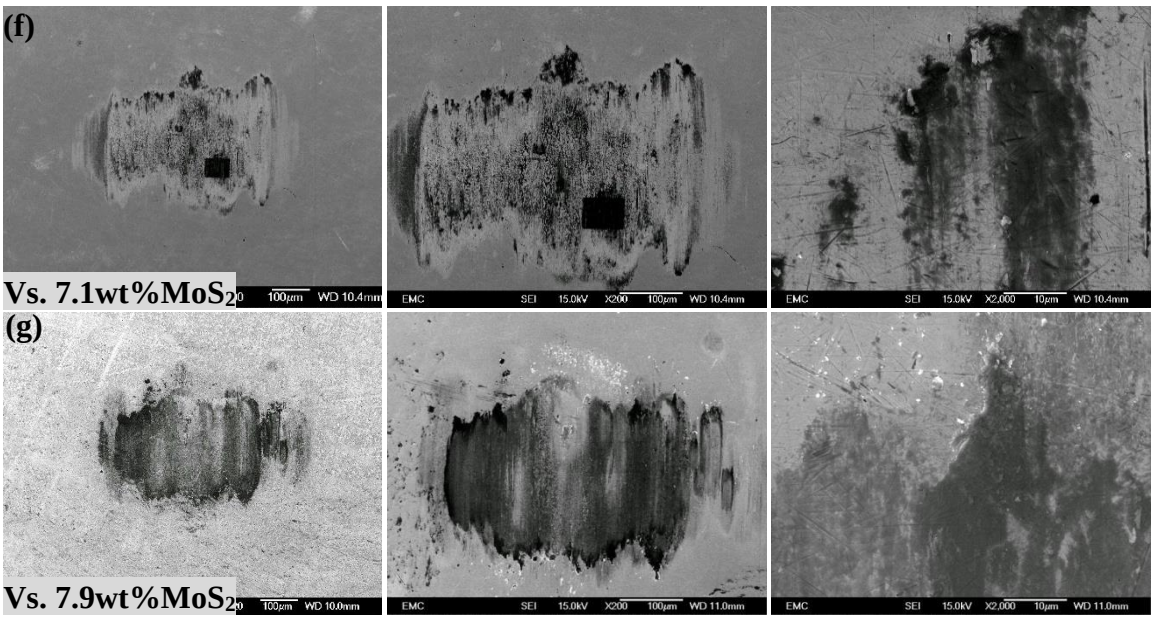

Figure 6.15 Surface morphologies of counterpart balls after sliding for 1000 s against mild steel substrate, Ni-P and different Ni-P/MoS_2 coatings.

Table 6.1 Composition of the counterballs after wear test against different coatings.

Element (wt%)	Vs. Ni-P	Vs. 1.2% MoS_2	Vs. 2.0% MoS_2	Vs. 4.1% MoS_2	Vs. 7.1% MoS_2	Vs. 7.9% MoS_2
O K	10.1	14.1	15.5	7.2	3.5	2.0
P K	4.5	2.0	1.3	4.9	0.6	0.1
Fe K	37.5	34.3	49.8	63.1	80.0	90.1
Cr K	0.5	0.5	0.7	0.9	1.3	1.7
Ni K	47.4	49.1	31.5	17.6	11.2	3.6
Mo K	0	0	0.7	3.7	2.1	1.8
S K	0	0	0.5	2.6	1.3	0.7

The counterpart steel balls were also imaged by BSE to reveal oxides. As seen from Fig. 6.16, a large wear track exists on the steel ball against the mild steel substrate. A uniform tribofilm with medium grey level appeared on the steel ball sliding against Ni-P coating, suggesting less oxidation on the latter sample. Lots of dark debris were found on the steel ball against the 1.2 wt% MoS_2 coating due to the serve oxidation. As the content of MoS_2 increases, the wear track on the counterpart steel ball displays a lighter colour and less debris. Noticeably, after sliding against the 7.9 wt% coating, the steel ball shows only a slight colour change in the wear track. The dark materials on the two ends contain a high percentage of MoS_2. They were transferred to the counterpart steel ball as lubrication therefore less frictional heat was generated and less oxidation occurred.

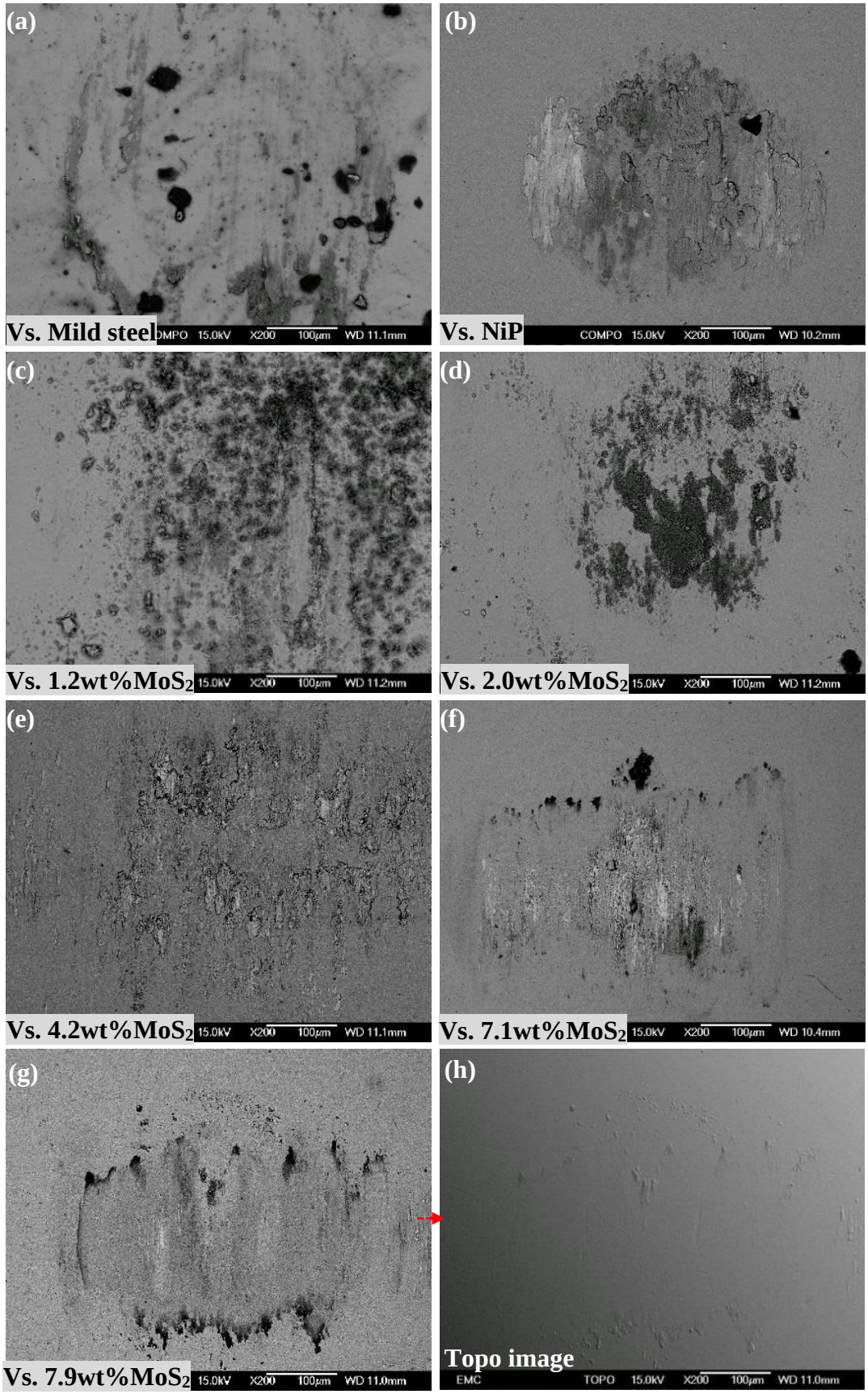

Figure 6.16 (a-g) BSE images of counterpart after 1000 s friction test against mild steel or different coatings, (h) Topological image of the wear scars on counterpart against 7.9 wt% MoS_2.

6.4 Discussion

6.4.1 Tribofilms and their effect on tribological performance

The intent of this section is to discuss the factors responsible for the extremely low friction coefficient and wear rate of the Ni-P/MoS_2 in air compared with substrate steel or Ni-P.

The hardness of the bearing steel ball (700 HV) is much greater than that of the mild steel substrate (170 HV) in the ball-on-substrate tribology system. Such a significant difference in hardness ensures that abrasive wear dominates the wear process of the mild steel substrate. SEM observations of the wear track in Fig. 6.2(a) show that some grooves are plowed as a result of abrasive wear. In addition, the high solubility between the counterpart steel ball and mild steel substrate causes severe adhesive wear displayed as bulged areas in the wear track. A lot of large wear debris are scattered on the worn surface, which are expected to be mixed oxides of Fe_2O_3 and Fe_3O_4 (validated by EDS results). Oxidation is believed to be detrimental to the wear resistance of mild steel, as the oxide debris are prone to break and roll over during sliding, and are likely to give rise to a change to the wear mechanism from two-body to three-body abrasive wear.

For the Ni-P coating, because the hardness of Ni-P (HV = 530) is lower than that of the bearing steel counterpart (HV = 700), debris particles generated and oxidized are crushed and pushed along the wear scar, i.e. not over-rolled. The adhesion force between the counterpart ball and Ni-P metal surfaces is strong, and therefore the wear particles slide firmly on the sliding surface and turn into incomplete tribofilms during a long sliding time. Wear resistance is improved due to the existence of the compact oxide films. The friction coefficient is still high (friction coefficient: 0.4) due to the strong bonding between the films on the coating and the counterpart ball.

The friction coefficient (μ) is the ratio of the frictional force, F to the normal force, W.

$$\mu = F/W \tag{6.1}$$

Therefore, the friction force and normal force depends on the real contact area, A with

shear force, τ and pressure stress, σ:

$$F = A\tau \text{ and } W = A\sigma. \tag{6.2}$$

The equation may be simplified to $\mu = \tau/\sigma$. Due to the lamellar structure of MoS_2, the inclusion of MoS_2 into the Ni-P coating greatly reduces the shear force (τ) causing a decrease in friction coefficient, especially when a smooth lubricating layer was formed.

A schematic diagram of the self-lubricating Ni-P/MoS_2 coating is illustrated in Fig. 6.17. The supposed formation process of MoS_2 tribofilm is as follows: at first, the embedded MoS_2 is heavily compressed under the friction load. Once friction starts, the movement of the counterpart pin will cause high shear stress near the contact surface and the MoS_2 in this area starts to deform. The stored MoS_2 particles in the matrix continuously and slowly release to the mating surface. Some MoS_2 lamellae will be exfoliated and become smaller crystals. During the friction process, the fine MoS_2 lamellas accumulate in the wear crevices or attach to the metal surface, creating a densely packed super-lubricating coating layer. The whole reconditioning process of the lubricants happens within the coating, away from the air environment. Furthermore, the lubricating film not only firmly attaches to the coating surface but also transfers to the counterpart, producing excellent tribological characteristics such as low friction coefficient, low wear rate and high oxidation resistance in the absence of oil or grease.

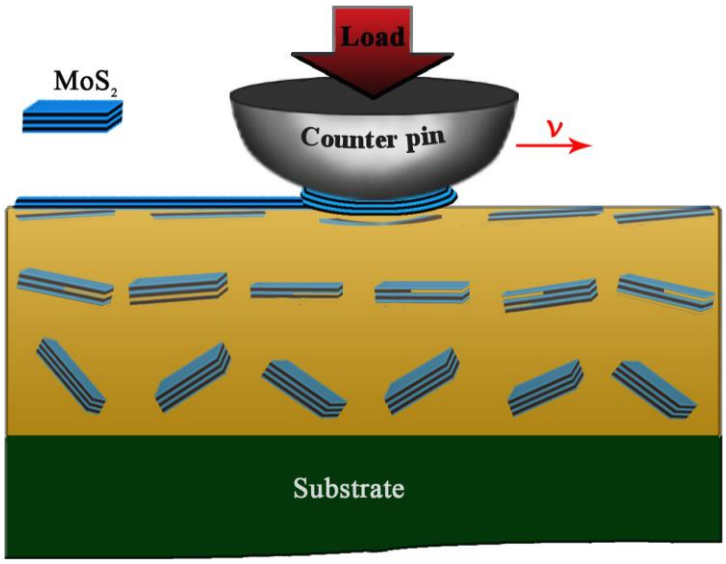

Figure 6.17 Schematic graph of the formation of the self-lubricating film on Ni-P/MoS_2 composite coating.

6.4.2 The working principle of Ni-P/MoS_2 composite coating

The tribological behaviour of MoS_2 has been studied for a long time. The main factors contributing to the successful lubrication performance of MoS_2 are thought to be the prevention of oxidation, formation and adhesion of a homogenous transfer film and intercrystalline slip [212,213,214,215,216].

Taking into account the SEM, EDX, TEM and friction results, and combined with its structure, the advantages of Ni-P/MoS_2 can be reviewed as follows:

- Electrodeposited Ni-P alloy possesses a high hardness which bears high contact stress and has a high resistance to wear. However, a coating with low hardness usually possesses a high wear rate, in which the MoS_2 particles in the coating will be pushed away quickly rather than form a lubricating tribofilm.

- MoS_2 are easily oxidized to MoO_3 and the latter can cause the material to stick, accelerate the deterioration of its easy shear performance and lead to an increase in fiction. In the composite coating, however, the MoS_2 were fully surrounded by Ni-P matrix and thus prevented from oxidizing. Accordingly these coatings can maintain a low friction coefficient for a long period.

- The adhesion sequence of MoS_2 films to metals is: copper > nickel >> stainless > gold. The sequence was deduced from friction experiments of MoS_2 single crystals against sputtered copper, nickel, gold, and 304 stainless steel [217]. The wear test on Ni-P/MoS_2 coating indeed confirmed that MoS_2 debris strongly adhered to the Ni matrix therefore it remains effective in lubrication rather than being squeezed out. The high content of MoS_2 ensured the formation of a complete tribofilm to isolate the metal-metal contact, in this case, Ni-iron contact.

6.5 Summary

1. The incorporation of MoS_2 particles in the composite strongly influences the friction performance of coatings. Compared to both mild steel substrate and Ni-P coating, the composite coatings show significant friction reduction. The

friction coefficient of the Ni-P/MoS_2 composite coatings were significantly lower than that of Ni-P coating, exhibiting a steady-state value of 0.05 during a 1-hour reciprocating test.

2. The mild steel substrate shows severe adhesive and abrasive wear while the Ni-P coating just shows a medium abrasion wear track. The embedment of MoS_2 particles into a Ni-P matrix did affect the wear resistance of Ni-P, i.e. the effects are increased or decreased. The coating with lower particle content (1.2 wt% MoS_2) exhibits a more severe wear condition while least wear was observed on the coating with 7.9 wt% MoS_2 with a low wear rate of 2.5×10^{-6} $mm^3\ N^{-1}\ m^{-1}$. The compact structure and the high content of MoS_2 are thought to be two critical conditions for the electrodeposited NiP/MoS_2 coating to produce a low wear rate.

3. The oxidation degree is severe for the substrate, medium for the Ni-P coating and very rare for the Ni-P/MoS_2 composite coating during wear testing. Such a result suggests that the MoS_2-containing tribofilm on the friction surfaces greatly reduces the friction temperature and also works effectively as a "separator" to block the sliding surface from the air.

4. A very slight wear track was found on the counterpart ball sliding against Ni-P/MoS_2 7.1 wt% and 7.9 wt% coatings because the MoS_2 lubricants have also been transferred onto the counterpart ball and form a lubricating film.

5. The FIB and TEM study demonstrate that the particles in the coating went through a shear stress-induced reorganization, evolved into crystalline fragments and finally mixed with amorphous matrix. The easy shear of MoS_2 lamellas and the intercrystalline slip between fragmented MoS_2 and amorphous Ni-P are thought to provide the critical mechanism for reduced friction, high wear resistance and enhanced oxidation resistance.

Chapter 7 Fabrication of self-lubricating Ni-P/WS_2 coatings by electrodeposition

7.1 Introduction

Layered materials like tungsten disulphide (WS_2) or Molybdenum disulfide (MoS_2) are widely used as solid lubricants or as additives in liquid lubricants [218,219]. Their low friction performance is typically associated with the easy shearing of the weak interlayer bonds (van der Waals) in these materials. WS_2 is preferred over MoS_2 in high-temperature applications as MoS_2 rapidly oxidizes to MoO_3 in atmospheres above 316 ℃ while the WS_2 has a good thermal stability up to 594 ℃. In addition, the friction coefficient of WS_2 is below 0.1 in argon until 815 ℃. Unfortunately, some reactive dangling bonds on the prismatic edges $(10\bar{1}0)$ of WS_2 are susceptible to humidification which usually leads to the degradation of the low friction property.

An alternative strategy is preparing WS_2 composite coatings that combine the advantage of WS_2 with other materials to produce ideal properties for a wide range of applications. Some composite coatings (CrN-WS_2, Ni-WS_2, Zn-WS_2, and bronze-WS_2) have already been prepared, exhibiting low friction characteristics in either vacuum or humid air [145,220,221,222]. Electrodeposited Ni-P alloys possess many advantages over other metals or alloys such as high hardness, high strength and good wear resistance. The research in this chapter will look into the overall merits of the co-electrodeposited nickel-phosphorous-WS_2 and analyse how effective the coating would be as a candidate for self-lubrication.

7.2 Experimental details

Electrodeposition was carried out on mild steel (4 cm × 1 cm) at 60 ℃ for 45 minutes under a current density of 2.5 A dm^{-2}. The electrodeposition bath contains $NiSO_4 \cdot 6H_2O$ 220 g/L, H_3BO_3 30 g/L, NaH_2PO_2 10 g/L, $HOC(COOH)(CH_2COOH)_2$ 12g/L,

$NiCl_2 \cdot 6H_2O$ 45g/L, different concentrations of WS_2 (1-25 g/L) and CTAB as listed in Table 7.1.

Table 7.1 Concentrations of WS_2 and CTAB for electrodeposition of Ni-P/WS_2 coating.

	Concentration of ingredients (g/L)					
WS_2 particle	1	3	7	10	15	25
CTAB	0.1	0.1	0.1	0.2	0.2	0.3

7.3 Results

7.3.1 Morphology and structure

Fig. 7.1 shows that the as-received WS_2 powders have an angular shape, with diameters in the range of 100-250 nm.

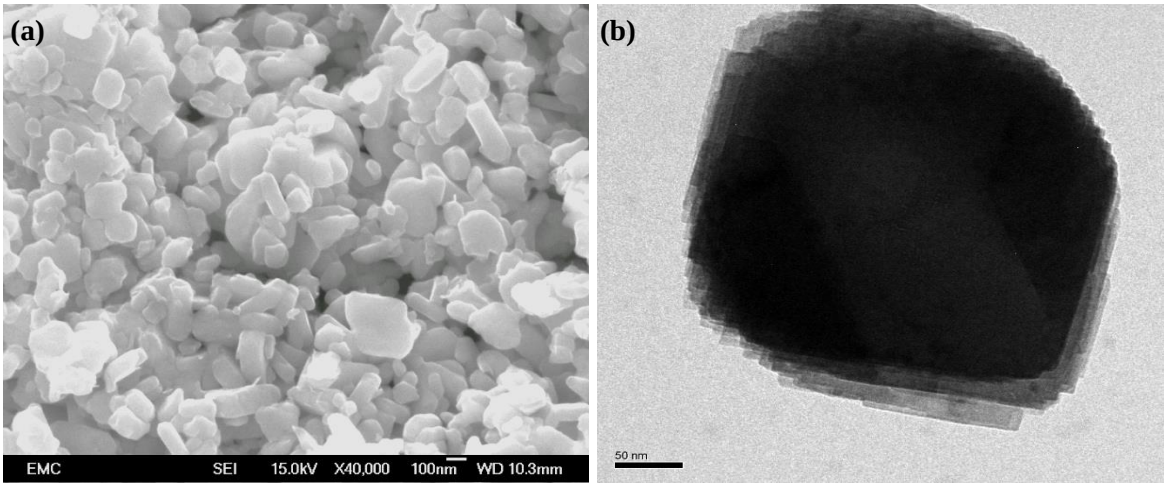

Figure 7.1 (a) SEI and (b) TEM images of WS_2 nanoparticles.

The particles were then dispersed in the ultrasonic bath and codeposited with Ni-P. As can be seen in Fig. 7.2, the prepared Ni-P/WS_2 coating is quite rough, with some clusters of protruding nodules on the surface. Higher magnification reveals the presence of large numbers of WS_2 particles in the coating. EDS was carried out on the same surface displayed in Fig. 7.2(a). The EDS spectrum exhibits that the coating primarily consists of the four elements: Ni, P, W and S, indicating the embedment of WS_2 particles into the coating by electro-codeposition.

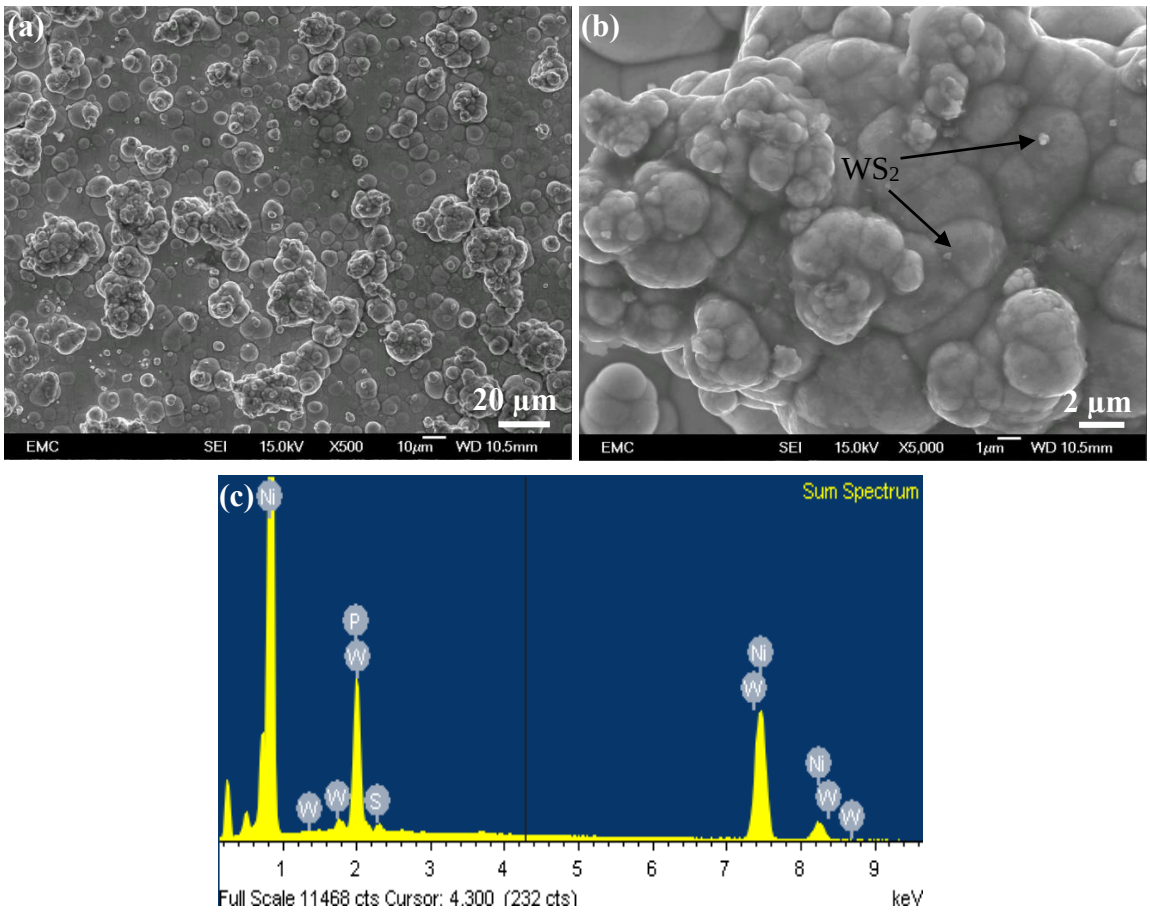

Figure 7.2 (a, b) SEI images of Ni-P/WS_2 coating under different magnifications; (c) EDS spectrum of Ni-P/WS_2 coating (C_{WS2} = 7 g/L, t = 45 min, J = 2.5 A dm^{-2}).

The TEM image in Fig. 7.3 displays a uniform spread of WS_2 particles inside the Ni-P matrices. The SAED (selected area electron diffraction) pattern of this sample exhibits a very weak broad ring, indicating the amorphous/nanocrystal structure of the electrodeposited coating.

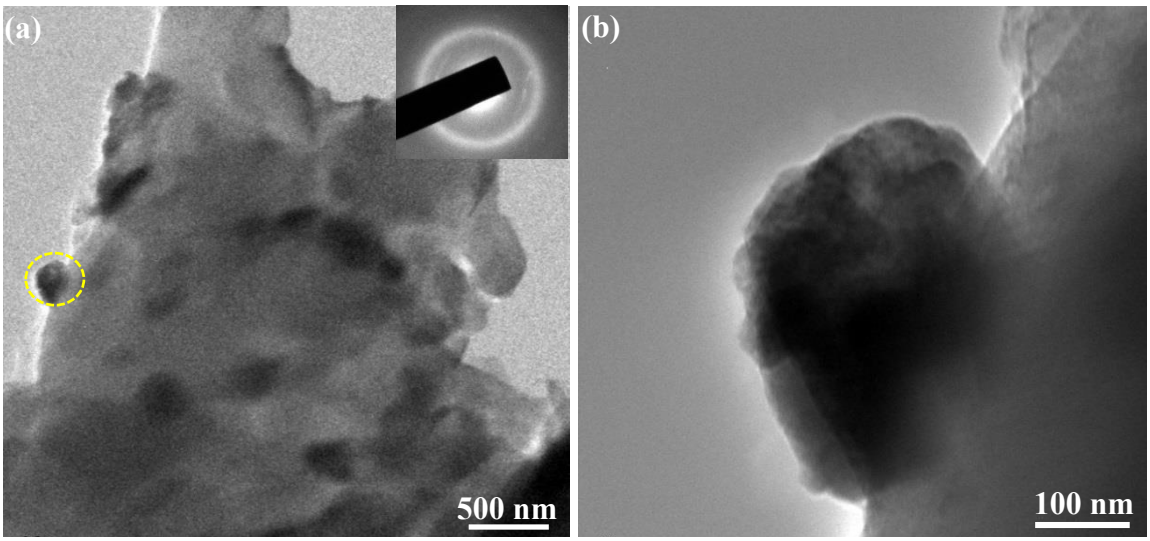

Figure 7.3 (a, b) TEM images of the Ni-P/WS_2 coating (C_{WS2} = 7 g/L, t = 45 min, J = 2.5 A dm^{-2}), the inset is SAED pattern of the whole area in (a).

7.3.2 Bath temperature

The bath temperature has a strong influence upon the plating process of the Ni-P/WS_2 coating. Fig. 7.4 exhibits that the sample deposited at 20 ℃ has a dark colour while the rest of the samples have a grey colour. Some parts of this coating were peeled off and left with light patches, suggesting a weak adhesion to the substrate. The SEM images in Fig. 7.5 show that the coatings deposited at 20 ℃ or 40 ℃ consist of clusters of nodules (around 4 μm in diameter) and cracks. The nodules in the coating grow to a diameter of 8 μm and cracks disappeared when the temperature was raised to 60 ℃. At the higher temperature, the deposited coatings usually have lower internal stress which prevents crack formation. However, if the temperature is too high (80 ℃), the stability of the aqueous electrodeposition solution is questionable. As shown in Fig. 7.6, the content of WS_2 particles in the coating was largely reduced as the electrodeposition temperature increases from 20 ℃ to 80 ℃. Overall, the optimum operating temperature for electrodeposition of the Ni-P/WS_2 coating is 60 ℃, with reasonable internal stress and WS_2 content.

Figure 7.4 Pictures of the temperature varied Ni-P/WS_2 samples (from left to right: 80°C, 60°C, 40°C, and 20°C).

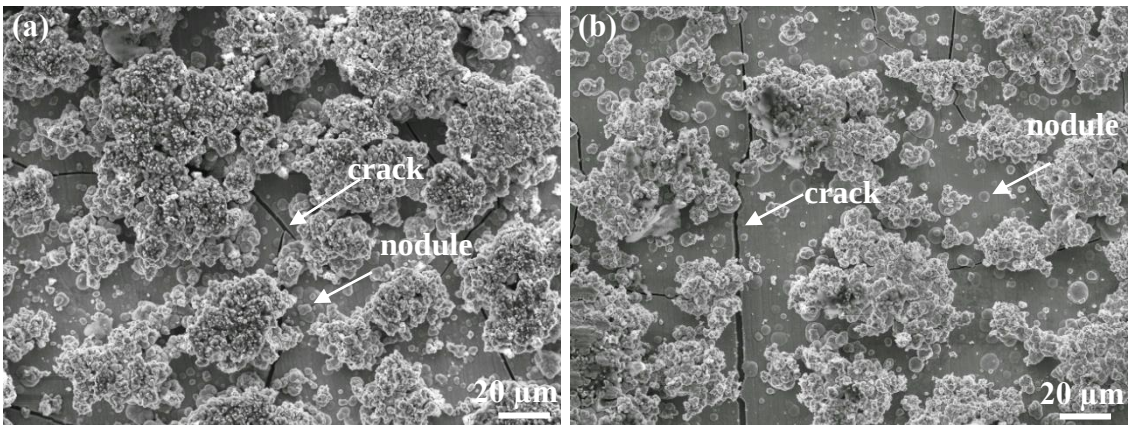

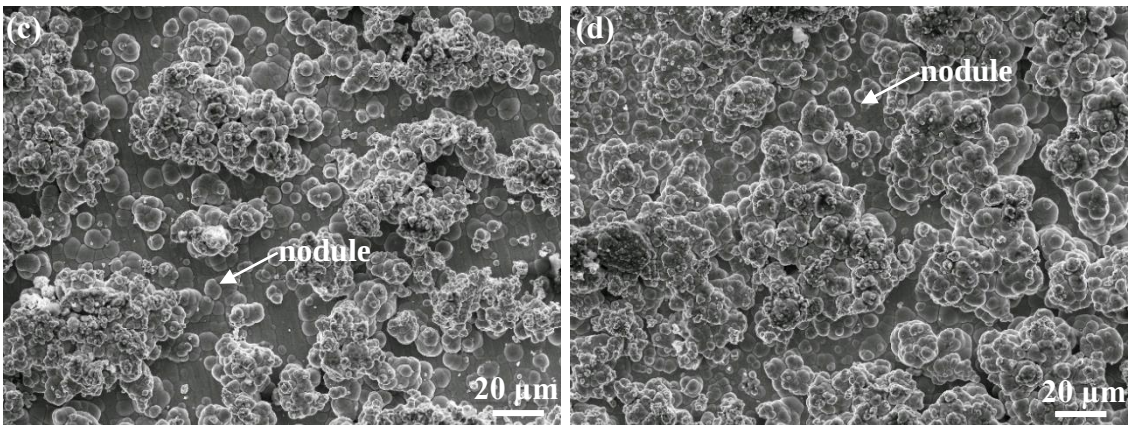

Figure 7.5 (a-d) SEI images of the Ni-P/WS_2 coatings deposited at different temperatures: 20 ºC, 40 ºC, 60 ºC and 80 ºC (C_{WS2} = 15 g/L, t = 45 min, J = 2.5 A dm^{-2}).

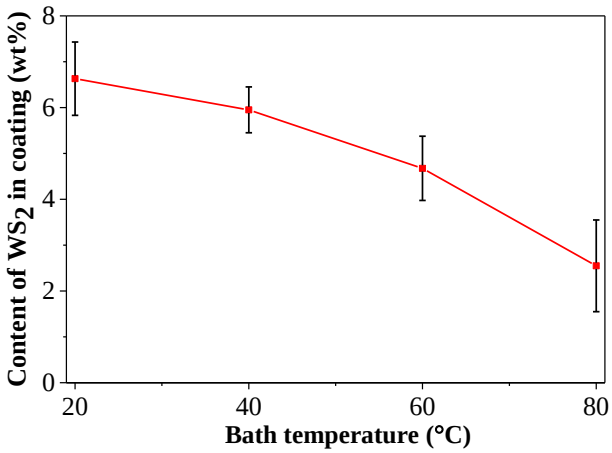

Figure 7.6 Weight percentage of WS_2 in coating vs. the electrodeposition temperature.

The relationships between the coefficient of friction and the sliding time for the samples deposited at varied temperatures are displayed in Fig. 7.7. Initially the coefficient of friction is around 0.25 for all the samples. The 20°C, 40°C and 80°C samples show an increase in friction coefficient for a period of time before coatings failed, and afterwards rise to a friction coefficient of approximately 0.75 due to the steel-steel contact. However, the electrodeposition temperature has quite a drastic effect on when the coating fails. The friction coefficients of the 20°C and 40°C sample rise sharply to 0.75 after exhibiting a low value for 20s and 110s respectively. Comparably, the 80°C sample lasted with a low friction coefficient below 0.5 for as long as 5 minutes. The 60°C sample is the only one that retains the coefficient of friction constant around 0.3 during the whole test duration. Therefore, the optimized temperature value for the best low friction performance is close to 60°C.

The sharp increase in the friction coefficient of the 20 ℃ or 40 ℃ coatings is attributed to the cracks in the structure, which make these coatings less resistant to the high load and shear stress and so break down in a short time. The peeling off of the coating will leave the substrate sliding against counterpart ball, resulting in a high friction coefficient around 0.8. The 80°C sample failed significantly later than the former two samples thanks to a crack-free structure. The low-friction performance at the initial stage indicates the WS_2 particles in the coating did reduce the friction coefficient. However, as the amount of WS_2 particles in the coating was quite small, the lubrication effect was not sufficient to prevent frictional heat and formation of wear debris during the friction process. Therefore, the friction coefficient gradually increased due to the accumulation of frictional heat and debris on the interface. The lowest and steadiest friction coefficient for the 60°C sample is attributed to its crack-free structure and high WS_2 content, which continuously releases WS_2 to lubricate the mating surface.

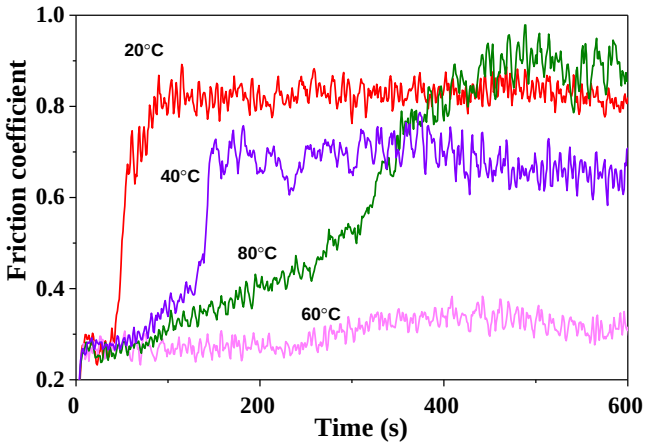

Figure 7.7 Graph showing the coefficient of friction versus time for Ni-P/WS_2 samples deposited at a range of electroplating temperatures.

7.3.3 WS_2 concentration

Fig. 7.8 shows how the coating deposits are affected by CTAB and WS_2 concentrations. The clusters of surface nodules have considerably increased for greater concentrations of WS_2 and CTAB. The semi-conductive WS_2 particles in the bath will be adsorbed on the cathode and result in an inhomogeneous distribution of current densities on the cathode. This will accelerate the growth of deposits around them and develop nodules from the matrix. This effect is more evident for the Ni-P/WS_2 coating deposited at higher WS_2 and

CTAB concentration, which created a rough surface with many nodule protrusions. This process is also similar to the growth mechanism of Ni-P/MoS_2 described in chapter 5.

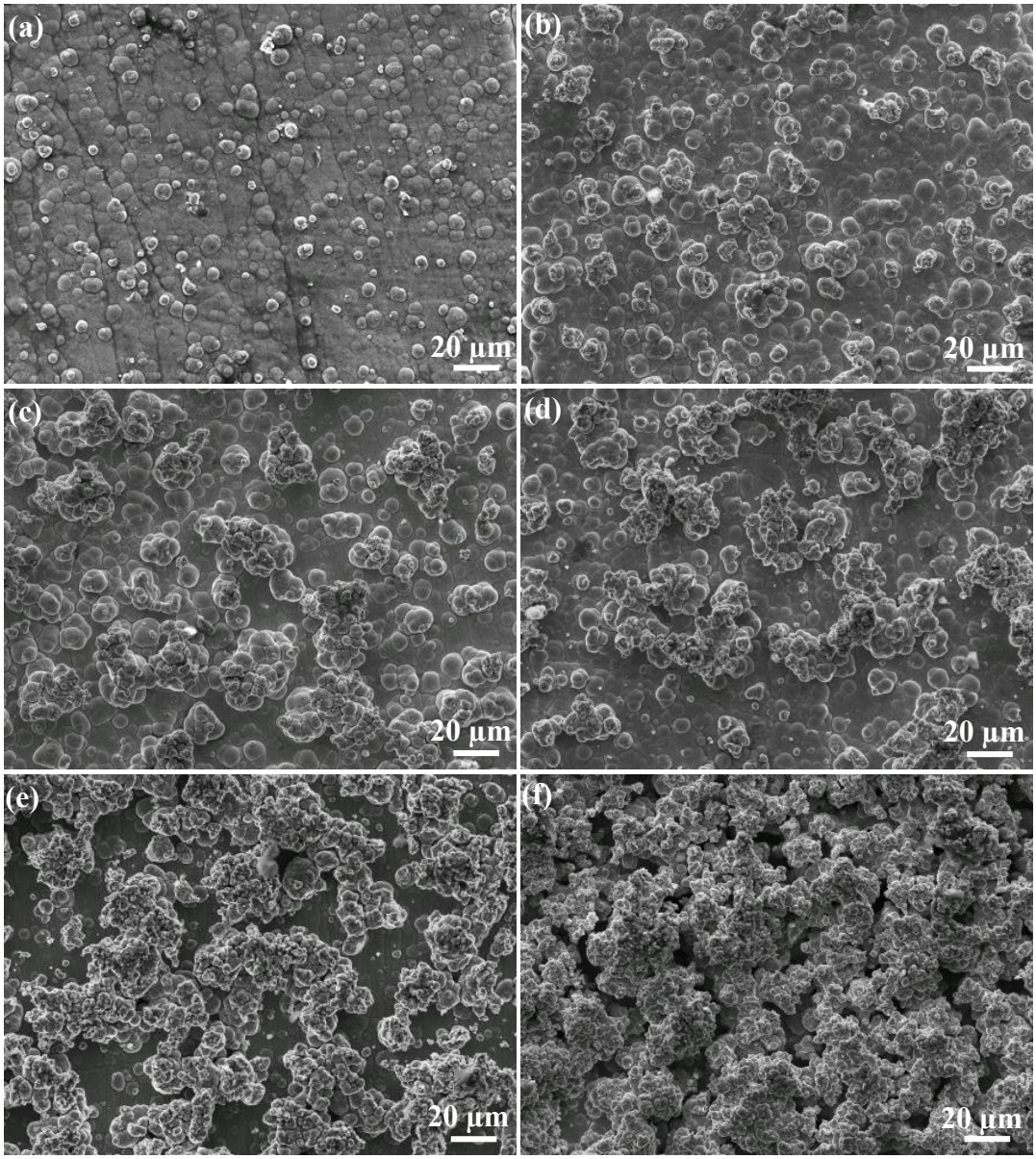

Fig. 7.8 (a-f) SEI images for Ni-P/WS_2 coatings deposited at WS_2 concentrations of 1, 3, 7, 10, 15 and 25 g/L in chronological letter order (T= 60 °C, t = 45 min, J = 2.5 A dm^{-2}).

As can be seen in Fig. 7.9, the amount of the incorporated WS_2 in the coating increases to 4.8 wt% as the WS_2 concentration in the bath rises up to 15 g/L. Higher particle concentration in solution usually leads to more adsorbed particles on the cathode which are subsequently embedded into the growing deposits. However, a slight decrease of the WS_2 content in the coating was found when the deposition concentration of WS_2 and CTAB changed to 25 g/L and 0.3 g/L respectively. This drop was partly attributed to the high concentration of CTAB in solution which easily adsorbed on the electrode and blocked the adsorption of WS_2 particles on the electrode. In addition, some dispersed

particles easily set down at the bottom of the electrolytic cell owing to the high concentration of WS_2. The graph 7.9(b) suggests that the incorporation of nano-size WS_2 particles effectively improves the hardness of the composite coating. The 15 g/L WS_2 sample has a hardness of 720 ± 50 HV, which is higher than the other samples as this coating has the maximum WS_2 content of 4.8 wt%.

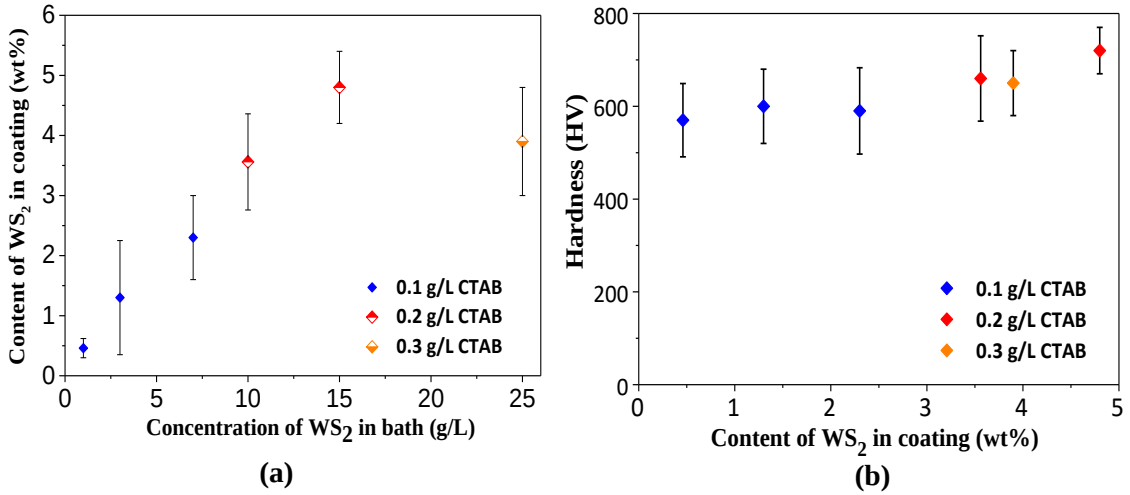

Fig. 7.9 (a) The WS_2 content in coating and (b) the Vickers hardness of coating against the concentration of WS_2 in the electrolyte solution.

Fig. 7.10 shows how the coefficient of friction changed during the wear test for the above coatings. All these coatings exhibit an initial frictional coefficient around 0.2. For the 0.5 wt%, and 1.3 wt% WS_2 coatings, the coefficient of friction then gradually increases to 0.7-0.8. The results indicate that the lubricating WS_2 was effective initially but gradually lost function during the wear process. For the 2.3 wt% WS_2 coatings, this sequence is delayed. In contrast, for the composite coatings with 3.6 wt% WS_2 and above, their coefficient of friction exhibited a stable frictional coefficient of 0.17-0.2 during whole friction test, much lower than the friction coefficient of Ni-P (0.5). The significant friction reduction is due to the low shear yield of the WS_2 and its high amount which can constantly provide a lubrication function for a long period.

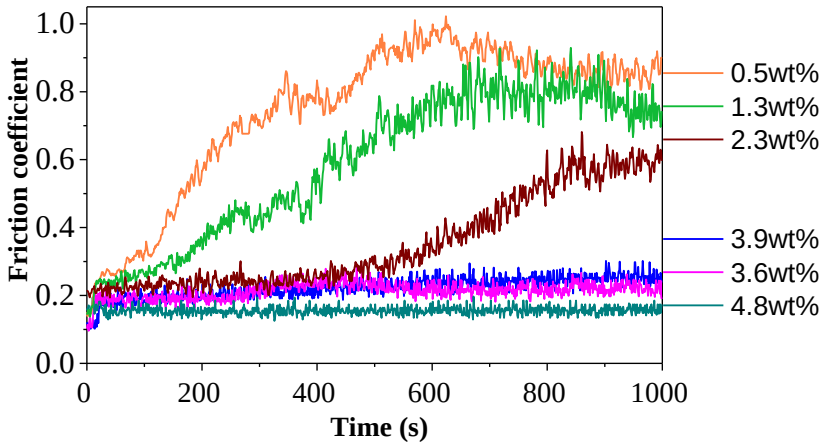

Fig. 7.10 Coefficient of friction versus time for the Ni-P/WS_2 coatings with different WS_2 contents.

As shown in Fig. 7.11, the Ni-P/WS_2 0.5 wt% coating was deeply abraded by the counterpart steel ball, leaving a wear track width of 450 μm. As the WS_2 content in sample increases, the wear track gets narrower. The Ni-P/WS_2 4.8 wt% sample exhibits the narrowest wear track of 260 μm and produces very few debris, suggesting its highly improved wear resistance. During the sliding test, higher content of WS_2 lubricants in the coating resulted in more effective lubrication on the surface and less shear force, therefore much lower wear rate was maintained.

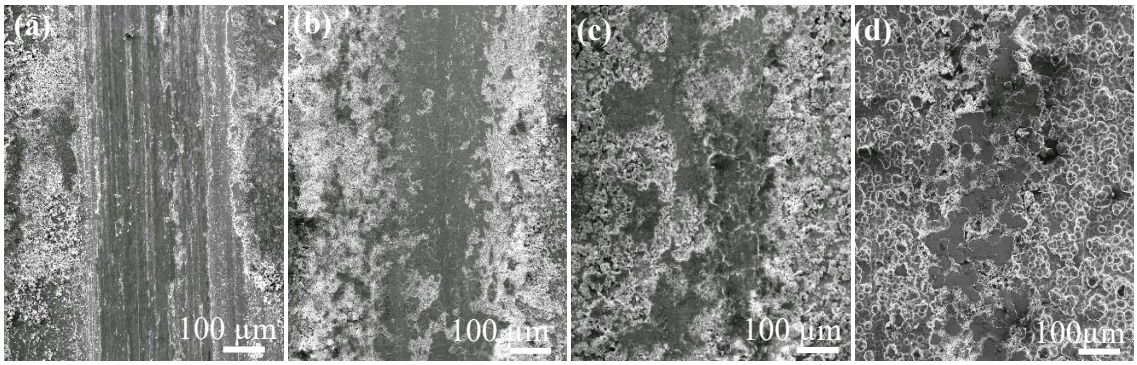

Figure 7.11 Comparison of wear tracks for different coatings: (a) 0.5 wt% WS_2, (b) 2.3 wt% WS_2, (c) 3.6 wt% WS_2, and (d) 4.8 wt% WS_2.

The morphology of the counterpart balls after the friction test were examined and displayed in Fig. 7.12. The counterpart ball exhibits a clear abrasion wear scar after sliding against the 0.5 wt% WS_2 coating. The increase of WS_2 content in the coating could greatly reduce the size of the wear scar on the counterpart ball and thus less wear damage appeared in the coating. There is only a tiny wear scar on the ball after sliding against 4.8

wt% WS_2 coating. It can be seen from Table 7.2 that the counterpart ball has the lowest percentage of oxygen after the friction test. The reduced oxidation is due to the increase of WS_2 particles in the coatings which significantly reduces the friction by the formation of the tribofilm. Less heat was produced as the WS_2 tribofilm prevented the metal-metal contact.

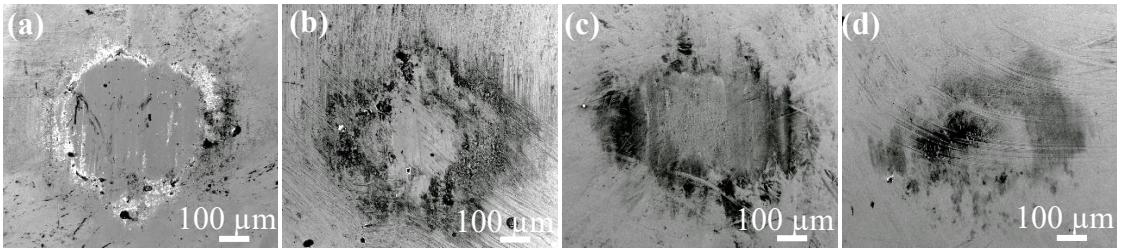

Figure 7.12 Surface morphologies of counterpart balls after 1000 s friction test against different Ni-P/WS_2 coatings: (a) 0.5 wt% WS_2, (b) 2.3 wt% WS_2, (c) 3.6 wt% WS_2, and (d) 4.8 wt% WS_2.

Table 7.2 EDS comparison of the whole wear scars on counterpart balls after test against different Ni-P/WS_2 coatings: 0.5 wt% WS_2, 2.3 wt% WS_2, 3.6 wt% WS_2, and 4.8 wt% WS_2.

Element (wt%)	Vs. 0.5 wt% WS_2	Vs. 2.3 wt% WS_2	Vs. 3.6 wt% WS_2	Vs. 4.8 wt% WS_2
O K	7.55	4.39	2.90	2.87
Ni K	0.17	4.40	7.21	2.66
P K	0.03	0.72	0.70	0.36
S K	0.05	0.07	0.08	0.17
W M	0.17	0.35	0.39	0.85
Cr K	1.53	1.50	1.38	1.48
Fe K	90.86	88.57	87.34	91.61

7.4 Summary

Ni-P/WS_2 coatings have been successfully prepared by optimizing bath temperature, CTAB and WS_2 concentration. The as-deposited coatings showed rough surfaces consisting of small nodule protrusions. The electrodeposition at 60 ℃ effectively prevented cracks in the coatings, which resulted in a better coating strength and lower friction coefficient. In general, the increase of the WS_2 and CTAB concentration in the electrolyte enhanced WS_2 contents in the coating. The coatings with WS_2 content of 0.5 - 4.8 wt% had a hardness range from 570 - 720 HV. Excellent low friction coefficients of 0.17 - 0.2 have been obtained for the coatings with WS_2 over 3.6 wt% in reciprocal friction

test against bearing steel balls. WS_2 in the coating matrix forms a reservoir to form a low shear stress tribofilm for wear lubrication.

Chapter 8 Overall discussion of composite electrodeposition

The results in Chapters 4-7 have shown the successful electrodeposition of Ni/BAM, Ni-P/MoS_2 and Ni-P/WS_2 for tribological applications. The incorporation of different kinds of particles has effectively reinforced the properties of Ni coatings in differing ways. The Ni/BAM coating exhibits blue luminescent emission under UV illumination, which could work alone or be incorporated into the coating system to monitor the wear of coatings. Composite Ni-P/MoS_2 and Ni-P/WS_2 coatings have demonstrated enhanced mechanical and frictional properties, displaying low friction coefficients of 0.05 and 0.17 respectively. The properties of these coatings are directly related to their structures which have been controlled by the varying of electrodeposition parameters such as: current, temperature, surfactant and particle concentrations. Systematic comparison and discussion of their effects will be presented here.

8.1 Effect of electrodeposition parameters on coating structure

8.1.1 Current distribution on cathode

As can be found in Fig. 8.1, the morphologies of Ni, Ni/BAM, Ni-P/MoS_2 and Ni-P/WS_2 coatings are totally different, varying from a flat surface to a rough surface. This distinct change is attributed to the diverse growth mechanism in metal and composite electrodeposition.

During the metal electrodeposition process, the metal ions in solution are driven by the Coulomb force E^*q_t (E represents the electric field, q_t represents the charge of ions) and move along the electric field, then become deposits after cathode reduction [223]. As illustrated in Fig. 8.1(a), the driving forces maintain the same value at different sites on the cathode owing to the equal current distribution, resulting in steady and uniform growth of deposits. As a result, the obtained coating usually exhibits a flat surface (Fig. 8.1(b)).

However, the growth model for a deposit is greatly changed in composite electrodeposition due to the introduction of the particles into the electrolyte. When non-conductive particles are added into the electrolytic solution, the electrolytic current is distorted in the vicinity of adsorbed particles as illustrated in Fig. 8.1(c). The BAM

particle ($BaMgAl_{11}O_{17}:Eu^{2+}$, BAM) has a crystal structure of β-alumina, which is electrically insulating. Therefore, Ni will not deposit on the particle and instead grow exclusively on the surrounding area. The resulting Ni/BAM coating exhibits a flat Ni base with some protrusions of BAM particles (Fig. 8.1(d)). Such a surface morphology has also been discovered in other electrodeposited composites like $Ni\text{-}Al_2O_3$ and Ni-diamond [224,225].

For the composite electrodeposition of conducting or semiconducting particles, the electrolytic current will centralize on the top of the adsorbed particles on the cathode which are extended into the solution (Fig. 8.1(e)). The ions in solution move at a higher velocity υ towards these points due to a higher Coulomb force E^*q_t, causing a higher growth rate at these locations. Hence nodular protrusions easily form on the electrodeposited coatings, sometimes producing a porous structure (Fig. 8.1(f, g, h)). Similar rough structures are not only found in WS_2 and MoS_2 electrodeposits [19,20], but also in the Ni-CNT, Ni-SiC electrodeposition systems [226,227].

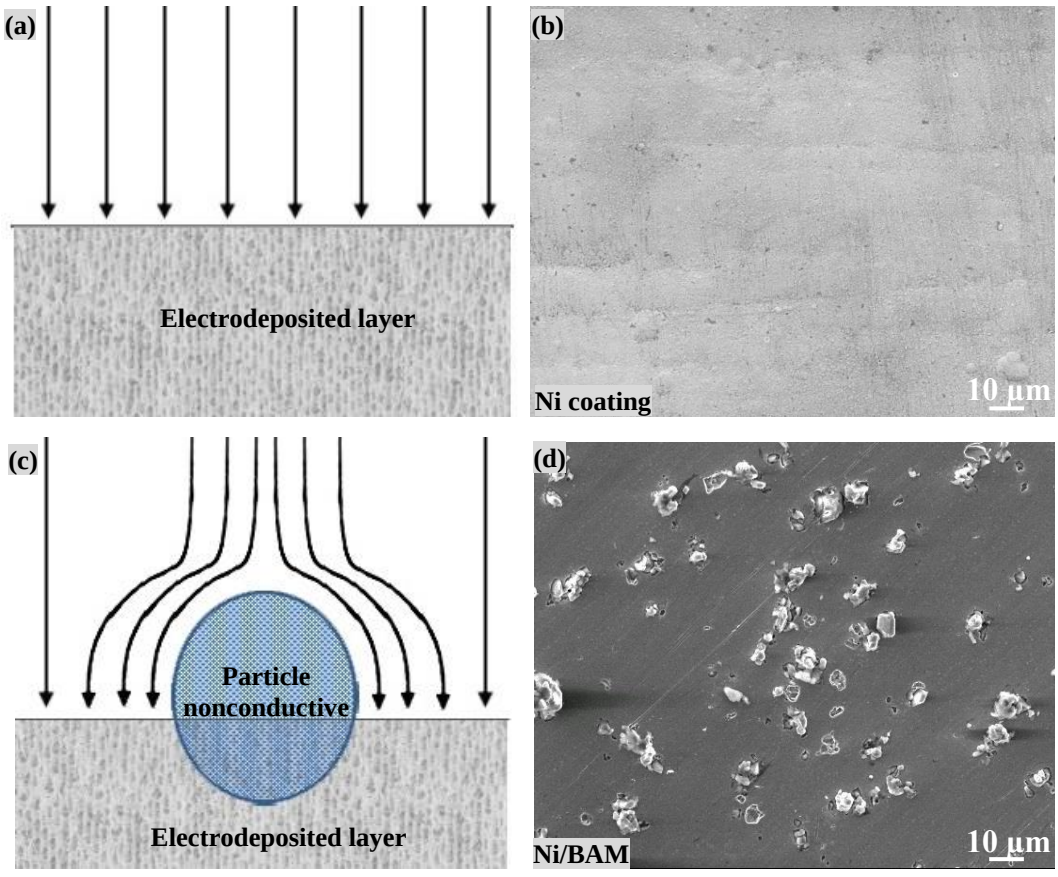

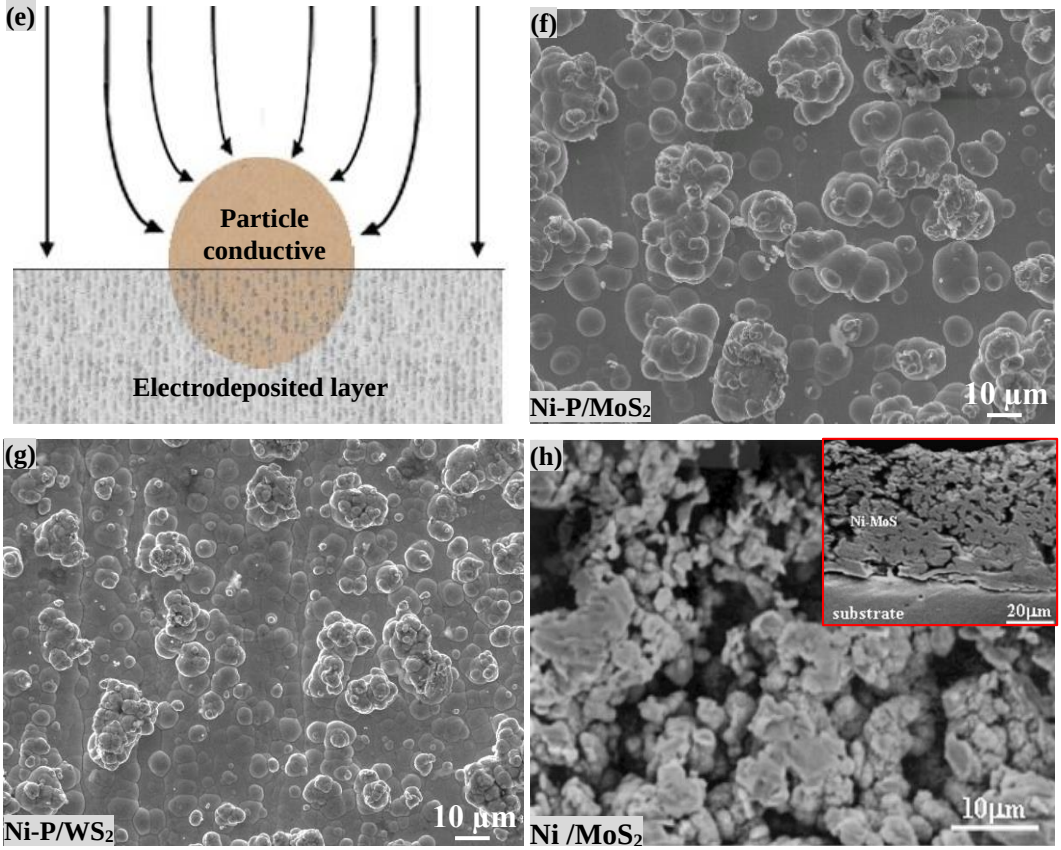

Figure 8.1 (a, c, e) Schematic view of electrolytic current distribution on the cathode without particle, with non-conductive particle and with conductive particle; (b, d, f, g, h) SEI images of as-deposited Ni, Ni/BAM, Ni-P/MoS_2, Ni-P/WS_2 and Ni/MoS_2 coatings; the inset in (h) is the cross-section SEI image of the Ni/MoS_2 coating [19].

8.1.2 Concentration of surfactant and particle

CTAB, $(C_{16}H_{33})N(CH_3)_3Br$, is one of the most common cationic surfactants used in composite electrodeposition, which could effectively charge the suspended particles positively by electrostatic adsorption. The modified particles will be attracted to the cathode surface under the applied potential, having a high possibility of being incorporated into deposits. The effect of CTAB on the Ni/BAM, Ni-P/MoS_2 and Ni-P/WS_2 electrodeposition systems has been summarized in Fig. 8.2. Clearly, the increase of CTAB concentration promotes the amount of the particles being incorporated into all the coatings. However, if the concentration of CTAB rises above 0.2 g/L the Ni-P coating became highly porous and were unable to withstand a high applied load, which is not desired in tribology. Even though the most optimized surfactant concentration is not the same for all these coatings, it is generally accepted that a CTAB concentration of 0.1 g/L is good for preparing a coating with high content of particles and compact structures [228,229].

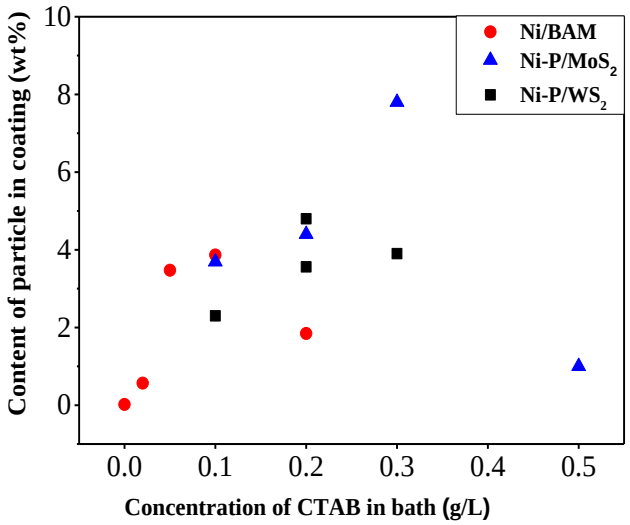

Figure 8.2 Relationship between the particle content in coating and the CTAB concentration in the bath for Ni/BAM, Ni-P/MoS_2 and Ni-P/WS_2 electrodepositions.

According to the Guglielmi and Celis's electrocodeposition model [43, 44], the particles in the bath first adsorb onto the cathode and subsequently are incorporated into the growing metal coating. A higher concentration of particles in the bath can increase the number of adsorbed particles on the cathode, therefore increasing the particle content in the electrodeposited coatings. This trend can be clearly found in all the Ni/BAM, Ni-P/MoS_2, Ni-P/WS_2 coatings (Fig. 8.3). The optimized particle concentration for the Ni/BAM, Ni-P/MoS_2, Ni-P/WS_2 coatings are 5 g/L, 10 g/L, 15 g/L respectively. The variation in value was mainly affected by the particle properties such as density, surface condition, shape and conductivity. Nevertheless, after reaching an optimal value, a further increase of particle concentration usually led to the reduction of particle content in the coating as excessive particles in the bath will agglomerate and sediment out quickly [230].

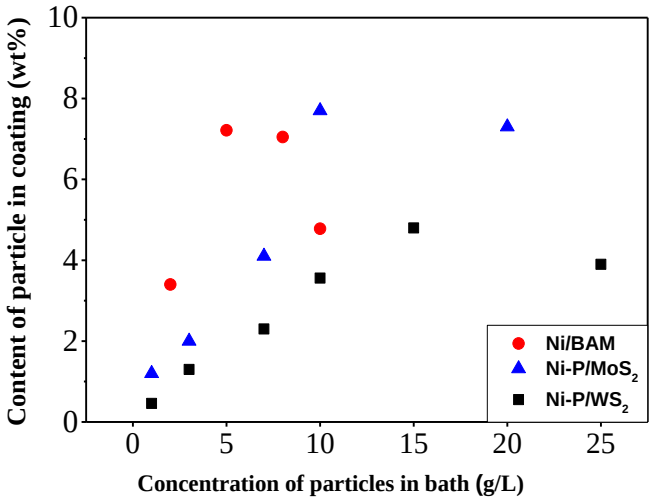

Figure 8.3 Relationship between the particle content in coating and the particle concentration in bath for electrodeposition of Ni/BAM, Ni-P/MoS_2 and Ni-P/WS_2 coatings.

8.1.3 Current density and temperature

Current density and temperature are two critical factors affecting the deposition kinetics of the Ni-P/MoS_2 and Ni-P/WS_2 coatings. At a low current density of 2.5 Adm^{-2} and a high temperature of 60 ℃, the charge transfer stage controls the precipitation kinetics which leads to slow reduction of metal ions on the cathode surface. When the current density is larger than 5 A dm^{-2} or the bath temperature becomes lower than 40 ℃, there will be a shortage of the supply of metal ions to the electrode surface. The diffusion of ions is in the control stage and the electricity current will be partly consumed by the reduction of hydrogen at the cathode surface. This process normally results in high internal stress in the coating, which could generate cracks in the coating once it exceeds the fracture strength of the coating [163, 164,165]. In an extreme case, some parts of the coating would be peeled off from the substrate, as listed in table 8.1.

Table 8.1 Description of the structure of the Ni-P/MoS_2 and Ni-P/WS_2 coatings deposited at different temperature and current density.

Parameters	Coating structure			
Current density	1 Adm^{-2}, compact	2.5 Adm^{-2}, compact	5 Adm^{-2}, crack	7 Adm^{-2}, big crack
Bath temperature	20 ℃, peel off	40 ℃, crack	60 ℃, compact	80 ℃, compact

8.2 Friction coefficient of composite coating

The incorporation of solid lubricants greatly enhances the tribology properties of the coating, but the reported friction coefficients vary a lot in different studies as listed in table 8.2. To explore the relationship between the friction coefficient and the particle content, the friction coefficients of the Ni-P/WS_2 and Ni-P/MoS_2 coatings are summarized in Fig. 8.4. Generally, an increase of the lubricant content in the coating results in a decrease of the friction coefficient, exhibiting the lowest value of 0.05 and 0.17 respectively for the Ni-P/MoS_2 and Ni-P/WS_2 samples. Higher content of lubricants in the coating could create more lubricant “spacer” between the friction surfaces and also form a lubricating tribofilm. The generated lubricating spacer or film is not only effective in reducing the friction coefficient and wear rate, but also in preventing the coating from oxidising.

Table 8.2 Comparison of friction coefficient, particle content in bath and particle content in coating for different electrodeposited MoS_2 or WS_2 composite coatings.

Electrodeposited coatings	Particle concentration	Particle content in coating	Friction coefficient
Ni-MoS_2 [20]	0-30 g/L	0-3 wt%	0.21-0.52
Ni-W-MoS_2 [21]	0-2 g/L	0-37 wt%	0.12-0.31
Ni-Co/MoS_2 [22]	0-1 g/L	0	0.15-0.20
Ni-P/WS_2 [144]	0	74 wt%	0.07

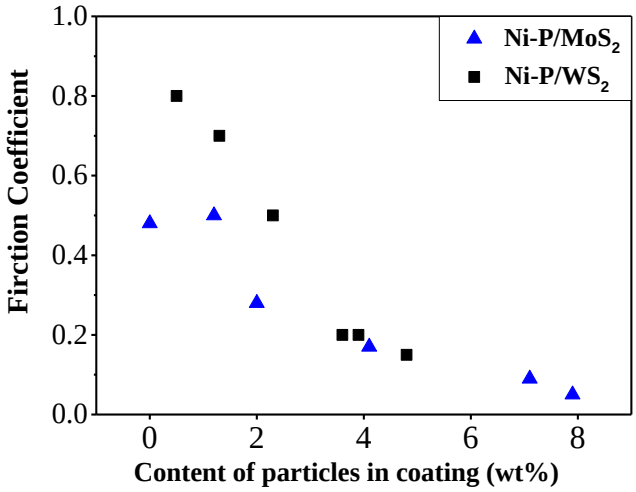

Figure 8.4 Relationship between the friction coefficient and the particle content for Ni-P/MoS_2 and Ni-P/WS_2 coatings.

8.3 Summary

Composite electrodeposition is an important technique for preparation of functional coatings, but the process is much more complex than simple metal electrodeposition. By comparing the Ni-BAM, Ni-P/MoS_2 and Ni-P/WS_2 deposition systems, it can be concluded that the coating structure and property are significantly affected by the following parameters: (1) the conductivity of the particle which changes the growth model of deposits and further affects the surface morphology; (2) the concentration of CTAB and particles in the bath which control the number of the adsorbed particles on the cathode and subsequently determine the particle content in the coating; (3) the applied current density and bath temperature which alter the kinetics of the electrodeposition process and furthermore vary the internal stress.

Chapter 9 Overall conclusions and suggestions for future work

9.1 Overall conclusions

The Ni/BAM luminescent coating, Ni-P/MoS_2 and Ni-P/WS_2 low-friction coatings have been successfully prepared by composite electrodeposition. The main conclusions can be stated as follows:

(1) The cationic surfactant CTAB shows a significant impact on the incorporation of BAM particles by changing the net charge on the particles and increasing the migration force to the cathode, with a high BAM area coverage of 11%. The PEG surfactant stabilises the suspension of particles in the bath by adsorbing on its surface and increasing steric hindrance, producing maximum coverages of 4.6%. A combination of CTAB+PEG in the solution is most effective. By optimizing the plating time and the concentration of BAM in the electrolyte, a maximum BAM area coverage of 15.9% was obtained in the Ni/BAM coating. The luminescent coating displays very intensive blue light emission under UV illumination and the use of embedded luminescent particles to monitor coating health have been demonstrated. Additionally, the Ni/BAM coating exhibited higher hardness, better anti-corrosion ability and lower wear rate compared to pure Ni coatings, suggesting the feasibility of using such Ni/BAM layers for wear sensing in industry.

(2) The electrodeposited Ni-P/MoS_2 coatings exhibit rough surfaces consisting of small nodule protrusions. A low current density of 2.5 A dm^{-2} was applied for electrodeposition to avoid cracking from a high internal stress generated at high current. The embedded amount of the incorporated MoS_2 particles in the coatings mainly depends on the concentrations of the CTAB surfactant and the MoS_2 particles in the bath, since the former could incur positive charge on the surface of particles and hence ensure they are easily attracted by the cathode and the latter controls the *number* of the adsorbed particles on the cathode. Heat treatment of

samples at 400 ℃ for 1 hour has notably increased the hardness of coating to be over 1100 HV, which is strengthened by the generation of Ni_3P precipitates.

(3) The friction coefficient of Ni-P/MoS_2 coating gradually decreases as more MoS_2 particles are incorporated, exhibiting a stable lowest value of 0.05 for the 7.9 wt% MoS_2 coating. Compared to the heavy abrasion wear on a Ni-P coating, this coating only shows slight wear. In addition, oxidation was rarely observed on the Ni-P/MoS_2 7.9 wt% coating during the wear test. Uniform and compact tribofilms abundant in MoS_2 have been found on both coating surfaces and counterpart balls owing to the strong adhesion of MoS_2 with Ni or Fe. The MoS_2 particles in the coating underwent shear stress-induced reorganization, became fine crystallites and dispersed onto amorphous Ni-P to form a tribofilm. The tribofilm could efficiently reduce friction due to the easy shear of MoS_2 lamellas. In the meantime, it prevented heat up and oxidation.

(4) Similar to Ni-P/MoS_2, the electrodeposited Ni-P/nano-WS_2 coating shows a rough surface with many nodule protrusions and the main structure is amorphous/nanocrystal Ni-P. Increasing the bath temperature from 20 ℃ to 60 ℃ eliminated coating cracks by reducing the internal stress in the coating. The increase of the WS_2 and CTAB concentration in the electrolyte causes an obvious increase of the WS_2 content in the coating, producing a highest WS_2 incorporation of 4.8 wt%. An evident drop in friction coefficient has been found in the Ni-P/WS_2 coatings as the WS_2 content increases, with the lowest value of 0.17. The embedded WS_2 particles in the coating were slowly and continuously released to the mating surfaces during the wear and thereby reduced the friction effectively for a long period.

9.2 Suggestions for future work

There are a number of areas where the research can be expanded on and improved through further experiments:

Firstly, the reciprocal wear test on the heat-treated Ni-P/MoS_2 coatings. Heat treatment at 400 ℃ has greatly increased the hardness of Ni-P coatings to 1150 HV due to the crystallization of Ni_3P , which is close to the reported hardness of hard chromium [231].

Secondly, it is worthwhile to do wear tests in other harsh environments such as in a vacuum, as these tests can give a better indication whether these low-friction coatings will be suitable for applications in the aerospace field. Normally WS_2 shows better tribology performance than MoS_2 in vacuum, especially at high temperature although in the air the former has a higher friction coefficient than the latter.

Thirdly, MoS_2 or WS_2 particles with different sizes and special structures like fullerene can be introduced into our coating system to study the effect of the particle size and structure on the self-lubricating property of the coating.

Finally, it would be interesting to combine the low-friction coating with the luminescent coating to make a smart coating. The multiple luminescent layers may provide a good monitoring of wear; a self-lubricating layer is added to ensure low friction. However, the challenges for multilayer coating are around adhesion issues which will influence the quality of any gradient multilayer system.

Appendix A

Calculation of initial contact pressure for spherical contact

As illustrated in Fig. A.1, the coating is considered as an infinite half space. Parameters of the bearing steel ball and the coating are listed in Table A.1.

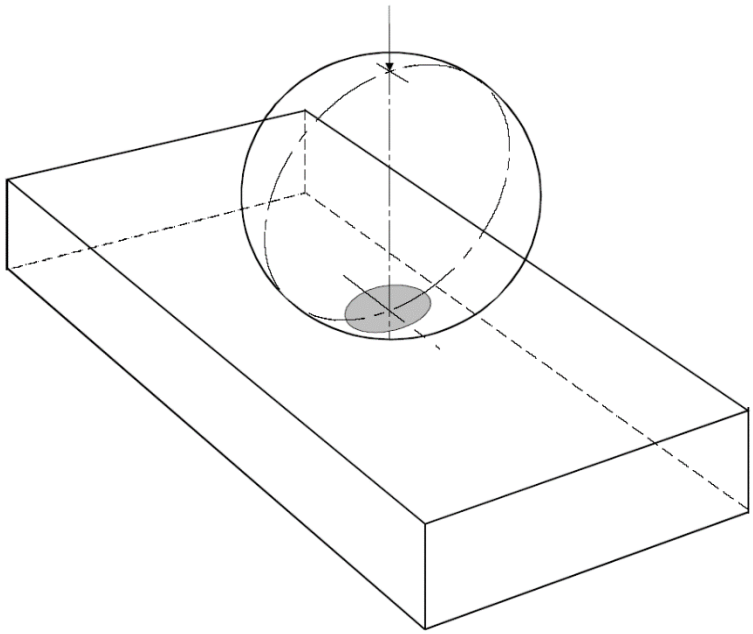

Figure A.1 A ball loaded on to a flat plate [203].

Table A.1 Parameters of pin and coating.

Items	Bearing Steel (Pin)	Ni (Coating)
Young's Modulus /GPa	208	207
Poisson's ratio	0.3	0.3
R / mm	3	∞

The effective radius *R'* and the reduced modulus *E** are determined by the following equations [203]:

$$R' = \left(\frac{1}{R_1} + \frac{1}{R_2}\right)^{-1} = \left(\frac{1}{3} + \frac{1}{\infty}\right)^{-1} = 3\ mm$$

$$E^* = \left(\frac{1 - v_1^2}{E_1} + \frac{1 - v_2^2}{E_2}\right)^{-1} = \left(\frac{1 - 0.3^2}{207} + \frac{1 - 0.3^2}{207}\right)^{-1} = 114\ GPa$$

The contact region under the applied load of 14 N is spherical with a radius *a'* given by:

$$a' = \sqrt[3]{\frac{3NR'}{4E^*}} = 0.065\ mm$$

Then, the peak contact pressure P_0 is given by:

$$P_0 = \frac{3N}{2\pi A a'^2} = 1.58\ G\text{Pa}$$

The yield stress is around 1/3 of the hardness. Thereby no plastic deformation occurs on the coatings with the hardness higher than 4.74 GPa (483 HV).

Appendix B

Research Publications:

The following are research publications generated as part of the work presented in the thesis.

(a) Y. He, S.C. Wang, F.C. Walsh, W.S. Li, L. He, P.A.S. Reed, The monitoring of coating health by in situ luminescent layers, RSC Advances 53 (2015) 42965-42970.
(b) Y. He, S.C. Wang, F.C. Walsh, W.S. Li, P.A.S. Reed, Self-lubricating Ni-P/MoS2 composite coating and shear-induced reorganization of particles (Submitted).

Conferences Attended:

- Microscience Microscopy Congress, 2015, Manchester, UK *(Poster).*
- Gordon Research Conference: Tribology, 2014, Boston, USA *(Poster).*
- Materials Research Exchange, 2014, Coventry, UK *(Poster).*
- 22nd Mission of Tribology Research, 2013, London, UK *(Talk*).

References:

1 K. Holmberg, M. Matthews, H. Ronkainen, Coatings tribology-contact mechanics and surface design, Tribology International 31 (1998) 107.

2 A. Siddhpura, R. Paurobally, A review of flank wear prediction methods for tool condition monitoring in a turning process, The International Journal of Advanced Manufacturing Technology 65 (2013) 371.

3 J. P. Feist, A. L. Heyes, Photo-Stimulated Phosphorescence for Thermal Condition Monitoring and Non destructive Evaluation in Thermal Barrier Coatings, Heat Transfer Engineering 30 (2009) 1087.

4 M.M. Gentleman, D.R. Clarke, Concepts for luminescence sensing of thermal barrier coatings. Surface and Coatings Technology 188 (2004) 93.

5 J.I. Eldridge, T.J. Bencic, Monitoring delamination of plasma-sprayed thermal barrier coatings by reflectance-enhanced luminescence, Surface and Coatigs Technology 201 (2006) 3926.

6 C. Muratore, D.R. Clarke, J.G. Jones, A.A. Voevodin, Smart tribological coatings with wear sensing capability, Wear 265 (2008) 913.

7 Surface Technology, Inc., Illuminating wear with composite electroless nickel coatings, Nickel 24 (2009) 9.

8 M. Maloney, Thermal barrier coating systems and materials, 2000, U.S. Patent 6,117,560.

9 M. Ganapathi, S.V. Eliseeva, N.R. Brooks, D. Soccol, J. Fransaer, K. Binnemans, Electrodeposition of luminescent composite metal coatings containing rare-earth phosphor particles, Journal of Materials Chemistry 22 (2012) 5514.

10 S.X. Zhang, T. Kono, A. Ito, T. Yasaka, H. Uchiike, Degradation mechanisms of the blue-emitting phosphor $BaMgAl_{10}O_{17}:Eu^{2+}$ under baking and VUV-irradiating treatments, Journal of Luminescence 106 (2004) 39.

11 F.D. Torre, H.V. Swygenhoven, M. Victoria, Nanocrystalline electrodeposited Ni: microstructure and tensile properties, Acta Materialia 50 (2002) 3957.

12 E. Gómez, S. Pané, E. Vallés, Electrodeposition of Co-Ni and Co-Ni-Cu systems in sulphate-citrate medium, Electrochimica Acta 51 (2005) 146.

13 L. Wang, J. Zhang, Y. Gao, Q. Xue, L. Hu, T. Xu, Grain size effect in corrosion behaviour of electrodeposited nanocrystalline Ni coatings in alkaline solution, Scripta Materialia 55 (2006) 657.

14 C. Ma, S.C. Wang, R.J. Wood, J. Zekonyte, Q.S. Luo, F. Walsh, The hardness of porous nanocrystalline Co-Ni electrodeposits. Metals and Materials International 19 (2013) 1187.

15 C. Ma, S.C. Wang, L.P. Wang, F.C. Walsh, R.J.K. Wood, The electrodeposition and characterisation of low-friction and wear-resistant Co-Ni-P coatings, Surface and Coatings Technology 235 (2013) 495.

16 C.T.J. Low, R.G.A. Wills, F.C. Walsh, Electrodeposition of composite coatings containing nanoparticles in a metal deposit, Surface and Coatings Technology, 201 (2006) 371.

17 F.C. Walsh, C. Ponce de Leon, A review of the electrodeposition of metal matrix composite coatings by inclusion of particles in a metal layer: An established and diversifying coatings technology, Transactions of the Institute of Materials Finishing 92 (2014) 83.

18 L. Rapoport, N. Fleischer and R. Tenne, Applications of WS_2(MoS_2) inorganic nanotubes and fullerene-like nanoparticles for solid lubrication and for structural nanocomposites, Journal of Material Chemistry 15 (2005) 1782.

19 L.M. Wang, Effects of surfactant BAS on MoS_2 codeposition behaviour, Journal of Applied Electrochemistry 38 (2008) 245.

20 Z.J. Huang, D.S. Xiong, MoS_2 coated with Al_2O_3 for Ni-MoS_2/Al_2O_3 composite coatings by pulse electrodeposition, Surface and Coatings Technology 202 (2008) 3208.

21 M.F. Cardinal, P.A. Castro, J. Baxi, H. Liang, F.J. Williams, Characterization and frictional behaviour of nanostructured Ni-W-MoS_2 composite coatings, Surface and Coatings Technology 204 (2009) 85.

22 L. Shi, C. Sun, W. Liu, Electrodeposited nickel-cobalt composite coating containing MoS_2, Applied Surface Science 254 (2008) 6880.

23 T. Bell, Towards a universal surface engineering road map, Surface Engineering 16 (2000) 89.

24 A. Clarke, A. Partridge, A strategic review of the surface engineering industry in the UK, 2006, NAMTEC.

25 C. Larson, Contract coaters, customers and closeness, Transactions of the IMF 78 (2000) 67.

26 J. R. Nicholls, Design of oxidation resistant coatings, Journal of the Minerals 52 (2000) 28.

27 A. Matthews, R. Artley, P. Holiday, 2005 revisited; the UK surface engineering industry to 2010, Surface Engineering Centre (NASURF), Farnborough, UK,1998.

28 S. J. Bull, Surface engineering in UK academia, Surface Engneering 13 (1997) 177.

29 D. Kennedy, Y. Xue, E. Mihaylova, Current and future applications of surface engineering, The Engineers Journal 59 (2005) 287.

30 K.Holmberg, A. Matthews, “Coatings TribologyTribology Series, 28 (series ed. D. Dowson) Elsevier, Amsterdam, 1994.

31 T. Horiuchi, K. Yoshida, M. Kano, M. Kumagai, T. Suzuki, Evaluation of DLC coating damage in the delamination and wear test, Tribology Online 5 (2010) 129.

32 R.C. Jaeger, Film Deposition - Introduction to Microelectronic Fabrication (2nd edition), Upper Saddle River: Prentice Hall, 2002, ISBN 0-201-44494-1.

33 P.J. Kelly, R.D. Arnell, Magnetron sputtering: a review of recent developments and applications, Vacuum 56 (2000) 159.

34 B. Wolf, Handbook of ion sources, CRC Press, 1995, ISBN 0-8493-2502-1.

35 L. Pawlowski, Finely grained nanometric and submicrometric coatings by thermal spraying: a review, Surface and Coatings Technology 202 (2008) 4318.

36 J. Coxon, Thermal spraying of liners, 2011. Accessed on 25th August 2015 [Online]. Available: https://www.highpowermedia.com/blog/3136/thermal-spraying-of-liners

37 C.U. Hardwicke, Y.C. Lau, Advances in thermal spray coatings for gas turbines and energy generation: a review, Journal of Thermal Spray Technology 22(5) (2013) 564.

38 I. Gurrappa, L. Binder, Electrodeposition of nanostructured coatings and their characterization - a review, Science and Technology of Advanced Materials 9 (2008) 043001.

39 B. Reddy, Advances in nanocomposites - synthesis, characterization and industrial applications, InTech, 2011.

40 Electroplating Wiki, Tangient LLC. Accessed on 25th August 2015 [Online]. Available: http://electroplating.wikispaces.com/

41 D. Thiemig, Investigation on the mechanism of electrocodeposition and the structure-properties correlation of nickel nanocomposites, 2009 (Doctoral dissertation, Dresden University of Technology).

42 E.A. Brandes, D. Goldthorpe, Electrodeposition of cermets.Metallurgia, 76 (1967) 195.

43 N. Guglielmi, Kinetics of the deposition of inert particles from electrolytic baths, Journal of Electrochemistry Society 119 (1972) 1009.

44 J.P. Celis, J.R. Roos, C. Buelens, A mathematical model for the electrolytic codeposition of particles with a metallic matrix, Journal of Electrochemistry Society 134 (1987) 1402.

45 B.J. Hwang, C.S. Hwang, Mechanism of Codeposition of Silicon Carbide with Electrolytic Cobalt, Journal of Electrochemistry Society 140 (1993) 979.

46 J. Fransaer, J.P. Celis, J.R. Roos, Analysis of the eectrolytic codeposition of non-brownian particles with metals, Journal of Electrochemistry Society 139 (1992) 413.

47 P.M. Vereecken, I. Shao, P.C. Searson, Particle codeposition in nanocomposite film, Journal of Electrochemistry Society 147 (2000) 2572.

48 P. Bercot, E. Pena-Munoz, J. Pagetti, Electrolytic composite Ni–PTFE coatings: an adaptation of Guglielmi's model for the phenomena of incorporation, Surface and Coatings Technology, 157 (2002) 282.

49 I. Shao, P.M. Vereecken, R.C. Cammarata, P.C. Searson, Kinetics of particle codeposition of nanocomposites, Journal of Electrochemistry Society 149 (2002) C610.

50 R.J. Hunter, Foundations of Colloid Science, 2nd edition, Oxford University Press, Oxford, New York, 2001.

51 A.J. Bard, L.R. Faulkner, Electrochemical methods: fundamentals and applications, 2nd Edition, John Wiley and Sons, New York, 2001.

52 D. Kopeliovich, Stabilization of colloids, 2013. Accessed on 25th August 2015 [Online]. Available: https:// http://www.substech.com/dokuwiki/doku.php?id=stabilization_of_colloids

53 Malvern Instruments Ltd., Zetasizer Nano Series User Manual, Issue 2.1, Worcestershire, UK, 2004.

54 E.J.W. Verwey, J.T.G. Overbeek, Theory of the stability of lyophobic colloids, Elsevier Publish Company, Amsterdam, 1948.

55 D. Myers, Surfaces, Interfaces and Colloids - Principles and Applications, 2nd edition, Wiley-VCH, New York, 1999.

56 SunKart, Steric and gel network stabilization, Wikipedia. Accessed on 25th August 2015 [Online]. Available: https://en.wikipedia.org/wiki/Colloid

57A. Siddhpura, R. Paurobally, A review of flank wear prediction methods for tool condition monitoring in a turning process, The International Journal of Advanced Manufacturing Technology 65 (2013) 371.

58 A. Flink, R. M'Saoubi, F. Giuliani, J. Sjöl én, T. Larsson, P.O.Å. Persson, M.P. Johansson, L. Hultman, Microstructural characterization of the tool-chip interface enabled by focused ion beam and analytical electron microscopy, Wear 266 (2009) 1237.

59 D. E. Dimla, Sensor signals for tool-wear monitoring in metal cutting operations - a review of methods, International Journal of Machine Tools and Manufacture 40 (2000) 1073.

60 J.L. Miller, D. Kitaljevich, In-line oil debris monitor for aircraft engine condition assessment, Proceedings of the IEEE Aerospace Conference 6 (2000) 49.

61 Lubrication System Diagnostic Sensors, Tedeco Products. Accessed on 25th August 2015 [Online]. Available: http://www.tedecoindustrial.com/electric.htm

62 Chip Detectors, Allen Aircraft Products, Inc. Accessed on 25th August 2015 [Online]. Available: http://www.allenaircraft.com/products/chip_detectors.html

63 W.A. Glaaeser, Wear rdebris classification, Modern tribology handbook by B. Bhushan, CRC Press, 2000.

64 Y. Iwai, T. Honda, T. Miyajima, S. Yoshinaga, M. Higashi, Y. Fuwa, Quantitative estimation of wear amounts by real time measurement of wear debris in lubricating oil, Tribology International 43 (2010) 388.

65 H.H. Shahabi, M.M. Ratnam, In-cycle monitoring of tool nose wear and surface roughness of turned parts using machine vision, The International Journal of Advanced Manufacturing Technology 40 (2008) 1148.

66 A. Zawada-Tomkiewicz, Analysis of surface roughness parameters achieved by hard turning with the use of PCBN tools, Estonian Journal of Engineering 17 (2011) 88.

67 S. Dallaire, M. Dufour, B. Gauthier, Characterization of wear damage in coatings by optical profilometry, Journal of Thermal Spray Technology 2 (1993) 363.

68 Y.K. Potdar, A.T. Zehnder, Measurements and simulations of temperature and deformation fields in transient metal cutting, Journal of Manufacturing Science and Engineering 125 (2003) 645.

69 K. Heidabeigi, H. Ahmadi, M. Omid, Adaptive vibration condition monitoring techniques for local tooth damage in gearbox, Modern Applied Science 4 (2010)104.

70 X. Li, A brief review: acoustic emission method for tool wear monitoring during turning. International Journal of Machine Tools and Manufacture 42 (2002) 157.

71 A. Siddhpura, R. Paurobally, A review of flank wear prediction methods for tool condition monitoring in a turning process, The International Journal of Advanced Manufacturing Technology 65 (2013) 371.

72 J. Bhaskaran, M. Murugan, N. Balashanmugam, M. Chellamalai, Monitoring of hard turning using acoustic emission signal, Journal of Mechanical Science and Technology 26 (2012) 609.

73 Z.Q. Zhang, G.L. Li, H.D. Wang, B.S. Xu, Z.Y. Piao, L.N. Zhu,Investigation of rolling contact fatigue damage process of the coating by acoustics emission and vibration signals, Tribology International 47 (2012) 25.

74Y.K. Potdar, A.T. Zehnder, Measurements and Simulations of Temperature and Deformation Fields in Transient Metal Cutting, Journal of Manufacturing Science and Engineering 125 (2003) 645.

75 D.K. Dwivedi, Sliding temperature and wear behaviour of cast Al-Si-Mg alloys, Materials Science and Engineering: A 382 (2004) 328.

76 A. Al-Habaibeh, R. Parkin, An autonomous low-cost infrared system for the on-line monitoring of manufacturing processes using novelty detection. The International Journal of Advanced Manufacturing Technology, 22 (2003) 249.

77 M.A. Davies, H. Yoon, T. L. Schmitz, T.J. Burns, M.D. Kennedy, Calibrated thermal microscopy of the tool-chip interface in machining, Machining Science and Technology 7 (2003) 167.

78 R.N.S. Rao, D.N. Rao, C.H.S. Rao, Online prediction of diffusion wear on the flank through tool tip temperature in turning using artificial neural networks, Proceedings of the Institution of Mechanical Engineers, Part B: Journal of Engineering Manufacture 220 (2006) 2069.

79 J.I. Eldridge, T.J. Bencic, C.M. Spuckler, J. Singh, D.E. Wolfe, Delamination-indicating thermal barrier coatings using YSZ:Eu sublayers, Journal of the American Ceramic Society 89 (2006) 3246.

80 W. Liu, Y. Wang, L. Cheng, Eu^{3+}-Doped YPO_4 Self-Monitoring Environmental Barrier Coating, Journal of the American Ceramic Society 94 (2011) 3449.

81 C.N. Xu, Y. Imai, Y. Adachi, Stress luminescent composition containing anisotropic stress luminescent materials and method of producing the same,Us 20060035079A1, 2006.

82 National Institute of Advanced Industrial Science and Technology, Japan, Visualization Technology for "Invisible" Danger, NDT.net, 2009. Accessed on 25th August 2015 [Online]. Available: http://www.ndt.net/search/docs.php3?id=7506&content=1

83 B.P.Chandra, in Luminescence of Solids (ed. D.R. Vij) , Plenum, New York, 1998.

84 J.A. Deluca, An introduction to luminescence in inorganic solids, Journal of Chemical Education 57 (1980) 541.

85 T.J.C. Feldmann, C.R. Ronda, P.J. Schmidt, Inorganic luminescent materials: 100 years of research and application, Advanced Functional Materials 13 (2003) 511.

86 M. Koedam, J.J. Opstelten, Measurement and computer-aided optimization of spectral power distributions, Lighting Research & Technology 3 (1971) 295.

87 C.R. Ronda , T. Justel, H. Nikol, Rare earth phosphors: fundamentals and applications, Journal of Alloys and Compounds 275 (1998) 669.

88 M.D. Feldstein, Composite coatings with light-emitting properties, Metal Finishing 97 (1999) 87.

89 N. Feldstein, Composite plated articles having light-emitting properties, 1996, US Patent 5516591.

90 C.M. Das, A.K. Grover, A.K. Suri, Co-deposition of luminescent particles with electroless nickel, Transactions of The Institute of Metal Finishing 80 (2002) 128.

91 L. Stappers, J. Fransaer, AFM study of the incorporation of particles during electrodeposition, Journal of Electrochemistry Society 154 (2007) D598.

92 S. Tangjitsitcharoen, C. Rungruang, N. Pongsathornwiwat, Advanced monitoring of tool wear and cutting states in CNC turning process by utilizing sensor fusion, Advanced Materials Research 189 (2011) 377.

93 J.H. Chang, F.Y. Hsu, M.J. Liao, C.A. Huang, A study of direct- and pulse-current chromium electroplating on rotating cylinder electrode, Applied Surface Science 253 (2007) 6829.

94 C.A. Huang, K.C. Li, W. Lin, M.C. Liao, The behaviour of electroplated hard-chromium on Cr-Mo steel subject to long-term annealing at 250 ℃, Materials Science and Engineering A 403 (2005) 222.

95 Z. Zeng, L. Wang, A. Liang, J. Zhang, Tribological and electrochemical behavior of thick Cr-C alloy coatings electrodeposited in trivalent chromium bath as an alternative to conventional Cr coatings, Electrochim Acta 52 (2006) 1366.

96 Z. Zeng, J. Zhang, Anti-wear properties of Cr-C and Ni-Co alloy coatings as substitutes for conventional nanocrystalline Cr coatings, Journal of Physics D: Applied Physics 41 (2008) 185303.

97 Z. Zeng, A. Liang, J. Zhang, Electrochemical corrosion behaviour of chromium-phosphorus coatings electrodeposited from trivalent chromium baths, Electrochimica Acta 53 (2008) 7344.

98 Nickel and nickel alloy plating operations: controlling the risk of skin exposure, Surface Engineering Association, Birmingham, UK, 2011.

99 K. Legg, Chromium and Cadmium Replacement Options for Advanced Aircraft, ROWAN TECHNOLOGY GROUP LIBERTYVILLE IL, 2003.

100 S. Eskin, O. Berkh, G. Rogalsky, J. Zahavi, Co-W alloys for replacement of conventional hard chromium, Plating and Surface Finishing 85 (1998) 79.

101 H.Z. Wang, S.W. Yao, S. Matsumura, Preparation, characterization and the study of the thermal strain in Ni-W gradient deposits with nanostructure, Surface and Coatings Technology 157 (2002) 166.

102 H. Capel, P.H. Shipway, S.J. Harris, Sliding wear behaviour of electrodeposited cobalt-tungsten and cobalt-tungsten-iron alloys, Wear 255 (2003) 917.

103 J.Y. Song, J. Yu, Residual stress measurements in electroless plated Ni-P films, Thin Solid Films 415 (2002) 167.

104 P. Sampath Kumar, P. Kesavan Nair, Studies on crystallization of electroless Ni-P deposits, Journal of Materials Processing Technology 56 (1996) 511.

105 K.H. Hur, J.H. Jeong, D.N. Lee, Microstructures and crystallization of electroless Ni-P deposits, Journal of Material Science 25 (1990) 2573.

106 H.C. Huang, S.T. Chung, S.J. Pan, W.T. Tsai, C.S. Lin, Microstructure evolution and hardening mechanisms of Ni-P electrodeposits, Surface and Coatings Technology 205 (2010) 2097.

107 C.S. Lin, C.Y. Lee, F.J. Chen, W.C. Li, Structural evolution and internal stress of nickel-phosphorus electrodeposits, Journal of Electrochemistry Society 152 (2005) 370.

108 K.H. Hou, M.C. Jeng, M.D. Ger, The heat treatment effects on the structure and wear behaviour of pulse electroforming Ni-P alloy coatings, Journal of Alloys and Compounds 437 (2007) 289.

109 X. Ji, S. Yang, J. Zhao, C. Yan, L. Jiang, Effect of Heat Treatment on Slurry Erosion Wear Resistance of Amorphous Ni-P Electrodeposits, Tribology Transactions 55 (2012) 86.

110 H.G. Schenzel, H. Kreye, Improved corrosion resistance of electroless nickel-phosphorus coatings, Plating Surface Finishing 77 (1990) 50.

111 B. Gillot, K. EI Amri, P. Pouderoux, J.P. Bonino, A. Rousset, Corrosion resistance in oxygen of electrolytic nickel and cobalt phosphorus coatings, Journal of Alloys and Compounds 189 (1992) 151.

112 D.H. Jeong, F. Gonzalez, G. Palumbo, K.T. Aust, U. Erb, The effect of grain size on the wear properties of electrodeposited nanocrystalline nickel coatings, Scripta Material 44 (2001) 493.

113 D.H. Jeong, U. Erb, K.T. Aust, G. Palumbo, The relationship between hardness and abrasive wear resistance of electrodeposited nanocrystalline Ni–P coatings, Scripta Materialia, 48 (2003) 1067.

114 L.P. Wang, Y. Gao, Q.J. Xue, H.W. Liu, T. Xu, A novel electrodeposited Ni-P gradient deposit for replacement of conventional hard chromium, Surface and Coatings Technology 200 (2006) 3719.

115 M.H. Staia, C. Eniruqez, F.S. Puchi, Influence of the heat treatment on the abrasive wear resistance of electroless Ni-P, Surface and Coatings Technology 94 (1997) 543.

116 G. Straffelini, D. Colombo, A. Molinari, Surface durability of electroless Ni-P composite deposits, Wear 236 (1999) 179.

117 H. Capel, P.H. Shipway, S.J. Harris, Sliding wear behaviour of electrodeposited cobalt-tungsten and cobalt-tungsten-iron alloys, Wear 255 (2003) 917.

118 V.D. Papachristos, C.N. Panagopoulos, P. Leisner, M.B. Olsen, U. Wahlstrom, Sliding wear behaviour of Ni-P-W composition-modulated coatings, Surface and Coatings Technology 105 (1998) 224.

119 A. Erdemir. Solid lubricants and self-lubricating films, Modern Tribology Handbook, B. Bhushan (Ed). CRC Press, USA, 2001.

120 K. Miyoshi, Solid lubricants and coatings for extreme environments: state-of-the-art survey. Glenn Research Center, Cleveland, Ohio, 2007.

121 J.F. Yang, B. Parakash, J. Hardell, Q.F. Fang, Tribological properties of transition metal di-chalcogenide based lubricant coatings. Frontiers of Materials Science, 6 (2012) 116.

122 N.M. Renevier, J. Hamphire, V.C. Fox, J. Witts, T. Allen, D.G. Teer, Advantages of using self-lubricating, hard, wear-resistant MoS_2-based coatings, Surface and Coatings Technology 142 (2001) 67.

123 T. Spalvins, J.S. Przybyszewski, Deposition of sputtered molybdenum disulphide films and friction characteristics of such films in vacuum, NASA TN D-4269, 1967.

124 T. Spalvins. Deposition of MoS_2 films by physical sputtering and their lubrication properties in vacuum, ASLE Transaction 12 (1969) 36.

125 J.M. Martin, H. Pascal, C. Donnet, T. LeMogne, J.L. Loubet, T. Epicier, Superlubricity of MoS_2: crystal orientation mechanisms, Surface and Coatings Technology 68 (1994) 427.

126 G.D. Gamulya, T.A. Kopeteva, I.L. Lebedeva, Effect of low temperatures on the wear mechanism of solid lubricant coatings in vacuum, Wear 160 (1993) 351.

127 J.F. Yang, Y. Jiang, J. Hardell, B. Prakash, Q.F. Fang, Influence of service temperature on tribological characteristics of self-lubricant coatings: A review, Frontiers of Materials Science 7 (2013) 28.

128 H.E. Sliney, High temperature solid lubricants, Part I: Layered lattice compounds and graphite. ASME Journal of Mechanical Engineering 96 (1974) 18.

129 A.K. Kohli, B. Prakash, Contact pressure dependency in frictional behaviour of burnished molybdenum disulphide coatings, Tribology Transactions 44(2001) 147.

130 A. Erdemir, Review of engineered tribological interfaces for improved boundary lubrication, Tribology International 38 (2005) 249.

131 J.S. Zabinski, M.S. Donley, S.D. Walck, T.R. Schneider, N.T. Mcdevitt, The effects of dopants on the chemistry and tribology of sputter-deposited MoS_2 films, Tribology Transactions 38 (1995) 894.

132 P. Niederhauser, H.E. Hintermann, M. Maillat, Moisture-resistant MoS_2-based composite lubricant films, Thin Solid Films 108 (1983) 209.

133 T. Spalvins, Frictional and morphological properties of Au-MoS_2 films sputtered from a compact target, Thin Solid Films 118 (1984) 375.

134 M.R. Hilton, R. Bauer, S.V. Didziulis, M.T. Dugger, J. Keem, J. Scholhamer, Structural and tribological studies of MoS_2 solid lubricant films having tailored metal-multilayer nanostructures, Surface and Coatings Technology 53 (1992)13.

135 D.G. Teer, J. Hampshire, V. Fox, V. Bellido-Gonzalez, The tribological properties of MoS_2 metal composite coatings deposited by closed field magnetron sputtering, Surface and Coatings Technology 94 (1997) 572.

136 N.M. Renevier, N. Lobiondo,V.C. Fox, D.G. Teer, J. Hampshire, Performance of MoS_2 metal composite coatings used for dry machining and other industrial applications, Surface and Coatings Technology 123 (2000) 84.

137 D.G. Teer, New solid lubricant coatings, Wear 251 (2001) 1068.

138 M.C. Simmonds, A. Savan, E Pflüger, H. Van Swygenhoven, Mechanical and tribological performance of MoS_2 co-sputtered composites, Surface and Coatings Technology126 (2000) 15.

139 L. Benea, P.L. Bonora, A. Borello, S. Martelli, F. Wenger, P. Ponthiaux, J. Galland, Composite electrodeposition to obtain nanostructured coatings, Journal of The Electrochemical Society148 (2001) 461.

140 K.H. Hou, M.D. Ger, L.M. Wang, S.T. Ke, The wear behaviour of electro-codeposited Ni-SiC composites, Wear 253 (2002) 994.

141 P. Narasimman, M. Pushpavanam, V.M. Periasamy, Wear and scratch resistance characteristics of electrodeposited nickel-nano and micro SiC composites, Wear 292 (2012) 197.

142 G. Wu, N. Li, D. Zhou, K. Mitsuo, Electrodeposited Co-Ni-Al_2O_3 composite coatings, Surface and Coatings Technology 176 (2004) 157.

143 G.H. Xu, M.H. Zhu, J.J. Liu, Z.R. Zhou, H. Liang, The effect of pre-treatment of substrate on fretting tribological behavior of MoS_2 coatings, Wear 255 (2003) 246.

144 W.X. Chen, J.P. Tu, Z.D. Xu, R. Tenne, R. Rosenstveig, W.L. Chen, H.Y. Gan, Wear and Friction of Ni-P electroless composite coating including inorganic fullerene-WS_2 nanoparticles, Advanced Engineering Materials, 4 (2002) 686-690.

145 M. Redlich, A. Gorodnev, Y. Feldman, I. Kaplan-Ashiri, R. Tenne, N. Fleischer, M. Genut, N. Feuerstein, Friction reduction and wear resistance of electro-co-deposited inorganic fullerene-like WS_2 coating for improved stainless steel orthodontic wires, Journal of Materials Research 23 (2008) 2909.

146 B. Andrés, F. Gustavsson, F. Svahn, S. Jacobson, Performance and tribofilm formation of a low-friction coating incorporating inorganic fullerene like nano-particles, Surface and Coatings Technology, 206 (2012) 2325.

147 L. Rapoport, M. Lvovsky, I. Lapsker, V. Leshchinsky, Y. Volovik, Y. Feldman, A. Margolin, R. Rosentsveig, R. Tenne, Slow release of fullerene-like WS_2 nanoparticles from Fe-Ni graphite matrix: a self-lubricating nanocomposite, Nano Letters 1 (2001) 137.

148 S. Ranganatha, T.V. Venkatesha, K. Vathsala, Electroless Ni-W-P coating and its nano-WS_2 composite: Preparation and Properties, Industrial & Engineering Chemistry Research, 51 (2012) 7932.

149 S. Sahin, Effects of boronizing process on the surface roughness and dimensions of AISI 1020, AISI 1040 and AISI 2714, Journal of materials processing technology 209 (2009) 1736.

150 Automatic determination of particle size distribution, Accessed on 25th August 2015 [Online]. http://www.microscopy.ethz.ch/downloads/particle-size.pdf

151 How does MeX work? Accessed on 25th August 2015 [Online]. Available: http://www.alicona.co.uk/home/products/mex/technical-principle.html

152 R. Egerton, Physical principles of electron microscopy: an introduction to TEM, SEM, and AEM, Springer, 2005.

153 H.G. Jiang, M. Rühle, E.J. Lavernia, On the applicability of the x-ray diffraction line profile analysis in extracting grain size and microstrain in nanocrystalline materials, Journal of materials research 14 (1999) 549.

154 A.K. Singh, Advanced x-ray techniques in research and industry, (2005). IOS Press.

155 T. Ungár, G. Tichy, J. Gubicza, R.J. Hellmig, Correlation between subgrains and coherently scattering domains, Powder Diffraction 20 (2005) 366.

156 D. Chicot, J. Lesage, Absolute hardness of films and coatings, Thin Solid Films 254 (1995) 123.

157 Macroscopic and Microscopic Examination of Weld Hardness. Accessed on 25th August 2015 [Online]. Available: http://www.weldpedia.com/2014/10/macroscopic-and-microscopic-examination.html

158 C. Ma, Electrodeposited nanocrystalline Ni-Co and Co-Ni-P coatings for hard chromium replacement, 2013 (Doctoral dissertation, University of Southampton).

159 N.G. Thompson. J.H. Payer, DC electrochemical test methods, 1998, ISBN-1877914630.

160 F. Mansfeld, K. Oldham, A modification of the Stern-Geary linear polarization equation, Corrosion Science, 11(1971) 787.

161 Y. Tsuru, M. Nomura, F.R. Foulkes, Effects of chloride, bromide and iodide ions on internal stress in films deposited during high speed nickel electroplating from a nickel sulfamate bath, Journal of Applied Electrochemistry 30 (2000) 231.

162 M. Zemanova, M. Krivosudska, M. Chovancova, V. Jork, Pulse current electrodeposited nanocrystalline Ni-W and Ni-Fe-W alloys, Materials Science and Engineering A 39 (2007) 460.

163 A.G. McCormack, M.J. Pomeroy, V.J. Cunnane, Microstructural development and surface characterization of electrodeposited nickel/yttria composite coatings, Journal of the Electrochemical Society 150 (2003) C356.

164 S.H. Kim, H.J. Sohn, Y.C. Joo, Y.W Kim, T.H. Yim, H.Y. Lee, T. Kang, Effect of saccharin addition on the microstructure of electrodeposited Fe-36 wt.% Ni alloy, Surface and Coatings Technology 199 (2005) 43.

165 J.K. Yu, M.Z. Wang, L.I. Qun, Y. Jun, L. Lian, Effects of saccharin on microstructure and property of electro-deposited Ni-Fe alloys, Transactions of Nonferrous Metals Society of China 19 (2009) 805.

166 Y. Li, H. Jiang, D. Wang, H. Ge, Effects of saccharin and cobalt concentration in electrolytic solution on microhardness of nanocrystalline Ni-Co alloys, Surface and Coatings Technology 202 (2008) 4952.

167 X.Y. Yuan, Y. Wang, D. Sun, H. Yu, Influence of pulse parameters on the microstructure and microhardness of nickel electrodeposits, Surface and Coatings Technology 202 (2008) 1895.

168 L. Benea, P.L. Bonora, A. Borello, S. Martelli, F. Wenger, P. Ponthiaux, J. Galland, Preparation and investigation of nanostructured SiC–nickel layers by electrodeposition, Solid State Ionics 151 (2002) 89.

169 S. Ekambaram, K.C. Patil, M. Maaza, Synthesis of lamp phosphors: facile combustion approach, Journal of Alloys Compound 393 (2005) 81.

170 S.J. Kim, D. Joseell, T.P. Moffat, Electrodeposition of Cu in the PEI-PEG-Cl-SPS additive system: reduction of overfill bump formation during super filling electrochemical/chemical deposition and etching, Journal of Electrochemistry Society 153 (2006) 616.

171 S.C. Wang, Z. Zhu, M.J. Starink, Estimation of dislocation densities in cold rolled Al-Mg-Cu-Mn alloys by combination of yield strength data, EBSD and strength models, Journal of microscopy 217 (2005) 174.

172 R. Mishra, R. Balasubramaniam, Effect of nanocrystalline grain size on the electrochemical and corrosion behavior of nickel, Corrosion Science 46 (2004) 3019.

173 C. Kerr, D. Barker, F. Walsh, Porosity and corrosion rate measurements for electroless nickel deposits on steel using electrochemical techniques, Transaction of the Institute of Metal Finishing 75 (1997) 81.

174 A.A. Aal, Hard and corrosion resistant nanocomposite coating for Al alloy, Materials Science and Engineering: A 474 (2008) 181.

175 P. Baghery, M. Farzam, A.B. Mousavi, M. Hosseini, Ni-TiO_2 nanocomposite coating with high resistance to corrosion and wear, Surface and Coatings Technology 204 (2010) 3804.

176 M.R. Vaezi, S.K. Sadrnezhaad, L. Nikzad, Electrodeposition of Ni-SiC nano-composite coatings and evaluation of wear and corrosion resistance and electroplating characteristics, Colloid Surface A, 315 (2008) 17.

177 N. Guglielmi, Kinetics of the deposition of inert particles from electrolytic baths, Journal of Electrochemistry Society 119 (1972) 1009.

178 J.P. Celis, J.R. Ross, C. Buelens, A mathematical model for the electrolytic codeposition of particles with a metallic matrix, Journal of Electrochemistry Society 134 (1987) 1402.

179 A. Gomes, M.I. da Silva Pereira, Pulsed electrodeposition of Zn in the presence of surfactants, Electrochimica Acta 51 (2006) 1342.

180 L. Chen, L. Wang, Z. Zeng, J. Zhang, Effect of surfactant on the electrodeposition and wear resistance of Ni-Al_2O_3 composite coatings, Materials Science and Engineering: A 434 (2006) 319.

181 A. Hovestad, L.J.J. Janssen, Electrochemical codeposition of inert particles in a metallic matrix, Journal of Applied Electrochemistry 25 (1995) 519.

182 Z.A. Hamid, A.M.A. Omar, The relation between anionic/non-ionic surfactant and electrodeposition of nickel-polytetrafluoro ethylene polymer composite, Anti-Corrosion Methods and Materials 46 (1999) 212.

183 I.R. Mafi, C. Dehghanian, Comparison of the coating properties and corrosion rates in electroless Ni-P/PTFE composites prepared by different types of surfactants, Applied Surface Science 257 (2011) 8653.

184 H.X. Guo, X.P. Zhao, H.L. Guo, Q. Zhao, Preparation of porous SiO_2/Ni/TiO_2 multicoated microspheres responsive to electric and magnetic fields, Langmuir 19 (2003) 9799.

185 L. Oniciu, L. Mureşan, Some fundamental aspects of levelling and brightening in metal electrodeposition, Journal of Applied Electrochemistry 21 (1991) 565.

186 J.O.M. Bockris, A.K. Reddy, Modern electrochemistry: an introduction to an interdisciplinary area, Springer Science & Business Media, New York, 1973.

187 V.D. Stankovic, M. Gojo, Electrodeposited composite coatings of copper with inert, semi-conductive and conductive particles, Surface and Coatings Technology 81 (1996) 225.

188 I. Paseka, Hydrogen evolution reaction on amorphous Ni-P and Ni-S electrodes and the internal stress in a layer of these electrodes, Electrochimica Acta 47 (2001) 921.

189 M.C. Chou, M.D. Ge, S.T. Ke, Y.R. Huang, S.T. Wu, The Ni-P-SiC composite produced by electro-codeposition, Materials Chemistry and Physics 92 (2005) 146.

190 A. Brenner, Electrodeposition of alloys, Journal of the Electrochemical Society 34 (1963) 111.

191 N. Guglielmi, Kinetics of the deposition of inert particles from electrolytic baths, Journal of Electrochemistry Society 119 (1972) 1009.

192 E. Pompei, L. Magagnin, N. Lecis, P.L. Cavallotti, Electrodeposition of nickel-BN composite coatings, Electrochemica Acta 54 (2009) 2571.

193 S.H. Yeh, C.C. Wan, Codeposition of SiC powders with nickel in a Watts bath, Journal of Applied Electrochemistry 24 (1994) 993.

194 M.K. Tripathi, D.K. Singh, V.B. Singh, Electrodeposition of Ni-Fe/BN Nano-Composite Coatings from a Non-aqueous Bath and Their Characterization, International Journal of Electrochemical Science 8 (2013) 3454.

195 L. Benea, P.L. Bonora, A. Borello, S. Martelli, F. Wenger, P. Ponthiaux, J. Galland, Composite electrodeposition to obtain nanostructured coatings, Journal of Electrochemistry Society 148 (2001) C461.

196 B.S.B. Reddy, K. Das, A.K. Datta, S. Das, Pulsed co-electrodeposition and characterization of Ni-based nanocomposites reinforced with combustion-synthesized, undoped, tetragonal-ZrO_2 particulates, Nanotechnology 19 (2008) 115603.

197 R. Elansezhian, B. Ramamoorthy, P. Kesavan Nair, Effect of surfactants on the mechanical properties of electroless (Ni-P) coating, Surface and Coatings Technology 203 (2008) 709.

198 A.H Graham, R.W. Lindsay, J.H. Read, Structure and mechanical properties of electroless nickel, Journal of Electrochemistry Society 112 (1965) 401.

199 C.K Chen, H.M Feng, H.C Lin, M.H Hon, The effect of heat treatment on the microstructure of electroless Ni-P coatings containing SiC particles, Thin Solid Films, 416 (2002) 31.

200 W.Y. Chen, S.K. Tein, F.B. Wu, J.G. Duh, Crystallization behaviors and microhardness of sputtered Ni-P, Ni-P-Cr and Ni-P-W deposits on tool steel, Surface and Coatings Technology 182 (2004) 85.

201J.P. Saiddington, G.R. Hoey, A Study of Transient Processes Preceding the Electrodeposition of Cr on Pt, Journal of The Electrochemical Society 120 (1973) 1475.

202 I. Apachitei, J. Duszczyk, L. Katgerman, P.J.B Overkamp, Electroless Ni-P Composite Coatings: The Effect of Heat Treatment on the Microhardness of Substrate and Coating, Scripta Materialia 38 (1998) 1347.

203 I Apachitei, F.D Tichelaar, J Duszczyk, L Katgerman, The effect of heat treatment on the structure and abrasive wear resistance of autocatalytic NiP and NiP-SiC coatings, Surface and Coatings Technology 149 (2002) 263.

204 A. Zoikis-Karathanasis, E.A. Pavlatou, N. Spyrellis, The effect of heat treatment on the structure and hardness of pulse electrodeposited NiP-WC composite coatings, Electrochimica Acta 54 (2009) 2563.

205 I. Apachitei, J. Duszczyk, L. Katgerman and P.J.B. Overkamp, Electroless Ni-P Composite Coatings: The effect of heat treatment on the microhardness of substrate and coating, Scripta Materialia 38 (1998) 1347.

206 S. Mehdizadeh, J.O. Dukovic, P.C. Andricacos, L.T. Romankiw, H.Y. Cheh, The influence of lithographic patterning on current distribution: A model for microfabrication by electrodeposition, Journal of the Electrochemical Society 139 (1992) 78.

207 C. Wang, Y. Zhong, W. Ren, Z. Lei, Z. Ren, J. Jia, A. Jiang, Effects of parallel magnetic field on electrocodeposition behavior of Ni/nanoparticle composite electroplating, Applied Surface Science 254 (2008) 5649.

208 M.C. Chou, M.D. Ger, S.T. Ke, Y.R. Huang, S.T. Wu, The Ni-P-SiC composite produced by electro-codeposition, Material Chemistry and Physic 92 (2005) 146.

209 M.H. Staia, E.J. Castillo, E.S. Puchi, D.B. Lewis, H.E. Hintermann, Wear performance and mechanism of electroless Ni-P coating, Surface and Coating Technology 86 (1996) 598.

210 A.J. Gould, Electroless nickel-a wear resistant coating, Transactions of the Institute of Metal Finishing 66 (1988) 58.

211 N.M. Renevier, J. Hamphire, V.C. Fox, J. Witts, T. Allen, D.G Teer, Advantages of using self-lubricating, hard, wear-resistant MoS_2-based coatings, Surface and Coatings Technology 142 (2001) 67.

212 E.W. Roberts, Thin solid lubricants in space, Tribology International 23 (1990)95.

213 W.O.Winer, Molybdenum disulphide as a lubricant: A review of the fundamental knowledge, Wear 10 (1967) 422.

214 R. Holinski, J. Gansheimer, A study of the lubricating mechanism of molybdenum disulphide, Wear 19 (1972)329.

215 M. Chhowalla, G.A. Amaratunga, Thin films of fullerene-like MoS_2 nanoparticles with ultra-low friction and wear, Nature 407 (2000) 164.

216 V. Buck, Morphological properties of sputtered MoS_2 films, Wear 91 (1983) 281.

217 G.C. Barton, S.V. Pepper, Transfer of molybdenum disulfide to various metals, NASA Technical Paper 1019.

218 L. Rapoport, Y. Bilik, Y. Feldman, M. Homyonfer, S.R. Chen, R. Tenne, Hollow nanoparticles of WS_2 as potential solid-state lubricants, Nature 387 (1997) 791.

219 C. Donnet, A. Erdemir, Historical developments and new trends in tribological and solid lubricant coatings, Surface and Coatings Technology 180 (2004) 76.

220 B. Deepthi, H.C. Barshilia, K.S. Rajam,, M.S. Konchady,, D.M. Pai,, J. Sankar, Structural, mechanical and tribological investigations of sputter deposited CrN-WS_2 nanocomposite solid lubricant coatings, Tribology International 44 (2011) 1844.

221 K. Vathsala, T.V. Venkatesha, S. Ranganatha, M.K. Punith Kumar, Zn-WS_2 Nanocomposite coatings on mild mteel: electrochemical aspects, Synthesis and Reactivity in Inorganic, Metal-Organic, and Nano-Metal Chemistry 42 (2012) 779.

222 L. Rapoport, M. Lvovsky, I. Lapsker, W. Leshchinsky, Y. Volovik, Y. Feldman, R. Tenne, Friction and wear of bronze powder composites including fullerene-like WS_2 nanoparticles, Wear 249 (2001) 149.

223 A. Brenner, Electrodeposition of alloys: principles and practice, Vol. 1. Elsevier, 2013.

224 Q. Feng, T. Li, Z. Zhang, J. Zhang, M. Liu, J. Jin, Preparation of nanostructured Ni/Al_2O_3 composite coatings in high magnetic field, Surface and Coatings Technology 201 (2007) 6247.

225 E.C. Lee, J.W. Choi, A study on the mechanism of formation of electrocodeposited Ni-diamond coatings, Surface and Coatings Technology 148 (2001) 234.

226 M. Srivastava, V.W. Grips, K.S. Rajam, Electrochemical deposition and tribological behaviour of Ni and Ni-Co metal matrix composites with SiC nano-particles, Applied Surface Science 253 (2007) 3814.

227 C. Guo, Y. Zuo, X. Zhao, J. Zhao, J. Xiong, Effects of surfactants on electrodeposition of nickel-carbon nanotubes composite coatings, Surface and Coatings Technology 202 (2008) 3385.

228 A.A. Aal, S.M. El-Sheikh, Y.M.Z. Ahmed, Electrodeposited composite coating of Ni-W-P with nano-sized rod-and spherical-shaped SiC particles, Materials Research Bulletin 44 (2009) 151.

229 F. Kılıç, H. Gül, S. Aslan, A. Alp, H. Akbulut, Effect of CTAB concentration in the electrolyte on the tribological properties of nanoparticle SiC reinforced Ni metal matrix composite (MMC) coatings produced by electrodeposition, Colloids and Surfaces A: Physicochemical and Engineering Aspects 419 (2013) 53.

230 B.S. Xu, H.D. Wang, S.Y. Dong, B. Jiang, W.Y. Tu, Electrodepositing nickel silica nano-composites coatings, Electrochemistry Communications 7 (2005) 572.

231 L.Wang, Y. Gao, T. Xu, Q. Xue, A Comparative study on the tribological behaviour of nanocrystalline nickel and cobalt coatings correlated with grain size and phase structure, Materials Chemistry and Physics 99 (2006) 96.

203 R.S. Dwyer-Joyce, Tribological design data part 3: Contact mechanics, The Tribology Group of The Institution of Mechanical Engineers, 1997. Accessed on 25th August 2015 [Online]. Available:
http://www.leonardocentre.co.uk/Media/Default/Documents/Book_3_contact_mechanics.pdf